ANALYTICAL AND EXPERIMENTAL METHODS FOR ADHESIVELY BONDED JOINTS SUBJECTED TO HIGH TEMPERATURES

by

Peter A. Gustafson

A dissertation submitted in partial fulfillment
of the requirements for the degree of
Doctor of Philosophy
(Aerospace Engineering)
in The University of Michigan
2008

Doctoral Committee:
Professor Anthony M. Waas, Chair
Professor Peretz P. Friedmann
Associate Professor Krishnakumar R. Garikipati
Mary A. Mahler, Raytheon Corporation

To my wife for the dreams that she inspires. To our family: past, present, and future. I love you all.

Acknowledgments

First and foremost, I offer my deepest thanks to my wife Tracy for her love and support during this unique period. Tracy, you brought joy to my life even in the darkest hours of this thesis. Your radiant smile is my daily inspiration. I cannot picture what life would be like if I had not found you.

Thank you Prof. Anthony M. Waas. This work was born of your encouragement and I am grateful for it. Your persistent excitement for solving engineering problems is contagious and the depth of your ideas can not be measured. I can only hope to maintain a shadow of your fervor as I continue my professional career.

Thank you to our family; Rev. Richard and Nancy Gustafson, Daniel and Elisha Gustafson, Janette and Craig Zeise, Theodore and Marilyn Datte, Stephanie Datte and Zachary Varner. Your support has been a blessing.

I gratefully acknowledge the faculty and staff at the University of Michigan. Prof. Peretz Friedmann, Prof. Carlos Cesnik, Prof. John Shaw, and Prof. Nicolas Triantafyllidis. Your instruction defined the field for me and deepened my interest in it. The experiments presented in this work were expertly and graciously supported by Terry Larrow, Thomas Griffin, David McClean, Eric Kirk, Chris Chartier, and Harold Eberhart. At times I lived in your offices; there are none better.

Thank you Prof. Anthony Waas, Prof. Peretz Friedmann, Prof. Krishna Garikipati, and Dr. Mary Mahler for serving on this dissertation committee. Your commitment to education is evidenced by the great sacrifices you make for your students.

There are several people who define this place for me. Thanks to Smith Thepvongs, Michael Bickle, L. James Sanchez, Sarah Brown, Dr. David and Dr. Heidi Lemmerhirt, Timothy and Emily Carlson, Deborah Buck, Natalie Spoelhof, John Boyer, and Robert Wohlgemouth. I am extremely grateful for your friendship.

To my colleagues, Amit Salvi, Dr. Wei Heok Ng, Dr. Hseng-Ji (Sam) Huang, Wooseok Ji, and Dr. Shunjun Song. I survived, at least in part, because of the things you taught me. Thank you.

Thanks to the Ford Motor Company and its employees for their support during

the early portion of this work. Thank you Dr. Tachi Chou, Dr. Raymond Kach, Dr. Agus Sudjianto, Dr. Xuming Su, and Dr. John Allison.

This work was supported by the Space Vehicle Technology Institute under grant NCC3-989 jointly funded by NASA and the DOD within the NASA Constellation University Institutes Project. Claudia Meyer was the project manager and Dr. Stanley Smeltzer III was project monitor.

Table of Contents

List of Tables

List of Figures

Figure

List of Appendices

Appendix

List of Symbols

$\alpha_{\kappa ii}$	Orthotropic thermal expansion coefficient of component κ
α_{pl}	Traction law shape factor
β, γ, ω	Lap joint system parameters
$\bar{\beta}$,$\bar{\gamma}$,$\bar{\omega}$,$\bar{\lambda}_1$,$\bar{\lambda}_3$	Dimensionless lap joint system parameters
$\beta\left(x, a, b\right)$	Beta probability density function
$\beta_{k,l}$	Regression coefficient
Δa	Apparent incremental crack advance
Δt	FE solver time increment
$\Delta u_{nm\,i}$	Relative displacement component
$\delta_i^{\mathrm{IP}}(j)$	Integration point relative displacement
ΔT	Temperature change from a reference temperature
$\Delta t_{\max}$	Maximum allowed increment size
$\Delta t_{\mathrm{mean}}^{10}$	Mean increment size for the smallest 10 increments
Δt	Increment size
$\frac{\delta}{\delta_{\mathrm{c}}}$	Traction law relative displacement
δ	Separation or displacement
δ_{c}	Critical separation
$\varepsilon_{\kappa ij}$	Strain in material κ
η_{inc}	Incremental efficiency
η_{iter}	Iterative efficiency
μ_{nmi}	Damping viscosity for nodes n, m at integration point i

μ	Friction coefficient
$\nu_{\kappa ij}$	Poisson's ratios of component κ
Γ_{actual}	Actual number of iterations
Γ_{min}	Ideal number of iterations
Π	Potential energy
φ	Area weighting factor
$\bar{\phi}_{\text{aR}}$,$\bar{\phi}_{\text{cR}}$	Dimensionless thermal to mechanical load ratios
$\bar{\bar{\phi}}_P$,$\bar{\bar{\psi}}_P$	Dimensionless mechanical load fractions
$\bar{\bar{\phi}}_{\text{tot}}$,$\bar{\bar{\psi}}_{\text{tot}}$	Dimensionless total load parameters
$\bar{\phi}_P$,$\bar{\psi}_P$	Dimensionless mechanical load parameters
$\bar{\phi}_{\Delta T}$,$\bar{\psi}_{\Delta T}$	Dimensionless thermal load parameters
ϕ_P,$\phi_{\Delta T}$	Mechanical and thermal load parameters
$\hat{\sigma}_{\kappa 11(x)}$	Longitudinal virtual stress in component κ
$\hat{\sigma}_{\kappa 22(x,y)}$	Transverse virtual stress in component κ
σ	Sample standard deviation of experimental quantities
$\sigma_{\kappa 11(x)}$	Longitudinal stress in component κ
$\sigma_{\kappa 22(x,y)}$	Transverse stress in component κ
σ_{c}	Cohesive strength of the adhesive system
$\bar{\sigma}_{\text{Ic}}$,$\bar{\tau}_{\text{IIc}}$	Normalized critical stresses
$\sigma_i(\delta_i^{\text{IP}}(j))$	Cohesive traction separation law of the adhesive system
$\sigma_\beta\left(\frac{\delta}{\delta_{\text{c}}}, a, b\right)$	Beta distribution traction law
$\bar{\sigma}_{a11}$	Dimensionless stress in the central adherend
$\bar{\bar{\sigma}}_{a11}$	Normalized dimensionless stress in the central adherend
$\sigma_{\text{sin}}\left(\frac{\delta}{\delta_{\text{c}}}\right)$	sinusoidal traction law
$\hat{\tau}_{\kappa 12(x)}$	Shear virtual stress in component κ
$\tau_{\kappa 12(x)}$	Shear stress in component κ

ξ_0, ξ_1	Example LHS parameters
$\zeta(j)$	Element local coordinate
a	Crack length measured from the hinge axis
a,b	Beta probability density function parameters
$\bar{a}$,$\bar{b}$,$\bar{\bar{a}}$,$\bar{\bar{b}}$	Dimensionless basis coefficients
b	Specimen width
c_0,c_1,d_1,d_0	Integration constants
c_{i+1}^M	Correction vector in the increment $i+1$
h	Adherend thickness
l_e	Length of current sub-element
l_l	Lap length
l_n	Notch length
l	Specimen length, m
l_g	Grip length
j	Integration point identifier
n_IP	Number of integration points
q_e	Sub-element extension degree of freedom
q_1,q_2,q_3,q_4	Nodal displacement degrees of freedom
t_κ	Material thicknesses of component κ
u_a	Axial displacement field
$u_{n\,i}$	Displacement component
u_i^M	Displacement vector in increment i
u_el	Element displacement vector
w_tip	DCB tip displacement
x,y,z	Cartesian coordinates
$\bar{x}$	Joint natural coordinate $\frac{x}{l_\mathrm{l}}$ measured from the left edge of the joint

$\bar{x}$	Sub-element natural coordinate $\frac{x}{l_e}$ measured from the left edge of the sub-element
$A(j)$	Cohesive area
$\bar{A}$,$\bar{B}$,$\bar{C}$,$\bar{D}$	Dimensionless basis coefficients
$\bar{\bar{A}}$,$\bar{\bar{B}}$,$\bar{\bar{C}}$,$\bar{\bar{D}}$	Dimensionless basis coefficients
A_{BPS}	Bond area
A_{crack}	Crack area
B_a, B_c	Element shape function derivatives
$C(a)$	Compliance function
C_μ	Zone of viscous influence
D	Plate stiffness
$E_{\kappa ii}$	Orthotropic engineering moduli of component κ
E	Elastic modulus
F	Force in an end post
$F_{nm\,i}$	Element force component
F_{el}	Element force vector
F_i^N	Force vector in increment i
G_{bij}	Orthotropic shear modulii of the adhesive
G_{c}	Critical energy release rate
$\bar{G}_{\mathrm{Ic}}^{\mathrm{a}}$	Normalized area method critical energy release rate
$G_{\mathrm{Ic}}^{\mathrm{i}}$	Inverse method critical energy release rate
$G_{\mathrm{Ic}}^{\mathrm{i\,ave}}$ $(T = 20)$	Average critical energy release rate at room temperature
$\bar{G}_{\mathrm{Ic}}^{\mathrm{i}}$	Normalized inverse method critical energy release rate
$\bar{G}_{\mathrm{Ic}}$,$\bar{G}_{\mathrm{IIc}}$	Normalized critical energy release rates
I	Area moment of inertia
$K_{nm\,i}$	Stiffness matrix component
$K_i^{k\,\mathrm{IP}}(j)$	Integration point mechanical stiffness

$K_i^{\mu\,\mathrm{IP}}(j)$	Integration point viscous stiffness
K_{el}	Element stiffness matrix
$M\,(x)$	Moment in cantilever arm
N_a, N_c	Element shape functions
$N_1(j)$,$N_2(j)$	Element shape functions
P	Mechanical load per unit depth
$\bar{P}$	Mechanical load per unit depth
$\bar{P}_{\mathrm{max}}$	Maximum mechanical load per unit depth
P_{fail}	Failure load
P_1,P_2	Element internal mechanical load DOFs, per unit depth
R^2	Linear correlation coefficient of determination
T	Temperature
U	Strain energy
V	Volume of the structural domain
W	Potential energy of external loads
W_{dis}	Work that is lost to dissipation
W_{ext}	External work during the displacement cycle
W_{frac}	Work that creates fracture surfaces
W_{pl}	Work that creates adherend permanent deformation
W_{tot}	Total work expended during a displacement cycle
$\bar{\bar{\Phi}}_{\mathrm{a}}$,$\bar{\bar{\Phi}}_{\mathrm{c}}$,$\bar{\bar{\Xi}}_{\mathrm{a}}$,$\bar{\bar{\Xi}}_{\mathrm{c}}$	Simplification coefficients
$\chi_{\Delta T}$,χ_P	Simplification coefficients
μ_{A_P},μ_{B_P},μ_{C_P},μ_{D_P}	Simplification coefficients
$\mu_{A_{\Delta T}}$,$\mu_{B_{\Delta T}}$,$\mu_{C_{\Delta T}}$,$\mu_{D_{\Delta T}}$	Simplification coefficients
μ_1,μ_2,μ_3,μ_4,μ_5	Simplification coefficients
θ_β,θ_γ,$\theta_{\Delta T}$,θ_P,Θ	Simplification coefficients
i	The direction component of a vector

n or nm	Acting on node n or between nodes n and m
[]	the *or* operator, i.e. [13] is 1 *or* 3 (no sum)
κ	$\kappa = [abcp]$ (no sum) Subscript representing central adherend (a), adhesive (b), outer adherend (c), and end post (p) respectively
ii	$i = [123]$ (no sum)
ij	$i, j = [123]$ where $i \neq j$ (no sum)

List of Acronyms

AL aluminum

AS4 AS4/3501-6

ASTM ASTM International

BDTL beta distribution traction law

BJFE bonded joint finite element

BPS button peel stress

CC compliance calibration

CCZM continuous cohesive zone method

CPE4I linear plain strain elements

CPU central processing unit

DACE design and analysis of computer experiments

DCB double cantilever beam

DCZM discrete cohesive zone method

DLJ double lap joint

DOD Department of Defense

DOE design of experiments

DOF degrees of freedom

ENF end notch flexure

FE finite element

LHS Latin hypercube sampling

NASA National Aeronautics and Space Administration

PDF probability density function

SLJ single lap joint

SO shear-only model

SP shear-peel model

SST simple structural test

STL sinusoidal traction law

TI titanium

TTL trapezoidal traction law

UEL user element subroutine

Abstract

Recent advances in material systems have expanded the temperature range over which adhesively bonded composite joints can be used. In this work, several tools are developed for use in modeling joints over a broad range of temperatures. First, a set of dimensionless parameters is established which can be used for analysis of joint performance for an orthotropic symmetric double lap joint. A critical dimensionless ratio of mechanical and thermal loads is identified. The ratio predicts characteristics of the resulting stress distribution. A bonded joint finite element is also developed, wherein a joint-specific finite element is formulated based on an analytical solution. The resulting element allows for mesh-independent joint evaluation and multi-joint simulation at a system or vehicle level. As a mid-level analysis technique, the element has significant predictive and cost advantages over the previously available methods. An advanced analysis technique, the discrete cohesive zone method, is developed and demonstrated in a general element formulation. Initially, the element is examined from the perspective of computational efficiency and robustness. Two efficient traction laws are formulated and are compared to a traction law that is in common use. The element is subsequently used to investigate the interactions of adhesive parameters in standard adhesive characterization experiments. This quantification of experimental sensitivities allows for a deliberate mapping of cumulative experimental results to an appropriate set of model constitutive parameters. With knowledge of the parameter interactions, a set of experimental results are interpreted to determine a set of adhesive constitutive parameters for T650/AFR-PE-4/FM680-1, a high temperature material system of current interest.

Chapter 1

Introduction

1.1 Motivation

The use of advanced composite materials has increased significantly over the last decade and is expected to be a dominant class of materials for aircraft and spacecraft for the foreseeable future. Composite materials have been used extensively in high performance and military application where cost is secondary to performance. Advances in manufacturing techniques, increased volumes, environmental concerns, and accumulated field experience have made the technology accessible for a larger customer base. This base includes commercial aircraft, energy generating structures, prosthetic devices, and consumer products.

Technological improvements in composite materials have been accompanied by an improvement in structural adhesives. As a result, the use of bonded joints has supplemented or replaced the use of traditional mechanical fasteners in composite and metallic structures. In these structures, adhesively bonded joints are in common use due to improved load distribution, increased service life, reduced machining cost, and/or reduced complexity, [4]. Confidence in such joints has grown with accumulated usage as evidenced by the implementation of bonded joints in the joint strike fighter and long range strike aircraft programs, [19, 121]. Additionally, adhesively bonded composite joints have expanded into the automotive industry, [82]. Despite this significant increase in usage, it is prudent to recall the claim of Her [56] that approximately 70% of structural failures initiate in joints. Therefore, joint design is critical to structural integrity.

Beyond the increased usage associated with lower costs and improved manufacturing techniques, recent advances in structural epoxies and adhesives have also expanded

the temperature range over which fibrous composite materials can be used. These epoxies and adhesives, developed to provide structural integrity at high temperature, are subjected to operating environments that are more severe than have been previously specified for bonded joints. Furthermore, the required manufacturing processes impose broad temperature ranges during the curing cycle. As a result, it is known that high stress gradients can exist near the edges of bonded joints due to mismatches in thermal expansion coefficients and elastic moduli, [77]. Components made from these materials carry a significant risk of adverse stress caused by differential thermal expansion. Due to the increased use of composite materials and bonded joints, the need for efficient and effective thermo-mechanical analysis tools is great.

The design of joints is often carried out in an ad-hoc fashion that relies heavily on laboratory testing and empirical models. If the role of temperature resistant composites is to expand, their use must be supported by an improved understanding of bonded joints. Additional research is required in order to expand the modeling capability for bonded joints and to determine the mechanical response of material systems over their range of use.

1.2 Objectives and outline of the dissertation

The present study is motivated by three primary objectives for bonded composite joints: the development of robust and efficient analytical tools, the reporting of constitutive interactions that are present in common test methods, and the accumulation of experimental data in support of the analytical developments in the dissertation. These are distinct objectives, each with a significant body of literature. In lieu of a comprehensive literature review in this introductory chapter, the primary objectives are briefly introduced and a contextual overview is provided in this section. A thorough literature review of the chapter-level objectives is provided in the introduction to each chapter. The structure of the dissertation is illustrated in figure 1.1.

1.2.1 Robust and efficient analytical tools

It is critical that robust modeling tools are developed for the design and analysis of adhesively bonded joints. Therefore, three separate techniques are developed that represent a variety of approaches to evaluating structures with bonded joints.

The first contribution is a set of dimensionless parameters for predicting the stress

field in a specific composite joint. To demonstrate the methodology, several virtual work solutions are computed for an orthotropic symmetric double lap joint that is subjected to thermal and mechanical loading. The solutions, presented in chapter 2, differ in complexity and accuracy. Each solution yields dimensionless parameters that can be used for comparative analysis of joint stress. Using the dimensionless parameters, a designer can quickly ascertain the effect of a change in that specific joint. To demonstrate the utility of the method, analytical stress predictions are compared to numerical results predicted by a finite element (FE) analysis and are found to be in good agreement.

A second and related technique is presented in chapter 3. FE models are widely employed for analyzing joints. Continuum FE techniques, however, have limitations that are revealed in any attempt to create a model for that purpose. In order to overcome some of these limitations, a bonded joint finite element (BJFE) is formulated. The BJFE provides a method to analyzing the stress field of a joint using a single finite element. In doing so, it overcomes two major obstacles in joint analysis: mesh generation and mesh dependency. To create the BJFE element, a virtual work solution for the joint is embedded as a shape function of the element. As a result, the strain and stress fields are accurately represented using a small number of degrees of freedom. The BJFE element is a mid-level analysis technique that allows effective comparison of multiple joints in a single analysis with no mesh dependency. It is targeted for early design and sizing studies where high-level analyses techniques are prohibitively expensive and high-fidelity material properties are unavailable.

A third analytical technique is presented in chapter 4 and is referred to as the discrete cohesive zone method (DCZM). Whereas the BJFE is developed for early analysis and design studies, the DCZM element is intended for high-level predictions and progressive failure analysis of bonded joints. Building on the foundation of its predecessors, the DCZM element is formulated as a set of non-linear springs that enforce a specified traction law.[1] The traction law is modular and can be chosen based on several criteria. The method incorporates crack initiation and propagation and allows for accurate computations of load history during joint failure. The effect of the traction law on the efficiency, robustness, and cost of the solution is also examined in chapter 4.

[1] The phrases "traction law" and "traction separation law" are used in the literature to describe spring-based cohesive constitutive relationships. For brevity, "traction law" is used in this dissertation.

1.2.2 Constitutive interactions in common experimental methods

The foundation for any validated failure analysis technique is a database of experimental observations that can be used for model comparison. In the context of modeling decohesion in structures, it is necessary to determine the critical parameters that govern failure. These include a set of crack initiation (σ_c) and propagation (G_c) parameters for each fracture mode.

Although the determination of σ_c and G_c is necessary for modeling the decohesive behavior of any adhesive or laminated system, it is also necessary to consider the assumptions that are made in computing these values from experimental results. Traditional data reduction techniques make assumptions about the traction law and experiments which may not correspond to the assumptions necessary for robust numerical modeling. In addition to uncertainty regarding the assumed traction law and its relation to the real traction response, there are also uncertainties and interactions (present in the models and experiments) that can affect the interpretation of an experimental result. Traditional methods of mapping the experimental result to a numerical implementation may provide a poor set of parameters for computation.

To address these uncertainties in the characterization experiments, a sensitivity analysis has been completed and is reported in chapter 5. The outcome of the sensitivity study provides a methodology for mapping a set of experimental results to a set of appropriate constitutive parameters. The methodology accounts for the unavoidable interactions and uncertainties that are present in all experiments. It also provides justification for choosing a traction law based on efficiency and robustness.

1.2.3 Accumulation of experimental data

Proper design of joints requires accurate descriptions of the material systems which compose the joint. As a result, this dissertation includes an investigation of the temperature dependence of a specific material system of current interest. T650/AFR-PE-4/FM680-1 is a temperature resistant material system that is being qualified for use in aeroshell structures [107] and other applications. It is essential that this material system be characterized over the range of its expected use; therefore, values of the necessary cohesive parameters have been determined in Mode I and Mode II up to 350 °C. The results of this investigation are presented in chapter 6.

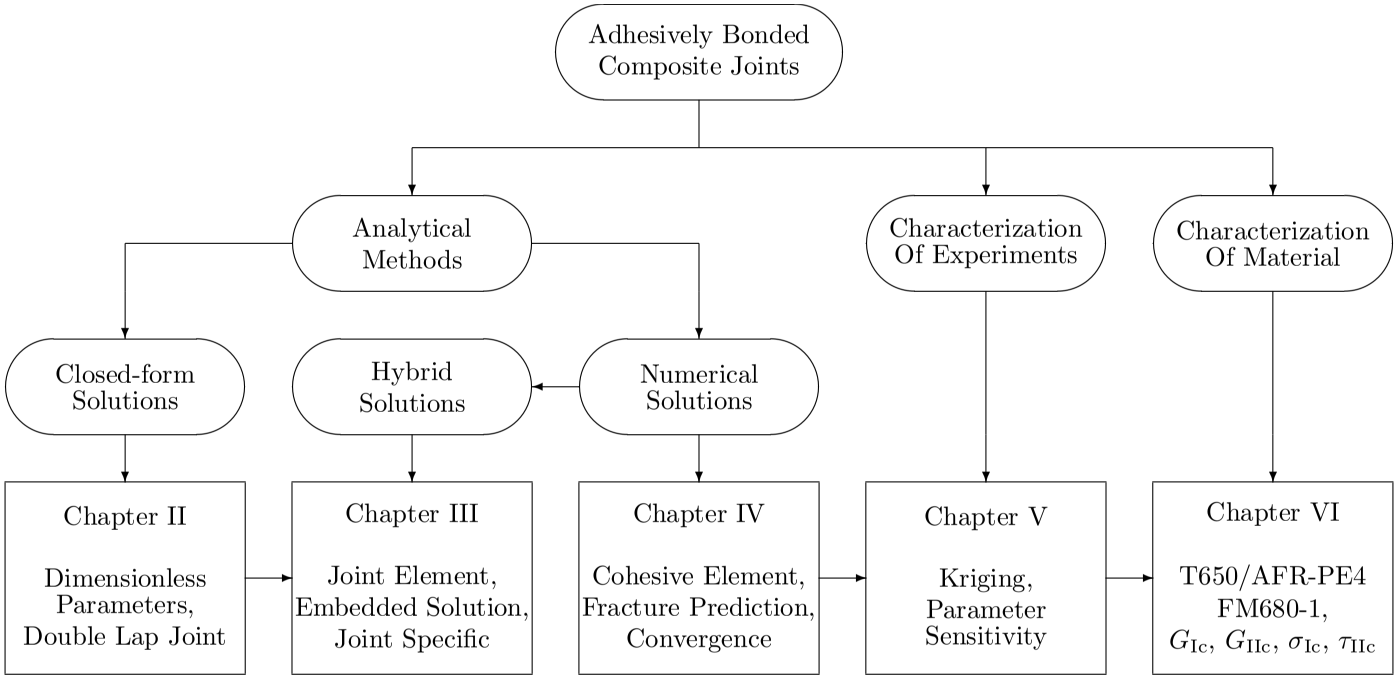

Figure 1.1 Structure of the dissertation

1.3 Significant contributions of this dissertation

The following contributions to the field of temperature dependent adhesively bonded joint analysis are reported in this dissertation:

1. Analytical solutions and dimensionless numbers for quick assessments of double lap joint performance when subjected to thermal and mechanical loads.
2. A dimensionless number characterizing the relative importance of mechanical and thermal loads (or any scalar load) to a lap joint.
3. A bonded joint finite element technique that can be used to compute all critical kinematic and kinetic values in a joint from a single element.
4. A 2D/3D implementation of a discrete cohesive zone method finite element with a modular traction law.
5. Two efficiency and robustness oriented traction laws for use in the prediction of adhesive/cohesive failure or delamination. Additionally, an implementation of a commonly used traction law as a module for the DCZM element.
6. A sensitivity analysis for three common adhesive tests. The outcome is a quantification of the interactions between constitutive and geometric parameters that are inseparable during experiments and modeling.
7. A technique for mapping a complete set of adhesive experimental results to a complete set of adhesive parameters. The technique accounts for the interactions that are present in the adhesive experiments.
8. A technique for inverse modeling of the value of G_{Ic} from the double cantilever beam test.
9. An experimental determination of the fracture parameters for T650/AFR-PE-4/FM680-1 over the temperature range of 20-350 °C. These parameters are required to predict failure in joints composed of this material system.

1.4 Publications related to this dissertation

The following publications are available at the time of the dissertation defense:

1. Peter A. Gustafson and Anthony M. Waas. *Efficient and robust traction laws for the modeling of adhesively bonded joints.* In Proceedings of the AIAA/ASME/ASCE/AHS/ASC 49$^{\mathrm{th}}$ Structures, Structural Dynamics, and Materials Conference, Apr 7-10 2008, Schaumburg, IL, number 2008-1847. American Institute of Aeronautics and Astronautics, 2008.
2. Peter A. Gustafson, Arnaud Bizard, and Anthony M. Waas. *Dimensionless parameters in symmetric double lap joints: An orthotropic solution for thermomechanical loading.* International Journal of Solids and Structures, 44(17):5774–5795, August 2007
3. Peter A. Gustafson and Anthony M. Waas. *T650/AFR-PE-4/FM680-1 Mode I critical energy release rate at high temperatures: Experiments and numerical*

models. In Proceedings of the AIAA/ASME/ASCE/AHS/ASC 48$^{\text{th}}$ Structures, Structural Dynamics, and Materials Conference, Apr 23-26 2007, Honolulu HI, number 2007–2305. American Institute of Aeronautics and Astronautics, 2007.

4. Peter A. Gustafson and Anthony M. Waas. *A macroscopic finite element for a symmetric double lap joint subjected to mechanical and thermal loading.* In Proceedings of the AIAA/ASME/ASCE/AHS/ASC 48$^{\text{th}}$ Structures, Structural Dynamics, and Materials Conference, Apr 23-26 2007, Honolulu HI, number 2007–2308. American Institute of Aeronautics and Astronautics, 2007. Also presented at: 16$^{\text{th}}$ International Conference on Composite Materials, Kyoto Japan, 2007.
5. Peter A. Gustafson and Anthony M. Waas. *A macroscopic joint finite element for a symmetric double lap joint.* In Proceedings of the American Society of Composites 21$^{\text{st}}$ Annual Technical Conference, number 204. American Society of Composites, Sept 2006.
6. Peter A. Gustafson, Arnaud Bizard, and Anthony M. Waas. *Dimensionless parameters in symmetric double lap joints: an orthotropic solution for thermo-mechanical loading.* In Proceedings of the AIAA/ASME/ASCE/AHS/ASC 47$^{\text{th}}$ Structures, Structural Dynamics, and Materials Conference, May 1-4 2006, Newport RI, number 2006–1959. American Institute of Aeronautics and Astronautics, 2006.

The contents of this dissertation that are not contained in the listed publications are in preparations for dissemination in conference or journal papers.

Chapter 2

Dimensionless parameters in symmetric double lap joints: an orthotropic solution for thermomechanical loading

Analysis of joints can be conducted using several methodologies. The two most prevalent methods are closed-form analytical solutions and numerical solutions; hybrid methods can also be developed. In this chapter, two closed-form thermomechanical analytical models are developed for orthotropic double lap joints with a view to identifying dimensionless parameters that describe the behavior of the joint under combined thermomechanical loads. The solutions, based on the principle of virtual work, differ in the complexity of the assumed stress field. The first solution is similar to Volkersen [104] with the addition of orthotropic and thermal effects. The second solution, extending the work of Davies [39], captures the peel stress as well as the traction free boundary condition at the adhesive edge. Relevant dimensionless parameters are identified in terms of geometric, material, and load quantities. A dimensionless load ratio is identified which dictates the shape of the stress distribution. This ratio can also be used to determine the dominant loading mechanism. Dimensionless stress plots are presented for representative lap joints.

2.1 Introduction

The main objective of this chapter is to develop appropriate dimensionless parameters that govern joint performance under combined thermal and mechanical loading. These

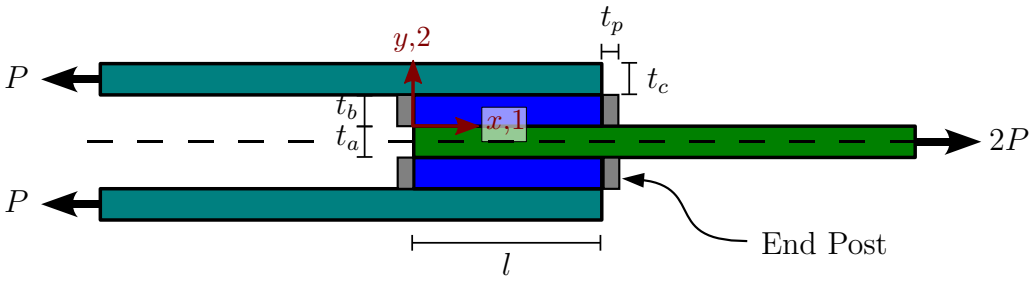

Figure 2.1 Schematic of the double lap joint with end posts

parameters can be used to identify the effects of material orthotropy and joint geometry on joint performance. Two thermomechanical models are presented for the symmetric double lap joint shown in figure 2.1, a common joint. The first model, referred to as the shear-only model (SO), can be considered a thermomechanical extension to Volkersen [104]. The joint response is calculated based on the assumption of a simplified stress field. The solution provides a basic methodology for predicting the effects of key parameters on the global shear response of the joint. A second model extends the first to allow for the calculation of peel stresses while simultaneously satisfying the traction free boundary condition at the adhesive edge. It will be referred to as the shear-peel model (SP). To establish the utility of these models, both are compared to a reference continuum finite element (FE) model. Finally, both analytical models are found to contain an identical dimensionless ratio of thermal to mechanical loads. The ratio can be used to identify the relative importance of the two load types to joint design.

2.2 A brief summary of double lap joint analytical models

Several authors have provided analytical solutions to bonded joints. The first author was Volkersen [104] who was followed by Goland and Reissner [51]. Both presented solutions to the single lap joint. An incomplete list of references on the single lap joint includes Hart-Smith [55], Peppiatt [80], Renton and Vinson [85], Allman [10], Her [56], and Yang et al. [117]. Summary articles have been provided by Benson [20] and Adams et al. [4]. A corresponding list of references on the double lap joint includes Hart-Smith [54], Gilibert and Rigolot [48], Sen and Jones [91], Sen and Jones [90], Her [56], Mendels et al. [69], and Mortensen and Thomsen [71]. The last of these is an analytical derivation of the governing equations, though the lack of an available closed-form solution causes the evaluation to be numerical. The double lap solution

of Davies [39] inspired the shear-peel model analysis of the current work. Though intended for single lap joints, the work of Volkersen [104] could be used for double lap joints with only slight modification.

There are several important issues in bonded lap joints which have been neglected or have been outside the scope of the analysis. Three of these issues will be considered in the derived models. First, in an idealized lap joint, the edge of the adhesive is a traction free surface. The average shear stress builds to an extremum over a small boundary region. Though this is captured in some models, it is not captured in the influential work of Goland and Reissner [51]. For example, in the double lap solution of Hart-Smith [54], inappropriate interpretation of the model could lead to a conclusion that the shear stress is maximized at the edge of the adhesive, where it is actually zero. Several authors have developed double lap joint models which capture the traction free boundary condition, however, the derived solutions are either numerical [90, 91] or the governing differential equation is of high order [108]. Though the models which do not resolve the traction free edge condition can be correctly interpreted by an analyst (as is required for the SO solution in section 2.3.1), it is advantageous and analytically more pleasing to satisfy this boundary condition when possible. It was noted by Benson [20] that a minimum 4^{th} order differential equation (of the displacement field) is required to capture the traction free surfaces. The SP solution of this work satisfies the requirement. The direct advantage over the SO solution is the ability to calculate peel stress.

A second issue in the available literature is a lack of accounting for the anisotropic material behavior of the joint constituents (adherends and adhesive) in analytical form. Exceptions exist, for example Erdogan and Ratwani [46] and Delale et al. [44], however, these are neither double lap joint models nor are *all* constituents anisotropic. This lack of an anisotropic material description is critical when considering laminated composite materials. Transverse properties are often significantly lower than in-plane properties for a given laminate, [54]. Recent research into transverse reinforcement of composite laminates such as z-pin [25, 30, 98] and 3D woven composites [31, 60, 73] increases the relevance of anisotropic joint solutions, particularly with respect to the anisotropic nature of the adhesive. Finally, since high temperature curing cycles are frequently needed for temperature resistant materials, prudence dictates that anisotropic material behavior should be included in thermomechanical analytical models. This need has been recognized and is an active area of current research.[1] In contrast, this chapter provides closed-form, parametric solutions with orthotropic material properties in

[1] Recent work includes: [19, 71, 72, 118, 120–122].

all constituents. The parametric nature of these solutions reveal insights into joint performance.

A third issue in the prior treatment of bonded joints is found at the corner interfaces between the adherends and the adhesive. In these locations, geometric discontinuities cause unbounded stress concentrations in any solution based on linear elastic continuum mechanics, [61]. Though non-linear material response might ensure that the stress remains finite, [122], the peak stresses at the corners are dependent on the specific geometry and material behavior. The possible effects are not considered in the analytical models presented in this dissertation since they require different modeling strategies rooted in fracture mechanics. The geometric discontinuity, however, affects the FE models which are used for comparison and therefore must be considered when evaluating the FE results. Specifically, it is important to recognize that the reference linear elastic FE model in this work is not a *correct* solution at the corners. It is flawed at these geometric discontinuities and the stress concentrations will not converge with increasing element density. Therefore, direct comparisons between the FE solution and the analytical solutions are only meaningful away from the singular corners. In contrast to FE based solutions which do not readily allow consistency from analysis to analysis, the closed-form analytical models in this dissertation do allow for meaningful comparison between different joint designs. The models have no mesh dependence and the predicted stresses remain finite for all joint geometries.

Finally, temperature effects were not considered in most of the analytical double lap joint models that are currently available. The authors are aware of the work of Hart-Smith [54], Chen and Nelson [26], Vinson and Zumsteg [103], and Adams et al. [2] who included thermal effects in their solutions. Hart-Smith provided a double lap joint solution which included thermal loading, however, the work focused on material non-linearities and did not capture the traction free boundary condition, [54]. The bonded joint solutions of Chen and Nelson [26] include thermal expansion, however, the materials are isotropic and no double lap analysis is included. The contributions of Vinson and Zumsteg [103] include a composite thermomechanical solution of a double lap joint. The solution is difficult to evaluate, however, as it requires the solution of eighteen simultaneous boundary conditions which can only be reasonably solved numerically. Qualitative assessments cannot be made since no plots of the predicted stresses were provided. Finally, the work of Adams et al. [2] focused on thermal loading in lap joints, however, the subject matter was single lap joints and the solutions were FE based. In the following sections of this paper, two thermomechanical analytical models of the double lap joint are presented and appropriate dimensionless

parameters are identified. These models are shown to be useful in evaluating the thermomechanical performance of the joint.

2.3 Analytically derived stress field in a double lap joint including thermal expansion

A schematic of a double lap joint is shown in figure 2.1; a symmetric geometry is assumed and two solutions are presented.

2.3.1 Model where the adhesive carries only shear stress

In the first solution, it is assumed that the stress field only varies along the direction of loading. The adherends are assumed to carry only longitudinal normal stress and the adhesive is assumed to carry only shear stress. Due to symmetry, the bending moments in the joint are assumed to be negligible and bending of the adherends is not included. Under these assumptions, the stress field is only a function of x.[2] Thermal expansion is assumed to be linear with temperature. Though it is likely they are significant [54], plasticity, creep, and other non-linearities of the constituents are ignored. With those restrictions and assuming plane strain deformation, the constitutive equations for material κ are governed by:

$$\begin{Bmatrix} \varepsilon_{\kappa 11}(x) \\ \varepsilon_{\kappa 22}(x) \\ \gamma_{\kappa 12}(x) \end{Bmatrix} = \begin{bmatrix} \frac{1-\nu_{\kappa 13}\,\nu_{\kappa 31}}{E_{\kappa 11}} & -\frac{\nu_{\kappa 23}\,\nu_{\kappa 31}+\nu_{\kappa 21}}{E_{\kappa 22}} & 0 \\ -\frac{\nu_{\kappa 13}\,\nu_{\kappa 32}+\nu_{\kappa 12}}{E_{\kappa 11}} & \frac{1-\nu_{\kappa 23}\,\nu_{\kappa 32}}{E_{\kappa 22}} & 0 \\ 0 & 0 & \frac{1}{G_{\kappa 12}} \end{bmatrix} \begin{Bmatrix} \sigma_{\kappa 11}(x) \\ \sigma_{\kappa 22}(x) \\ \tau_{\kappa 12}(x) \end{Bmatrix} + \begin{bmatrix} \alpha_{\kappa 33}\,\nu_{\kappa 31} + \alpha_{\kappa 11} \\ \alpha_{\kappa 33}\,\nu_{\kappa 32} + \alpha_{\kappa 22} \\ 0 \end{bmatrix} \Delta T \tag{2.1}$$

A plane stress assumption could be substituted by setting the out-of-plane Poisson terms to zero ($\nu_{\kappa 13} = \nu_{\kappa 31} = 0$). The central adherend is referred to as material a; an equilibrium element for the central adherend is pictured in figure 2.2(a). Figure 2.2(b) represents the outer adherend, referred to as material c. In these two areas,

[2] Although they greatly simplify the computation of the stress field, these assumptions do not strictly satisfy equilibrium requirements.

x-equilibrium requires:

$$\begin{aligned} \frac{d\sigma_{a11}(x)}{dx} &= -\frac{2}{t_a}\tau_{b12}(x), \\ \frac{d\sigma_{c11}(x)}{dx} &= -\frac{1}{t_c}\tau_{b12}(x), \end{aligned} \tag{2.2}$$

where x is measured from the left edge of the adhesive. Solving equation 2.2 for $\tau_{b12}(x)$ and equating leads to:

$$t_c \frac{d\sigma_{c11}(x)}{dx} = \frac{t_a}{2}\frac{d\sigma_{a11}(x)}{dx}. \tag{2.3}$$

The natural boundary conditions at the edge of adherend a are:

$$\begin{aligned} \sigma_{a11}(0) &= 0, \\ \sigma_{a11}(l) &= \frac{2P}{t_a}. \end{aligned} \tag{2.4}$$

Equation 2.4 is the longitudinal normal stresses in the central adherend at the edges of the joint. Combining equations 2.2-2.4 yields a relationship between stresses in the central and outer adherends:

$$\sigma_{c11}(x) = \frac{P}{t_c} - \frac{t_a}{2t_c}\sigma_{a11}(x). \tag{2.5}$$

Since the shear stress is assumed to be constant through the thickness of the adhesive, the shear stress in the adhesive is determined by equation 2.2 and the solution to equation 2.5. As summarized in appendix A, equations 2.2-2.5 can be combined using the principle of virtual work to solve for the central adherend stress. Doing so leads to a differential equation in the following form:

$$\frac{d^2\sigma_{a11}(x)}{dx^2} + \omega^2\sigma_{a11}(x) + \psi_{\Delta T} + \psi_P = 0. \tag{2.6}$$

In equation 2.6, the thermal and mechanical loads enter the differential equation in the form of system parameters ($\psi_{\Delta T}$ and ψ_P). Before stating the values of the system parameters (ω^2, $\psi_{\Delta T}$, and ψ_P), it is reasonable to non-dimensionalize equation 2.6,

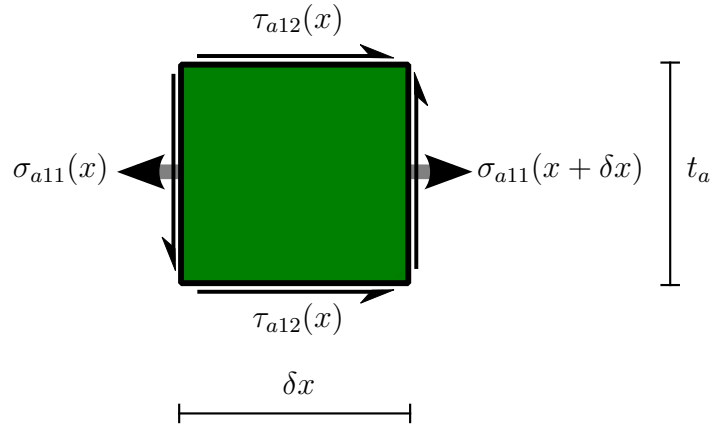

(a) Equilibrium element of the central adherend

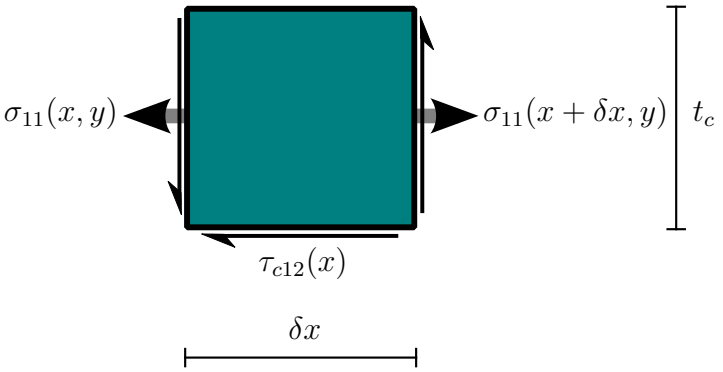

(b) Equilibrium element of the outer adherend

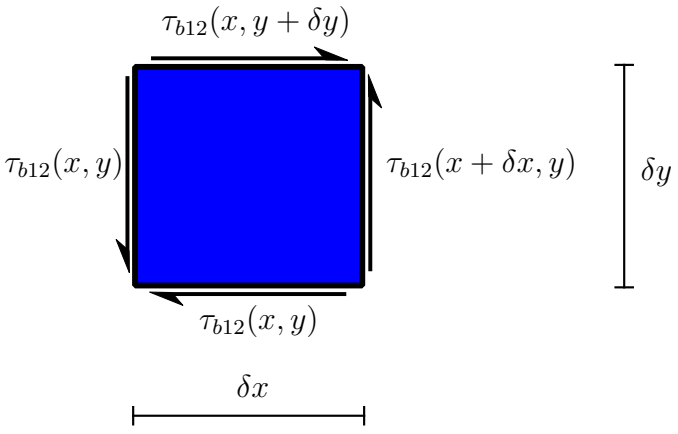

(c) Equilibrium element of the adhesive

therefore the following substitutions are made:

$$\begin{aligned}
\bar{\psi}_{\Delta T} &= \psi_{\Delta T}\frac{l^2}{E_{a11}},\\
\bar{\psi}_{P} &= \psi_{P}\frac{l^2}{E_{a11}},\\
\bar{x} &= \frac{x}{l},\\
\bar{\omega} &= l\omega,\\
\bar{\tau}_{b12}(\bar{x}) &= \frac{\tau_{b12}(l\bar{x})}{E_{a11}},\\
\bar{\sigma}_{a11}(\bar{x}) &= \frac{\sigma_{a11}(l\bar{x})}{E_{a11}}.
\end{aligned} \tag{2.7}$$

In equation 2.7, the dimensionless axial stress $\bar{\sigma}_{a11}(\bar{x})$ could be confused with the axial strain ε_{a11}. It is not the axial strain, since the stress field is not uniaxial. In other analytical models, the average shear stress has been chosen as the normalizing factor. In contrast in this work, the modulus of the central adherend (E_{a11}) is used for the normalization since a thermal load without an externally applied mechanical load results in a zero average shear stress. Though this choice loses the convenient "stress concentration factor" associated with the average shear stress normalization, it is necessary to avoid a singular result for thermal loads. Upon substitution, equation 2.6 becomes:

$$\frac{d^2\bar{\sigma}_{a11}\left(\bar{x}\right)}{d\bar{x}^2} + \bar{\omega}^2\bar{\sigma}_{a11}\left(\bar{x}\right) + \bar{\psi}_{\Delta T} + \bar{\psi}_{P} = 0, \tag{2.8}$$

which is a dimensionless form of the governing equation. The parameters $\bar{\omega}^2$, $\bar{\psi}_{\Delta T}$ and $\bar{\psi}_{P}$ are:

$$\begin{aligned}
\bar{\omega}^2 =& \frac{2\,G_{b12}l^2}{t_b}\left[\frac{(\nu_{c13}\nu_{c31}-1)}{E_{c11}t_c} + \frac{2(\nu_{a13}\nu_{a31}-1)}{E_{a11}t_a}\right],\\
\bar{\psi}_{\Delta T} =& \left[\frac{4\,G_{b12}l^2\left(\alpha_{c33}\nu_{c31} - \alpha_{a33}\nu_{a31} + \alpha_{c11} - \alpha_{a11}\right)}{E_{a11}t_at_b}\right]\Delta T,\\
\bar{\psi}_{P} =& -\left[\frac{4\,G_{b12}l^2\left(\nu_{c13}\nu_{c31}-1\right)}{E_{a11}E_{c11}t_at_bt_c}\right]P.
\end{aligned} \tag{2.9}$$

Equation 2.9 contains dimensionless parameters for both thermal and mechanical loading. Thermal expansion of the adhesive is not a factor in this model since the adhesive is assumed to carry no longitudinal normal stress.[3] A solution to equation 2.6

[3] The assumption of zero longitudinal normal stress in the adhesive greatly simplifies the calculations and is reasonable for calculating shear stress (and peel stress in the SP solution) as long as

is:

$$\bar{\sigma}_{a11}(\bar{x}) = \bar{a}\sin(\bar{\omega}\bar{x}) + \bar{b}\cos(\bar{\omega}\bar{x}) - \frac{\bar{\psi}_{\Delta T} + \bar{\psi}_P}{\bar{\omega}^2}. \tag{2.10}$$

Boundary conditions for longitudinal normal stress are:

$$\begin{aligned} \bar{\sigma}_{a11}(0) &= 0, \\ \bar{\sigma}_{a11}(1) &= \frac{2P}{t_a E_{a11}}. \end{aligned} \tag{2.11}$$

Application of the boundary conditions leads to:

$$\begin{aligned} \bar{a} =& -\left[\frac{E_{c11}\, t_b\, t_c}{2\, G_{b12}\, l^2\, \sin\bar{\omega}\, (\nu_{c13}\, \nu_{c31} - 1)} + \frac{\cos\bar{\omega} - 1}{\bar{\omega}^2\, \sin\bar{\omega}}\right] \bar{\psi}_P - \frac{(\cos\bar{\omega} - 1)}{\bar{\omega}^2\, \sin\bar{\omega}}\bar{\psi}_{\Delta T}, \\ \bar{b} =& \frac{\bar{\psi}_{\Delta T} + \bar{\psi}_P}{\bar{\omega}^2}. \end{aligned} \tag{2.12}$$

Equation 2.12 completes the SO solution. Plots of the solution are shown in figures 2.5-2.9.

The SO solution minimizes solution complexity. As a result, it lacks certain desirable features. It neither predicts a traction free adhesive edge, nor does it quantify the peel stress. Despite these shortcomings, the model is useful. For example, it provides an orthotropic solution which includes consideration of thermal expansion. In equation 2.9, it identifies important dimensionless parameters which dictate the joint stress distribution. In the present form, the solution can be used as a first order analysis tool in the design and sizing of composite bonded double lap joints. The SO solution also provides a foundation for the more advanced formulation derived in the next section. It is that formulation which predicts a zero traction at the adhesive edge.

2.3.2 Model where the adhesive carries shear and peel stress

The second double lap joint solution is the shear-peel model, an extension of the shear-only model analysis. The adhesive is no longer confined to carry only shear stress. Instead, it is assumed to carry shear and peel stresses as shown (in a general

the strain energy due to this stress component is a small relative to the total strain energy. The model breaks down in joints with similar adherend thermal expansion and a large differential thermal expansion relative to the adhesive. In those joints, the longitudinal thermal stress of the adhesive will be greater than the adhesive shear and peel stresses. Therefore, a different type of analysis is appropriate.

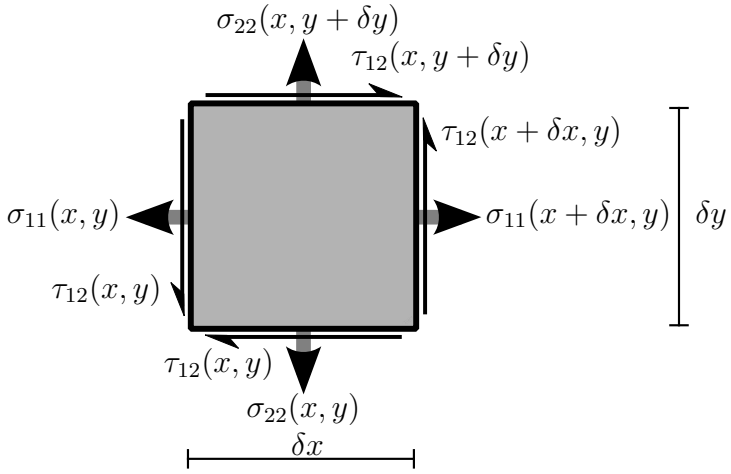

Figure 2.2 Generalized equilibrium parallelepiped

form) in figure 2.2. The adherends are assumed to be stiff and carry only normal stresses as in the SO solution. For convenience, a fictitious structural element called an "end post" is located at the edge of the adhesive. This post is assumed to transfer shear stress at adhesive the edge to the adherends. In making this assumption, the traction boundary condition is satisfied *a priori*. This modeling approach has been used for double lap joints as described by Davies [39]; the current model can be considered an extension. The end post element, shown in figure 2.1 and highlighted in figure 2.3, is carried through the calculations until it is made infinitesimal ($t_p \to 0$) to restore the correct geometry.

With the exception of the peel stress in the adhesive layer, the stress fields in the adherends are as described in the SO solution. The x-equilibrium equations in section 2.3.1 hold, however, y-equilibrium in the adhesive is included in the analysis.

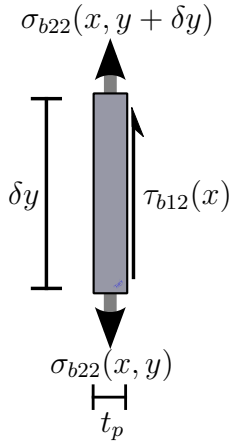

Figure 2.3 Equilibrium element of the left end post

Force equilibrium in the y direction of the adhesive requires:

$$\frac{\partial \sigma_{b22}(x,y)}{\partial y} = -\frac{d\tau_{b12}(x)}{dx}, \tag{2.13}$$

where $\sigma_{b22}(x,y)$ is assumed to be linear[4] in y:

$$\sigma_{b22}(x,y) = c_0 + c_1 y. \tag{2.14}$$

For convenience, the peel stress at the adhesive interface is assumed to be zero, $\sigma_{b22}(x,t_b) = 0$, therefore:

$$\sigma_{b22}(x,y) = c_0\left(1 - \frac{y}{t_b}\right). \tag{2.15}$$

Though this assumption could be challenged, it enables y-equilibrium to be considered with minimum solution complexity and is justified when the average adhesive peel stress is considered in section 2.5.[5] Combining equations 2.13 and 2.15 leads to:

$$\sigma_{b22}(x,y) = \frac{t_a}{2}(y - t_b)\frac{d^2\sigma_{a11}(x)}{dx^2}. \tag{2.16}$$

Force equilibrium in the y direction on the left end post requires:

$$\frac{dF(y, x=0)}{dy} = -\tau_{b12}(0). \tag{2.17}$$

The force carried by the end post is also assumed to be linear in y:

$$F(y, x=0) = d_0 + d_1 y. \tag{2.18}$$

Combining equations 2.2 and 2.18 leads to:

$$F(y, x=0) = \frac{t_a}{2}\frac{d\sigma_{a11}(x=0)}{dx}y + d_0. \tag{2.19}$$

Using similar arguments for the right end post and applying the equilibrium requirement that the total end post force vanishes on each side, the end post governing

[4] A linear stress field is the lowest order function that satisfies equilibrium.

[5] This assumption is removed in the bonded joint finite element formulation presented in chapter 3.

equations are:

$$\begin{aligned} F(y, x=0) &= \frac{t_a}{2}\frac{d\sigma_{a11}(x=0)}{dx}\left(y - \frac{t_b}{2}\right), \\ F(y, x=l) &= -\frac{t_a}{2}\frac{d\sigma_{a11}(x=l)}{dx}\left(y - \frac{t_b}{2}\right). \end{aligned} \tag{2.20}$$

Having established the equilibrium requirements, application of the principal of virtual forces leads to a differential equation of the form:

$$\frac{d^4\sigma_{a11}(x)}{dx^4} + \beta\frac{d^2\sigma_{a11}(x)}{dx^2} + \gamma\sigma_{a11}(x) + \phi_{\Delta T} + \phi_P = 0. \tag{2.21}$$

As in the SO solution, the thermal and mechanical loads enter equation 2.21 in the form of system parameters ϕ_T and ϕ_P. Delaying explicit statement of the parameters, non-dimensionalizing substitutions can be made:

$$\begin{aligned} \bar{x} &= \frac{x}{l}, \\ \bar{\beta} &= l^2\beta, \\ \bar{\gamma} &= l^4\gamma, \\ \bar{\sigma}_{a11}(\bar{x}) &= \frac{\sigma_{a11}(l\bar{x})}{E_{a11}}, \\ \bar{\tau}_{b12}(\bar{x}) &= \frac{\tau_{b12}(l\bar{x})}{E_{a11}}, \\ \bar{\phi}_{\Delta T} &= \phi_T\frac{l^4}{E_{a11}}, \\ \bar{\phi}_P &= \phi_P\frac{l^4}{E_{a11}}. \end{aligned} \tag{2.22}$$

As summarized in appendix A, the combination of equations 2.2, 2.16, 2.20, and 2.22 yield a differential equation for the normalized stress in the central adherend:

$$\frac{d^4\bar{\sigma}_{a11}(\bar{x})}{d\bar{x}^4} + \bar{\beta}\frac{d^2\bar{\sigma}_{a11}(\bar{x})}{d\bar{x}^2} + \bar{\gamma}\bar{\sigma}_{a11}(\bar{x}) + \bar{\phi}_{\Delta T} + \bar{\phi}_P = 0. \tag{2.23}$$

The dimensionless system parameters are:

$$\begin{aligned}
\bar{\beta} &= \frac{3\,E_{b22}\,l^2}{2\,G_{b12}\,t_b^2\,\left(\nu_{b23}\,\nu_{b32}-1\right)},\\
\bar{\gamma} &= \frac{3\,E_{b22}\,l^4}{t_b^3\,\left(\nu_{b23}\,\nu_{b32}-1\right)}\left[\frac{\left(\nu_{c13}\,\nu_{c31}-1\right)}{E_{c11}\,t_c}+\frac{2\,\left(\nu_{a13}\,\nu_{a31}-1\right)}{E_{a11}\,t_a}\right],\\
\bar{\phi}_{\Delta T} &= \left[\frac{6E_{b22}l^4\left(\alpha_{c33}\nu_{c31}-\alpha_{a33}\nu_{a31}+\alpha_{c11}-\alpha_{a11}\right)}{E_{a11}t_at_b^3\left(\nu_{b23}\nu_{b32}-1\right)}\right]\Delta T,\\
\bar{\phi}_P &= -\left[\frac{6E_{b22}l^4\left(\nu_{c13}\nu_{c31}-1\right)}{E_{a11}E_{c11}t_at_b^3t_c\left(\nu_{b23}\nu_{b32}-1\right)}\right]P.
\end{aligned} \tag{2.24}$$

A solution to equation 2.23 is:

$$\bar{\sigma}_{a11}(\bar{x}) = \bar{A}e^{\bar{\lambda}_1\bar{x}}+\bar{B}e^{-\bar{\lambda}_1\bar{x}}+\bar{C}e^{\bar{\lambda}_3\bar{x}}+\bar{D}e^{-\bar{\lambda}_3\bar{x}}-\frac{\bar{\phi}_{\Delta T}}{\bar{\gamma}}-\frac{\bar{\phi}_P}{\bar{\gamma}}. \tag{2.25}$$

The bi-quadratic equation 2.25 has two dimensionless system parameters $\bar{\lambda}_1$ and $\bar{\lambda}_3$ given by:

$$\bar{\lambda}_{[13]}^2 = \frac{-\bar{\beta}\pm\sqrt{\bar{\beta}^2-4\bar{\gamma}}}{2}, \tag{2.26}$$

which are presented in terms of the orthotropic material properties in appendix C.1.

The appearance of $\bar{\beta}$ and $\bar{\gamma}$ in $\bar{\lambda}_{[13]}^2$, (which govern the axial and shear stress distributions along the adherend (equation 2.13) and adhesive (equation 2.16)) illustrates the relative importance of the adhesive and adherend mechanical properties and the joint geometry. Similarly, $\bar{\phi}_{\Delta T}$ and $\bar{\phi}_P$ are two load parameters that are a combination of adhesive and adherend thermal and mechanical properties, loading, and joint geometry.

The basis functions $\bar{A}$, $\bar{B}$, $\bar{C}$, and $\bar{D}$ in equation 2.25 are determined by application of the boundary conditions. The boundary conditions are presented in full form in appendix B as equation B.1 and in reduced form in equation 2.27.

$$\begin{aligned}
\bar{D}+\bar{C}+\bar{B}+\bar{A}-\frac{\bar{\phi}_{\Delta T}+\bar{\phi}_P}{\bar{\gamma}} &= 0\\
e^{-\bar{\lambda}_3}\bar{D}+e^{\bar{\lambda}_3}\bar{C}+e^{-\bar{\lambda}_1}\bar{B}+e^{\bar{\lambda}_1}\bar{A}-\frac{\bar{\phi}_{\Delta T}+\bar{\phi}_P}{\bar{\gamma}}-\frac{2P}{E_{a11}t_a} &= 0\\
-\bar{\lambda}_3\bar{D}+\bar{\lambda}_3\bar{C}-\bar{\lambda}_1\bar{B}+\bar{\lambda}_1\bar{A} &= 0\\
-\bar{\lambda}_3e^{-\bar{\lambda}_3}\bar{D}+\bar{\lambda}_3e^{\bar{\lambda}_3}\bar{C}-\bar{\lambda}_1e^{-\bar{\lambda}_1}\bar{B}+\bar{\lambda}_1e^{\bar{\lambda}_1}\bar{A} &= 0
\end{aligned} \tag{2.27}$$

Physically, the boundary conditions represent axial normal stress and shear stress at the ends of the central adherend. The *reduced form* of the boundary conditions are

achieved by allowing the end posts to approach zero thickness (taking the limit as $t_p \to 0$). This procedure forces the shear stress at the post locations to zero which results in a traction free surface at the adhesive edge.

The solution of equation 2.27 for $\bar{A}$, $\bar{B}$, $\bar{C}$, and $\bar{D}$ requires lengthy combinations of the system parameters. They are presented in a compact form in equation 2.28 where certain repeating values have been represented as sets of coefficients (μ). The values of the μ coefficients are presented in appendix C.2. With the presentation of equation 2.28, the SP solution is now completed.

$$\begin{aligned}
\bar{A} &= \frac{\mu_{A_T}\,\bar{\phi}_{\Delta T} + (\mu_{A_T} + \mu_2\,\mu_3\,\mu_{A_P})\;\bar{\phi}_P}{\mu_1} \\
\bar{B} &= \frac{\mu_{B_T}\,\bar{\phi}_{\Delta T} + (\mu_{B_T} + \mu_2\,\mu_3\,\mu_{B_P})\;\bar{\phi}_P}{\mu_1} \\
\bar{C} &= \frac{\mu_{C_T}\,\bar{\phi}_{\Delta T} + (\mu_{C_T} + \mu_2\,\mu_3\,\mu_{C_P})\;\bar{\phi}_P}{\mu_1} \\
\bar{D} &= \frac{\mu_{D_T}\,\bar{\phi}_{\Delta T} + (\mu_{D_T} + \mu_2\,\mu_3\,\mu_{D_P})\;\bar{\phi}_P}{\mu_1}
\end{aligned} \tag{2.28}$$

The SP solution overcomes some of the effects previously ignored in bonded joint analysis. Most significantly, it is an *orthotropic thermomechanical solution* which ensures that the shear stress at the traction free edge is zero. It does so with the *minimal* required complexity of a fourth order governing differential equation.

The analysis is an elastic solution and neglects the effect of adhesive and adherend plasticity, if any, on the joint. This effect, however, has been addressed analytically, [54]. The inclusion of plasticity is best treated through a numerical solution.

2.3.3 Dimensionless ratio of thermal and mechanical loads

Using the dimensionless loading parameters defined in equations 2.9 and 2.24, a dimensionless load ratio ($\bar{\phi}_{\mathrm{aR}}$) and total load ($\bar{\phi}_{\mathrm{tot}}$) can be defined.

$$\begin{aligned}
\bar{\phi}_{\mathrm{aR}} &= \frac{\bar{\phi}_{\Delta T}}{\bar{\phi}_P} = -\frac{E_{c11}\,t_c\;(\alpha_{c33}\,\nu_{c31} - \alpha_{a33}\,\nu_{a31} + \alpha_{c11} - \alpha_{a11})\;\Delta T}{(\nu_{c13}\,\nu_{c31} - 1)\;P} \\
\bar{\phi}_{\mathrm{tot}} &= \bar{\phi}_P + \bar{\phi}_{\Delta T}
\end{aligned} \tag{2.29}$$

The ratio $\bar{\phi}_{\mathrm{aR}}$ is a measure of the relative importance of thermal and mechanical loads. The dimensionless number given in equation 2.29 is based on the stress in the central adherend $\bar{\sigma}_{a11}(\bar{x})$. Using equation 2.5 and similarly collecting terms into dimensionless

loads, a conjugate dimensionless load ratio can be written for the stress field in the outer adherend $\bar{\sigma}_{c11}(\bar{x})$;

$$\bar{\phi}_{cR} = \frac{E_{a11}\, t_a\, \left(\alpha_{c33}\, \nu_{c31} - \alpha_{a33}\, \nu_{a31} + \alpha_{c11} - \alpha_{a11}\right)\, \Delta T}{2\left(\nu_{a13}\, \nu_{a31} - 1\right)\, P}. \tag{2.30}$$

The importance of the load ratios $\bar{\phi}_{[ac]R}$ must not be underestimated. When $|\bar{\phi}_{[ac]R}| \ll 1$, mechanically induced stress dominates the stress field in the adherend. Conversely, when $|\bar{\phi}_{[ac]R}| \gg 1$, the thermally induced stress field is dominant. Finally, when $|\bar{\phi}_{[ac]R}| \approx 1$, thermal and mechanical loads are both significant to the total stress field. Using $\bar{\phi}_{\mathrm{aR}}$ as a guide, it is easy to show that some common joints (such as aluminum to carbon fiber reinforced polymer matrix composite) can be dominated by thermal loading when a large ΔT is present. It is significant that the dimensionless load ratio is the same whether the SO or the SP is used to derive it. It is, therefore, independent of the adhesive stress field assumption.

Examining equations 2.29 and 2.30, it is apparent that the dimensionless load ratio in one adherend depends largely on the stiffness of the other adherend.

With the dimensionless load ratio in mind, a load-based normalization can be defined by rewriting the axial stress as:

$$\bar{\bar{\sigma}}_{a11} = \frac{\bar{\sigma}_{a11}}{\bar{\bar{\phi}}_{\mathrm{tot}}}, \tag{2.31}$$

or, more intuitively:

$$\bar{\sigma}_{a11}(\bar{x}) = \bar{\bar{\sigma}}_{a11}(\bar{\bar{\phi}}_P, \bar{x}) \cdot \bar{\bar{\phi}}_{\mathrm{tot}}. \tag{2.32}$$

This second normalization can be propagated throughout the solution so that the SO and SP solutions are written as:

$$\begin{aligned} \bar{\bar{\sigma}}_{a11}(\bar{x}) &= \bar{\bar{a}}\sin(\bar{\omega}\bar{x}) + \bar{\bar{b}}\cos(\bar{\omega}\bar{x}) - \frac{1}{\bar{\omega}^2}, \\ \bar{\bar{\sigma}}_{a11}(\bar{x}) &= \bar{\bar{A}}\left(\bar{\bar{\phi}}_P\right) e^{\bar{\lambda}_1\bar{x}} + \bar{\bar{B}}\left(\bar{\bar{\phi}}_P\right) e^{-\bar{\lambda}_1\bar{x}} + \bar{\bar{C}}\left(\bar{\bar{\phi}}_P\right) e^{\bar{\lambda}_3\bar{x}} + \bar{\bar{D}}\left(\bar{\bar{\phi}}_P\right) e^{-\bar{\lambda}_3\bar{x}} - \frac{1}{\bar{\gamma}}. \end{aligned} \tag{2.33}$$

The boundary conditions become:

$$\begin{aligned} \bar{\bar{\sigma}}_{a11}(0) &= 0, \\ \bar{\bar{\sigma}}_{a11}(1) - \frac{2P}{t_a E_{a11} \bar{\bar{\phi}}_{\mathrm{tot}}} &= 0, \end{aligned} \tag{2.34}$$

for the SO solution and:

$$\begin{aligned}
\bar{\bar{D}}\left(\bar{\bar{\phi}}_P\right) + \bar{\bar{C}}\left(\bar{\bar{\phi}}_P\right) + \bar{\bar{B}}\left(\bar{\bar{\phi}}_P\right) + \bar{\bar{A}}\left(\bar{\bar{\phi}}_P\right) - \frac{1}{\bar{\gamma}} &= 0, \\
e^{-\bar{\lambda}_3}\bar{\bar{D}}\left(\bar{\bar{\phi}}_P\right) + e^{\bar{\lambda}_3}\bar{\bar{C}}\left(\bar{\bar{\phi}}_P\right) + e^{-\bar{\lambda}_1}\bar{\bar{B}}\left(\bar{\bar{\phi}}_P\right) + e^{\bar{\lambda}_1}\bar{\bar{A}}\left(\bar{\bar{\phi}}_P\right) - \frac{1}{\bar{\gamma}} - \frac{2P}{E_{a11}t_a\bar{\phi}_{\text{tot}}} &= 0, \\
-\bar{\lambda}_3\bar{\bar{D}}\left(\bar{\bar{\phi}}_P\right) + \bar{\lambda}_3\bar{\bar{C}}\left(\bar{\bar{\phi}}_P\right) - \bar{\lambda}_1\bar{\bar{B}}\left(\bar{\bar{\phi}}_P\right) + \bar{\lambda}_1\bar{\bar{A}}\left(\bar{\bar{\phi}}_P\right) &= 0, \\
-\bar{\lambda}_3 e^{-\bar{\lambda}_3}\bar{\bar{D}}\left(\bar{\bar{\phi}}_P\right) + \bar{\lambda}_3 e^{\bar{\lambda}_3}\bar{\bar{C}}\left(\bar{\bar{\phi}}_P\right) - \bar{\lambda}_1 e^{-\bar{\lambda}_1}\bar{\bar{B}}\left(\bar{\bar{\phi}}_P\right) + \bar{\lambda}_1 e^{\bar{\lambda}_1}\bar{\bar{A}}\left(\bar{\bar{\phi}}_P\right) &= 0,
\end{aligned} \tag{2.35}$$

for the SP solution.

Using the load ratio $\bar{\phi}_{\text{aR}}$, the basis functions can be split into linear equations of the mechanical fraction of the load. Defining the mechanical load fraction as:

$$\bar{\bar{\phi}}_P = \frac{\bar{\phi}_P}{\bar{\phi}_{\text{tot}}} = \left(1 + \bar{\phi}_{\text{aR}}\right)^{-1}, \tag{2.36}$$

the functions $\bar{\bar{a}}$ and $\bar{\bar{b}}$ from equation 2.33 for a load normalized solution can be written as:

$$\begin{aligned}
\bar{\bar{a}} &= -\frac{E_{c11}\, t_b\, t_c}{2\, G_{b12}\, l^2\, \sin\bar{\omega}\, \left(\nu_{c13}\, \nu_{c31} - 1\right)}\, \bar{\bar{\phi}}_P - \frac{\cos\bar{\omega} - 1}{\bar{\omega}^2\, \sin\bar{\omega}}, \\
\bar{\bar{b}} &= \frac{1}{\bar{\omega}^2}.
\end{aligned} \tag{2.37}$$

Similarly, the $\bar{\bar{A}}$, $\bar{\bar{B}}$, $\bar{\bar{C}}$, and $\bar{\bar{D}}$ functions can be written as:

$$\begin{aligned}
\bar{\bar{A}}\left(\bar{\bar{\phi}}_P\right) &= \frac{\mu_3\mu_{A_P}}{\mu_1\mu_2}\, \bar{\bar{\phi}}_P + \frac{\mu_{A_T}}{\mu_1}, \\
\bar{\bar{B}}\left(\bar{\bar{\phi}}_P\right) &= \frac{\mu_3\mu_{B_P}}{\mu_1\mu_2}\, \bar{\bar{\phi}}_P + \frac{\mu_{B_T}}{\mu_1}, \\
\bar{\bar{C}}\left(\bar{\bar{\phi}}_P\right) &= \frac{\mu_3\mu_{C_P}}{\mu_1\mu_2}\, \bar{\bar{\phi}}_P + \frac{\mu_{C_T}}{\mu_1}, \\
\bar{\bar{D}}\left(\bar{\bar{\phi}}_P\right) &= \frac{\mu_3\mu_{D_P}}{\mu_1\mu_2}\, \bar{\bar{\phi}}_P + \frac{\mu_{D_T}}{\mu_1},
\end{aligned} \tag{2.38}$$

where the μ parameters are given in appendix C.2. In these forms, it becomes apparent that the functions $\bar{\bar{a}}$, $\bar{\bar{b}}$, $\bar{\bar{A}}$, $\bar{\bar{B}}$, $\bar{\bar{C}}$, $\bar{\bar{D}}$ (and by extension $\bar{a}$, $\bar{b}$, $\bar{A}$, $\bar{B}$, $\bar{C}$, $\bar{D}$) govern the stress distribution via the thermal and mechanical load ratio, $\bar{\phi}_{\text{aR}}$. This conclusion enhances its relevance to the study of thermomechanical loading of lap joints.

The forms presented in equations 2.37 and 2.38 allows an iterative version of the SO or SP solution to be applied using numerical methods, when the mechanical load is

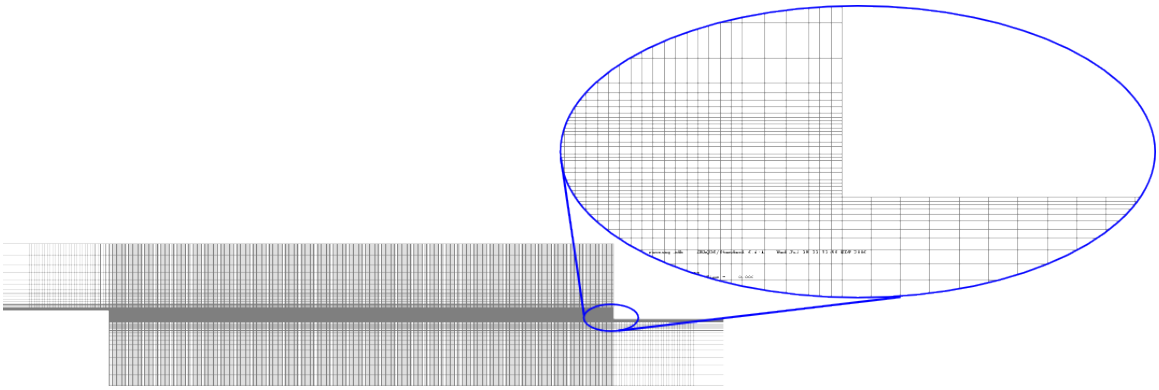

Figure 2.4 The FE mesh

Table 2.1 Geometric and loading assumptions for model comparison

(a) ASTM double lap joint geometric features (mm).

Component	Thickness	Length
Outer Adherend	1.6	76.2
Adhesive	0.2 *or* 1.0	12.7
Central Adherend	3.2	76.2

(b) Assumed loading.

Load Type	Value
P (N·mm^{-1})	10
ΔT (^{o}C)	10

dependent on the thermal load. For example, they allow the solution of displacement constrained thermomechanical problems. The approach also facilitates the inclusion of an analytically derived shape function into an application specific finite element. An example of this usage is presented in chapter 3.

2.4 A continuum FE model of a symmetric double lap joint

2.4.1 Benchmarking

To establish confidence in the SO and SP models derived in section 2.3, a comparison with a linear elastic FE solution is presented in this section. A 2D FE model has been generated for the ASTM International (ASTM) double lap joint [12]. The mesh is

Table 2.2 Assumed material properties in FE, SO, and SP solutions (moduli in GPa, expansion coeffs. in $\mu\epsilon{\cdot}^{o}\mathrm{C}^{-1}$)

Material	Aluminum	Titanium	AS4/3501-6 (0^o)	FM300
E_{11}	70	110	148	1.98
E_{22}	70	110	10.6	1.98
E_{33}	70	110	10.6	1.98
G_{12}	26.3	41.4	5.61	0.71
G_{13}	26.3	41.4	5.61	0.71
G_{23}	26.3	41.4	3.17	0.71
ν_{12}	0.33	0.33	0.30	0.40
ν_{13}	0.33	0.33	0.30	0.40
ν_{23}	0.33	0.33	0.59	0.40
α_{11}	23	9	-0.8	20
α_{22}	23	9	29	20
α_{33}	23	9	29	20

shown in figure 2.4 and the assumed geometries are given in table 2.1(a). The solution was obtained from Abaqus® using linear plain strain elements (CPE4). Only half of the joint was modeled due to symmetry. The stress concentrations at the material interfaces were not resolved in the vicinity of the corner despite a fine mesh, since the singular stress field cannot be resolved with the linear elastic FE technique. Therefore, direct comparison is not made at the corners. Mechanical and thermal loading was specified as listed in table 2.1(b). The mechanical load was applied far away from the lap joint and the thermal load was applied to all nodes. Displacement symmetry constraints were enforced along the mid-plane of the central adherend. Non-linear geometric stiffness was assumed.

Aluminum (AL) is the central adherend in all models; the outer adherends were AL, titanium (TI), and AS4/3501-6 (AS4), [57]. For simplicity, the adhesive properties were assumed to be isotropic and were estimated base on Cytec FM300 adhesive.[6] The assumed material properties are summarized in table 2.2.

Stresses for all models are reported at the mid plane of the adhesive. For the peel stress in the SP model, the mid-plane is the average peel stress. All peel stress comparisons are made to within 0.05 mm of the adhesive edge (25% of the adhesive thickness for the 0.20 mm adhesive models). The choice of appropriate comparison limit is complicated by the large gradients near the joint edge. The 0.05 mm location

[6]It is difficult to find bulk adhesive properties for adhesive materials.

was chosen to be sufficiently far away from the edge so as to avoid comparison in the areas of the FE model that are dominated by the singular stress field. In those areas, the mesh dependent result has singular tensile and compressive stresses at the opposing interfaces with the adherends. In contrast, the SP predicted stress is not mesh dependent, is monotonically increasing in the comparison zone, and is finite. A consistent choice of comparison limit, therefore, ensures that the value of the SP predicted stress will correlate with the strength of the stress singularity near the edge (where a strong peel stress is predicted).

2.5 Comparison of continuum FE and analytical model results for ASTM lap specimens

Figures 2.5-2.9 show the stress predicted by the SO, SP, and FE models due thermal and mechanical loads applied to several joints.

2.5.1 Aluminum-Aluminum joint

Examining the AL-AL results shown in figures 2.5(a) and 2.5(d), all three of the models predict that the shear and peel stress due to thermal loading is small.[7] This result is obvious, since the two adherends have no mechanical load and possess the same expansion coefficient.

Model predictions for an AL-AL joint with applied mechanical load are shown in figures 2.5(b) and 2.5(e). The first of these two figures shows the normalized shear stress ($\bar{\tau}_{b12}$) in the joint. The correlation between the FE, SO, and SP models is generally good, though the SO and SP models over predict the shear stress near the edges in comparison to the FE solution. Total shear (the area under the $\bar{x}$-$\bar{\tau}_{b12}$ curves) is preserved because the SO and SP solutions under predict the stress in the middle of the joint relative to the FE model. The traction free boundary condition is only captured by the FE and SP solutions, as expected.

The plots in figure 2.5(e) show the peel stress due to mechanical load as predicted by FE and SP solutions. It is apparent that differences exist in predicted peel stresses. Near the edges of the joint, however, a direct correlation is found. This correlation

[7] This is the special case of adherends with similar thermal expansion subjected to primarily thermal loads. If the expansion coefficient of the adhesive was substantially different from that of the adherends, it would be appropriate to conduct a different type of analysis with primary focus on the adhesive expansion.

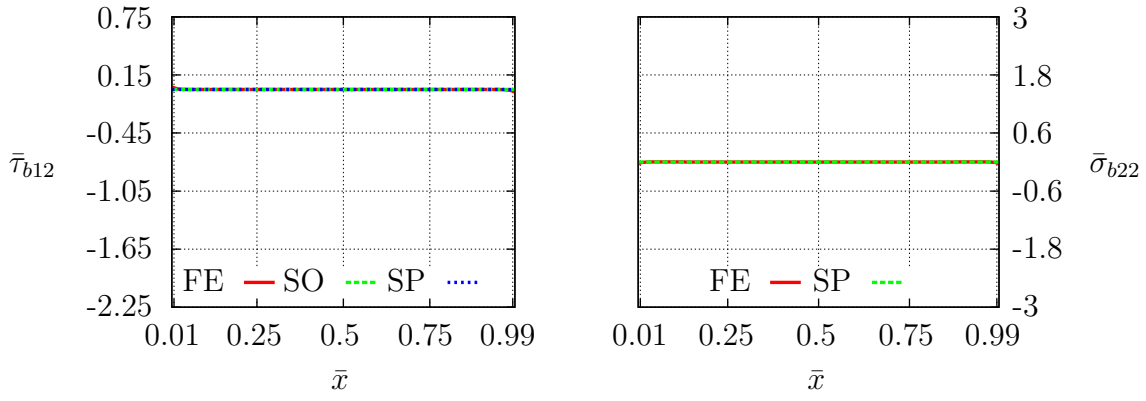

(a) $\bar{\tau}_{b12}$ due to $\bar{\phi}_{\Delta T}$

(b) $\bar{\sigma}_{b22}$ due to $\bar{\phi}_{\Delta T}$

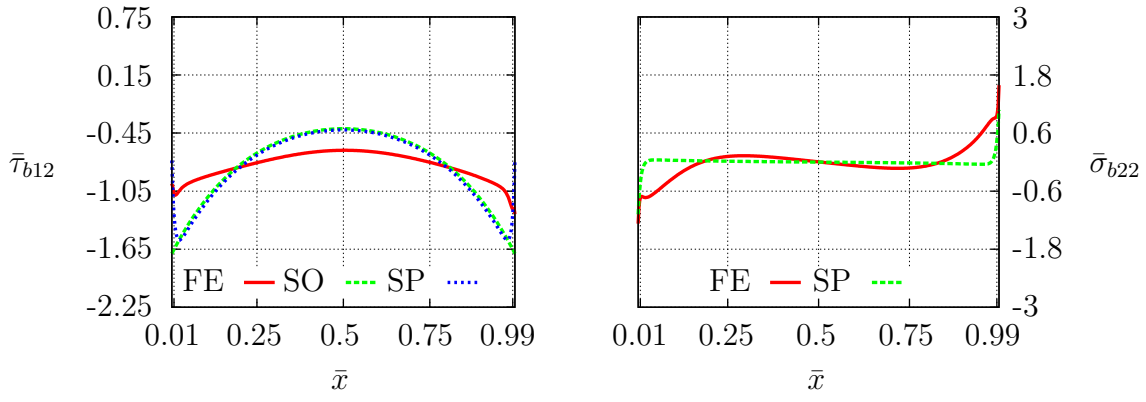

(c) $\bar{\tau}_{b12}$ due to $\bar{\phi}_P$

(d) $\bar{\sigma}_{b22}$ due to $\bar{\phi}_P$

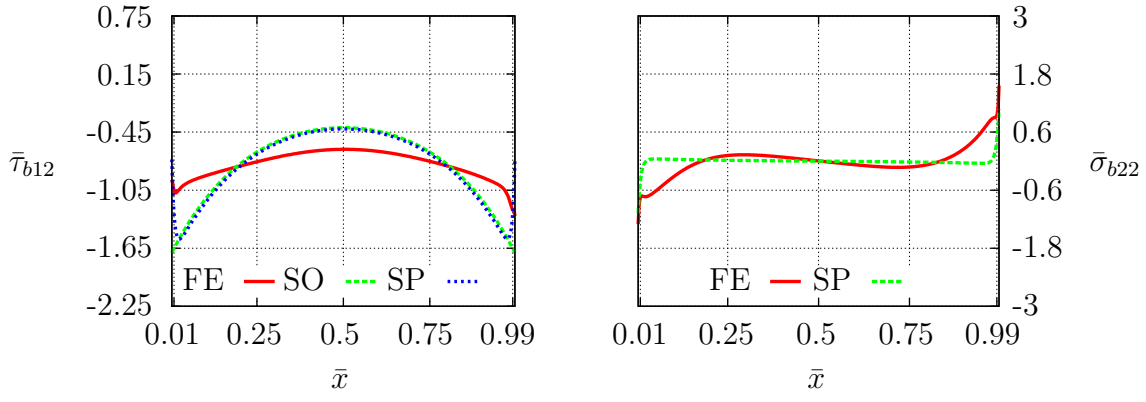

(e) $\bar{\tau}_{b12}$ due to $\bar{\phi}_P$+$\bar{\phi}_{\Delta T}$

(f) $\bar{\sigma}_{b22}$ due to $\bar{\phi}_P$+$\bar{\phi}_{\Delta T}$

Figure 2.5 FE, SO, and SP models of an AL-AL double lap joint with 0.2 mm FM300 adhesive. $\bar{\phi}_{\mathrm{aR}} = 0$

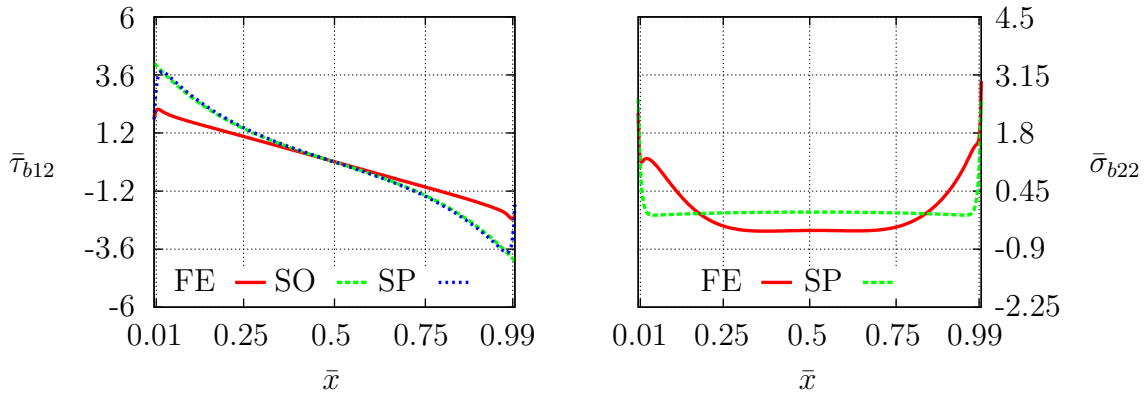

(a) $\bar{\tau}_{b12}$ due to $\bar{\phi}_{\Delta T}$

(b) $\bar{\sigma}_{b22}$ due to $\bar{\phi}_{\Delta T}$

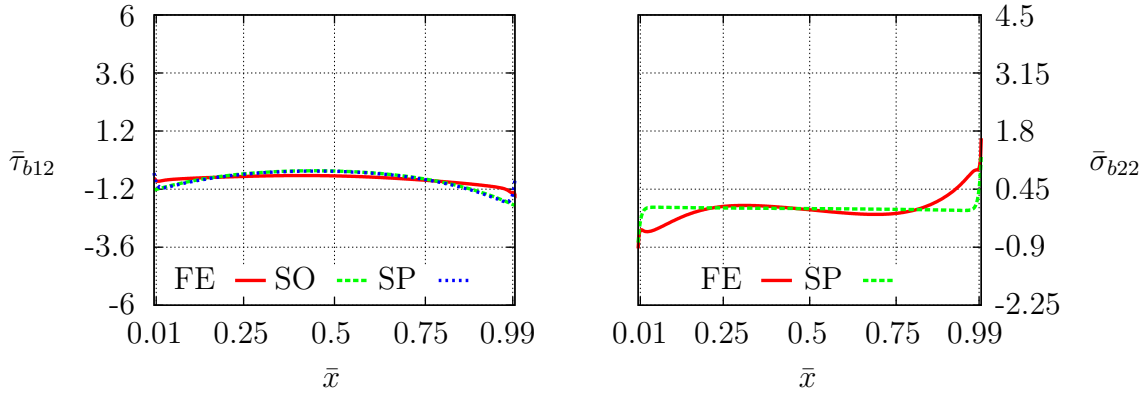

(c) $\bar{\tau}_{b12}$ due to $\bar{\phi}_{P}$

(d) $\bar{\sigma}_{b22}$ due to $\bar{\phi}_{P}$

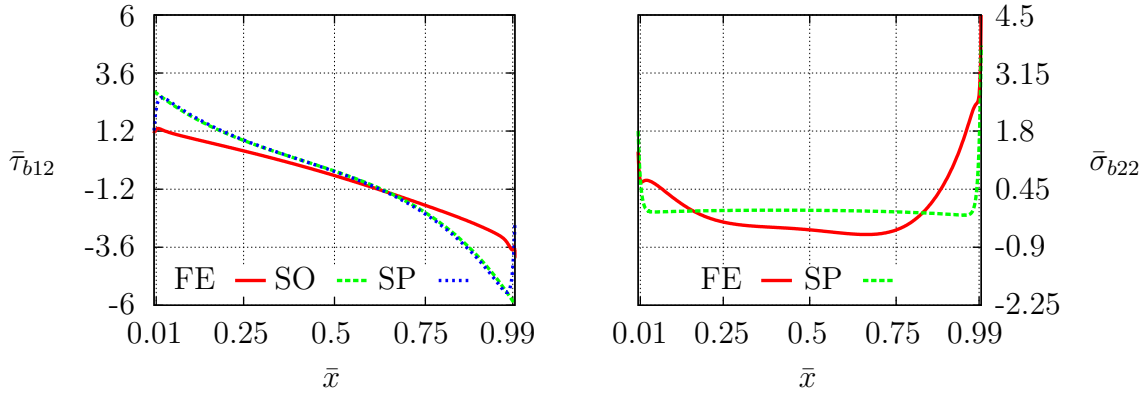

(e) $\bar{\tau}_{b12}$ due to $\bar{\phi}_{P}$+$\bar{\phi}_{\Delta T}$

(f) $\bar{\sigma}_{b22}$ due to $\bar{\phi}_{P}$+$\bar{\phi}_{\Delta T}$

Figure 2.6 FE, SO, and SP models of an AL-TI double lap joint with 0.2 mm FM300 adhesive. $\bar{\phi}_{\mathrm{aR}} = -3.68$

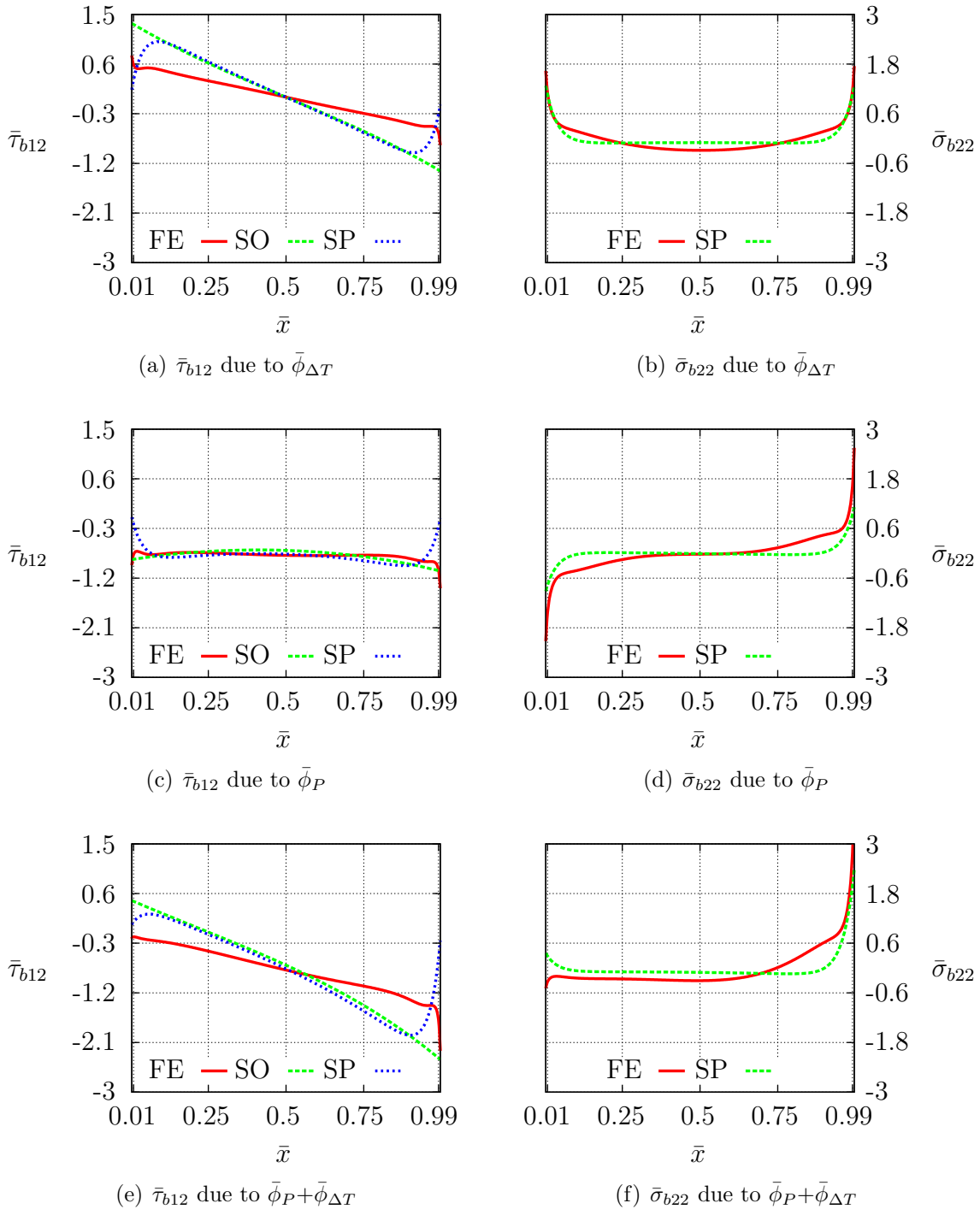

(a) $\bar{\tau}_{b12}$ due to $\bar{\phi}_{\Delta T}$

(b) $\bar{\sigma}_{b22}$ due to $\bar{\phi}_{\Delta T}$

(c) $\bar{\tau}_{b12}$ due to $\bar{\phi}_{P}$

(d) $\bar{\sigma}_{b22}$ due to $\bar{\phi}_{P}$

(e) $\bar{\tau}_{b12}$ due to $\bar{\phi}_{P}+\bar{\phi}_{\Delta T}$

(f) $\bar{\sigma}_{b22}$ due to $\bar{\phi}_{P}+\bar{\phi}_{\Delta T}$

Figure 2.7 FE, SO, and SP models of an AL-TI double lap joint with 1.0 mm FM300 adhesive. $\bar{\phi}_{\mathrm{aR}} = -3.68$

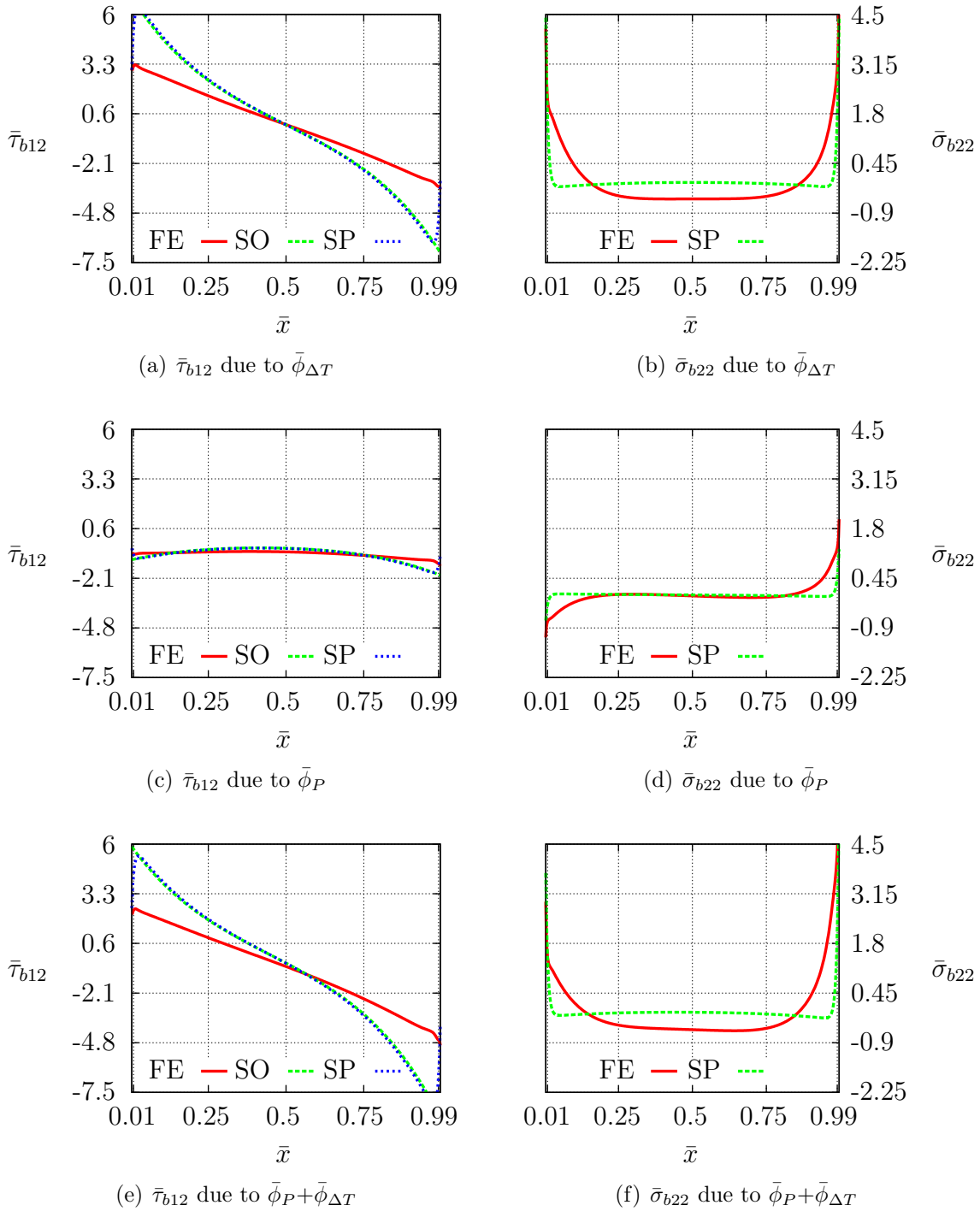

(a) $\bar{\tau}_{b12}$ due to $\bar{\phi}_{\Delta T}$

(b) $\bar{\sigma}_{b22}$ due to $\bar{\phi}_{\Delta T}$

(c) $\bar{\tau}_{b12}$ due to $\bar{\phi}_{P}$

(d) $\bar{\sigma}_{b22}$ due to $\bar{\phi}_{P}$

(e) $\bar{\tau}_{b12}$ due to $\bar{\phi}_{P}+\bar{\phi}_{\Delta T}$

(f) $\bar{\sigma}_{b22}$ due to $\bar{\phi}_{P}+\bar{\phi}_{\Delta T}$

Figure 2.8 FE, SO, and SP models of an AL-AS4 (0^o) double lap joint with 0.2 mm FM300 adhesive. $\bar{\phi}_{\mathrm{aR}} = -7.33$

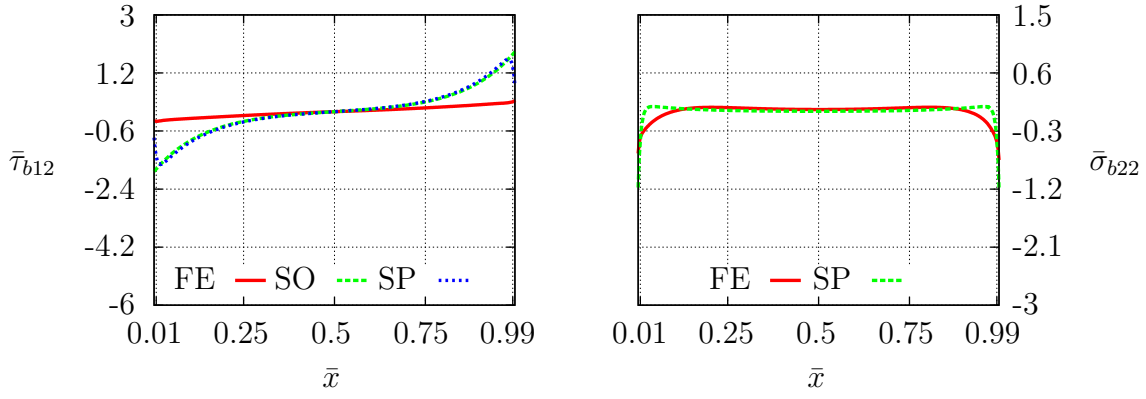

(a) $\bar{\tau}_{b12}$ due to $\bar{\phi}_{\Delta T}$

(b) $\bar{\sigma}_{b22}$ due to $\bar{\phi}_{\Delta T}$

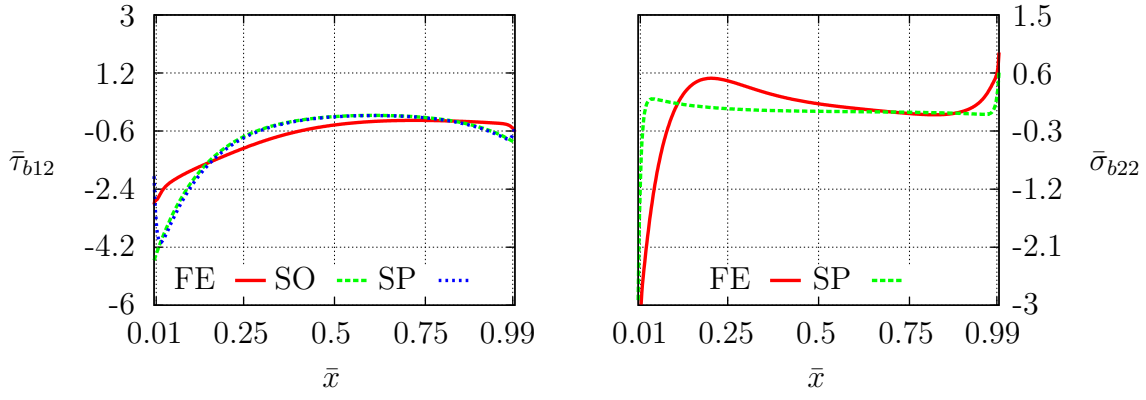

(c) $\bar{\tau}_{b12}$ due to $\bar{\phi}_{P}$

(d) $\bar{\sigma}_{b22}$ due to $\bar{\phi}_{P}$

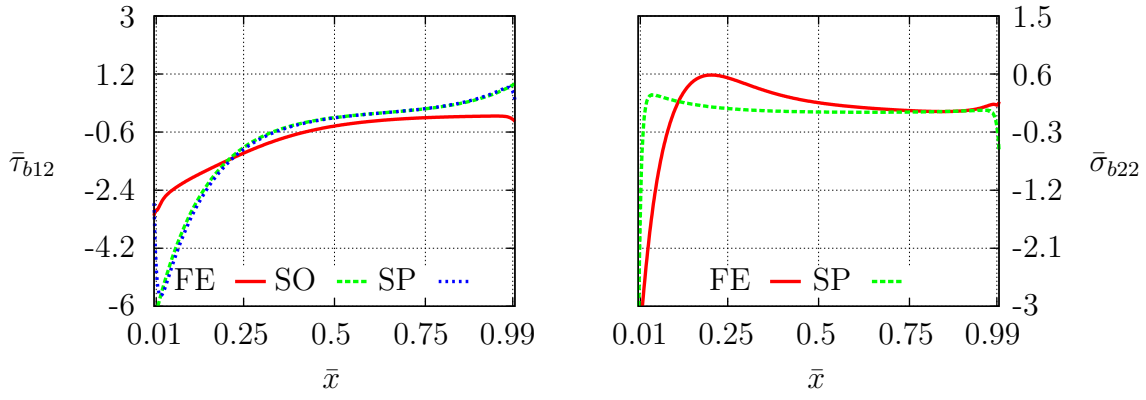

(e) $\bar{\tau}_{b12}$ due to $\bar{\phi}_{P}$+$\bar{\phi}_{\Delta T}$

(f) $\bar{\sigma}_{b22}$ due to $\bar{\phi}_{P}$+$\bar{\phi}_{\Delta T}$

Figure 2.9 FE, SO, and SP models of an AL-AS4 (90^o) double lap joint with 0.2 mm FM300 adhesive. $\bar{\phi}_{\text{aR}} = 0.40$

between the two solutions at the near edge location is important, since peel stress is often a cause of failure in lap joints. Similarly, figures 2.5(c) and 2.5(f) show the predicted stress state due to a mixed loading condition, where both thermal and mechanical loads are applied. In the AL-AL joint, it is clear that mechanical loading dominates the stress state as predicted by the load ratio ($\bar{\phi}_{\mathrm{aR}} = 0$).

2.5.2 Aluminum-Titanium joint

The FE, SO, and SP model predictions for AL-TI lap joints are shown in figures 2.6 and 2.7. There are several observations which add confidence in the use of the derived dimensionless parameters. First, figures 2.6(a) and 2.7(a) show strong correlation between the FE model and the SO and SP models when thermal loading is applied to joints with differing adhesive thicknesses. The predicted shear stress is zero in the middle of the joint, which is required when there is no mechanical load. Also, the SO and SP solutions for mechanical load in figures 2.6(b) and 2.6(d) and figures 2.7(b) and 2.7(d) have similar correlation to the AL-AL joint. They show that the shear stress concentration at the edges is larger when the adhesive is thin than when it is thick.

Mixed loading for AL-TI joints is shown in figures 2.6(c) and 2.6(f) (for 0.2 mm adhesive thickness) as well as figures 2.7(c) and 2.7(f) (for 1.0 mm adhesive thickness). These figures show that the SO and SP solutions compare favorably with the FE solution over the majority of the joint when the loading is thermal and mechanical. As in the AL-AL comparison, both SO and SP models tend to over-predict the shear stress and the SP solution reasonably predicts the peel stress near the edges of the AL-TI joint. Finally, in comparing figures 2.6(a)-2.6(f) to figures 2.7(a)-2.7(f), both the SO and SP models correlate well with the FE solution as the thickness of the adhesive is increased.

2.5.3 Aluminum-AS4/3501-6 joints

The stress predictions for the AL-AS4 joints are shown in figures 2.8-2.9. Uniaxial fiber alignment for the orthotropic AS4 is aligned with the x axis in figures 2.8 and with the z axis in figures 2.9. Though the latter is an unlikely joint arrangement, it is a useful exercise to examine the orthotropic nature of the SO and SP solutions. It is apparent in figures 2.8(a) and 2.8(d) and figures 2.9(a) and 2.9(d) that differences in the orthotropic expansion coefficients have a significant effect. The sign of the stress changes upon a 90^o orientation change. The magnitude of the stress is significantly

lower as the fibers are aligned perpendicular to the cross section of the joint. This result is intuitive, since the material is much more compliant when loaded in the 90^o orientation.

2.5.4 The effect of $\bar{\phi}_{\mathrm{aR}}$ on load dominance

Upon examining all predicted stress results in figures 2.5-2.9, the effect of the thermo-mechanical load ratio $\bar{\phi}_{\mathrm{aR}}$ is apparent. The AL-AL joint, at $|\bar{\phi}_{\mathrm{aR}}| = 0$, is dominated by mechanical load. Both AL-TI joints, at $|\bar{\phi}_{\mathrm{aR}}| = 3.68$, have significant contributions from both thermal and mechanical load. Comparing AL-AS4 (0^o, $|\bar{\phi}_{\mathrm{aR}}| = 7.33$) and ($90^o$, $|\bar{\phi}_{\mathrm{aR}}| = 0.40$) joints in figure 2.8 and figure 2.9, the stress field in AL-AS4 (0^o) lap joints is primarily due to thermal loading whereas the stress field in AL-AS4 (90^o) joint derives primarily from mechanical load. These results show the importance of $\bar{\phi}_{\mathrm{aR}}$ in decoupling the effects of thermal and mechanical load; the effects of $\bar{\beta}$ and $\bar{\gamma}$ are reflected in the axial and shear stress distribution in the adherend and adhesive. Further, $\bar{\phi}_{\mathrm{aR}}$ provides an effective metric for determining the relative importance of thermal and mechanical loads to shear and peel stresses.

2.6 Conclusion

Two closed-form analytical models for the stress distribution in an orthotropic double lap joint have been presented with a view to identifying key dimensionless parameters that govern joint behavior under thermo-mechanical loads. The shear-only model assumes only shear stress exists in the adhesive and produces a similar result to the work of Volkersen with the addition of thermal expansion. It is a tractable solution with valuable dimensionless parameters, though is does not capture peel stress or a traction free edge. It is a useful tool for basic thermomechanical design and sizing of joints. The shear-peel model, which is similar but more complex than the shear-only model, does account for shear and peel stress. The 4^{th} order governing differential equation allows for proper representation of the traction free adhesive edge. Like the shear-only model, the shear-peel model has valuable dimensionless parameters which can be used as tools in joint design and sizing. Unlike linear elastic FE solutions, finite stress concentrations are predicted by the shear-only and shear-peal models. Therefore, they can be used for quick iteration in joint sizing and for meaningful joint comparison based solely on constitutive material properties and joint geometry. The

orthotropic nature of the solutions are especially valuable for composite materials which often have diminished transverse properties or transverse reinforcement.

Dimensionless parameters, written in terms of the joint geometry as well as the orthotropic adherend and adhesive properties, have been identified and shown to be useful in interpreting the stress distribution in the joint. Two dimensionless load parameters ($\bar{\phi}_{\Delta T}$ and $\bar{\phi}_P$) and a critical dimensionless load ratio ($\bar{\phi}_{\mathrm{aR}}$) and its conjugate parameter ($\bar{\phi}_{\mathrm{cR}}$) have been identified. These parameters predict the stress distribution within the joint. The dimensionless load ratio is identically derived using either the shear-only or shear-peel solutions. It can be used as measure of the relative importance of mechanical and thermal loading in a joint of known (or expected) loading. The $\bar{\phi}_{\mathrm{aR}}$ ratio also allows for isolation of the thermal and mechanical portions of the solution. The isolation facilitates an iterative solution when the combined thermal and mechanical loads are interdependent.

Chapter 3

A bonded joint finite element for a symmetric double lap joint subjected to mechanical and thermal loads

Chapter 2 provides a closed-form joint analysis based on the principle of virtual work, a classical analytical method. Chapter 4 describes a numerical technique, the finite element method, where the joint analysis is provided via a unique discrete cohesive zone element. In this chapter, a hybrid method is developed incorporating features of classical analytical and numerical methods. A bonded joint finite element for a symmetric double lap joint is presented. It is capable of calculating field quantities in the lap zone while using only four degrees of freedom.

The element stiffness and load vector formulations have unique, load dependent, non-linear shape functions based on an analytical solution. The adaptive shape functions are formulated in terms of the dimensionless mechanical load fraction ($\bar{\bar{\phi}}_P$) and total load ($\bar{\bar{\phi}}_{\text{tot}}$) and are capable of predicting the thermal and mechanical load response. The bonded joint element has been implemented as a user element in the Abaqus® commercial finite element code. A comparison of the stress predictions for the bonded joint element and a 2D continuum model are presented and are found to be in good agreement. Therefore, the element provides a computationally efficient and mesh independent stress prediction. The single element reproduces the analytical solution with minimal analyst input and can be easily incorporated into early design and sizing studies.

3.1 Introduction

Despite decades of development, the design and modeling of bonded joints is an active area of research. Continuum finite element (FE) models are the current state of the art and are widely available in the literature where work began as early as 1971 ([109], and [3] are early references). More recently, promising advances in cohesive zone (including [59, 64, 65, 102, 115]), discrete cohesive zone ([113], chapter 4), fracture mechanics ([106]), probabilistic prediction ([18], [62]), virtual crack closure technique (including [49, 50, 63, 105, 110, 112, 114]), and other adhesive region models (including [74], [52], [53]) have greatly increased the predictive capability of FE techniques. Cohesive zone models have been incorporated into commercial software including Abaqus® [1] and Genoa® [29], as well as freely available research codes like Tahoe® [87]. Despite their availability, the listed techniques are expensive and require extensive user expertise. There are ongoing efforts to develop rapid analysis techniques ([75, 76, 94]), a key enabling technology for vehicle designers.

Though models built with the tools listed above can be accurate, they rely on the presence of a meshed joint. Continuum elements represent the adherends; the adhesive is represented by continuum elements or a discrete traction law. There is substantial overhead in creating and analyzing joints using these and other continuum numerical methods. Mesh generation and manipulation is an obstacle for anything beyond academic geometries. Mesh density is also a consideration, since the computational time for basic joints can be significant if non-linear material properties and material degradation criterion are included. As a result, there are ongoing efforts to evaluate analytical techniques that are less mesh dependent. For example, the Composites Affordability Initiative has recommended a p-based analysis code for analysis of adhesively bonded joints,[1] since the use of p-based codes should be less mesh dependent than h-based FE codes. Similarly, Bednarcyk et al. [19] used a higher order, semi-analytical theory (developed for functionally graded materials) to analyze a double lap and a bonded doubler joint. These techniques was reported to be less mesh dependent than h-based analysis methodologies. In this chapter, a bonded joint finite element (BJFE) is developed as a specialized element and technique for efficient joint analysis. The BJFE has no mesh dependency and requires minimal meshing overhead.

[1] http://www.esrd.com [Feb. 2007]

3.2 Background

The aim of this chapter is to develop a BJFE capable of predicting basic joint performance analysis with a limited number of degrees of freedom and with little meshing overhead. As a result, this element could be adopted for initial joint sizing in FE models at all system levels. The element is capable of predicting stress and strain fields of orthotropic constituents in thermal and mechanical loading environments. The orthotropy of a joint is of particular concern in laminated composite materials since transverse properties are often significantly lower than in-plane properties in a laminate, [54]. Further, since high temperature curing cycles are frequently needed for temperature resistant materials, prudence dictates that orthotropic material behavior should be included in thermo-mechanical FE models.

In considering the solution accuracy required for the BJFE technique, there are many factors which affect the stress field and associated joint failure. These include adhesive spew [3] and the geometric discontinuity and unbounded stresses associated with stepwise geometries, [61]. Additionally, material non-linearity has a significant effect on the stress field [54, 122] and requires a level of material characterization that is often unavailable early in an analysis cycle. All of the specialized joint analysis techniques (cohesive elements, the virtual crack closure technique, and others) require high level material properties. In many circumstances, a designer has insufficient information or time to obtain a *highly accurate* solution and instead would prefer a simple, directionally correct analysis. These types of analyses are often useful in tradeoff studies and to identify likely problem areas needing further study.

With that goal in mind, it might be considered adequate to perform linear elastic FE analysis with a basic geometry (*ie* square corners), similar to the continuum FE analysis used for comparison in this chapter. In such a solution, however, the singular stress field causes a broad range of predicted stresses near the edges, particularly at the material interfaces. This is an undesirable and unavoidable feature that emerges when a linear elastic material description is used for a corner consisting of two materials that are perfectly bonded.

For example, a typical double lap joint result for predicted $\bar{\sigma}_{b22}$ is highlighted in figure 3.1.[2] It is apparent that the peel stress can be accurately determined as a function of longitudinal position over most of the joint. In the critical areas near the edges of the joint, however, the predicted stress field varies widely and is mesh dependent. The severity of the mesh dependency is shown in figure 3.2, where the

[2] The typical result is taken from a model associated with figures 2.1 and 2.4.

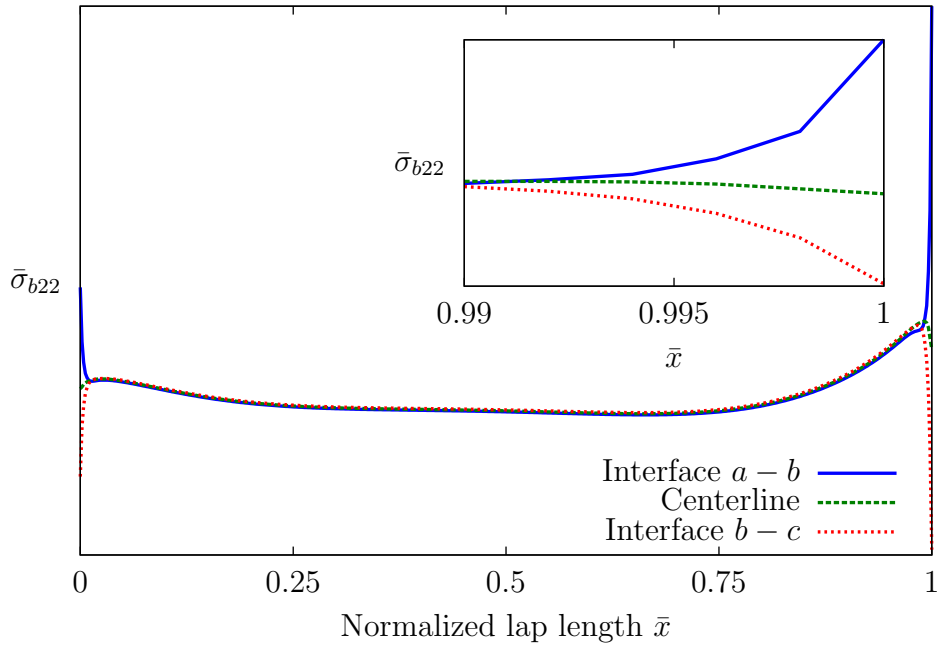

Figure 3.1 Typical linear elastic peel stress distribution due to mixed loading

predicted stress increases without bound with increasing element density. Even when non-linear material properties are assumed, which sometimes can ensure that the stress remains bounded [54], mesh dependency and convergence remain a concern. When this is the case, it is common practice to create several costly meshes at different densities in order to verify that the stress results have converged. Smeltzer III and Lundgren [94] is a recent example of this practice.

In view of the alternatives presented above and in order to be useful to an analyst, the BJFE must accurately represent the value of the most critical stresses in the joint while consistently and correctly predicting the trends from joint to joint. It must accomplish this with no mesh dependency and insignificant meshing overhead. Further, its use must not directly burden the user with the significant calculations typically associated with analytical solutions such as those in chapter 2. In the remaining sections of this chapter, a bonded joint element is developed to meet these requirements.

The predicted stresses and resulting displacements have non-trivial spatial non-linearities and as such are not well represented by a small number of linear or quadratic finite elements. The displacement field, however, can be represented by appropriate load dependent adaptive shape functions $N\left(\bar{\bar{\phi}}_P\right)$ with a single element. Based on the stress predictions presented in section 3.3, an element with a load dependent stiffness matrix $K\left(\bar{\bar{\phi}}_P\right)$ and consistent loading vector $F\left(\bar{\bar{\phi}}_P\right)$ are presented in the following

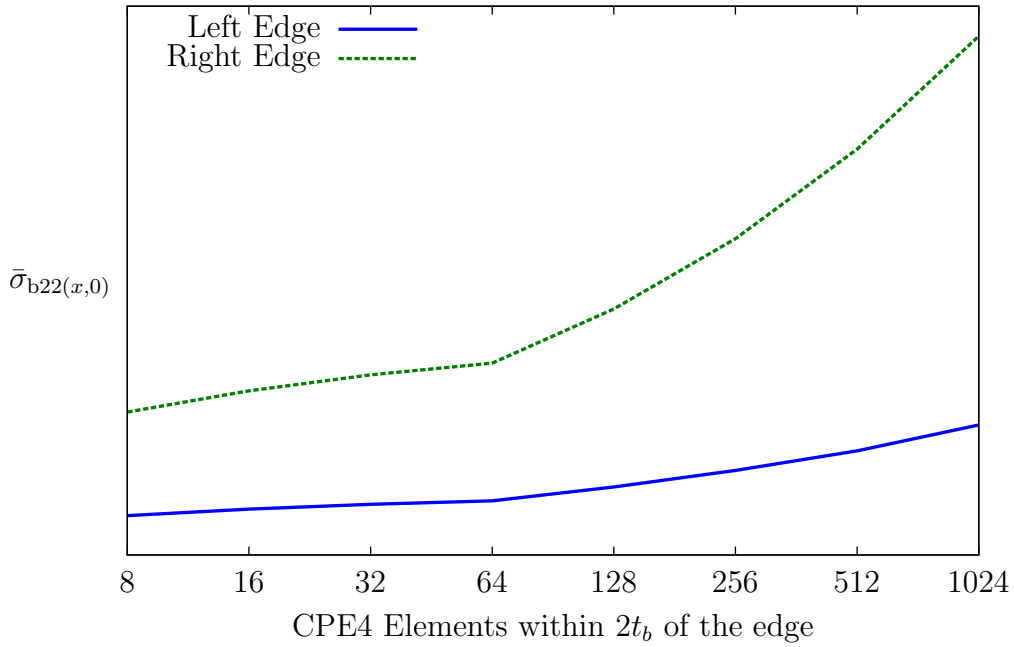

Figure 3.2 Typical mesh "convergence" study for linear elastic stepwise geometry

sections.

3.2.1 The element concept

A schematic of the BJFE element concept is shown in figure 3.3. In it, the complete lap joint is replaced with a single finite element with six degrees of freedom (DOF). Four displacement DOF (q_1, q_2, q_3, q_4) are used to represent four discrete displacement locations and two internal DOF (P_1, P_1) are used to determine the load "character". The displacement field is interpolated with application-specific adaptive shape functions, detailed in section 3.4. The load "character" is a ratio of the thermal and mechanical loads and governs the internal displacement field via the adaptive shape functions. The adaptive shape functions allow accurate predictions of the stress and strain field in a double lap joint through use of a single finite element.

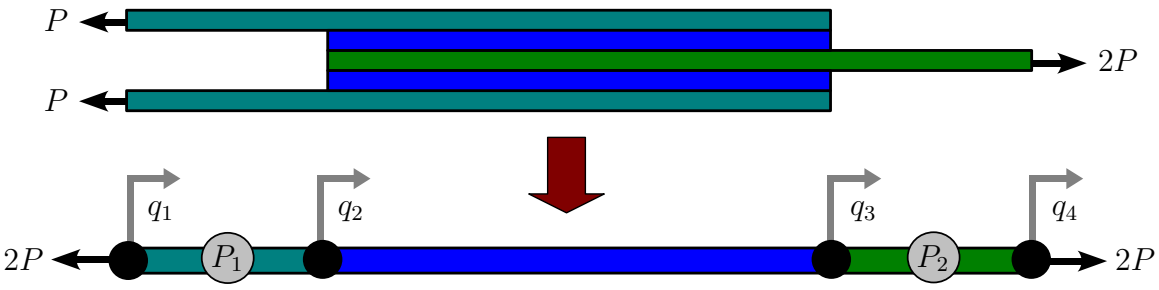

Figure 3.3 Symmetric double lap joint and BJFE representation.

3.3 Derivation of the advanced shear and peel model

In chapter 2, two dimensionless solutions are developed for a symmetric, orthotropic double lap joint subjected to thermomechanical loading. The primary purpose of those solutions is to establish relevant dimensionless parameters that predict the stress field. Using those parameters and the "simple" analytical solutions that they are based on, the effects of various material and loading properties on a joint stress field can be determined. The solutions were not precise in their predictions, despite being adequate to correctly predict trends. It is anticipated that the user of the BJFE would desire more precision, therefore, a third analytical solution is developed for the BJFE. The solution is more "complex" than those that were presented in chapter 2. It is designed, however, for automated use within the BJFE where solution complexity is no longer an issue.

A double lap joint is schematically represented in figure 2.1. The central adherend is referred to as material a and the outer adherend is referred to as material c. Material b is the adhesive and is thin in comparison to the adherends. The objective is to develop adaptive shape functions based on the equilibrium stress due to thermal and mechanical loading. The material is assumed to be linear elastic and orthotropic with linear orthotropic thermal expansion. The joint is assumed to deform in plane strain and the material constitutive response is given by equation 2.1.

A general parallelepiped is shown in figure 2.2. Force equilibrium in x and y directions can be written as:

$$\begin{aligned}
\sum F_1 &= 0, \\
&= \delta y \left(\sigma_{11}(x+\delta x, y) - \sigma_{11}(x,y)\right) + \delta x \left(\tau_{12}(x, y+\delta y) - \tau_{12}(x,y)\right), \\
\sum F_2 &= 0, \\
&= \delta x \left(\sigma_{22}(x, y+\delta y) - \sigma_{22}(x,y)\right) + \delta y \left(\tau_{12}(x+\delta x, y) - \tau_{12}(x,y)\right).
\end{aligned} \tag{3.1}$$

Equation 3.1 can be rewritten as the shear-normal stress relationship for each constituent:

$$\begin{aligned} \frac{\partial \sigma_{11}(x,y)}{\partial x} &= -\frac{\partial \tau_{12}(x,y)}{\partial y}, \\ \frac{\partial \sigma_{22}(x,y)}{\partial y} &= -\frac{\partial \tau_{12}(x,y)}{\partial x}. \end{aligned} \tag{3.2}$$

In chapter 2, the adherends were assumed to carry only longitudinal normal stress and the adhesive was assumed to carry only shear and peel stresses. In this chapter, those assumptions are relaxed so that the adherends also transmit shear stress. For convenience, the adherend shear stress fields are assumed to vary linearly in y throughout the specimen.[3] As a result, equation 3.2 dictates that the adherend longitudinal normal stresses are functions of x only; the peel stresses are linear functions of x and y. The longitudinal normal stress in the adhesive is still assumed to be zero, therefore equation 3.2 dictates that the shear stress in the adhesive is a function of x only.[4]

Traction free boundaries are present on the top and bottom surfaces of the joint. The centerline of the central adherend is free of shear due to symmetry. These requirements are expressed as:

$$\begin{aligned} \tau_{c12}(x, t_b + t_c) &= 0, \\ \sigma_{c22}(x, t_b + t_c) &= 0, \\ \tau_{a12}(x, -\frac{t_a}{2}) &= 0. \end{aligned} \tag{3.3}$$

Stress continuity at the joint interfaces requires:

$$\begin{aligned} \sigma_{b22}(x, 0) &= \sigma_{a22}(x, 0), \\ \sigma_{c22}(x, t_b) &= \sigma_{b22}(x, t_b), \\ \tau_{b12}(x, 0) &= \tau_{a12}(x, 0), \\ \tau_{c12}(x, t_b) &= \tau_{b12}(x, t_b). \end{aligned} \tag{3.4}$$

Finally, longitudinal normal stress boundary conditions are imposed by the mechanical

[3] A linear assumption is the lowest order polynomial which satisfies the equilibrium equations.
[4] The limitations imposed by this assumption are described in chapter 2.

loads at the edges of central adherend a and are expressed as:

$$\begin{aligned} \sigma_{a11}(0) &= 0, \\ \sigma_{a11}(l) &= \frac{2P}{t_a}. \end{aligned} \tag{3.5}$$

By sequentially writing a linear form for each stress component (using the stress field assumptions) and by applying boundary and continuity conditions to determine the linear constants, equations can be written for each stress component in terms of the central adherend stress $\sigma_{a11}(x)$. The process is as described in chapter 2 with the addition of several stress components ($\tau_{a12}(x,y)$, $\sigma_{a22}(x,y)$, $\tau_{c12}(x,y)$, $\sigma_{c22}(x,y)$). The resulting stress equations are detailed on the left side of table A.2.

In addition to the boundary conditions specified in equations 3.3-3.5, the adhesive edge shear stress is forced to zero using the end post technique described in chapter 2. The stresses in the edge posts are also listed on the left side of table A.2.

The solution for the central adherend normal stress ($\sigma_{a11}(x)$) is computed application of the principle of virtual forces as detailed in appendix A. In brief summary of the computation, each stress component is a function of $\sigma_{a11}(x)$. For each component, a corresponding virtual stress component is written in terms of the virtual normal stress $\hat{\sigma}_{a11}(x)$. (The virtual stress components are shown on the right side of table A.2.) By integrating potential energy over the volume of the joint and minimizing for any admissible $\hat{\sigma}_{a11}(x)$, a differential equation is written for the central adherend stress field $\sigma_{a11}(x)$ as a function of all material properties and loads.

$$\frac{d^4\sigma_{a11}(x)}{dx^4} + \beta\frac{d^2\sigma_{a11}(x)}{dx^2} + \gamma\sigma_{a11}(x) + \phi_{\Delta T} + \phi_P = 0. \tag{3.6}$$

In equation 3.6, all material terms have been grouped according to their order of derivative (β and γ) and all load terms have been grouped into thermal ($\phi_{\Delta T}$) and mechanical parameters (ϕ_P). Equation 3.6 is identical in form to the shear-peel model solution differential equation (equation 2.23) in chapter 2, as is its solution. The material constants β and γ and the load constants $\phi_{\Delta T}$ and ϕ_P are more complex due to the increase in the retained stress components in the potential energy minimization.[5] The solution to equation 3.6 was given as equation 2.33 in a normalized form and the

[5]The improved accuracy of this model over its predecessor is a direct result of the addition of these previously neglected terms.

same normalization is applied here.

$$\begin{aligned}
\bar{x} &= \frac{x}{l}, \\
\bar{\beta} &= l^2\beta, \\
\bar{\gamma} &= l^4\gamma, \\
\bar{\phi}_{\Delta T} &= \phi_{\Delta T}\frac{l^4}{E_{a11}}, \\
\bar{\phi}_P &= \phi_P\frac{l^4}{E_{a11}}, \\
\bar{\bar{\phi}}_{\text{tot}} &= \bar{\phi}_P + \bar{\phi}_{\Delta T}, \\
\bar{\bar{\phi}}_P &= \frac{\bar{\phi}_P}{\bar{\bar{\phi}}_{\text{tot}}}, \\
\bar{\bar{\sigma}}_{\kappa ij}(\bar{x}) &= \frac{\sigma_{\kappa ij}(l\bar{x})}{E_{a11}\bar{\bar{\phi}}_{\text{tot}}}.
\end{aligned} \tag{3.7}$$

In equation 3.7, $\bar{x}$ is the dimensionless spatial coordinate measured from the left edge of the joint, $\bar{\beta}$ and $\bar{\gamma}$ are dimensionless material parameters, and $\bar{\phi}_P$ and $\bar{\phi}_{\Delta T}$ are the dimensionless mechanical and thermal loads. The dimensionless total load is $\bar{\bar{\phi}}_{\text{tot}}$ and is used to further normalize the stresses $\bar{\bar{\sigma}}_{\kappa ij}(\bar{x})$. Similarly, the mechanical fraction of the dimensionless total load is $\bar{\bar{\phi}}_P$. Each of the terms in equation 3.7 are explicitly reported in terms of the constitutive and load quantities in appendix E.

The solution form reported in equation 2.33 is reused with updated parameters:

$$\bar{\bar{\sigma}}_{a11}\left(\bar{x}, \bar{\bar{\phi}}_P\right) = \bar{\bar{A}}\left(\bar{\bar{\phi}}_P\right)e^{\bar{\lambda}_1\bar{x}} + \bar{\bar{B}}\left(\bar{\bar{\phi}}_P\right)e^{-\bar{\lambda}_1\bar{x}} + \bar{\bar{C}}\left(\bar{\bar{\phi}}_P\right)e^{\bar{\lambda}_3\bar{x}} + \bar{\bar{D}}\left(\bar{\bar{\phi}}_P\right)e^{-\bar{\lambda}_3\bar{x}} - \frac{1}{\bar{\gamma}}. \tag{3.8}$$

This solution to equation 3.6 is an equation for the normalized central adherend stress ($\bar{\bar{\sigma}}_{a11}\left(\bar{x}, \bar{\bar{\phi}}_P\right)$), from which all stress components can be determined using equation 3.7 and the equations in table A.2. As in the prior chapter, the material parameters in equation 3.8 are recast as the roots of the bi-quadratic differential equation.

$$\bar{\lambda}^2_{[13]} = \frac{-\bar{\beta} \pm \sqrt{\bar{\beta}^2 - 4\bar{\gamma}}}{2}. \tag{3.9}$$

The equations for the dimensionless basis functions ($\bar{\bar{A}}$, $\bar{\bar{B}}$, $\bar{\bar{C}}$, $\bar{\bar{D}}$) are:

$$\begin{aligned}
\bar{\bar{A}}\left(\bar{\bar{\phi}}_P\right) &= \frac{\mu_3\ \mu_{A_P}}{\mu_1\ \mu_2}\ \bar{\bar{\phi}}_P + \frac{\mu_{A_{\Delta T}}}{\mu_1}, \\
\bar{\bar{B}}\left(\bar{\bar{\phi}}_P\right) &= \frac{\mu_3\ \mu_{B_P}}{\mu_1\ \mu_2}\ \bar{\bar{\phi}}_P + \frac{\mu_{B_{\Delta T}}}{\mu_1}, \\
\bar{\bar{C}}\left(\bar{\bar{\phi}}_P\right) &= \frac{\mu_3\ \mu_{C_P}}{\mu_1\ \mu_2}\ \bar{\bar{\phi}}_P + \frac{\mu_{C_{\Delta T}}}{\mu_1}, \\
\bar{\bar{D}}\left(\bar{\bar{\phi}}_P\right) &= \frac{\mu_3\ \mu_{D_P}}{\mu_1\ \mu_2}\ \bar{\bar{\phi}}_P + \frac{\mu_{D_{\Delta T}}}{\mu_1}.
\end{aligned} \tag{3.10}$$

In equation 3.10, the basis functions are linear in the mechanical fraction of the total load ($\bar{\bar{\phi}}_P$). As a result, they effectively separate the thermal and mechanical loads. The basis functions are composed of several material parameter combinations, denoted by μ, whose values are listed in appendix C.2. In combination, equations 3.8-3.10 provide a solution to the double lap joint that is sufficiently accurate to accomplish the goals of the BJFE.[6]

3.4 Formulation of the finite element

A schematic of the BJFE is shown in figure 3.3. The element is one dimensional; all displacement DOF are oriented along the 1-axis. Two of the displacement DOF (q_1 and q_4) are external and connect the joint element to the external structure. The remaining displacement DOF are internal to the element and are used in conjunction with supplemental equations in order to determine the mechanical loading fraction ($\bar{\bar{\phi}}_P$) required by the adaptive shape function. The mechanical load that is carried across the joint can be calculated using internal DOF P_1 and P_2.

The derivation of the element is presented in stages. First the outer section sub-elements are formulated from the equilibrium stress equation. The formulation is subsequently generalized for the lap region sub-element. An equilibrium formulation is required since the displacement field is governed by an adaptive shape function that is dependent on load character.

[6]The solution in this section is incomplete without additional information provided in chapter 2. Specifically, the application of boundary conditions is required to bridge between the differential equation equation 3.6 and the stress solution equation 3.8.

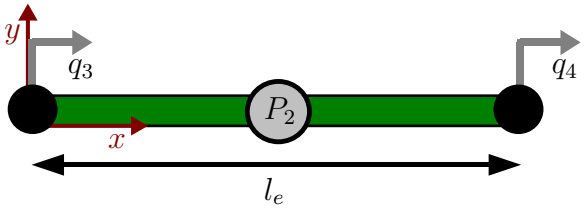

(a) Sub-element for the central adherend outside of the lap region

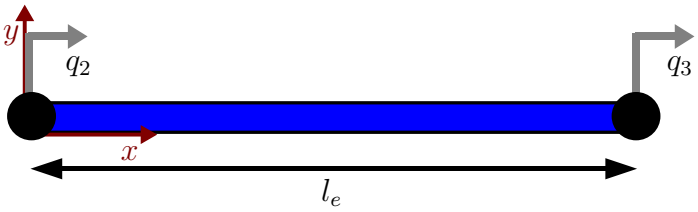

(b) Sub-element for the lap region of the double lap joint

Figure 3.4 BJFE sub-elements

3.4.1 Stiffness and load contribution of the adherends outside of the lap region

The stress in the adherend structures outside the lap region are assumed to have no transverse stress ($\sigma_{k22} = 0$). The orthotropic adherend constitutive relationship is given in equation 2.1. All Poisson terms will be set to zero in the initial portion of the derivation. Thus, the sub-elements outside the lap region are equivalent to truss elements. A more general analysis would include these Poisson terms, however, retaining them in this derivation deters the demonstration without adding value.

As a preface to the remainder of this section, the following derivation may seem unnecessary since the truss element has linear shape functions and is well understood. The reader could skip to the next section without loss of substance. The subsequent derivation of the lap region's adaptive shape functions, however, is completed using the same steps. The intermediate results of that derivation are too long to be included in the text. As a result, a detailed derivation is presented for this sub-element where it can be easily understood.

With a view to deriving the adaptive shape functions in the lap region, the stress field in the outer center adherend is written directly from equilibrium:

$$\sigma_{a11}\left(\bar{x}\right) = \frac{P}{t_a}, \tag{3.11}$$

where $\bar{x}$ is the natural coordinate of this section, defined as:

$$\bar{x} = \frac{x}{l_e}. \tag{3.12}$$

The sub-element local x, y directions are defined from the left edge of the sub-element and the sub-element length is l_e as shown in figure 3.4(a). The sub-element displacement DOF are temporarily replaced by a single extensional DOF given by:

$$q_e = q_4 - q_3. \tag{3.13}$$

From equations 2.1 and 3.11, the strain field can be written as:

$$\varepsilon_{a11}(\bar{x}) = \frac{\sigma_{a11}(\bar{x})}{E_{a11}} + \alpha_{a11}\Delta T. \tag{3.14}$$

Integration of the strain field yields the axial displacement field,

$$u_a(\bar{x}) = \int_0^{\bar{x}} \varepsilon_{a11}(\bar{x}) \left(\frac{dx}{d\bar{x}}\right) d\bar{x}. \tag{3.15}$$

The extension (q_e) is given by:

$$\begin{aligned} u_a(\bar{x}=1) &= q_e, \\ &= l_e \left[\frac{P}{E_{a11} t_a} + \alpha_{a11}\Delta T\right]. \end{aligned} \tag{3.16}$$

The intent of this section is to understand the subsequent lap region derivation, therefore, recall that the joint section stress field given in equation 3.8 is written in terms of dimensionless loads. To generalized the loads for this sub-element, non-dimensionalizing substitutions are made:

$$\begin{aligned} P &= \bar{\psi}_P \; E_{a11} \; t_a, \\ \Delta T &= \frac{\bar{\psi}_T}{\alpha_{a11}}, \end{aligned} \tag{3.17}$$

Parameters $\bar{\psi}_{\Delta T}$ and $\bar{\psi}_P$ are dimensionless thermal and mechanical loads. Additionally, all critical values can be written in terms of the mechanical load fraction ($\bar{\bar{\psi}}_P$) and

the total load ($\bar{\bar{\psi}}_{\text{tot}}$):

$$\begin{aligned} \bar{\bar{\psi}}_{\text{tot}} &= \bar{\psi}_T + \bar{\psi}_P, \\ \bar{\psi}_P &= \bar{\bar{\psi}}_P \, \bar{\bar{\psi}}_{\text{tot}}, \\ \bar{\psi}_T &= \bar{\bar{\psi}}_{\text{tot}} \left(1 - \bar{\bar{\psi}}_P\right). \end{aligned} \tag{3.18}$$

Combining equations 3.11, 3.14-3.16, and 3.18, the axial displacement field can be written as:

$$u_a\left(\bar{x}\right) = l_e \, \bar{\bar{\psi}}_{\text{tot}} \, \bar{x}, \tag{3.19}$$

and the extension DOF can be written as:

$$q_e = l_e \, \bar{\bar{\psi}}_{\text{tot}}. \tag{3.20}$$

The displacement field of equation 3.19 is written in terms of the unknown total load ($\bar{\bar{\psi}}_{\text{tot}}$). Using equation 3.20, the total load can be isolated as a linear function of the extension DOF (q_e),

$$\bar{\bar{\psi}}_{\text{tot}} = \frac{q_e}{l_e}. \tag{3.21}$$

In equations 3.19 and 3.21, a linear displacement field is recovered and can be written as a shape function $N(\bar{x}, \bar{\bar{\psi}}_P)$.

$$\begin{aligned} u_a\left(\bar{x}\right) &= \bar{x} \; q_e \\ &= N(\bar{x}, \bar{\bar{\psi}}_P) \; q_e \end{aligned} \tag{3.22}$$

As the shape function has been determined from equilibrium, the mechanical load fraction ($\bar{\bar{\psi}}_P$) is implicitly included in equations 3.21 and 3.22 (although it has been eliminated). Equation 3.22 is otherwise unremarkable, however, it is a necessary step in the process of *deriving* a shape function from the equilibrium equations.[7] Using equation 3.22, the strain and stress can be written in terms of q_e and the shape function derivative $B(\bar{x}, \bar{\bar{\psi}}_P)$,

$$\begin{aligned} \varepsilon_{a11}\left(\bar{x}\right) &= \left(\frac{d\bar{x}}{dx}\right) \frac{d}{d\bar{x}} \; u_a\left(\bar{x}\right), \\ &= \frac{B(\bar{x}, \bar{\bar{\psi}}_P) \; q_e}{l_e}, \end{aligned} \tag{3.23}$$

[7]The standard FE process is to assume a polynomial shape function and derive all quantities from the resulting displacement field.

$$\begin{aligned}\sigma_{a11}\left(\bar{x}\right) &= E_{a11}\left(\varepsilon_{a11} - \alpha_{a11}\Delta T\right), \\ &= E_{a11}\left(\frac{B(\bar{x},\bar{\bar{\psi}}_P)q_e}{l_e} - \alpha_{a11}\Delta T\right).\end{aligned} \tag{3.24}$$

In the example of the central adherend outside the lap section, $B(\bar{x},\bar{\bar{\psi}}_P) = 1$.

The strain energy and external work terms are:

$$\begin{aligned}U &= \int_0^{t_a}\int_0^1 \sigma_{a11}\left(\bar{x},\bar{\bar{\psi}}_P\right)\delta\varepsilon_{a11}\left(\bar{x},\bar{\bar{\psi}}_P\right)\left(\frac{dx}{d\bar{x}}\right)\, d\bar{x}\, dy, \\ W &= Pq_e.\end{aligned} \tag{3.25}$$

In contrast to equation 3.11 which was used to obtain the shape functions, equation 3.24 and equation 3.25 are written in terms of the temperature change and load (ΔT and P). This is necessary to correctly compute the strain energy and work required for obtaining the stiffness matrix and load vector.

Restoring the discrete displacements (q_3, q_4) in place of the extension (q_e), the strain energy is:

$$U = \frac{E_{a11}\left(q_4 - q_3\right)\int_{y_0}^{y_1}\int_0^1 B\left(\bar{x},\bar{\bar{\psi}}_P\right)\left(\left(q_4 - q_3\right)B\left(\bar{x},\bar{\bar{\psi}}_P\right) - \alpha_{a11}l_e\Delta T\right)\, d\bar{x}\, dy}{2\, l_e}. \tag{3.26}$$

With the work and strain energy fully defined, the potential energy equation can be used to extract the stiffness matrix and load vector:

$$\begin{aligned}\frac{d}{d\vec{q_e}}\,\Pi &= \frac{d}{d\vec{q_e}}\,\left(U - W\right), \\ &= 0, \\ &\rightarrow K_e\vec{q_e} = \vec{F}_e.\end{aligned} \tag{3.27}$$

The sub-element stiffness matrix, K_e, is:

$$K_e = \frac{\sum_\kappa E_{\kappa 11}\int_{y_{\kappa 0}}^{y_{\kappa 1}}\int_0^1 B_\kappa^2\left(\bar{x},\bar{\bar{\psi}}_P\right)d\bar{x}\, dy_\kappa}{l_e}\begin{bmatrix} 1 & -1 \\ -1 & 1 \end{bmatrix} \tag{3.28}$$

and the sub-element load vector, $\vec{F}$, is:

$$\vec{F}_e = P \left\{ \begin{array}{c} -1 \\ 1 \end{array} \right\} + \sum_{\kappa} \alpha_{\kappa 11} E_{\kappa 11} \left(\int_{y_0}^{y_1} \int_{0}^{1} B_\kappa \left(\bar{x}, \bar{\bar{\psi}}_P \right) d\bar{x}\, dy_\kappa \right) \Delta T \left\{ \begin{array}{c} -1 \\ 1 \end{array} \right\} \quad (3.29)$$

In this section which focuses on the central adherend sub-element, the summations in equations 3.28 and 3.29 include only the central adherend ($\kappa = a$). It is evident that when $B\left(\bar{x}, \bar{\bar{\psi}}_P\right) = 1$ (for this sub-element), the appropriate truss element stiffness is recovered. Therefore, the sub-element stiffness and load quantities can be derived from equilibrium using non-dimensionalized loads and their ratios. Identical sub-element formulations are used for the central adherend and outer adherends (external to the lap region).

Stiffness and load contribution of the adhesively lap section

In the prior section, a general method was developed for calculating a stiffness matrix and load vector which are load dependent. More specifically, the stiffness matrix and load vector were derived as functions of the ratio of dimensionless thermal and mechanical loads, rewritten in terms of the mechanical load fraction ($\bar{\bar{\psi}}_P$). Although the truss type element derivation necessarily resulted in a linear displacement field and a load independent stiffness matrix, the method is general. In this section, it is used to develop an adaptive shape function for the displacement field of the lap region of a symmetric double lap joint.

Following the order of the derivation in the prior section and applying it to the sub-element shown in figure 3.4(b), the equilibrium stress field must be known. Within the assumptions of its derivation.[8], the double lap joint stress field has the following

[8]See section 3.3

components for the adherends and adhesive:

$$
\begin{aligned}
&\sigma_{a11}\left(\bar{x},\bar{\bar{\phi}}_P,\bar{\bar{\phi}}_{\text{tot}}\right)\\
&\quad=E_{a11}\bar{\bar{\phi}}_{\text{tot}}\left(\bar{\bar{A}}\left(\bar{\bar{\phi}}_P\right)e^{\bar{\lambda}_1\bar{x}}+\bar{\bar{B}}\left(\bar{\bar{\phi}}_P\right)e^{-\bar{\lambda}_1\bar{x}}+\bar{\bar{C}}\left(\bar{\bar{\phi}}_P\right)e^{\bar{\lambda}_3\bar{x}}+\bar{\bar{D}}\left(\bar{\bar{\phi}}_P\right)e^{-\bar{\lambda}_3\bar{x}}-\frac{1}{\bar{\gamma}}\right),\\
&\sigma_{b12}\left(\bar{x},\bar{\bar{\phi}}_P,\bar{\bar{\phi}}_{\text{tot}}\right)=-\frac{t_a}{2}\left(\frac{d\bar{x}}{dx}\right)\left(\frac{d}{d\bar{x}}\sigma_{a11}\left(\bar{x},\bar{\bar{\phi}}_P,\bar{\bar{\phi}}_{\text{tot}}\right)\right),\\
&\sigma_{b22}\left(\bar{x},y,\bar{\bar{\phi}}_P,\bar{\bar{\phi}}_{\text{tot}}\right)=\frac{t_a}{2}\left(\frac{d\bar{x}}{dx}\right)^2\left(\frac{d^2}{d\bar{x}^2}\sigma_{a11}\left(\bar{x},\bar{\bar{\phi}}_P,\bar{\bar{\phi}}_{\text{tot}}\right)\right)(y-t_b),\\
&\sigma_{c11}\left(\bar{x},\bar{\bar{\phi}}_P,\bar{\bar{\phi}}_{\text{tot}}\right)=\frac{P}{t_c}-\frac{t_a\sigma_{a11}\left(\bar{x},\bar{\bar{\phi}}_P,\bar{\bar{\phi}}_{\text{tot}}\right)}{2\,t_c}.
\end{aligned}
\tag{3.30}
$$

The stress components not listed in equation 3.30 can be determined but are of less interest.

In the discrete space of the FE model, the known (or desired) quantities are the applied temperature change (ΔT, assumed to be constant throughout the element) and the nodal loads and displacements. The load quantities must be recast into their dimensionless forms to conform to the governing equation for $\sigma_{a11}(x)$. Non-dimensionalizing parameters are defined so that:

$$
\begin{aligned}
\Delta T&=\frac{\Theta}{\theta_{\Delta T}}\bar{\phi}_{\Delta T},\\
P&=\frac{\Theta}{\theta_P}\bar{\phi}_P.
\end{aligned}
\tag{3.31}
$$

Application of equation 3.31 to the equilibrium stress field and constitutive law, the

strain can be written as a linear function of the total load $\bar{\bar{\phi}}_{\text{tot}}$:

$$\begin{aligned}
\frac{\varepsilon_{a11}\left(\bar{x},\bar{\bar{\phi}}_P,\bar{\bar{\phi}}_{\text{tot}}\right)}{\bar{\bar{\phi}}_{\text{tot}}} =& (1-\nu_{a13}\nu_{a31}) \\
& \cdot\left(e^{-\bar{\lambda}_3\bar{x}}\bar{\bar{D}}\left(\bar{\bar{\phi}}_P\right)+e^{\bar{\lambda}_3\bar{x}}\bar{\bar{C}}\left(\bar{\bar{\phi}}_P\right)+e^{-\bar{\lambda}_1\bar{x}}\bar{\bar{B}}\left(\bar{\bar{\phi}}_P\right)+e^{\bar{\lambda}_1\bar{x}}\bar{\bar{A}}\left(\bar{\bar{\phi}}_P\right)-\frac{1}{\bar{\gamma}}\right) \\
& +\frac{\Theta}{\theta_{\Delta T}}\left(1-\bar{\bar{\phi}}_P\right)\left(\alpha_{a33}\nu_{a31}+\alpha_{a11}\right), \\
\frac{\varepsilon_{c11}\left(\bar{x},\bar{\bar{\phi}}_P,\bar{\bar{\phi}}_{\text{tot}}\right)}{\bar{\bar{\phi}}_{\text{tot}}} =& \frac{E_{a11}t_a\left(\nu_{c13}\nu_{c31}-1\right)}{2E_{c11}t_c} \\
& \cdot\left(e^{-\bar{\lambda}_3\bar{x}}\bar{\bar{D}}\left(\bar{\bar{\phi}}_P\right)+e^{\bar{\lambda}_3\bar{x}}\bar{\bar{C}}\left(\bar{\bar{\phi}}_P\right)+e^{-\bar{\lambda}_1\bar{x}}\bar{\bar{B}}\left(\bar{\bar{\phi}}_P\right)+e^{\bar{\lambda}_1\bar{x}}\bar{\bar{A}}\left(\bar{\bar{\phi}}_P\right)\right) \\
& +\frac{\Theta}{\theta_{\Delta T}}\left(1-\bar{\bar{\phi}}_P\right)\left(\alpha_{c11}+\alpha_{c33}\nu_{c31}\right) \\
& +\frac{1}{E_{c11}t_c}\left(1-\nu_{c13}\nu_{c31}\right)\left(\frac{E_{a11}t_a}{2\bar{\gamma}}+\frac{\bar{\bar{\phi}}_P\frac{\Theta}{\theta_P}}{1}\right).
\end{aligned} \tag{3.32}$$

It is assumed that the total elongation is the same for the adherends. Therefore, the elongation equations are:

$$\begin{aligned}
q_e &= \left(\frac{dx}{d\bar{x}}\right)\int_0^1 \varepsilon_{a11}\left(\bar{x},\bar{\bar{\phi}}_P,\bar{\bar{\phi}}_{\text{tot}}\right)d\bar{x}, \\
q_e &= \left(\frac{dx}{d\bar{x}}\right)\int_0^1 \varepsilon_{c11}\left(\bar{x},y,\bar{\bar{\phi}}_P,\bar{\bar{\phi}}_{\text{tot}}\right)d\bar{x}.
\end{aligned} \tag{3.33}$$

As in the prior section, the sub-element elongation q_e is defined as:

$$q_e = q_3 - q_2. \tag{3.34}$$

In equation 3.33, the elongation is written as a function of the dimensionless total load ($\bar{\bar{\phi}}_{\text{tot}}$). The total load is not known *a priori* and must be eliminated in favor of an available quantity (the total elongation q_e) so that a stiffness matrix can be calculated. This is accomplished by application of the boundary conditions to the

result of equation 3.33:

$$\begin{aligned}
\left(\frac{dx}{d\bar{x}}\right)\int_0^{\bar{x}} \varepsilon_{a11}\left(\bar{x},\bar{\bar{\phi}}_P,\bar{\bar{\phi}}_{\text{tot}}\right)d\bar{x}\Bigg|_{\bar{x}=0} &= 0,\\
\left(\frac{dx}{d\bar{x}}\right)\int_0^{\bar{x}} \varepsilon_{a11}\left(\bar{x},\bar{\bar{\phi}}_P,\bar{\bar{\phi}}_{\text{tot}}\right)d\bar{x}\Bigg|_{\bar{x}=1} &= q_e,\\
\left(\frac{dx}{d\bar{x}}\right)\int_0^{\bar{x}} \varepsilon_{c11}\left(\bar{x},\bar{\bar{\phi}}_P,\bar{\bar{\phi}}_{\text{tot}}\right)d\bar{x}\Bigg|_{\bar{x}=0} &= 0,\\
\left(\frac{dx}{d\bar{x}}\right)\int_0^{\bar{x}} \varepsilon_{c11}\left(\bar{x},\bar{\bar{\phi}}_P,\bar{\bar{\phi}}_{\text{tot}}\right)d\bar{x}\Bigg|_{\bar{x}=1} &= q_e.
\end{aligned} \tag{3.35}$$

Specifically, the elongation is zero when $\bar{x} = 0$ ($\bar{x} = 0$ is the reference from which elongation is measured) and the total elongation is q_e when $\bar{x} = 1$. Applying these boundary conditions and solving for the total load ($\bar{\bar{\phi}}_{\text{tot}}$) as a function of elongation (q_e) in each strain equation, the total load can be replaced in equation 3.32:

$$\begin{aligned}
\bar{\bar{\phi}}_{\text{tot}_a} &= \bar{\bar{\Phi}}_{\text{a}} q_e,\\
\bar{\bar{\phi}}_{\text{tot}_c} &= \bar{\bar{\Phi}}_{\text{c}} q_e.
\end{aligned} \tag{3.36}$$

The intermediate terms ($\bar{\bar{\Phi}}_{\text{a}}$, $\bar{\bar{\Phi}}_{\text{c}}$) are detailed in appendix E. Substituting equation 3.36 into equation 3.32, the displacement field is known in terms of total elongation and the shape functions. shape functions and their derivatives can now be written for each adherend:

$$\begin{aligned}
u_a\left(\bar{x},\bar{\bar{\phi}}_P,q_e\right) &= N_a\left(\bar{x},\bar{\bar{\phi}}_P\right)q_e,\\
u_c\left(\bar{x},\bar{\bar{\phi}}_P,q_e\right) &= N_c\left(\bar{x},\bar{\bar{\phi}}_P\right)q_e,\\
B_a\left(\bar{x},\bar{\bar{\phi}}_P\right) &= \frac{d}{d\bar{x}}N_a\left(\bar{x},\bar{\bar{\phi}}_P\right),\\
B_c\left(\bar{x},\bar{\bar{\phi}}_P\right) &= \frac{d}{d\bar{x}}N_c\left(\bar{x},\bar{\bar{\phi}}_P\right).
\end{aligned} \tag{3.37}$$

The shape functions in equation 3.37 are detailed in the appendix D. With established shape functions, the stiffness matrix and load vector can be integrated numerically using equations 3.38 and 3.39.

$$K_e = \frac{\sum_{\kappa} E_{\kappa 11}\int_{y_{\kappa 0}}^{y_{\kappa 1}}\int_0^1 B_\kappa^2\left(\bar{x},\bar{\bar{\phi}}_P\right)d\bar{x}\,dy_\kappa}{l_e}\begin{bmatrix} 1 & -1\\ -1 & 1\end{bmatrix} \tag{3.38}$$

$$\vec{F}_e = P \left\{ \begin{array}{c} -1 \\ 1 \end{array} \right\} + \sum_{\kappa} \alpha_{\kappa 11} E_{\kappa 11} \left(\int_{y_0}^{y_1} \int_{0}^{1} B_\kappa \left(\bar{x}, \bar{\bar{\phi}}_P \right) d\bar{x}\, dy_\kappa \right) \Delta T \left\{ \begin{array}{c} -1 \\ 1 \end{array} \right\} \quad (3.39)$$

In equations 3.38 and 3.39, the summation includes both adherends ($\kappa = a, c$). The sub-element stiffness matrix is adaptive to the character of the load through $\bar{\bar{\phi}}_P$. The strain in the adherends is related, via the material constitutive response given in equation 2.1, to the stress fields known from equation 3.8 and table A.2. These strains are related to the stiffness matrix by shape functions derivatives.

The final requirement for element calculations is knowledge of the mechanical load (P), used to determine the load character ($\bar{\bar{\phi}}_P$) of the lap section sub-element.

Calculation of the load carried across the lap section

Using the equilibrium equation for the central adherend outside the lap section, it is known that the internal load can be determined from:

$$q_e = \frac{P_2 l_e}{E_{a11} t_a} + \alpha_{a11} l_e \Delta T. \quad (3.40)$$

In terms of the displacement DOF, the above equation can be written as an additional equation in the sub-element stiffness matrix and load vector:

$$\left[\begin{array}{ccc} \frac{E_{a11} t_a}{l_e} & -\frac{E_{a11} t_a}{l_e} & 1 \end{array} \right] \left\{ \begin{array}{c} q_3 \\ q_4 \\ P_2 \end{array} \right\} = \left\{ -E_{a11}\, t_a \alpha_{a11}\, \Delta T \right\}. \quad (3.41)$$

In equation 3.41, the mechanical load (P_2) can be written as an additional degree of freedom and that is available during every increment.[9]

3.4.2 The FE implementation

The BJFE formulation requires an iterative solution since the mechanical load in the joint is not known in general. Therefore, the adaptive shape functions have been implemented as a user element subroutine (UEL) for Abaqus®, a commercial non-linear FE package.

[9] The current formulation of the element carries two internal load degrees of freedom, P_1 and P_2 as shown in figure 3.3. Strictly speaking, this only requires one additional DOF.

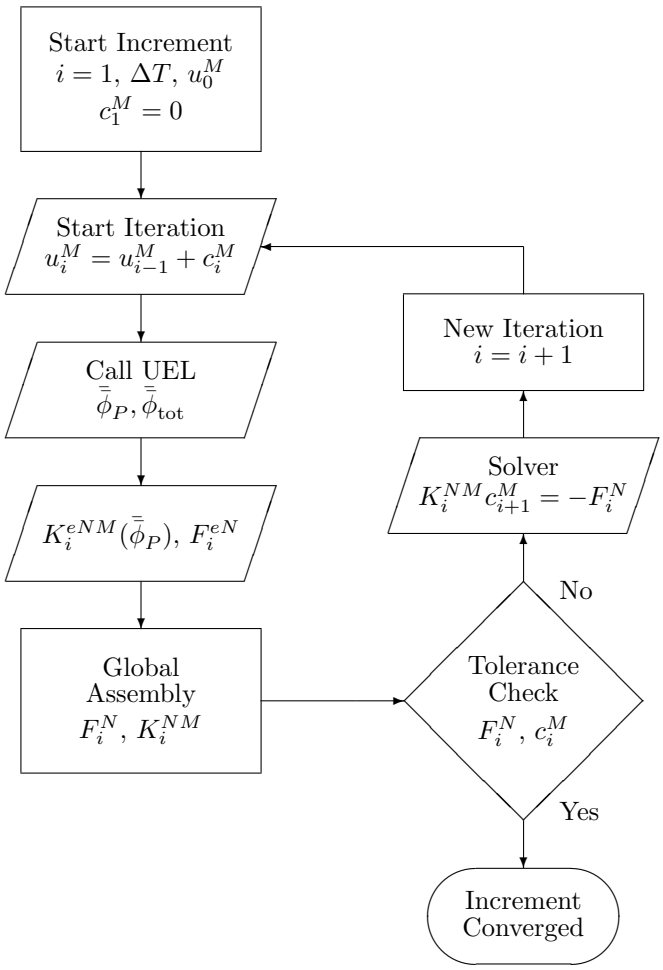

Figure 3.5 The solution procedure for the BJFE user element subroutine.

The displacement, stress, and strain fields are dependent on the ratio of the mechanical to thermal load through the mechanical load fraction ($\bar{\bar{\phi}}_P$). This ratio must be calculated by the BJFE. A general approach for any solution algorithm was developed in section 3.4.1. In the UEL implementation, the Newton-Raphson solution algorithm [93] allows complete elimination of the mechanical load DOF. Though the equations[10] describing the algorithm are deferred to chapter 4, a flowchart of the Newton-Raphson algorithm (as it relates to the BJFE) is shown in figure 3.5.

In addition to the constitutive and geometric quantities, the inputs to the BJFE are the current iteration's displacements (u_i^M) and the relative temperature change (ΔT). The first step in the UEL is to compute the (constant) central and outer sub-element stiffnesses using equation 3.28. The central and outer sub-element load vectors are then computed using equation 3.29 and u_i^M. By first computing the load vectors in

[10] See equations 4.17-4.22).

the outer sub-elements, the mechanical load can be used to calculate consistent shape functions and stiffnesses in the lap region.[11] The thermal load (ΔT) is assumed to be constant through the element and is applied as a user distributed load [1] into the BJFE. The initial iteration's value of ΔT is determined automatically by the solver based on the method chosen by the user. The default is a linear ramping of the temperature change over the step.

With knowledge of the current iteration's value of the mechanical load fraction ($\bar{\bar{\phi}}_P$), the current iteration's shape functions and matrices are calculated for the lap zone sub-element. The lap zone stiffness matrix and load vector are integrated numerically using a modified midpoint rule. The modification offsets the integration point by $\frac{1}{2}$ interval so that the extremes of the joint section are included in the integration. Equal weighting is given to each interval, except that the end points have a weighting of $\frac{1}{2}$ the other intervals.

The number of integration points is defined by the user. The number is usually dictated by the desire to resolve stress gradients within the lap zone.[12] The field quantities are calculated from table A.2 (at each integration point) based on the calculated ΔT and P for the increment. Using this procedure, all stress and strain quantities of interest are calculated in a manner consistent with the shape function displacement field. Further, the shape functions and the resulting stiffness matrix are consistent in the Newton-Raphson algorithm and therefore exhibit quadratic termination, [27]. Though the displacement interpolation is non-linear in $\bar{\bar{\phi}}_P$, the element tangent stiffness is a smooth function of $\bar{\bar{\phi}}_P$ over the majority of the range of $\bar{\bar{\phi}}_P$. Worst-case analyses converged with relative ease in all attempts.

The final task of the UEL is to assemble the sub-element stiffness matrices and load vectors into element-level matrices with four DOF (using standard assembly techniques [27]) and return them to the solver.

[11] The outer sub-element load vectors provide the current iteration's values of the mechanical loads in the lap region sub-element (provided by P_1 and P_2 in the general procedure). These forces should be equal if no body forces are applied, however, it is possible that they differ during iteration and have negligible differences after the solution completes (according to the specified convergence tolerances). Therefore, the two values are averaged for the purposes of calculating P and $\bar{\bar{\phi}}_P$.

[12] The stiffness and load matrices converge with a smaller number of integration points than is usually desired for stress evaluation.

3.5 Benchmarking

The stress prediction of the BJFE has been compared to a plane strain continuum FE model. In the BJFE, the entire model consists of a *single element*. In the continuum model, a 2D mesh has been generated. Both models are based on the ASTM International (ASTM) double lap joint, [12]. The continuum mesh is shown in figure 2.4 and the assumed geometries are given in table 2.1(a). The solver is Abaqus® Standard and the continuum mesh consists entirely of linear plain strain elements (CPE4I). Half of the joint is modeled due to symmetry. Loading is specified as listed in table 2.1(b). The mechanical load is applied far away from the lap joint and the thermal load is applied to all nodes. Displacement symmetry constraints are enforced along the mid-plane of the central adherend. Non-linear geometric stiffness is assumed.

Aluminum (AL) is the central adherend in all models; the outer adherends are titanium (TI) and AS4/3501-6 (AS4) [57]. For simplicity, the adhesive properties are assumed to be isotropic and are estimated based on Cytec FM300 adhesive. The assumed material properties are summarized in table 2.2 of appendix A. The shear stresses from the continuum model are reported at the centerline of the adhesive. The centerline is the most representative location for comparison with the uniform shear stress predicted by the BJFE. The peel stress in the continuum model is reported at the interface between the adhesive and the central adherend. The choice of location has a large effect on the predicted peel stress, as was shown in figure 3.1. The adhesive to central adherend interface (*a*-*b*) comparison location is chosen because the BJFE model can be used as a measure of the *severity* of the stress field caused by the singularity at this location. The peel stress reported from the BJFE is the average peel stress through the thickness (the stress equation is evaluated at $y = \frac{t_b}{2}$).

3.5.1 Comparison of the BJFE and continuum FE models

Plots of stresses predicted by the continuum and BJFE models are shown in figures 3.6-3.10. Figure 3.6 shows the predictions for a AL-AL double lap joint. When this joint is subjected to thermal loading, as is shown in figures 3.6(a) and 3.6(b), both models predict that the stress is negligible.[13] This stress result is intuitive, since the two adherends have identical thermal expansion coefficients. Figures 3.6(c) and 3.6(d) show shear and peel stress predictions of the AL-AL joint subjected to mechanical

[13]This is the special case of identical adherends. Thermal expansion of the adhesive is the *primary* source of loading. As reported in chapter 2, a different analytical procedure may be more appropriate.

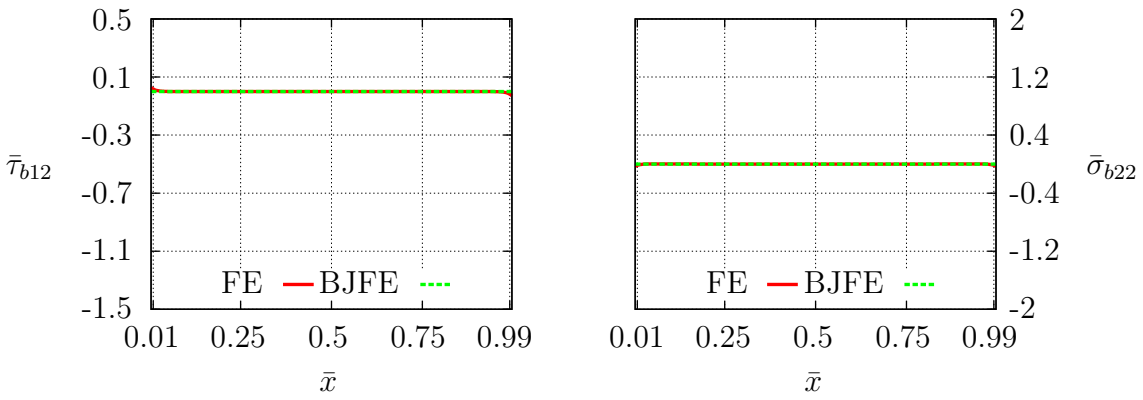

(a) $\bar{\tau}_{b12}$ due to $\bar{\phi}_{\Delta T}$ (b) $\bar{\sigma}_{b22}$ due to $\bar{\phi}_{\Delta T}$

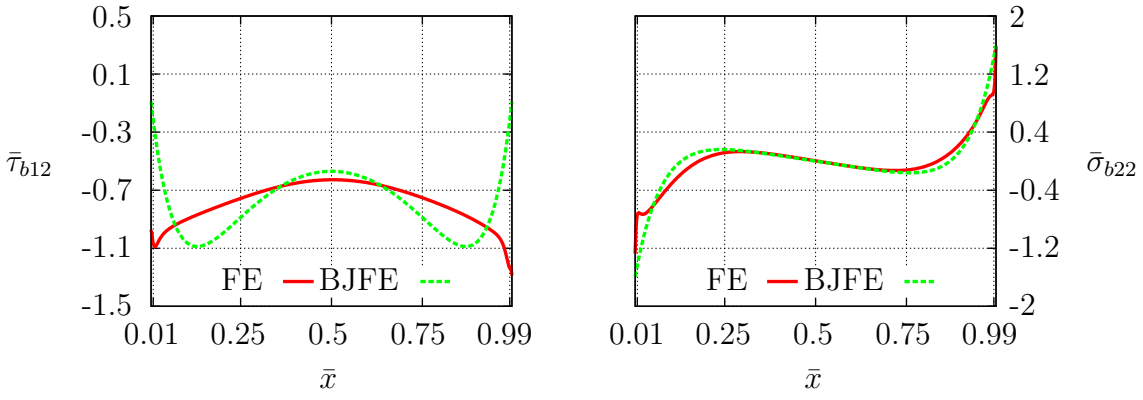

(c) $\bar{\tau}_{b12}$ due to $\bar{\phi}_{P}$ (d) $\bar{\sigma}_{b22}$ due to $\bar{\phi}_{P}$

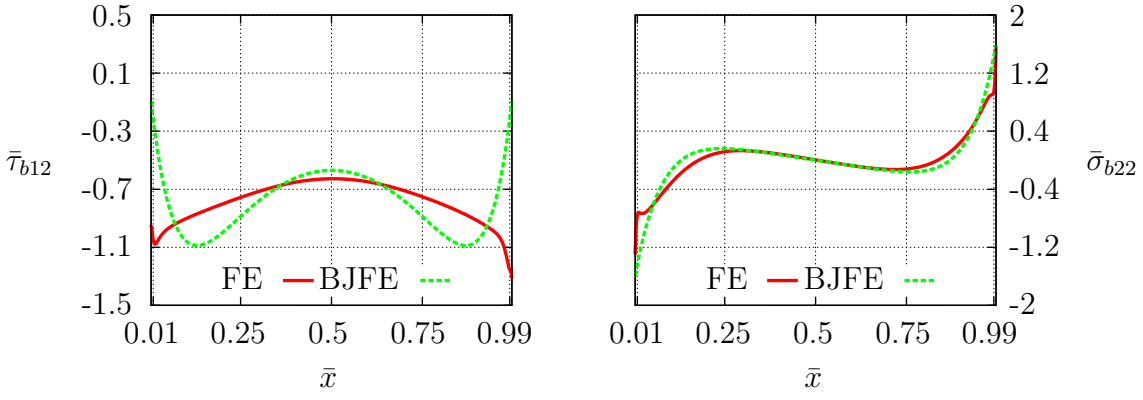

(e) $\bar{\tau}_{b12}$ due to $\bar{\phi}_{P}+\bar{\phi}_{\Delta T}$ (f) $\bar{\sigma}_{b22}$ due to $\bar{\phi}_{P}+\bar{\phi}_{\Delta T}$

Figure 3.6 Continuum and BJFE models of AL-AL joint with 0.2 mm adhesive

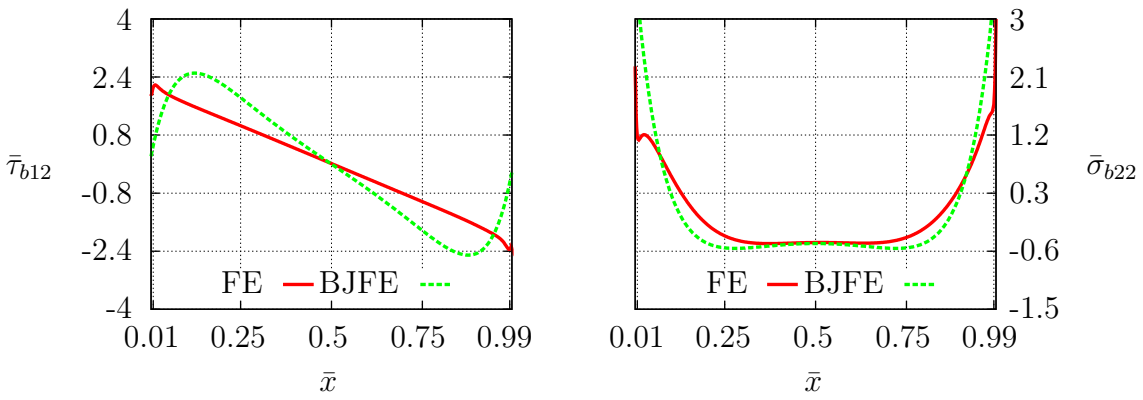

(a) $\bar{\tau}_{b12}$ due to $\bar{\phi}_{\Delta T}$ (b) $\bar{\sigma}_{b22}$ due to $\bar{\phi}_{\Delta T}$

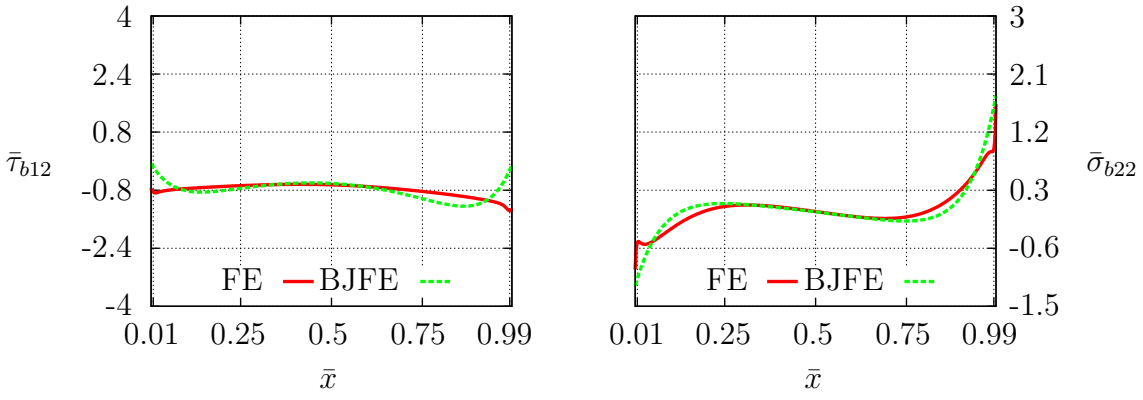

(c) $\bar{\tau}_{b12}$ due to $\bar{\phi}_P$ (d) $\bar{\sigma}_{b22}$ due to $\bar{\phi}_P$

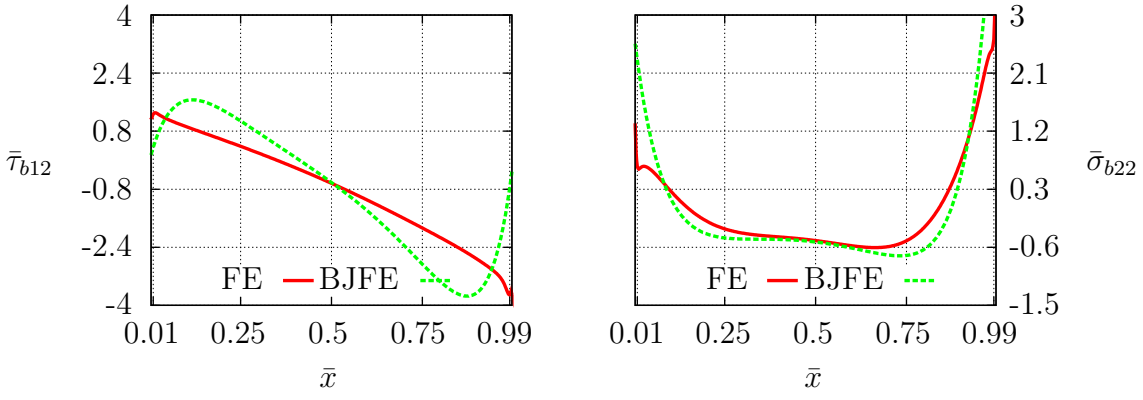

(e) $\bar{\tau}_{b12}$ due to $\bar{\phi}_P+\bar{\phi}_{\Delta T}$ (f) $\bar{\sigma}_{b22}$ due to $\bar{\phi}_P+\bar{\phi}_{\Delta T}$

Figure 3.7 Continuum and BJFE models of AL-TI joint with 0.2 mm adhesive

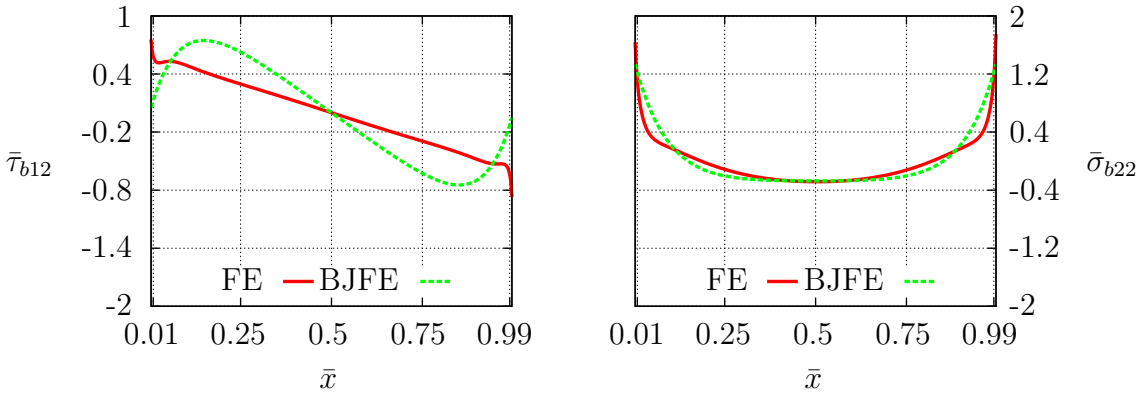

(a) $\bar{\tau}_{b12}$ due to $\bar{\phi}_{\Delta T}$

(b) $\bar{\sigma}_{b22}$ due to $\bar{\phi}_{\Delta T}$

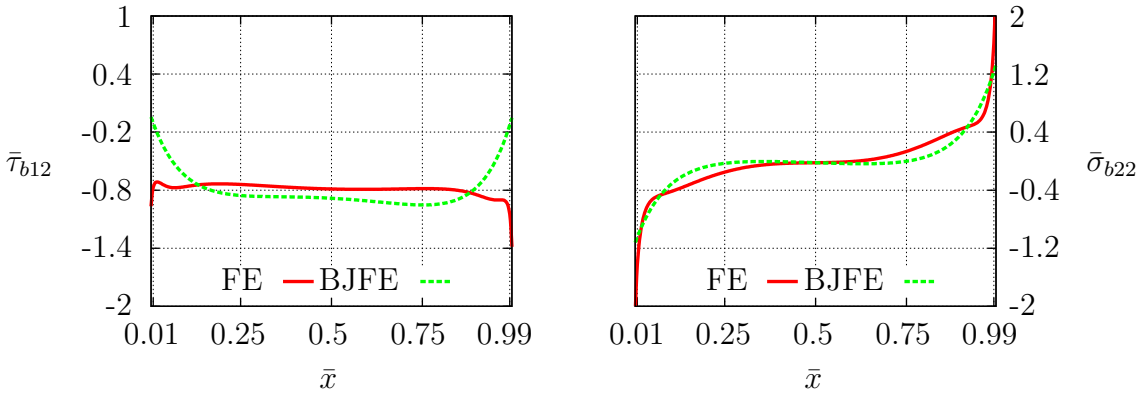

(c) $\bar{\tau}_{b12}$ due to $\bar{\phi}_{P}$

(d) $\bar{\sigma}_{b22}$ due to $\bar{\phi}_{P}$

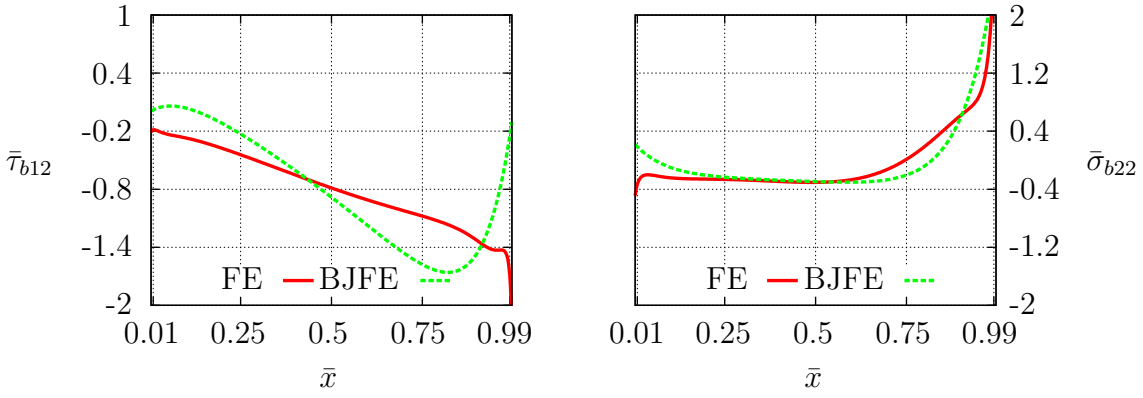

(e) $\bar{\tau}_{b12}$ due to $\bar{\phi}_{P}$+$\bar{\phi}_{\Delta T}$

(f) $\bar{\sigma}_{b22}$ due to $\bar{\phi}_{P}$+$\bar{\phi}_{\Delta T}$

Figure 3.8 Continuum and BJFE models of AL-TI joint with 1.0 mm adhesive

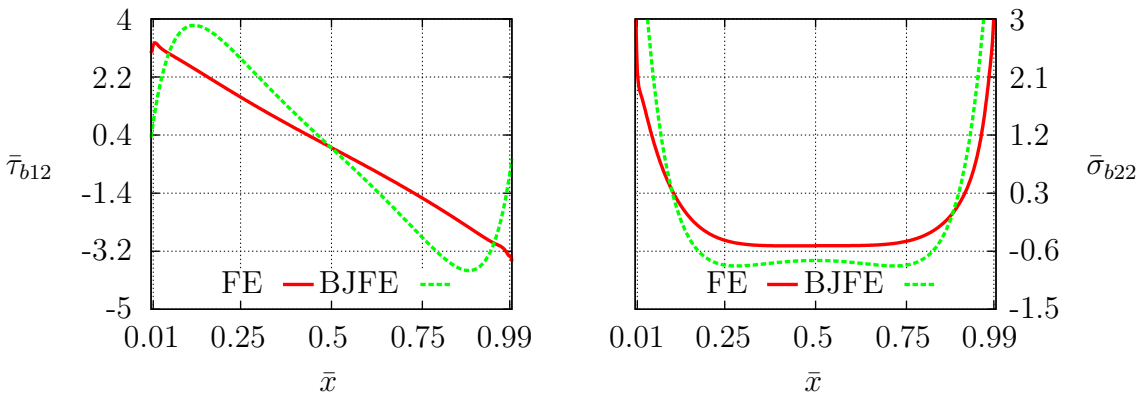

(a) $\bar{\tau}_{b12}$ due to $\bar{\phi}_{\Delta T}$ (b) $\bar{\sigma}_{b22}$ due to $\bar{\phi}_{\Delta T}$

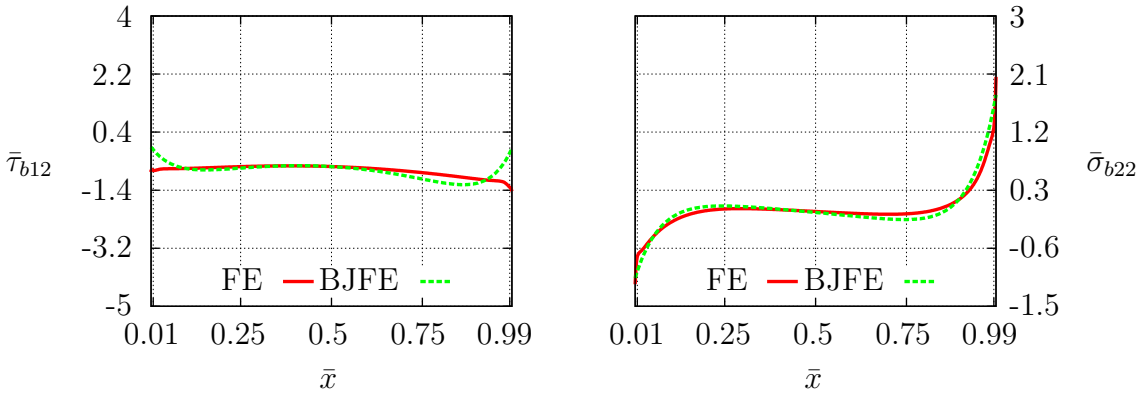

(c) $\bar{\tau}_{b12}$ due to $\bar{\phi}_P$ (d) $\bar{\sigma}_{b22}$ due to $\bar{\phi}_P$

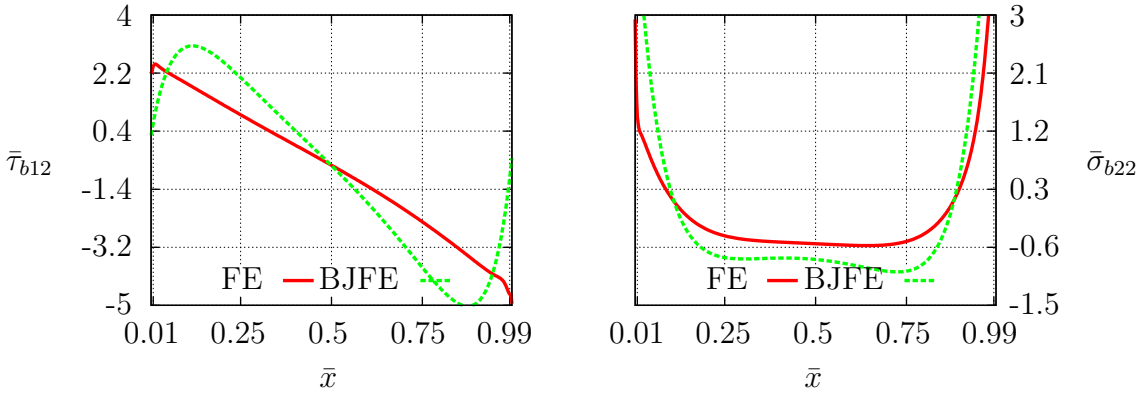

(e) $\bar{\tau}_{b12}$ due to $\bar{\phi}_P+\bar{\phi}_{\Delta T}$ (f) $\bar{\sigma}_{b22}$ due to $\bar{\phi}_P+\bar{\phi}_{\Delta T}$

Figure 3.9 Continuum and BJFE models of AL-AS4 (0^o) joint with 0.2 mm adhesive

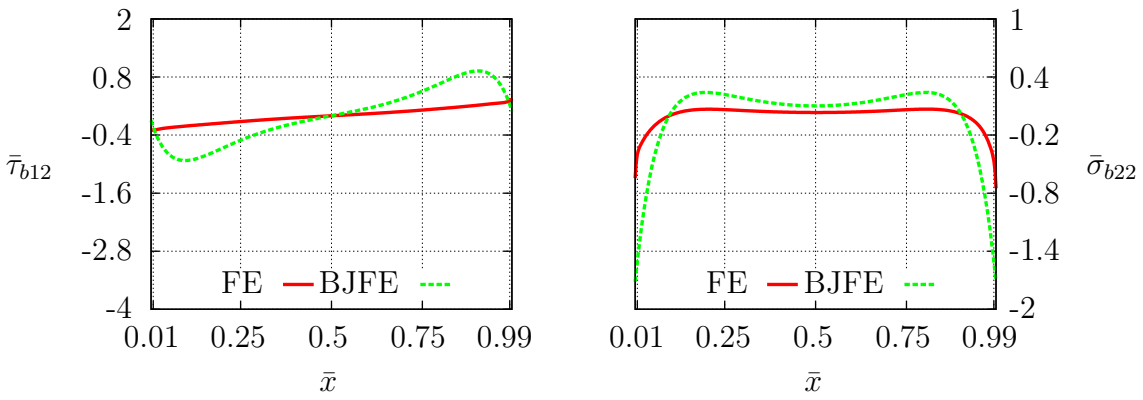

(a) $\bar{\tau}_{b12}$ due to $\bar{\phi}_{\Delta T}$ (b) $\bar{\sigma}_{b22}$ due to $\bar{\phi}_{\Delta T}$

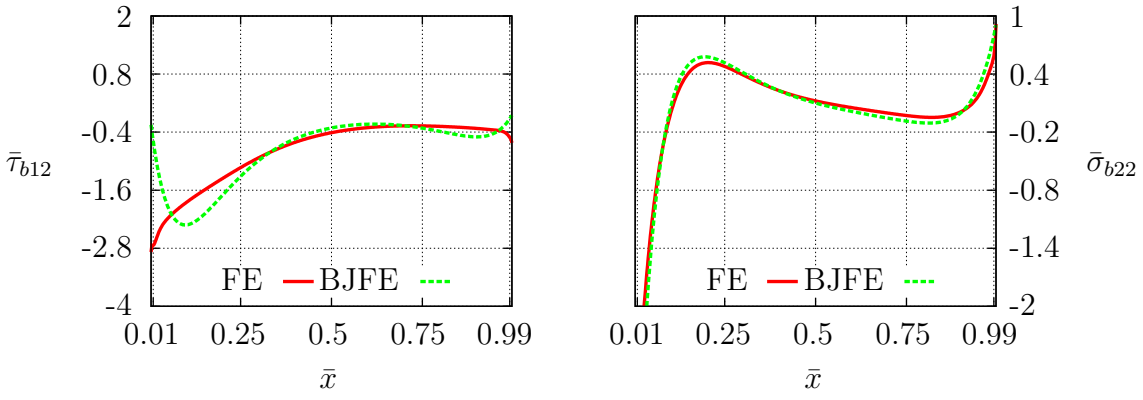

(c) $\bar{\tau}_{b12}$ due to $\bar{\phi}_{P}$ (d) $\bar{\sigma}_{b22}$ due to $\bar{\phi}_{P}$

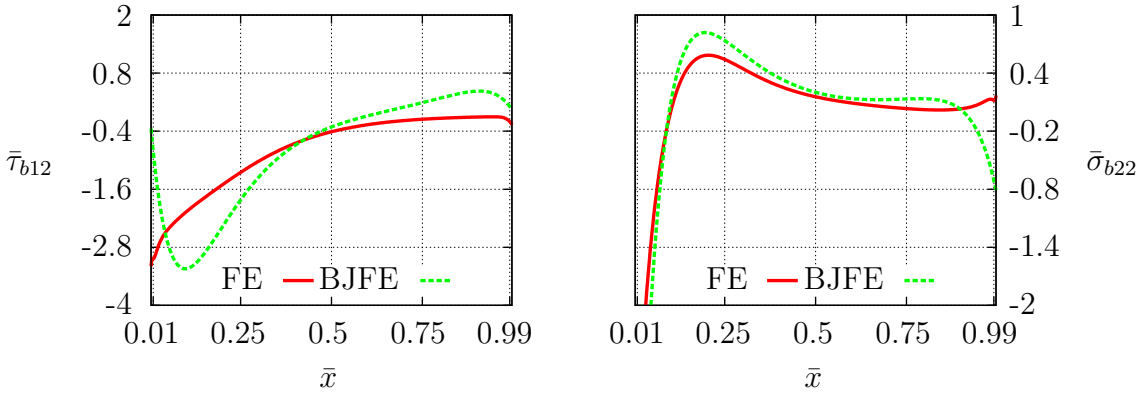

(e) $\bar{\tau}_{b12}$ due to $\bar{\phi}_{P}+\bar{\phi}_{\Delta T}$ (f) $\bar{\sigma}_{b22}$ due to $\bar{\phi}_{P}+\bar{\phi}_{\Delta T}$

Figure 3.10 Continuum and BJFE models of AL-AS4 (90^o) joint with 0.2 mm adhesive

loading; good agreement is exhibited in both figures. The peak shear stress predicted by the BJFE is similar to that predicted by the continuum model, though there is a difference in predicted peak location. The peel stress predicted by the BJFE is in adequate agreement with the continuum model and its value does not suffer from any mesh dependency. Figures 3.6(e) and 3.6(f) show mixed loading for the AL-AL joint which are almost identical to the mechanical load predictions for this joint.

Figure 3.7 shows the stresses predicted by the continuum and BJFE models for an AL-TI joint. Thermal loading is non-trivial and the stress predictions resulting from it are shown in figures 3.7(a) and 3.7(b) for shear and peel. In this joint type, the predicted shear stress is in good agreement for thermal, mechanical, and mixed loading, as is shown in figures 3.7(a), 3.7(c), and 3.7(e). In all cases, the peak shear stress predicted by the BJFE adequately matches the continuum model. The peak location is consistently found to be further from the edge in the BJFE than in the continuum model. Looking at the peel stress predictions shown in figures 3.7(b), 3.7(d), and 3.7(f), good agreement is found again. The stress predicted by the BJFE is similar to the continuum model and is representative of the (unconverged) singular peel stress result.

The BJFE solution is orthotropic; an example of a composite application is shown in figures 3.9 and 3.10. The figures show two AL-AS4 joints subjected to thermal, mechanical, and mixed loading. The laminate shown in figure 3.9 has fibers oriented longitudinally (0^o) and the laminate shown in figure 3.10 has fibers oriented transversely (90^o). Despite the unlikelihood of the 90^o fiber orientation (relative to the joint loading axis) in practical applications, the two figures shows that the BJFE solution is in adequate agreement with the continuum solution in both cases and for all three load types.

In comparing figures 3.6-3.10 to the corresponding plots in chapter 2, it is apparent that the virtual work solution used in the BJFE is more accurate than are the simpler solutions. This is a direct result of the inclusion of additional stress terms in the virtual work solution. Based on the cumulative agreement shown in figures 3.6-3.10, it can be concluded that the BJFE element adequately predicts the shear stress in a double lap joint. The peel stress predicted by the BJFE model is found to be consistently in agreement with the value of the (unconverged) singular stress field in all figures. Therefore, it can be used as a mesh independent indicator of peel stress, useful for joint-to-joint comparison.

Model	Nodes	Elements	DOF
CPE4I	22100	21600	44300
BJFE	4	1	4

Table 3.1 Approximate size of the double lap joint FE models

3.6 Conclusion

In this chapter, a bonded joint finite element has been developed. It is capable of predicting the lap joint field quantities in the lap zone using four degrees of freedom. It does so without burdening the user with mesh dependency or significant meshing overhead. The BJFE is formulated by embedding an analytical solution directly within the element. Its stiffness and load response are based on adaptive non-linear shape functions that are dependent on the load character. All critical terms are formulated as functions of the dimensionless mechanical load fraction ($\bar{\bar{\phi}}_P$) allowing for solution via an iterative, non-linear FE solver. To demonstrate its capability, the element has been implemented as a user element subroutine in the commercial finite element package Abaqus®.

Based on comparison with continuum FE solutions, the four node BJFE is capable of adequately predicting stress and strain in a joint due to thermal and mechanical loads. With this element, initial sizing and trade studies can be accomplished with a significantly reduced meshing investment and a reduction in computation time (compared with the continuum finite element method). The element lays a foundation for advancements in bonded joint elements. Using the techniques demonstrated in this chapter, it is anticipated that available analytical solutions can be reformulated as application specific bonded joint elements.

Chapter 4

A discrete cohesive zone element formulation for efficient and robust computation

In this chapter, a discrete cohesive zone method element is developed for predicting decohesion in a finite element model. Finite elements provide flexibility that is not present in closed-form analytical methods (chapter 2) and hybrid methods (chapter 3). The discrete cohesive zone method element is formulated as a combination of non-linear springs and dashpots. The springs enforce a modular traction law allowing a user specified form of the law to be applied. The dashpots allow for viscous regularization in the event of unstable crack propagation. Three traction laws are described and are compared in their computational efficiency and robustness. The smooth traction laws (based on the beta distribution and sine functions) are found to have greater computational efficiency than the trapezoidal traction law. Efficiency gains are due to the elimination of the stiffness discontinuities associated with the trapezoidal traction law. The sinusoidal traction law is found to be more robust and efficient than the other traction laws.

4.1 Introduction

Finite element modeling and other forms of computational analysis have become indispensable tools in system design and mission preparation. An active area of research is the application of these methods to the field of adhesive systems, bonded joints, and delamination. Though finite element (FE) modeling of adhesively bonded

joints began as early as 1971 [3, 109], it remains an active area of research.[1]

The continuous cohesive zone method (CCZM) models are particularly well suited to composite materials where the length scale of the process zone is larger than any characteristic length of the material [21, 35, 81, 88, 100, 101, 116]. Cohesive zone models have begun to be incorporated into commercial software including Abaqus® [1, 23] and Genoa® [29] as well as freely available research codes like Tahoe® [87]. Though they are an important advancement, these "production level" continuum cohesive elements have not been widely adopted. A primary obstacle to their widespread use is the local and highly non-linear constitutive response of the adhesive materials and their adherends. In addition, bonded joints can be subject to catastrophic failure modes that are accompanied by large and sudden changes in load and structural stiffness. When combined, these two analytical obstacles cause difficulty in obtaining a converged solution and have prevented widespread deployment of the available analysis techniques. Research is underway to develop improvements to the available methods [75, 76, 94].

Using simple arguments, Hillerborg et al. [58] provided the essential components of a spring-based traction law element capable of analyzing crack formation and propagation. The "fictitious crack" element featured the ability to predict new cracks based on a stress criterion (σ_c) while also predicting crack growth based on an energy criterion (G_c). The concept has experienced a (independently conceived) revival and found application to laminated composite materials [96, 97], geometrically non-linear behavior [111], and Mode II fracture [113]. The method has recently been referred to as the discrete cohesive zone method (DCZM). Similar elements were presented by Cui and Wisnom [33] and Shahwan and Waas [92].

The DCZM technique is a promising alternative to the CCZM. Continuous cohesive zone elements have been found to be mesh sensitive (in some circumstances), to suffer from convergence difficulty during the softening portion of the cohesive law, and to have sensitivity to aspect ratio, [6, 42, 43, 123]. A comprehensive description of the strengths and weaknesses of the cohesive zone methodologies is provided by Xie and Waas [113]. In contrast to CCZM, the DCZM methodology treats the process zone as a point-wise spring foundation that is discretized to node pairs of adjoining surfaces. The method is scalable to the node spacing and is claimed to be free of mesh dependency, [58, 113]. The stiffness matrix is sparse and is therefore computationally efficient. Though it does not avoid instability due to strain softening, careful application of damping stabilization can improve convergence.

[1] See chapter 3 for a list of recent references.

Reliable and efficient convergence remains the largest computational hurdle in deployment of robust cohesive models. The propagation of a softening law through a structure is computationally challenging, [38]. Attempts to address this difficulty have had mixed success. Arc length methods have been reported by several authors [7, 70, 102], however, they tend to suffer from large spurious oscillations. It was claimed that a lack of mesh refinement caused the oscillation, though it is unclear what role the strain softening traction law may have played. Line search algorithms are often considered a remedy for lack of convergence, however, complications arise for non-conservative problems, [8]. When used in conjunction with the primary methods of this work, neither of these methods were found to have significant additional benefits.

In this chapter, the approach to obtain robust convergence is to apply a traction law with "smooth" stiffness gradients.[2] Smooth laws have been used, though it does not appear that they were designed with improved convergence as their primary goal. For example, Goyal et al. [53] used a law based on the exponential function with no stiffness discontinuities. A line search algorithm was employed and the stiffness was set to zero when the law was undergoing strain softening. It was claimed that convergence difficulties were eliminated, though independent verification is still pending. Alfano and Crisfield [7] claim that the use of the tangent modulus should give better convergence of the residual norms; therefore, a tangent stiffness was used for the current work. Corigliano et al. [28] also used an exponential traction law; however, no claim was made about convergence.

The DCZM element is developed for use in modeling decohesion in structures. The element features a computationally efficient traction separation formulation, optional viscous damping for stabilization, standard 2D and 3D interfaces, and a modular interface for specifying a traction law. Three traction laws are implemented, one which is in common use and the others which are designed specifically for convergence efficiency. A comparison of the convergence efficiency and robustness of the three laws is provided based on models of two coupon-level tests.

4.2 The discrete cohesive zone method

The element in this work (hereafter referred to as "the current element") evolved from the formulation of Xie and Waas [113] (hereafter referred to as "the Xie element"). The formulation has been modified to provide a (perceived) improvement in user

[2] An option for viscous damping is included in the formulation.

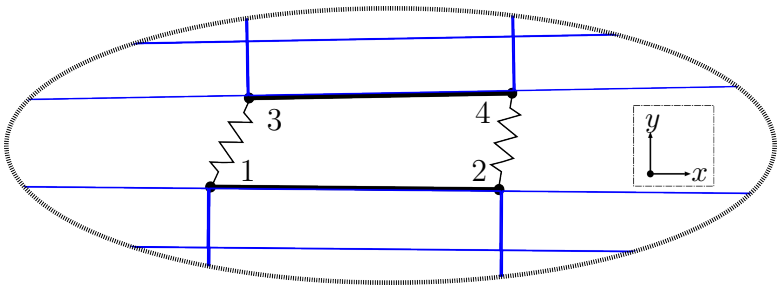

Figure 4.1 Four-node 2D DCZM element with surrounding elements. Adhesion is enforced with non-linear springs between node pairs.

interface, the addition of user controlled damping, and a modularity in traction law. For ease of explanation and comparison, the derivation of the current element details a 2D implementation. Since 3D problems are of critical importance, the code for the element has been written as a 3D element. Any descriptive language or calculation in the derivation can immediately be extended to three dimensions.

The DCZM element is illustrated (in 2D form) in figure 4.1 and conforms to the layout for a 2D four-node element in Abaqus®. A similar conforming layout is also provided for the 3D version of element. Recall that the current element evolved from the Xie element. Compared to that element, the first modification is to the node layout. The node numbering and connectivity in the Xie element does not follow common convention. It is a four-node element with two "dummy" nodes, meaning the element transmits forces only at two nodes. The dummy nodes serve to measure the cohesive area that the element represents. Although the nodal layout of the Xie element is capable of providing the intended function of the element, it is recognized that a standard node layout is usually desired. As a result, there are no dummy nodes in the current element and the contact area is measured from nodes that are active. All nodes in the current element transfer adhesive forces.

4.2.1 The key element matrices

Although the current node arrangement has the advantage of providing a conventional node layout, it requires a slight increase in *per contact node* computational cost over that of the Xie node arrangement. Most active nodes are active in two elements. Evaluation of stiffness and force is required at each active node in each element. Unlike the Xie element, however, the current element is formulated so that an arbitrary number of integration points can be used. As a result, the current element has the potential to be a "softer" element, smoothing transitions in non-linear traction laws.

Additional integration points offer the possibility of improved convergence [40] in marginally stable analysis (at a given mesh density) or the use of lower mesh densities.[3] As a second option for improved convergence over the Xie element, the current element offers modularity for the form of the traction law. Three forms are presented and compared in section 4.4. The traction law is written generically as $\sigma_i(\delta_i^{\mathrm{IP}}(j))$ in the element derivation.

Although the current element (in 2D form) is a four-node element, in practice it is an element consisting of four two-node non-linear spring elements and four two-node linear dashpot elements. These sub-elements transmit spring forces in the x (shear) and y (peel) directions for each of two node pairs. Therefore, the element force vector and stiffness matrix shown in equation 4.1 appear as they would appear if four spring elements were assembled.

$$K_{\mathrm{el}} = \begin{bmatrix} K_{14x} & 0 & 0 & 0 & 0 & 0 & -K_{14x} & 0 \\ 0 & K_{14y} & 0 & 0 & 0 & 0 & 0 & -K_{14y} \\ 0 & 0 & K_{23x} & 0 & -K_{23x} & 0 & 0 & 0 \\ 0 & 0 & 0 & K_{23y} & 0 & -K_{23y} & 0 & 0 \\ 0 & 0 & -K_{23x} & 0 & K_{23x} & 0 & 0 & 0 \\ 0 & 0 & 0 & -K_{23y} & 0 & K_{23y} & 0 & 0 \\ -K_{14x} & 0 & 0 & 0 & 0 & 0 & K_{14x} & 0 \\ 0 & -K_{14y} & 0 & 0 & 0 & 0 & 0 & K_{14y} \end{bmatrix}, \quad (4.1)$$

$$F_{\mathrm{el}} = \begin{bmatrix} -F_{14x} & -F_{14y} & -F_{23x} & -F_{23y} & F_{23x} & F_{23y} & F_{14x} & F_{14y} \end{bmatrix}^T$$

A detailed derivation of the components of equation 4.1 is deferred to section 4.2.3.

4.2.2 Justification for use of internal damping

The second major modification to the Xie element is the addition of internal damping. In Xie and Waas [113] it was reported that the Xie element had no convergence difficulties associated with a triangular traction law. In this work, it was observed that the local stability and convergence of a model may depend on the traction separation

[3] The author has experienced circumstances where an increase in the number of integration points in the DCZM elements has allowed a DCB model to obtain a converged solution that would otherwise fail to converge (with a fixed mesh density and a set of adhesive parameters). This aspect of the element formulation is not thoroughly explored in this work. Instead, the smooth traction laws (presented in sections 4.4.2-4.4.3) are formulated to improve convergence. No claim is made regarding the robustness of the integration point strategy as a method to improve convergence or reduce CPU cost in a DCB or other analysis, only that the potential exists to do so.

behavior of the constituents and the strain energy of the specimen. For example, the crack advance of the double cantilever beam (DCB) experiment was observed to be discontinuous on occasion, advancing in small increments. Though the DCB exhibited a globally stability, the local instabilities in the experiment require additional investigation. The stability traits are mirrored in the FE model based on the DCZM element. In addition, the ability of the solver to obtain a *converged solution* may also depend on the mesh density (since the model's increments of deformation and crack advance are intimately tied to this density).

In physical tests, it is common for this stepwise (stick-slip) dynamic crack propagation to occur. Further, it is difficult to construct a cohesive element that is unconditionally convergent for an implicit static solver, since crack propagation stability is dependent on the energetics of the system. Ideally, all forms of dynamic crack advance (including stepwise dynamic) would be addressed with a dynamic element formulation and a dynamic FE solver (implicit or explicit). There are many circumstances, however, where an implicit static solver is preferred and appropriate. It is common to add dissipative mechanisms to the static formulation, [24, 102]. The addition can stabilize the solution and facilitate convergence.

Damping capability is built into many solvers. In Abaqus®, for example, a cohesive analysis could include dissipation at every degree of freedom[4] or locally at the cohesive section[5]. If dynamic cracking occurs in small stepwise increments and a dynamic analysis is not desired, it is justifiable to add small amounts of dissipation to the implicit static solution. The global solution variables (stiffness, load) require small changes. Dissipation could be considered to represent the energy that goes into sound, heat, or other viscous damping effects. If dynamic cracking occurs in large increments, dissipation may be the only available method for achieving a converged solution with a static solver. In either case, comparison between the FE model and the experimental data may determine if this modeling technique is justified. Caution must be used, however, since different geometries will exhibit different stability boundaries. The energy lost to viscous dissipation can have comparable magnitude to the energy associated with crack formation.

To facilitate convergence, a user controlled option of viscous dissipation was formulated into the current DCZM element. Dissipation is added via linear dashpots on each node pair in each direction.

[4]Via the (**STATIC, STABILIZE*) keyword
[5]Via the (**SECTION CONTROLS, VISCOSITY=*μ) keyword

4.2.3 Components of the DCZM force vector and stiffness matrix

The element load vector and stiffness matrix components presented in equation 4.1 are derived here in this section. The displacement vector (in the element local orientation) is given by:

$$u_{\text{el}} = \begin{bmatrix} u_{1x} & u_{1y} & u_{2x} & u_{2y} & u_{3x} & u_{3y} & u_{4x} & u_{4y} \end{bmatrix}^T. \tag{4.2}$$

Each component of the reaction force $F_{nm\,i}$ (acting between nodes n and m, direction i) and stiffness matrix $K_{nm\,i}$ is composed of the combination of traction law (superscript k) and viscous (superscript μ) components:

$$\begin{aligned} F_{14i} =& F^k_{14i} + F^\mu_{14i}, \\ F_{23i} =& F^k_{23i} + F^\mu_{23i}, \\ K_{14i} =& K^k_{14i} + K^\mu_{14i}, \\ K_{23i} =& K^k_{23i} + K^\mu_{23i}. \end{aligned} \tag{4.3}$$

Traction law contributions to the element matrices

The traction law component of the force vector is a moment balanced sum of integration point forces over an arbitrary number of equally spaced integration points (n_{IP}):

$$\begin{aligned} F^k_{14i} =& \sum_{j=1}^{n_{\text{IP}}} N_1(j) \cdot F_i^{k\,\text{IP}}(j), \\ F^k_{23i} =& \sum_{j=1}^{n_{\text{IP}}} N_2(j) \cdot F_i^{k\,\text{IP}}(j). \end{aligned} \tag{4.4}$$

In equation 4.4, the integration point forces $F_i^{k\,\text{IP}}(j)$ are weighted by shape functions in order to translate the forces and moments into nodal forces:

$$\begin{aligned} N_1(j) &= \left(\frac{1 - \zeta(j)}{2} \right), \\ N_2(j) &= \left(\frac{1 + \zeta(j)}{2} \right). \end{aligned} \tag{4.5}$$

The local coordinate $\zeta(j)$ for integration point number ($j = [1\,,\,...\,,\,n_{\mathrm{IP}}]$) varies linearly from -1 to 1 at the left and right edges of the element:

$$\zeta(j) = \left(\frac{2}{n_{\mathrm{IP}} - 1}\right) \cdot (j - 1) - 1. \tag{4.6}$$

The integration point forces are:

$$F_i^{k\,\mathrm{IP}}(j) = \sigma_i(\delta_i^{\mathrm{IP}}(j)) \cdot A^{\mathrm{IP}}(j), \tag{4.7}$$

where the traction law is given by $\sigma_i(\delta_i^{\mathrm{IP}}(j))$ and $A^{\mathrm{IP}}(j)$ is the integration point area. The form of the law is arbitrary and the DCZM element is modular to accept any form provided by the user. Three forms have been evaluated and are reported in section 4.4.

The integration point relative displacements are determined by a linear interpolation of the relative displacement of the nodal degrees of freedom (DOF):

$$\delta_i^{\mathrm{IP}}(j) = N_1(j) \cdot \Delta u_{14i} + N_2(j) \cdot \Delta u_{23i}. \tag{4.8}$$

The node pair relative displacements are:

$$\begin{aligned} \Delta u_{14i} =& u_{4i} - u_{1i}, \\ \Delta u_{23i} =& u_{3i} - u_{2i}, \end{aligned} \tag{4.9}$$

and the integration points areas are:

$$A^{\mathrm{IP}}(j) = \frac{b \cdot (x_2 - x_1)}{\varphi\,(n_{\mathrm{IP}} - 1)}. \tag{4.10}$$

In equation 4.10, the elemental contact area $(b \cdot (x_2 - x_1))$[6] is distributed to the integration points as $n_{\mathrm{IP}} - 1$ parcels. All integration points have the same area (one parcel) except for the nodal integration points which divide the final parcel into two parts. This parcelling is accomplished by the term (φ) in the denominator of equation 4.10:

$$\varphi = \begin{cases} 2 & \text{if} \quad j = \{1, n_{\mathrm{IP}}\}, \\ 1 & \text{if} \quad j \neq \{1, n_{\mathrm{IP}}\}. \end{cases} \tag{4.11}$$

The integration point positions include the node positions, therefore, a minimum of two integration points are required. Figure 4.2 provides an example of the integration point layout and area weighting for $n_{\mathrm{IP}} = 5$.

[6] b is the depth of the element in the third dimension and is assumed to be one in the 2D element.

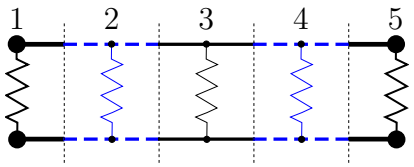

Figure 4.2 Example of DCZM element with 5-point integration. The spacing is uniform and the contact area is uniformly distributed with the exception of the nodal integration points. The nodal integration points are allotted 1/2 the contact area associated with the internal integration points.

With the force vector derivation complete, the traction law stiffness components are derived in a similar way. The integration point stiffness is:

$$K_i^{k\,\mathrm{IP}}(j) = \frac{d}{d\,\delta_i^{\mathrm{IP}}(j)}\,\sigma_i(\delta_i^{\mathrm{IP}}(j)) \cdot A^{\mathrm{IP}}(j), \tag{4.12}$$

and the element stiffness matrix components are:

$$\begin{aligned} K_{14i}^k &= \sum_{j=1}^{n_{\mathrm{IP}}} N_1(j) \cdot K_i^{k\,\mathrm{IP}}(j), \\ K_{23i}^k &= \sum_{j=1}^{n_{\mathrm{IP}}} N_2(j) \cdot K_i^{k\,\mathrm{IP}}(j). \end{aligned} \tag{4.13}$$

The derivative in equation 4.12 is discontinuous at the critical displacements for the trapezoidal traction law (TTL), therefore, it is applied in a discrete ($\Delta u \leq \Delta u_c$) sense.

Dissipative contributions to the element matrices

Having completed the derivation for the traction law contributions to the elemental matrices, it was reported in section 4.2 that a method of energy dissipation is required (for some geometries and traction laws) to facilitate a converged solution. In the current element, dissipation is implemented as an internal dashpot on each relative degree of freedom. The dashpot components of the force are given by:

$$\begin{aligned} F_{14i}^{\mu} &= \mu_{14i} \cdot \Delta\dot{u}_{14i}, \\ F_{23i}^{\mu} &= \mu_{23i} \cdot \Delta\dot{u}_{23i}, \end{aligned} \tag{4.14}$$

where the viscosities (μ_{14i}, μ_{23i}) are non-zero only in a viscous zone defined by a user specified multiplier ($C_\mu > 1$) of the critical relative displacement δ_c:

$$\mu_{nm\,i} = \begin{cases} \mu_i & \text{if} \quad \delta_i \leq C_\mu\,\delta_c, \\ 0 & \text{if} \quad \delta_i > C_\mu\,\delta_c. \end{cases} \tag{4.15}$$

In the author's experience, the effective C_μ value depends on the traction law. Values between 3 and 5 have been effective for the TTL (described in section 4.4.1) and 2 has been effective for the beta distribution traction law (BDTL) and sinusoidal traction law (STL) (described in sections 4.4.2-4.4.3). The relative velocities of the nodes are the time derivative of the relative displacements in equation 4.9.

In practice, the dashpot forces given in equation 4.14 only need be applied during unstable time increments of a solution. The time incrementation scheme drives the increment to a small value if a converged solution is not readily found. Therefore, the DCZM implementation sets the viscosities (μ_{14i}, μ_{23i} in equation 4.14) to zero unless the time increment is small ($\Delta t < 10^{-4}$). Localized dissipation is active during (potentially unstable or non-convergent) increments of initial separation and subsequent softening. Dissipation is removed once adhesive failure has been established.[7]

For an iterative static solver with time based incrementation (such as the Newton method solver in Abaqus® [1]), it is beneficial for convergence to account for the viscous dissipation in the stiffness matrix. The "viscous stiffness" contribution for a given increment of time (Δt) is given by:

$$\begin{aligned} K^{\mu}_{14i} &= \frac{\mu_{14i}}{\Delta t}, \\ K^{\mu}_{23i} &= \frac{\mu_{23i}}{\Delta t}. \end{aligned} \tag{4.16}$$

The derivations in this section were presented in the local coordinate frame of the element, however, the element formulation is general. All forces and stiffnesses are rotated into the global coordinate system by the user element subroutine (UEL).

4.2.4 The FE implementation

With equation 4.16, all components of the element stiffness matrix and load vector are complete. The DCZM element has been implemented as a UEL in the general purpose

[7] The use of damping for stabilization is case dependent, therefore, no universal recommendation can be made for the parameters $\mu_{nm\,i}$ and C_μ.

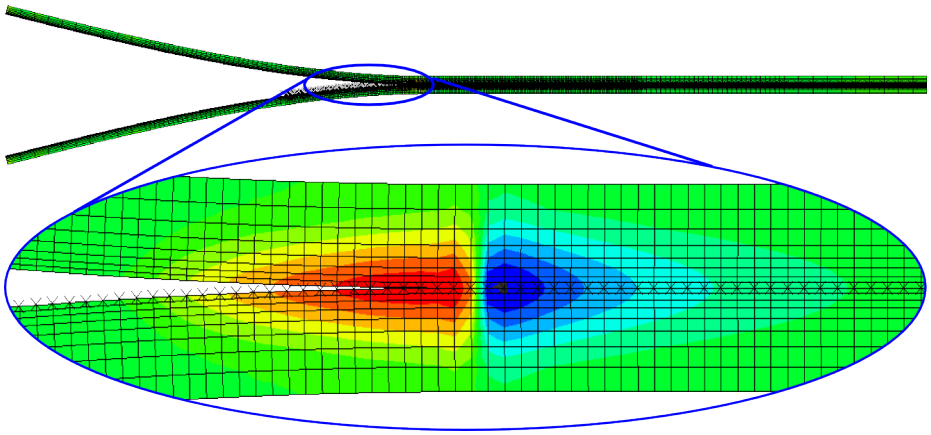

Figure 4.3 Typical process zone using the DCZM element

non-linear solver Abaqus® Standard. A typical peeling process zone associated with crack propagation is shown in figure 4.3.

4.3 Solution efficiency

In section 4.2, it was reported that crack stability depends on the specimen loading and the traction law. A detailed description of this dependency is reported in this section. Two topics must be considered when addressing solution efficiency for the computation of cohesive problems: structural instability and numerical convergence.

4.3.1 The critical crack separation

In structures with adhesive bonds, structural instability can occur due to sudden failure of the bonded interface. In static FE analysis of adhesive failure, the absence of inertial accounting can cause an imbalance between the strain energy release rate and the energy dissipation due to permanent deformation. This imbalance can cause a significant change in the stiffness and load of the system. As a result, an incremental FE solver may fail to converge to an equilibrium solution.

At a fixed level of strain energy release rate near the critical value, the stability margin is dependent on the critical crack separation (δ_c) in figures 4.4, 4.5, and 4.10. In relative terms, if the value of δ_c is large, the system is soft. For a fixed displacement in this state, load transfer occurs over a large material volume and the strain energy is small for the global displacement. As the global displacement increases, the load paths smoothly transition to neighboring elements via a gradual and dispersed stiffness

change. The solver finds the equilibrium path with relative ease. Conversely, if δ_c is small, the load transfer is concentrated into a small material volume with a large strain energy. An increase in global displacement causes a localized change in stiffness and displacement field. Therefore, it is more difficult for the solver to find the equilibrium path.

Based on these arguments, larger values of δ_c result in more efficient solutions due to ease of convergence.

4.3.2 The stiffness gradient

A second consideration in solution efficiency is the continuity of the traction law. Consider the Newton solver as described by Simulia [93]. Linearization of the virtual work equations yields:

$$F^N(u_i^M + c_{i+1}^M) = 0. \tag{4.17}$$

F^N is the force component conjugate to the Nth variable in the problem. u_i^M and c_{i+1}^M are the values of the Mth variable in iteration i and the absolute error (i.e. the correction vector) of the Mth variable in iteration $i+1$. A Taylor expansion of equation 4.17 yields:

$$F^N(u_i^M) + \frac{\partial F^N(u_i^M)}{\partial u_i^P}\, c_{i+1}^P + \frac{\partial^2 F^N(u_i^M)}{\partial u_i^P\, \partial u_i^Q}\, c_{i+1}^P\, c_{i+1}^Q + ... = 0. \tag{4.18}$$

If the force functions are sufficiently smooth and u_i^M is a close approximation of the true solution, the higher order terms in equation 4.18 are negligible. The correction can be iteratively computed via:

$$K_i^{NP}\, c_{i+1}^P = -F_i^N, \tag{4.19}$$

where K_i^{NP} is the tangent stiffness matrix defined by:

$$K_i^{NP} = \frac{\partial F^N(u_i^M)}{\partial u^P}, \tag{4.20}$$

and the residual force vector is:

$$F_i^N = F^N(u_i^M). \tag{4.21}$$

Subsequent iterations are computed as:

$$u_{i+1}^{M} = u_{i}^{M} + c_{i+1}^{M}, \tag{4.22}$$

until a converged solution is obtained.

In this scheme, the value of the correction is linearly computed from the current residual vector and the current tangent stiffness matrix. Convergence is accepted when the values of F_i^N and c_{i+1}^M are sufficiently small. If the higher order derivatives (the stiffness gradient) in equation 4.18 are large, however, then the higher order terms can be significant. This causes equation 4.20 to compute a poor approximation for the correction vector, leading to convergence difficulties. When this occurs, it is necessary to reduce the solver increment size. The reduction results in higher computational cost. In this way, the smoothness of the traction law is a critical component of the solution efficiency and robustness.

4.4 The traction laws

The DCZM element described in section 4.2 is modular in the application of traction laws. It has been shown that the form of the traction law is not critical in the global load displacement response, [47, 66, 78, 84, 102, 113, 119]. Therefore, the modularity of the DCZM element offers some flexibility in controlling the cohesive model. More specifically, the form of the traction law can be specified to suit one of several purposes. For example, the law applied in the FE model can be the "most accurate" representation of the actual traction separation response. Alternatively, the law can also be formulated for the simplicity of implementation [8] or for the purposes of numerical efficiency and robustness. In this section, these last two objectives are adopted and three traction laws are evaluated.

A feature of each implementation is that the element will unload along a line from the origin to the force associated with the extreme separation. Reload follows the same path as the prior unloading path, preserving any material degradation.

4.4.1 The trapezoidal traction law

The trapezoidal traction law (schematically shown in figure 4.4) is a widely used traction law. It is a generalization of the triangular law used in the Xie element [113] and elsewhere. Implementation is convenient due to the simplicity of formulating the

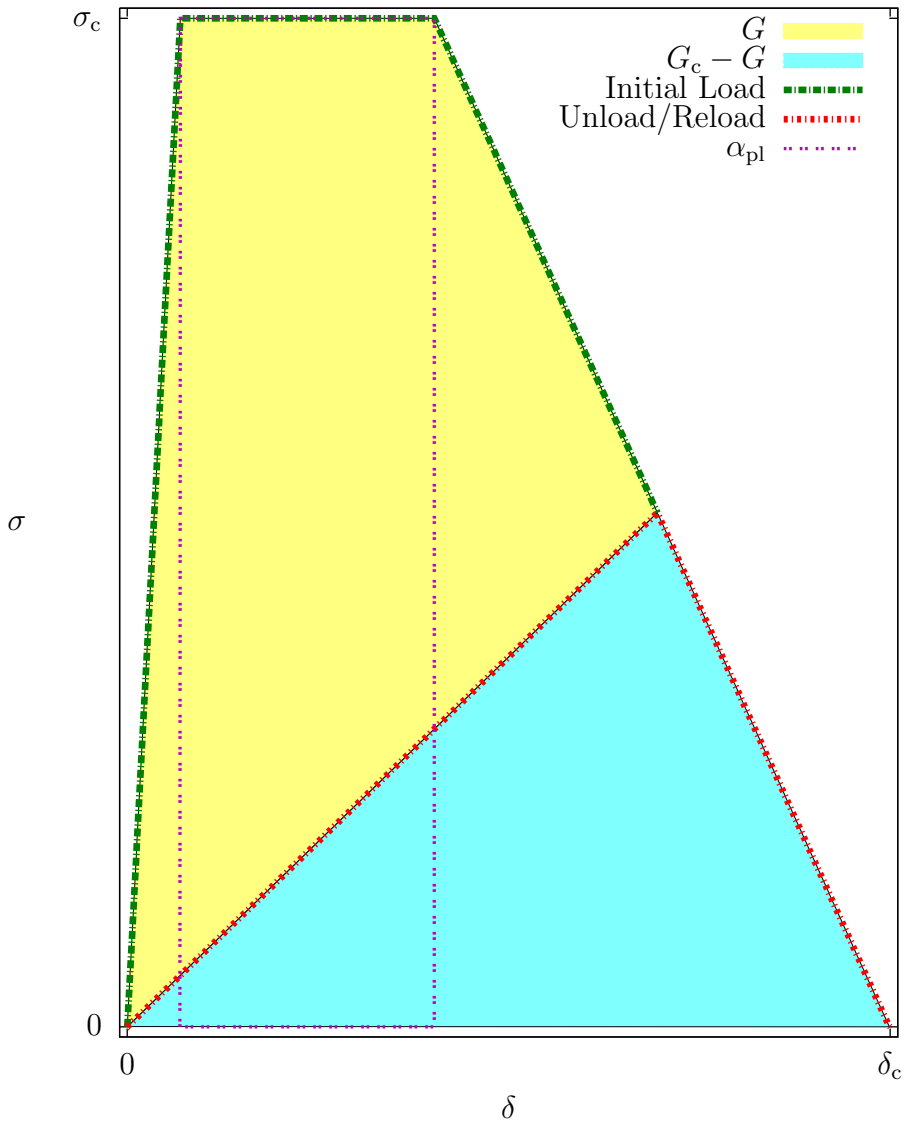

Figure 4.4 The trapezoidal traction law

three linear regions of the law. The three regions are referred to as the initial linear response region, the optional "plastic" region, and the strain softening region.

Each fracture mode (I, II, III) requires three parameters to implement the TTL. In two dimensional problems, the required parameters are the critical energy release rates (G_{Ic}, G_{IIc}), the critical stresses (σ_{Ic}, τ_{IIc}), and the shape factors (α^I_{pl}, $\alpha^{II}_{\mathrm{pl}}$) that define the "plasticity". In the TTL, the shape factor is the ratio of the rectangular area in the flat section of the traction law to the total area enclosed by the traction law (G_c). Shown in figure 4.4, α_{pl} is bound by zero (restoring a triangular law) and one.

Efficiency considerations related to the TTL

Despite being simple in implementation, the TTL is a law that can suffer from severe convergence difficulties. For example, as the peak stress is crossed in the triangular law ($\alpha_{\text{pl}} = 0$), the tangent stiffness undergoes a change in sign from positive to negative. The local stiffness gradient is infinite, potentially[8] causing a significant decrease in the the increment size. These discontinuities were recognized by Alfano and Crisfield [7] and were referred to as limit points. Furthermore, after convergence passed the limit point at a given integration point, large solution increments can be restored only when no other integration points are near their critical separation. When hundreds or thousands of discontinuous integration points exist, the solution can fail to converge or the average increment size can cause the analysis to be prohibitively expensive.

If plasticity is introduced into the TTL, convergence may improve since the magnitude of the step stiffness change is reduced. Unfortunately, a second limit point is necessarily introduced; therefore, the effect on efficiency is uncertain.

Beyond the stiffness discontinuities, the efficiency of the TTL is also effected by the value of the three parameters that are used to define it. The cohesive strength (σ_{c}), the shape factor (α_{pl}), and the critical energy release rate (G_{c}) all affect δ_{c}; therefore, they affect convergence. The efficiency is also affected by the critical energy release rate (G_{c}) through the effects directly described by classical fracture mechanics and crack stability.

To improve convergence efficiency, there is value in the use of a "smooth" constitutive law which avoids stiffness discontinuities. Traction laws with "smooth" derivatives have been examined before, [70, 86] however, the form of the law appears to have been chosen for mathematical convenience instead of numerical considerations. No quantitative assessment of the relative "convergence efficiency and robustness" of the laws were reported.

The objective of the remainder of this chapter is to evaluate several traction laws. In addition to the TTL, two smooth traction laws are developed based on the beta distribution and sine functions.

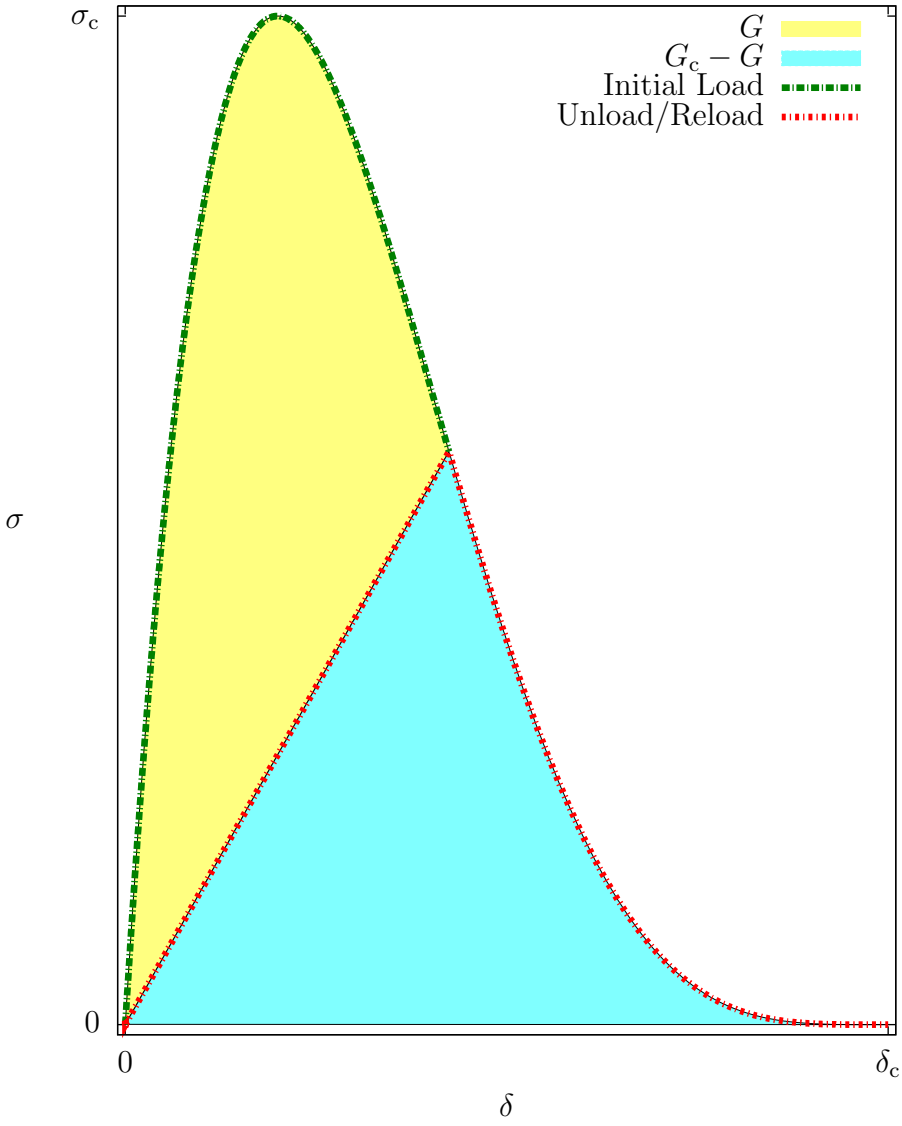

Figure 4.5 The beta distribution traction law.

4.4.2 The beta distribution traction law

Consider the beta probability distribution:

$$\beta\left(x,a,b\right) = \frac{x^{a-1}(1-x)^{b-1}}{\int_0^1 u^{a-1}(1-u)^{b-1}\,du}, \tag{4.23}$$

where the denominator is the beta function. As a probability distribution, the value of its integral is one over the interval $x = [0,1]$.

$$\int_0^1 \beta\left(x,a,b\right) dx = 1 \tag{4.24}$$

Therefore, the distribution can be mapped to a finite traction-separation space with known values of G_c.

Mapping the BDTL to the critical energy release rate

Two parameters are required (G_c, σ_c) and two requirements must be met to complete the mapping. First, the maximum value of $\beta\left(\frac{\delta}{\delta_\mathrm{c}},a,b\right)$ is mapped to the critical stress through a multiplicative constant. Subsequently, the traction law can be written as:

$$\sigma_\beta\left(\frac{\delta}{\delta_\mathrm{c}},a,b\right) = \frac{\sigma_\mathrm{c}\,\beta\left(\frac{\delta}{\delta_\mathrm{c}},a,b\right)}{\beta_{\max}\left(a,b\right)}. \tag{4.25}$$

In equation 4.25, $\beta_{\max}\left(a,b\right)$ is the maximum value of the probability density function (PDF). Second, the traction law must integrate to the value of G_c.

$$\int_0^{\delta_\mathrm{c}} \frac{\sigma_\mathrm{c}}{\beta_{\max}\left(a,b\right)}\,\beta\left(\frac{\delta}{\delta_\mathrm{c}},a,b\right)\,d\delta = G_\mathrm{c} \tag{4.26}$$

A change of variables is required to map the integral in equation 4.26 into the space of the PDF:

$$d\delta = \delta_\mathrm{c}\,dx, \tag{4.27}$$

which allows equation 4.26 to be written as:

$$\frac{\sigma_\mathrm{c}\,\delta_\mathrm{c}}{\beta_{\max}\left(a,b\right)}\int_0^1 \beta\left(x,a,b\right)\,dx = G_\mathrm{c}. \tag{4.28}$$

[8] It is common to use step changes in constitutive response in FE modeling and doing so does not always cause convergence difficulties. It is the magnitude of the step that is important as well as the number of integrations points that are actively transitioning.

In equation 4.28, the integral portion of the left hand side evaluates to one, therefore the critical displacement is calculated as:

$$\delta_{\mathrm{c}} = \frac{\beta_{\max}(a,b)}{\sigma_{\mathrm{c}}} G_{\mathrm{c}}. \tag{4.29}$$

The maximum value of the beta distribution ($\beta_{\max}(a,b)$) must be calculated. After multiplying the right hand side of (4.23) by its denominator, equation 4.30 must be extremized:

$$(1-x)^{b-1}\ x^{a-1}. \tag{4.30}$$

Setting the x derivative of equation 4.30 to zero yields:

$$(a-1)\ (1-x)^{b-1}\ x^{a-2} - (b-1)\ (1-x)^{b-2}\ x^{a-1} = 0. \tag{4.31}$$

Equation 4.31 can be solved for $x_{\max}$ which is a maximum for values of a and b that are appropriate for the BDTL:

$$x_{\max} = \frac{a-1}{b+a-2}. \tag{4.32}$$

Inserting equation 4.32 into the distribution function, the maximum value is:

$$\beta_{\max}(a,b) = \frac{{x_{\max}}^{a-1}(1-x_{\max})^{b-1}}{\int_0^1 u^{a-1}(1-u)^{b-1}\,du}. \tag{4.33}$$

With equation 4.33, the mapping of the traction law is complete. The BDTL, shown in figure 4.5, has been implemented as a traction law module to accompany the DCZM element.

Efficiency considerations related to the BDTL

It has been established that the form of the traction law affects the computational efficiency through the increment size. Specifically, it was shown that the second derivative of the traction law, when large, can cause difficulty is obtaining an accurate correction vector. In this section, the stiffness gradient of the BDTL is investigated.

The parameters a and b have a significant effect on the efficiency of the solution as well as the ability of the solution to obtain a converged equilibrium. In order for the traction law to be reasonable and resemble the TTL, the appropriate ranges are $1 < a < 3$ and $a < b < 10$. These values are not all appropriate for use in an

element; the primary criteria are the stiffness gradients and the overall shape of the distribution.

As shown in the figure 4.6, low values of a and high values of b skew the beta distribution to the left. High values of b also cause an increase in concavity on the down slope of the curve. A value of a just larger than 1.0 would closely match the traditional triangular traction law while providing a continuous derivative, however, the left skew causes large stiffness gradients and significant convergence difficulty. Similarly, the resulting system models are less stable since smaller portions of a structure transfer load. (The energy release rate is higher for a fixed configuration.) Beyond generalities, figure 4.8 shows that the stiffness gradients near $\frac{\delta}{\delta_c} = 0$ approach infinity as a approaches 1.0. For a greater than 2.0, the stiffness gradients remain large near the origin where the stiffness starts at zero. Figures 4.7 and 4.9 examine the effect of small variations around the value $a = 2.0$ and show that even small diversions cause significant stiffness gradients. Therefore, $a = 2.0$ is the most appropriate for this traction law.[9] A value of $b = 5.0$ was assigned based on the general shape of the BDTL, though the parameter is not as critical to model convergence (subject to its constraints).

[9] This result could have be anticipated after examining the form of the beta distribution equation, however, the figures 4.6-4.9 provide an efficient means of interpretation.

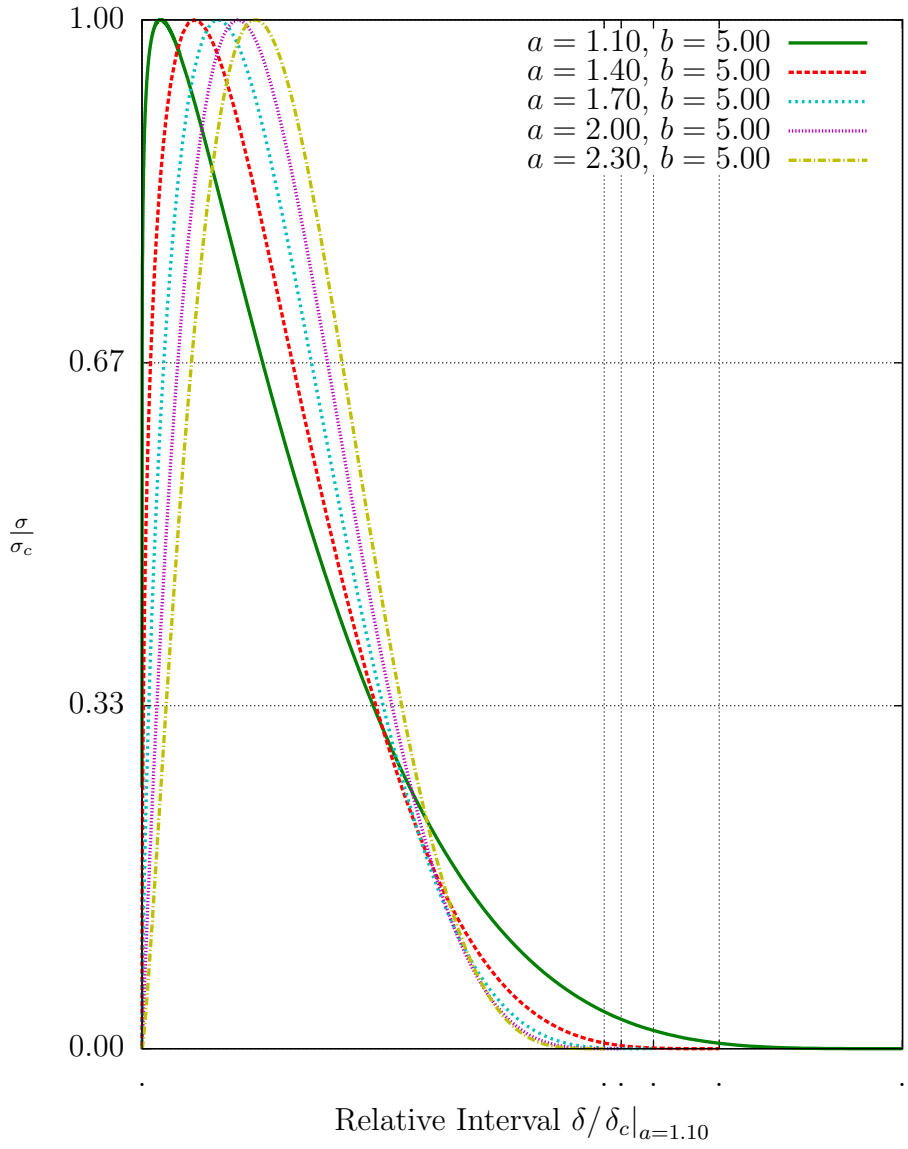

Figure 4.6 The effect of broad variation of a on the BDTL. Small values of a skew the distribution to the left.

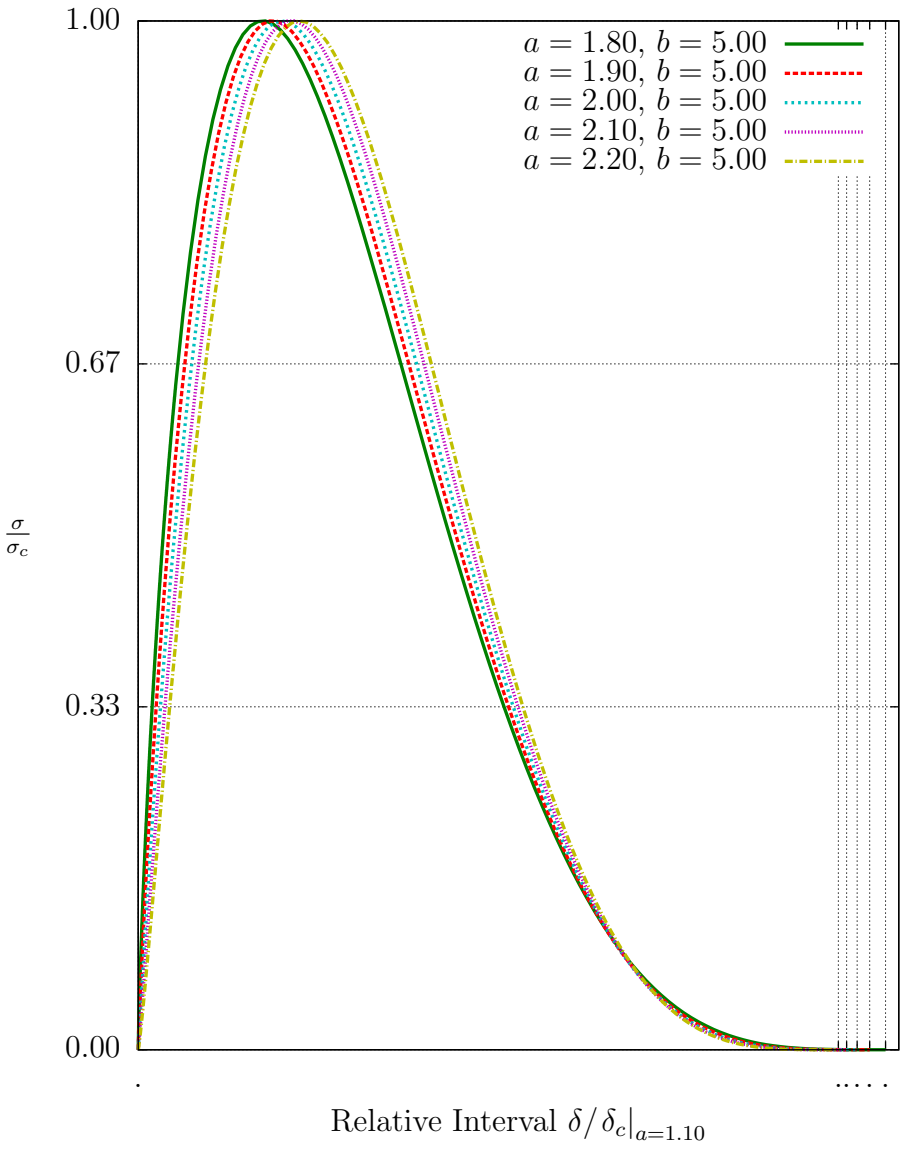

Figure 4.7 The effect of narrow variation of a on the BDTL

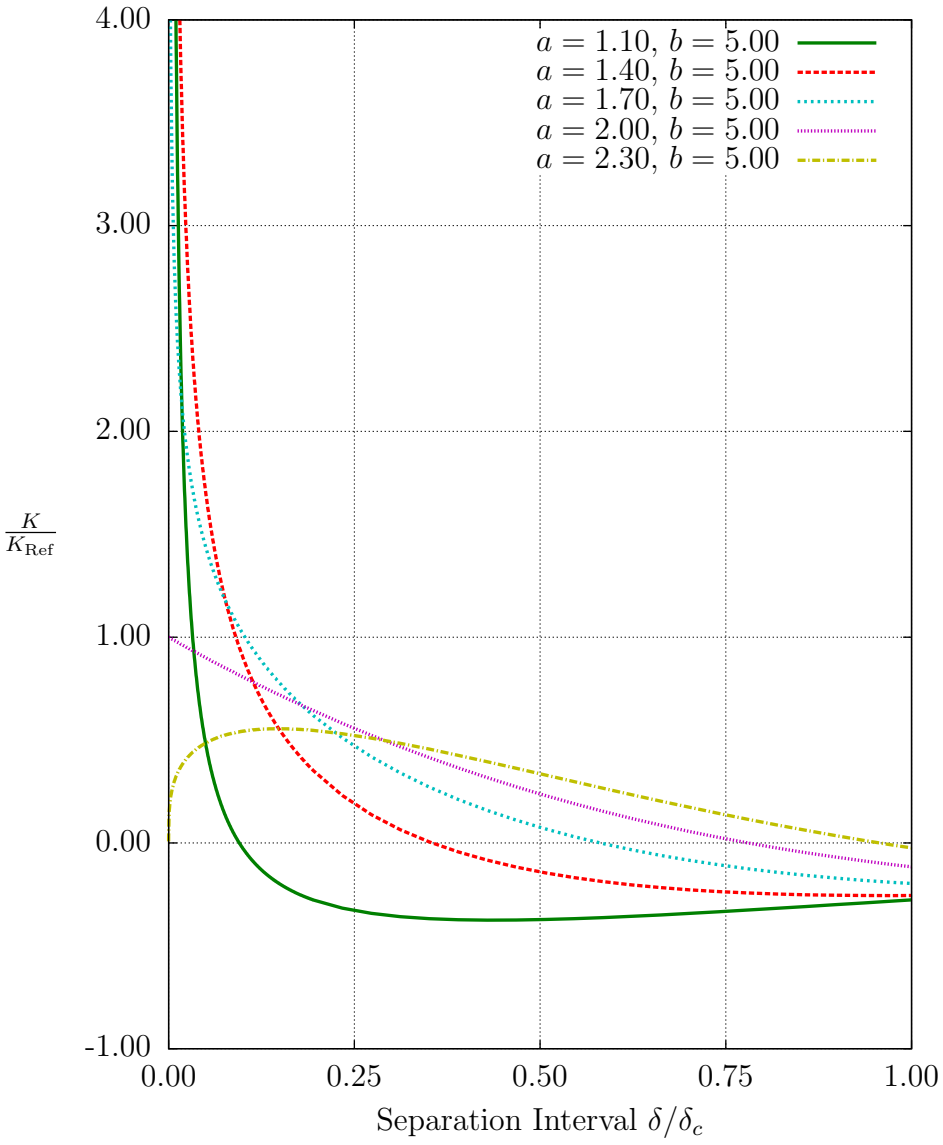

Figure 4.8 The effect of broad variation of a on the tangent stiffness. The stiffness gradients are substantial as a departs from 2.0.

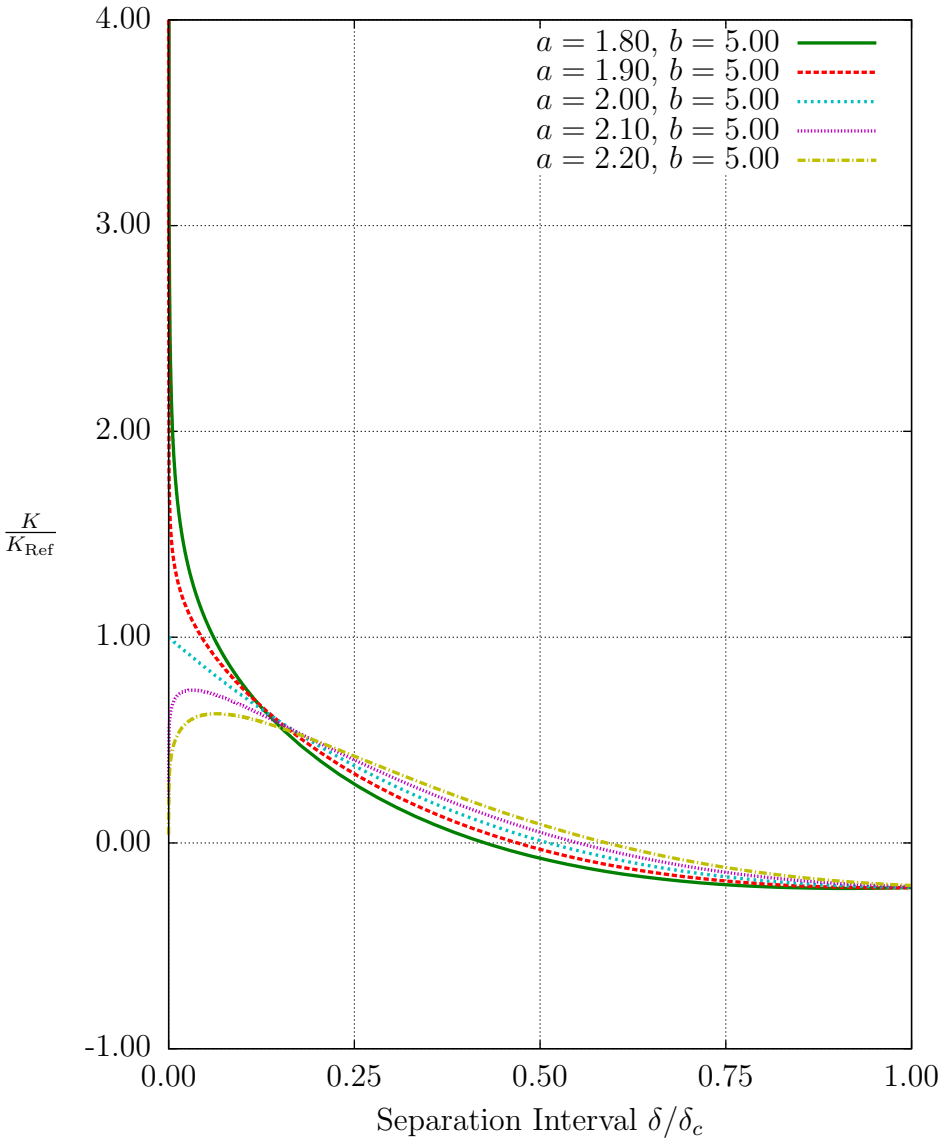

Figure 4.9 The effect of narrow variation of a on the tangent stiffness. Even a small departure from $a = 2.0$ causes large stiffness gradients.

4.4.3 The sinusoidal traction law

Although the BDTL is a smooth law resembles the shape of the TTL, it is possible to derive a law that is more smooth. In the limit of obtaining a (non-zero) smooth stiffness derivative, a parabolic traction law could be assumed. Unfortunately, such an assumption would require that all cohesive integration points are simultaneously at relative displacements where the stiffness is changing (since the resulting stiffness gradient would be a non-zero constant). Although the maximum stiffness derivative would be minimized, the linearity assumptions of the Newton solver would be a poor global approximation during every iteration.

In a typical analysis, only a small portion of the cohesive integration points are in critical zones. The remainder of the cohesive elements are likely to transfer relatively low tractions. Therefore, it is desirable for the traction law to have regions of near linearity, particularly in the lower tractions, so that a relatively small number of integration points are undergoing a significant change in stiffness during an iteration.

The BDTL provides this feature at some level, however, the initial derivative of the stiffness (in the low traction region) is non-zero. A function with a zero initial derivative and a low maximum derivative is the sine function. As a result, it may be a good function on which to model a traction law.

As with all the traction laws, the integral of a sinusoidal stress-relative displacement curve must equal the critical energy release rate (G_c) and the maximum value must map to the critical stress (σ_c). The following traction law meets these requirements:

$$\begin{aligned} \sigma_{\sin}\left(\frac{\delta}{\delta_c}\right) &= \sigma_c \sin(\pi\frac{\delta}{\delta_c}), \\ \delta_c &= \frac{\pi G_c}{2\sigma_c}. \end{aligned} \tag{4.34}$$

The integration point stiffness is a constant times the cosine function and the second derivative remains relatively small at a constant times the sine function. The traction law in equation 4.34 is shown in figure 4.10.

The STL provides a mathematically convenient formulation for a traction law. It is symmetric about its midpoint and its initial stiffness is relatively low, therefore, it does not resemble the common traction laws. The STL, however, offers a clear advantage over the traditional laws. The initial stiffness derivative of the STL is zero while the maximum stiffness derivative is relatively small. An evaluation of the efficiency of the STL is next.

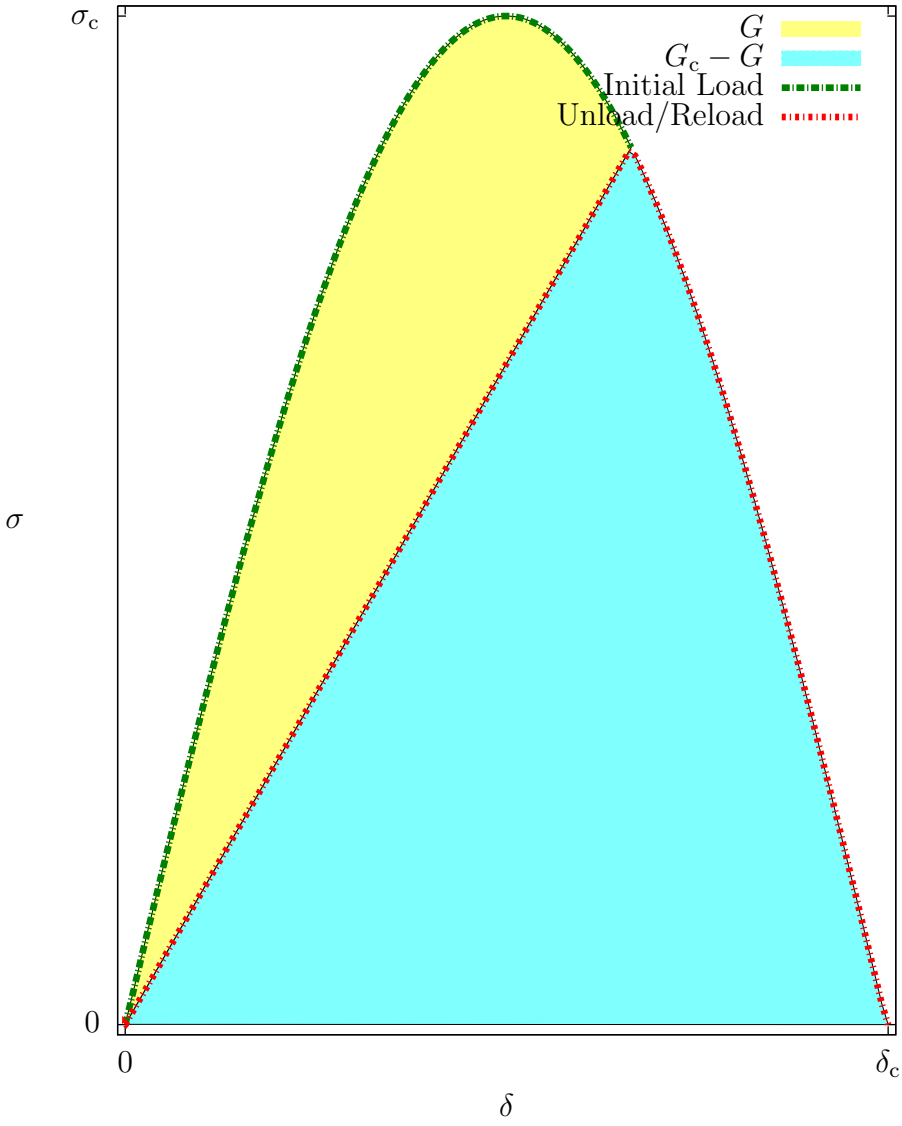

Figure 4.10 The sinusoidal traction law

4.5 Comparison of traction law solution efficiency and robustness

In brief summary of section 4.4.3, the traction law affects the solution efficiency through the stiffness gradient as well as through its effect on δ_c. The critical stress is also affects δ_c and efficiency.

The purpose of the smooth laws is to improve the solution efficiency and robustness by minimizing the stiffness discontinuities and gradients. Whereas convergence and stability are well defined for a solution algorithm, they are not well defined at the level of the constitutive law. To evaluate the solution efficiency of the traction laws, it is useful to compare available metrics.

Two metrics for solution efficiency will be used to compare the traction laws. The first is the average size of the smallest increments during a given solution. The stiffness gradient affects the likelihood of obtaining a converged solution and the minimum increment size is a simple metric which correlates to the ease of convergence. The second efficiency metric is the number of iterations required to obtain a given solution. Although the number of iterations also correlates with the ease of convergence, it is also a direct metric of the CPU cost of a given solution. The number of iterations will be identical across job repetition regardless of system resources, provided that the solver algorithm remains fixed.[10]

Two efficiency metrics will be used since neither metric is an adequate (independent) representation of the solution efficiency. For example, it is possible in an unstable model (like a single lap joint) for a solver to converge without finding the peak load point, [24], particularly if large increments are maintained. As a result, a cap on increment size is often required to ensure the peak load is found in a model. Efficiency conclusions would be misleading if the peak load is not captured, however, the cap adds a significant number of iterations that would not be required. This makes the number of iterations an imperfect metric of efficiency. Conversely, the number of iterations (the direct CPU cost) is not the same for each increment. A given increment size could converge in one iteration or tens of iterations, therefore, increment size is an imperfect metric of efficiency. Since neither metric is ideal, both will be used in the comparison.

The increment based solution efficiency is defined as the ratio of the mean increment size for the smallest ten increments ($\Delta t^{10}_{\text{mean}}$) to the maximum allowed increment

[10] Alfano and Crisfield [7, 8] established a precedent for using the average increment size and the total number of iterations as metrics for convergence efficiency.

size ($\Delta t_{\max}$).

$$\eta_{\text{inc}} = \text{Mean } \frac{\Delta t^{10}_{\text{mean}}}{\Delta t_{\max}} \tag{4.35}$$

The smallest ten increments in a given analysis are exclusive of any step completion increments. The maximum increment size ($\Delta t_{\max}$) is specified to ensure the peak load is captured. Ten increments are averaged in order to remove isolated effects and to allow for an indication of increment size recovery.

The iteration based solution efficiency is defined as:

$$\eta_{\text{iter}} = \frac{\Gamma_{\min}}{\Gamma_{\text{actual}}}. \tag{4.36}$$

$\Gamma_{\min}$ is the minimum number of iterations which would be required to solve the system (based on the specified size limits) and Γ_{actual} is the actual number of iterations that are required. In both equation 4.35 and equation 4.36, the solution efficiency is set to zero if the job does not converge.

A comparison of the effective solution efficiency for a large set of single lap joint (SLJ) and end notch flexure (ENF) analyses were run with three[11] traction laws. The two model types exhibit different failure mechanisms and global stabilities. The SLJ analysis exhibits catastrophic failure, however, there is no surface interaction once the cohesive bond has failed. The ENF analysis maintains global stability, however, the surfaces remain in contact and continue to interact after adhesive failure. The two model types are representative of many applications of cohesive elements.

4.5.1 Efficiency comparison

For the SLJ models, a histogram of the solution efficiency based on minimum increment size is shown in figure 4.11. Figure 4.12 provides a similar comparison of the iteration efficiency. Each is based on 1024 SLJ model runs. In the figures, the differences between the jobs within a given traction law are the governing parameters of the law (G_{IIc}, τ_{IIc}, etc) and the geometry.[12] The TTL models each have unique values of shape factor (α_{pl}), whereas the triangular law models all have a zero shape factor (by definition). In all SLJ analyses, a viscous damping coefficient of $\mu = 10^4$ was used to

[11] The three laws are the trapezoidal traction law, the beta distribution traction law, and the sinusoidal traction law. In the plots of efficiency, the trapezoidal traction law is subdivided into a triangular law and the general trapezoidal law.

[12] The design and analysis of computer experiments analysis sites from chapter 5 are used as an array of parameter values for the efficiency comparison.

improve convergence due to the catastrophic failure associated with the test.

From the SLJ iteration efficiency results (η_{iter}), it is apparent that the smooth traction laws require fewer iterations (on average) than the TTL. The overall effect of the traction law on the minimum iteration efficiency (η_{inc}), however, is inconclusive. There are no definitive trends in the data. It is likely that the catastrophic failure mode of the SLJ test drives the minimum increment size downwards at the point of failure and that the success of viscous stabilization is quasi-random among the different models. The triangular and general forms of the trapezoidal traction law have nearly identical convergence characteristics for the SLJ test.

A more definitive result is found in the ENF model efficiency. Figures 4.13 and 4.14 report minimum increment and iteration efficiencies for 1024 ENF model runs. As with the SLJ models, the difference between the models within a law are the values of the adhesive parameters (G_{IIc}, τ_{IIc}, etc) and the geometry. In this set of figures, it is clear that the smooth traction laws outperform the laws based on the TTL. The minimum increment size remains larger and the number of iterations is smaller for the smooth laws. Among the triangular and trapezoidal forms of the TTL, there is a negligible difference in performance. In comparing the smooth laws, the STL clearly outperforms the BDTL in both metrics of efficiency.

4.5.2 Robustness comparison

A final metric of traction law performance is the overall ability of the solution to converge for an analysis type. Key to this metric is the reliability of convergence. If a traction law is fast for some analyses but fails to converge for other analyses, then the law is non-optimal. An analyst is likely to choose a more reliable law with a higher cost than a cheap law that is suspect with respect to convergence reliability.

Table 4.1 reports the percentage of analyses that were successfully completed for the two model types. Using the TTL as the baseline, the BDTL was slightly less reliable and the STL was significantly more reliable for the SLJ model type. The ENF model type was more definitive as the BDTL and STL were both robust in comparison to the TTL. More than twice as many analyses were successfully completed when the smooth laws were used than when the TTL law was used. Of all the traction laws, the STL was the most reliable in both model types by a large margin.

Table 4.1 Percentage of jobs that converged to completion

	Triangular	TTL	BDTL	STL
SLJ	65.9%	65.9%	61.4%	80.7%
ENF	29.8%	25.0%	61.7%	76.7%

4.6 Conclusion

In this chapter, a FE element has been developed for use in modeling decohesion in structural applications. The element features a sparse stiffness matrix, optional viscous damping for stabilization, standard 2D and 3D interfaces, and a modular interface for specifying the desired traction law. Three traction laws are implemented, one which is in common use and the others which are developed with the objective of computational efficiency and robustness.

A comparison of the efficiency of the three laws is shown in the context of their application to two coupon-level experiments. In both model types, the smooth laws (the beta distribution traction law and the sinusoidal traction law) reduce the number of iterations required to converge through the specified loading. The effect of traction law on the minimum increment size is mixed. The smooth laws have a positive effect on the minimum increment size in the ENF models, whereas in the SLJ model their effect is ambiguous. The global instability of the SLJ structure dominates this result, driving the minimum increment size down in both model types. Of the two efficiency metrics, the number of iterations is the most direct metric of computational cost. The efficiency based on minimum increment size is a useful metric primarily when the number of iterations is influenced by other modeling requirements.

The choice of traction law has a significant effect on the overall solution robustness. The SLJ models based on the BDTL were found to be slightly less robust than the TTL; SLJ models based on the STL were found to be more robust. For ENF models, the smooth traction laws were significantly more likely to result in a converged solution than models with the TTL. Of the three laws, the STL was found to be the most efficient and the most robust. The BDTL is more efficient than the TTL, but robustness depends on the problem being solved.

The general trend of improved convergence and robustness resulting from use of the smooth laws implies that traction law shape should be considered when modeling adhesively bonded structures. The use of a smooth law is likely to reduce the overall cost of computation without effecting the global response or accuracy of the solution.

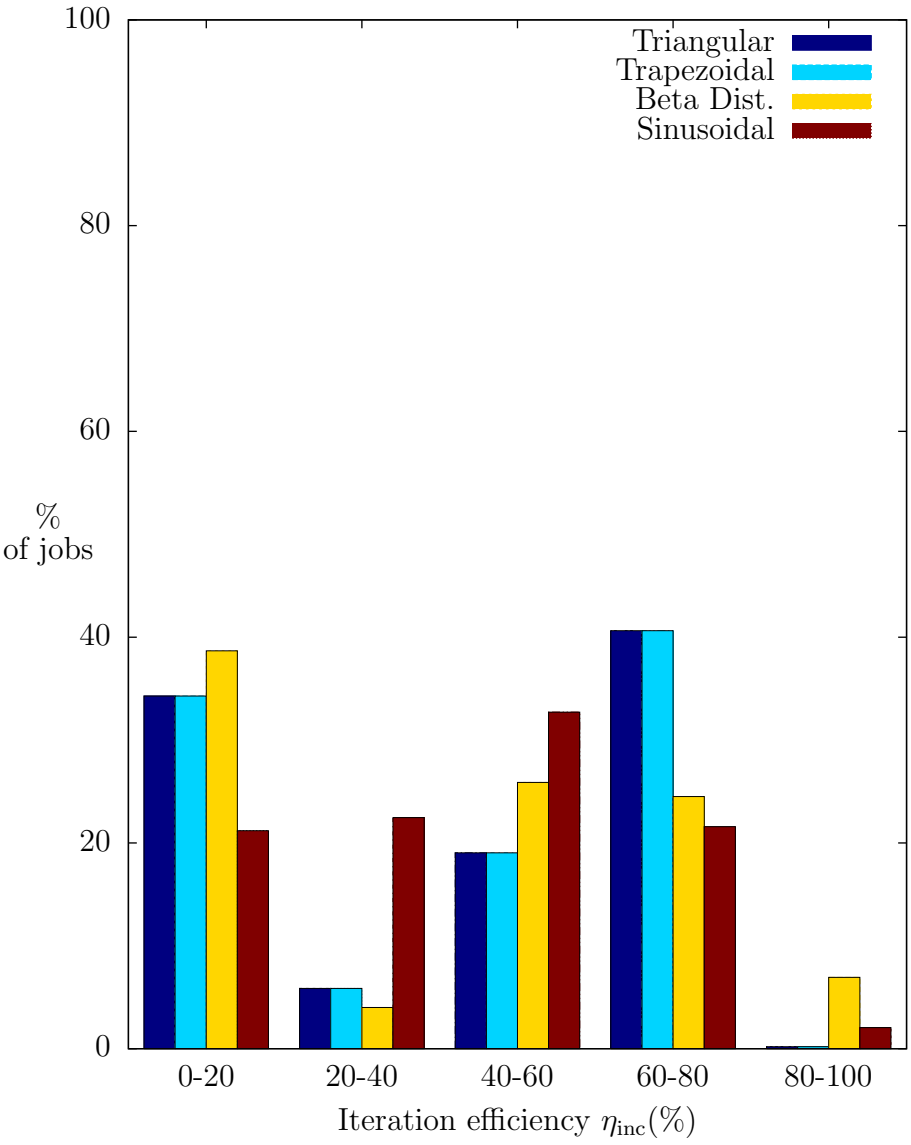

Figure 4.11 A measure of efficiency for SLJ models based on increment size. The η_{inc} metric is inconclusive for this model type.

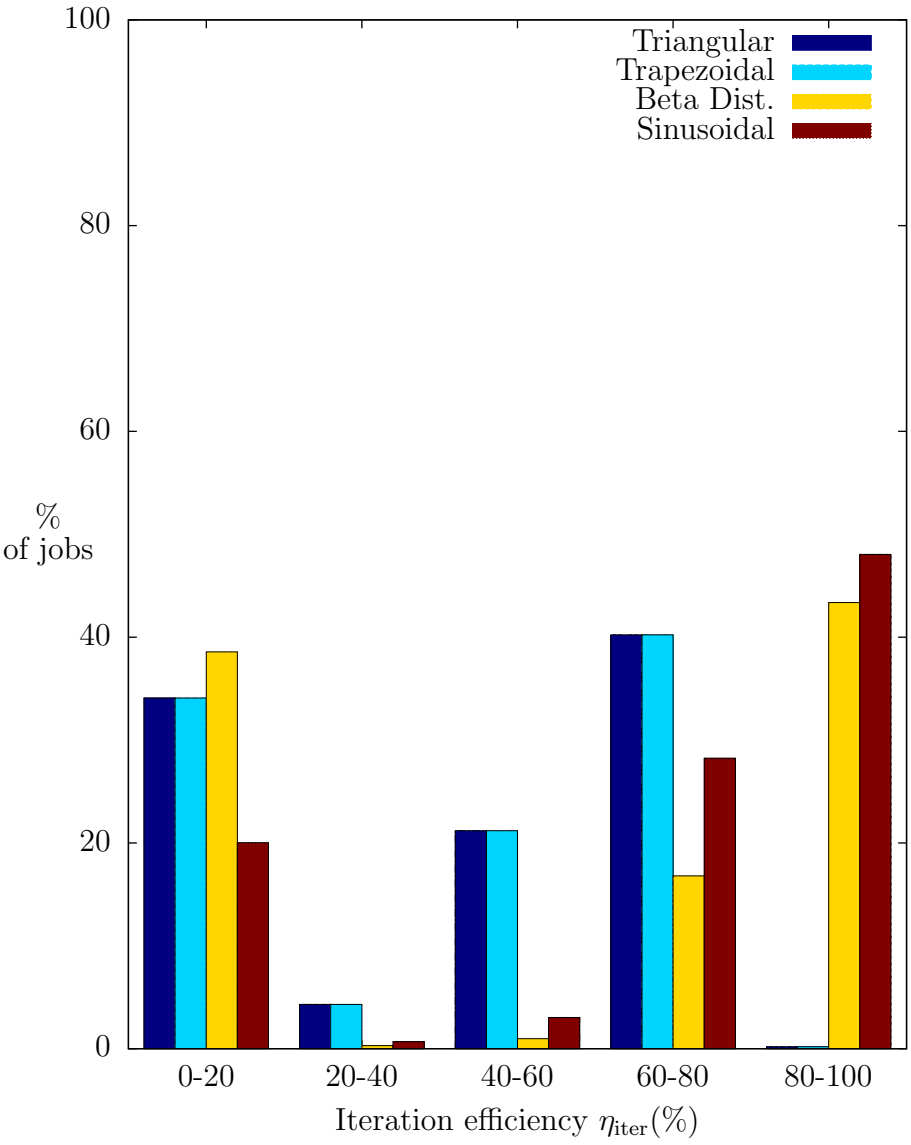

Figure 4.12 A measure of efficiency for SLJ models based on the number of iterations. The smooth laws are significantly more efficient based on the η_{iter} metric for this model type.

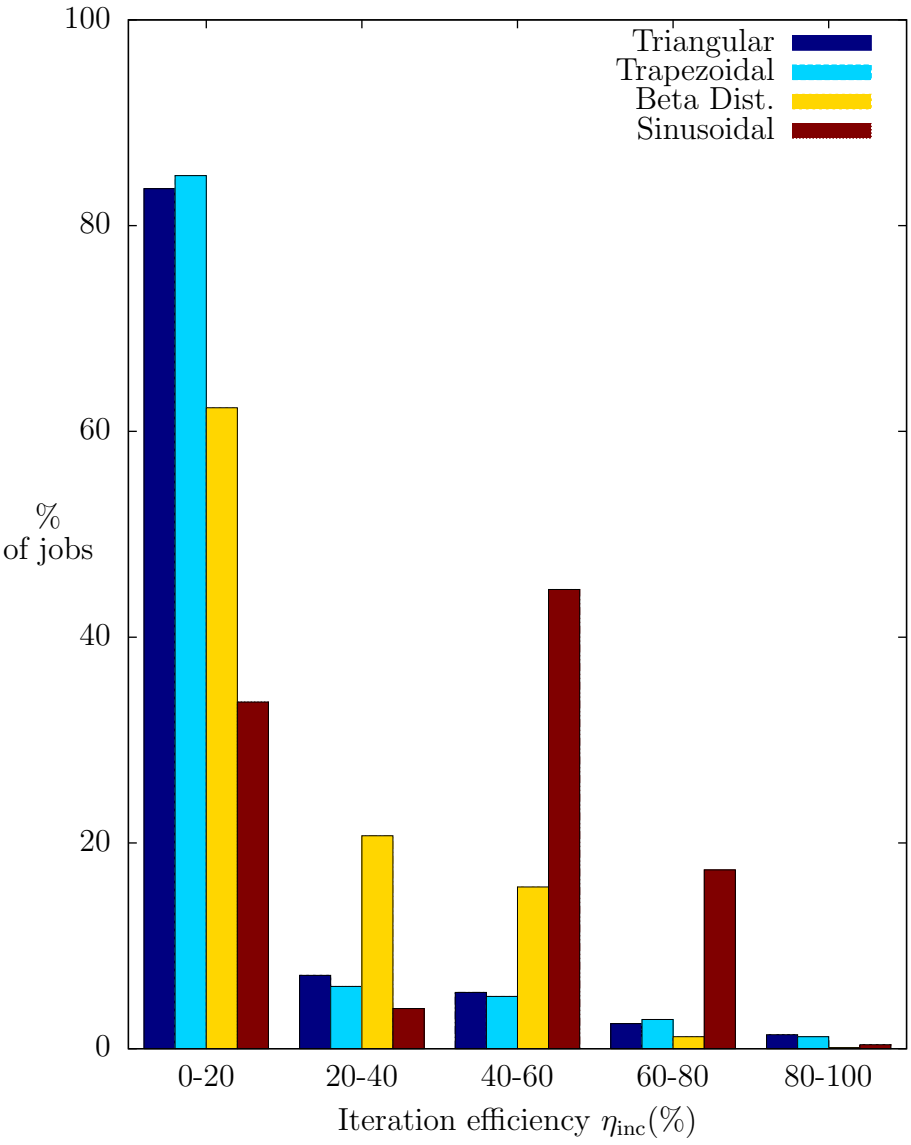

Figure 4.13 A measure of efficiency for ENF models based on increment size. The smooth laws are significantly more efficient based on the η_{inc} metric for this model type.

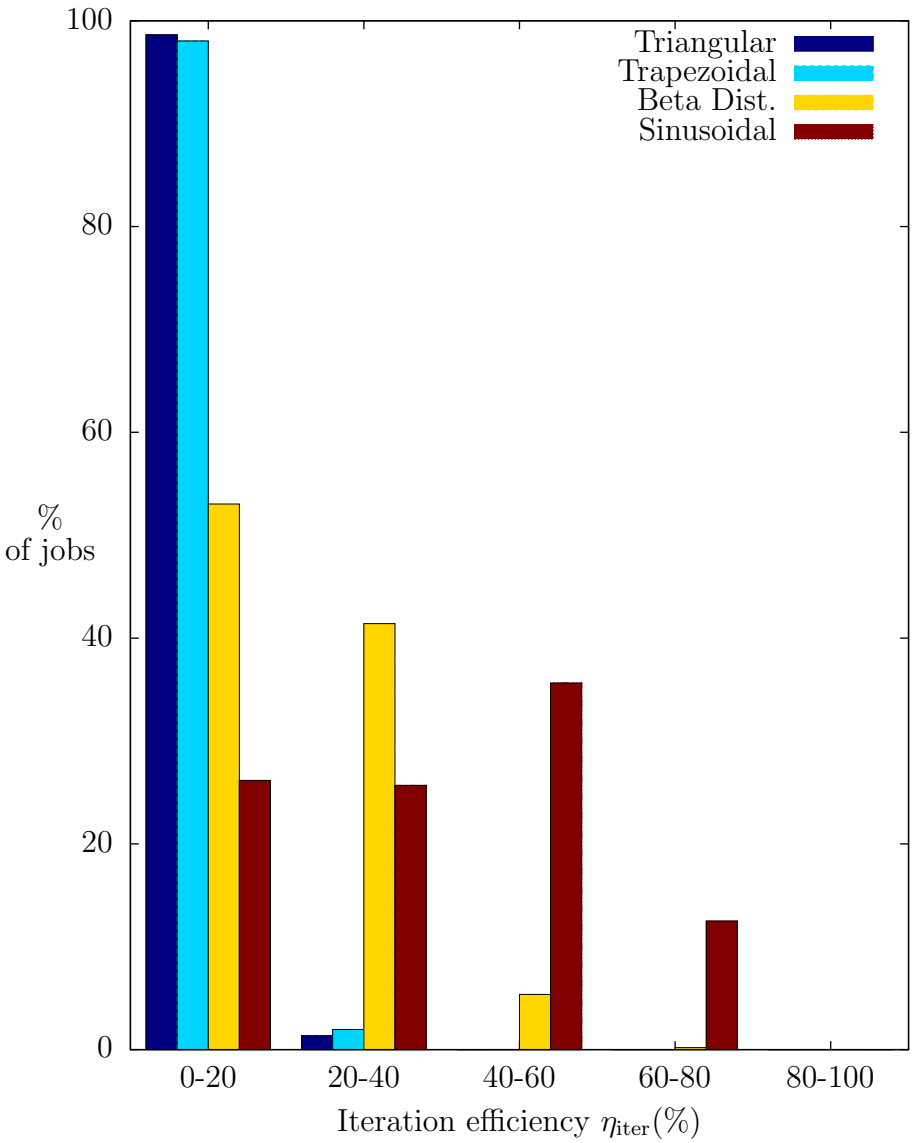

Figure 4.14 A measure of efficiency for ENF models based on the number of iterations. The smooth laws are significantly more efficient based on the η_{iter} metric for this model type.

Chapter 5

The interactions of adhesive constitutive parameters and their effects on common adhesive experiments

Experimental characterization of material systems is necessary for prediction of joint behavior. Proper reduction of experimental data requires a thorough understanding of the experiments. The discrete cohesive zone method, developed in chapter 4, requires a set of material parameters; therefore, the sensitivity of the results from three coupon level adhesive experiments to these parameters is considered next.

The experiments described in this chapter are used to determine sets of parameters for adhesive constitutive models. The assumed form of the traction law is emphasized (used in modeling cohesive failure) and the interactions between parameters of the law are examined. It is shown that the double cantilever beam test is excellent with limited interactions; the end notch flexure and single lap joint tests have interactions which require careful attention in mapping their outputs to an appropriate set of adhesive parameters. It is also shown that the traction law is insignificant to the outcome of the models; therefore, the choice of a computationally efficient traction law is justified. The sensitivities are illustrated through many finite element models with parameters that are chosen via Latin hypercube sampling. Surrogate models are created via kriging analysis and are used to compute the sensitivities.

5.1 Background

Experiments are conducted for several reasons including characterization and validation. The outcomes of *simple* experiments are often used as the inputs for predictive models of other systems.[1] This is particularly true in inverse modeling and modeling for experimental correlation. In these applications, most aspects of a given experiment are used as inputs to a model.

All characterization experiments have a number of control variables as well as a number of unknowns. As inputs, the control variables primarily consist of geometric properties but can also include constitutive parameters that are determined in other experiments (i.e. moduli, Poisson's ratios). The unknowns usually consist of constitutive behavior (i.e. yield strengths, critical energy release rates) but may also consist of quantities that are difficult to measure during the experiment (i.e. crack length). Due to the nature of the experimental work presented in chapter 6, these control variables and unknowns are herein referred to as "inputs". The term "outputs" will be reserved for the metrics used for correlation (i.e. the predicted or experimentally measured quantity such as the maximum load or the slope of the load-displacement curve).

In standardized coupon-level characterization experiments, there are generally accepted methods to determine the unknowns from the control variables. An ideal experiment would have a one-to-one mapping between a complete set of inputs and the value of the output metric. For example, a tensile specimen of uniform material with a known cross section (the set of inputs) can be used in conjunction with a strain gauge and load cell measurement (the outputs) to determine the modulus of the material. This idealization is not often found in practice. It is possible that the "solvable" mechanics of the system are such that the inputs and outputs are under-determined. Alternatively, each input has a level of uncertainty, based on a measurement uncertainty or a stochastic process, such that the output metric is not unique to a single set of inputs.

As an example of an under-determined system, consider a series of experiments conducted on a capped hollow tube of unknown material. Due to the caps over the ends of the tube, the specific cross section of the tube is unknown. Assume that an experimentalist must provide the best possible prediction of the outcome of a torsion test based on the outcomes of a single tensile and a single bending test. In order to

[1] The emphasis added to the word "simple" is due to its generality. Experiments need not be "simple" to yield useful information, nor do the systems that are being predicted need to be more complex than the experiments used to generate inputs. The emphasis is indicative of common desire. "Simple" can mean "well understood", "inexpensive", or any other desirable quality.

accomplish this prediction, the experimentalist would generate models of all three tests. An output metric would be measured during each preliminary experiment (such as the measured slopes of the load-displacement curves in the tensile and bending tests). In order to best predict the outcome of the torsion test, the experimentalist would map these outputs to an appropriate set of inputs. In this case, "appropriate" means that the inputs cause the tension and bending models to reproduce the measured load-displacement slopes from the experiments. Due to the uncertainties present in the specimen, the set of inputs (the assumed modulus and cross section) that produce the desired output are not unique. Consequently, the experimentalist must choose the set of inputs that are most likely to predict the outcome of the torsion experiment. The experimentalist could also specify a range of appropriate inputs that are capable of reproducing the preliminary tests and subsequently predict a range of possible outcomes for the torsion experiment.

In chapter 6, a constitutive model is developed for the prediction of adhesively bonded structural systems that consist of T650/AFR-PE-4/FM680-1. To develop this constitutive model, a set of experiments has been conducted. Prior to reporting the constitutive model, however, this chapter lays the foundation on which the model is developed. In this chapter, the focus is primarily on the experiments, with contextual references to chapter 6. In chapter 6, the focus is primarily on the outcome of the tests with references to the conclusions presented in this chapter.

The experiments that are used in chapter 6 to determine the adhesive parameters are the double cantilever beam (DCB) test, the button peel stress (BPS) test[2], the end notch flexure (ENF)[3] test, and the single lap joint (SLJ) test. In practice, each has been used to determine a specific constitutive parameter (G_{Ic}, σ_{Ic}, G_{IIc}, and τ_{IIc}). A method of computing the corresponding constitutive parameters based on the measured load and displacement exists, though uncertainties remain in each experiment.

A critical uncertainty in the experiments is the constitutive response of the adhesive. The shape of the constitutive relation cannot be easily determined and is therefore assumed. The constitutive response further consists of all the parameters that define the assumed form (and their stochastic distributions). It is the values of these parameters that are sought in the individual coupon level experiments. A second uncertainty in the experiments is the geometric features, such as the time history of the crack length. Finally, stochastic uncertainty is present in each experiment, such as

[2] The author is not aware of a test that is generally accepted for the determination of σ_{Ic} in composite materials. Consequently, an appropriate BPS experiment is developed to determine σ_{Ic}.

[3] The standard for the ENF test is still evolving, [36].

in the constitutive response of the adherends. In a composite specimen, for example, the adherends consist of fibers and matrix that have undergone a manufacturing cycle. During this cycle, process defects can impact the effective constitution of the adherends. The remainder of this chapter is devoted to exploring how the input uncertainties affect the outputs of the adhesive tests and, consequently, how these uncertainties affect the mapping of the outputs back into the "best" constitutive model for the adhesive.

It has been shown that the shape of the traction law is not important, [102, 113], though this has not been robustly established for all common tests. The author is not aware of systematic studies that have illustrated the adhesive parameter interactions and how those interactions affect the experiments.

5.1.1 Review of the standard tests

The DCB test

The principal objective of the DCB test is to determine the value of G_{Ic} for a given adhesive or inter-laminar interface. The test is well established and commonly used [86] and a significant body of literature exists. The experimental load displacement curve has two distinct phases. They will be referred to as the linear elastic and crack advance phases.

Analytical solutions have been published for each of the two phases, [70, 79]. For example, working under the assumption that G_{Ic} is the sole critical parameter, Mi et al. [70] provides an analytical solution for the two portions of the curve. The linear elastic response is governed by:

$$P = \frac{3}{2}\frac{EI\delta}{a_0^3}, \tag{5.1}$$

and the crack advance is governed by:

$$\delta = \frac{2}{3}\frac{(b\, G_{\mathrm{Ic}} EI)^{\frac{3}{2}}}{EIP^2}. \tag{5.2}$$

If all the terms of equations 5.1 and 5.2 are well known and the underlying assumptions hold, they can be used to compute G_{Ic}. In practice, however, the uncertainties associated with the terms in equations 5.1 and 5.2 require more sophisticated data reduction in order to map the test result to an appropriate value of G_{Ic}.

To address the uncertainties present in DCB testing, ASTM International (ASTM) provides recommended procedures for the experiment and for data reduction, [14].[4] Three possible data reduction methods are recommended: modified beam theory, compliance calibration (CC), and modified CC. The CC techniques are used to compensate for the material and geometric uncertainties that are present in the beam theory solutions. A "critical load" is required in each data reduction option. That load can be the maximum load, the point of deviation from linearity, the point of visual delamination, or the so-called 5% increase in compliance[5]. Regardless of the chosen data reduction technique, the computed value of G_{Ic} is proportional to that critical load.

Another common data reduction technique is the direct energy balance method, also known as the area method. After initial linear loading to the "critical load", the load decreases predictably (i.e. equation 5.2) while a measurable crack advance is driven. The specimen is unloaded while the data acquisition system remains active. In this way, the load-displacement curve can be numerically integrated to determine the external work that is expended during the test. The work is proportional to the critical load for a well behaved sample whose behavior can be approximately described by linear elastic fracture mechanics. To determine G_{Ic} using the direct energy balance approach, the work is divided by the crack advance area, where any appropriate crack measurement technique can be used to determine the area. An advantage of the area method is that it inherently provides an average value for G_{Ic} over relatively large area of the adhesive material. As it cannot account for the "R-curve", it is not recommended for systems where fiber bridging is likely, [14]. Due to its simplicity and inherent averaging, the area method is used in chapter 6 as one of two methods to determine G_{Ic} for the T650/AFR-PE-4/FM680-1 adhesive system.

With the intent of understanding the sensitivity of the DCB output to the test parameters, it is recognized that all of the DCB data reduction methods find that G_{Ic} is proportional to the maximum line load ($\bar{P}_{\mathrm{max}}$). As a result, the finite element (FE) design and analysis of computer experiments (DACE) sensitivity study presented in section 5.2 uses the predicted value of $\bar{P}_{\mathrm{max}}$ as the model output. In short, the study presents the sensitivity of the value of $\bar{P}_{\mathrm{max}}$ to the model inputs.

[4] The ASTM recommends usage only on unidirectional ply materials due to fiber bridging and the "R-curve". Fiber bridging is less likely in woven adherends and is not a concern for the pre-cured adherends used in chapter 6.

[5] The 5% compliance analysis method uses the initial slope of the load-displacement curve as a reference and establishes the critical load at the intersection the curve with a ray from the origin. The ray has a slope that is 5% lower than the reference slope.

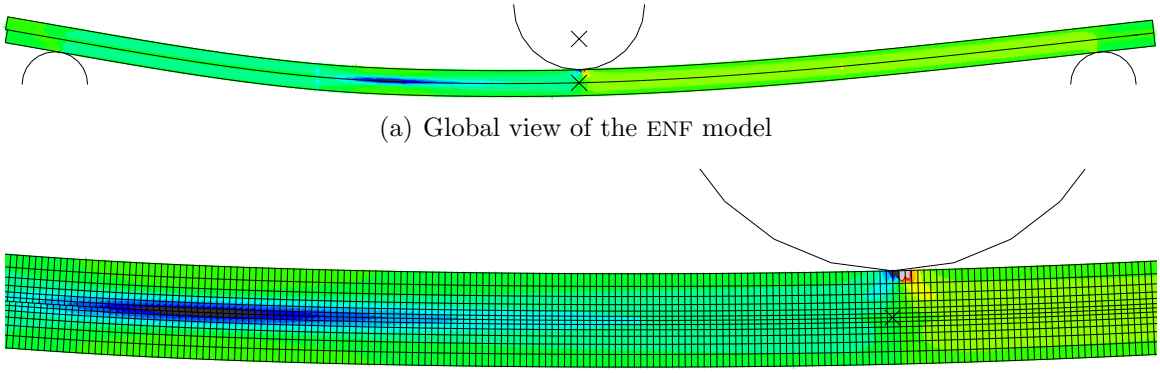

(a) Global view of the ENF model

(b) Local view of the ENF model

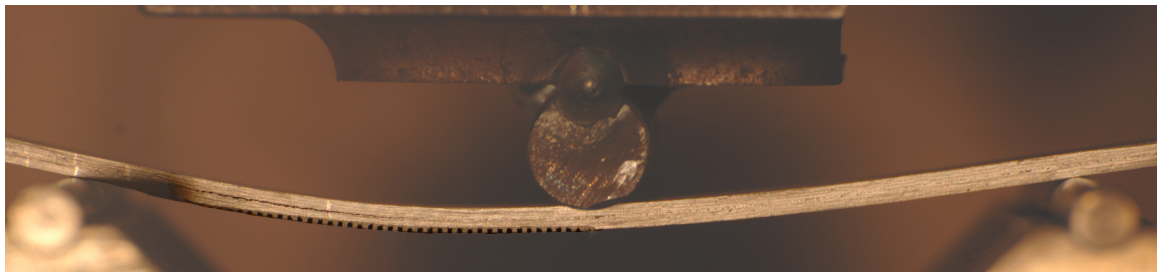

(c) A typical ENF experiment

Figure 5.1 A typical ENF model and experiment

The ENF test

Although the ASTM has resolved to adopt the end notch flexure test as the standard test for determining the value of G_{IIc}, the standard has not yet been ratified and is evolving, [36]. As a result, there are several experimental and analysis techniques that have been considered. Davidson and Zhao [36] have recently evaluated a large number of data reduction techniques, of which two will be described.

An analytical solution[6], used by a number of authors [5, 34, 41, 83, 89], is given by:

$$G_{\mathrm{IIc}} = \frac{9\,\bar{P}_{\max}\,\delta\,a_0^2}{2\,(2\,l^3 + 3\,a_0^3)}. \tag{5.3}$$

As in the DCB data reduction techniques, the analytical solution presented in equation 5.3 has uncertainties which make it impractical for determining G_{IIc} from experimental data. To overcome these uncertainties, CC methods are available, including:

$$G_{\mathrm{IIc}} = \frac{\bar{P}_{\max}}{2}\frac{\partial C\,(a)}{\partial a}\bigg|_{a_0}. \tag{5.4}$$

[6]Davidson and Zhao [36] provide references for three separate analytical solutions.

In equation 5.3, $C(a)$ is a best fit compliance curve of the form:

$$C\,(a) = A + m\,a^3. \tag{5.5}$$

$C(a)$ is established by measuring the compliance of a given specimen over a variety of crack lengths. Equations 5.3 and 5.4 both compute a G_{IIc} that is proportional to the maximum load during the test. Therefore, the sensitivity analysis in section 5.3 uses the value of $\bar{P}_{\max}$ as the measured outcome of the FE model. As with the DCB test, the analytical solution (equation 5.3) assumes that G_{IIc} completely governs the adhesive crack propagation. This assumption will be tested in section 5.3.

The SLJ test

The SLJ test is considered next. The ASTM claims that the SLJ test is the most widely used test for comparative studies of bonded products, [13]. It is used to determine the *comparative apparent* shear strength of a given system. Of the three tests discussed in this chapter, the SLJ test has the most complex mechanism of failure and is the least able to provide a direct mapping to the desired constitutive parameter (τ_{IIc}).

Although several analytical solutions exist for the stress distribution in the SLJ joint[7], the stress field can not be uniquely determined due to the reentrant corners in the joint. In practice, the reported output of a SLJ test is the "apparent shear strength", defined as the failure load divided by the lap area. This value is useful only for comparison purposes and is not useful as a constitutive parameter. When the adhesive system is modeled as a cohesive zone (as in this dissertation), the reentrant corners of the joint are eliminated and a critical shear stress (τ_{IIc}) can more clearly be defined as a constitutive parameter. Unfortunately, this does not overcome the complexity of the SLJ test. An appropriate value of τ_{IIc} must be carefully extracted from the test results.

To emphasize this point, the ASTM provides several recommended procedures for the SLJ test, [15, 16]. In doing so, they warn of the risks associated with improper interpretation of the test result. Basic procedures for interpreting the outcome of the SLJ test are given in [13].[8]

[7] Volkersen [104] provided the first shear-lag analytical solution to the SLJ.

[8] In the introduction to this standard, it is claimed that the failure load is usually controlled by the tensile stress of the adhesive and not by the shear stress. The results presented in section 5.4 of the current work are much more explicit in reporting the relevance of the adhesive constitutive relationship.

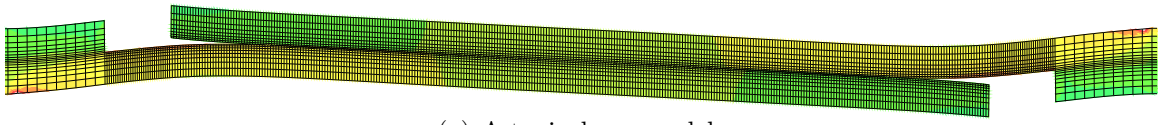

(a) A typical SLJ model

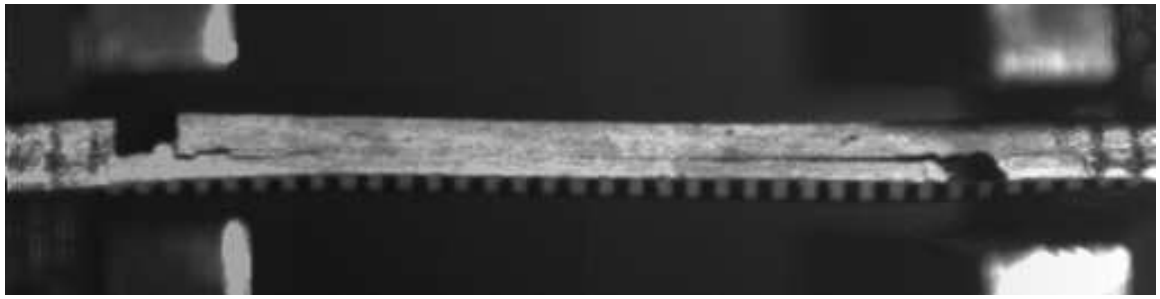

(b) A typical SLJ experiment

Figure 5.2 A typical SLJ model and experiment. These images were taken just prior to failure.

While recognizing the complexity of the SLJ test, it is apparent that the most quantifiable output from the test is the maximum line load ($\bar{P}_{\max}$). Therefore, the sensitivity analysis presented in section 5.4 uses this value as the model output. In doing so, it illustrates the relationships between the input variables (including the critical adhesive constitutive parameters) and the experimental output variable.

5.1.2 Kriging analysis using the DACE toolkit

To explore the effect of the inputs and their uncertainties on the critical experimental outputs, FE studies have been conducted on the three common adhesive tests using kriging analysis and the DACE toolkit, [67].[9] In each of the adhesive experiments, a set of variables is identified that may have significant effect on the model output. First among these variables are the adhesive constitutive parameters; they are the parameters to be determined in chapter 6. Emphasis is placed on the adhesive constitution since the available analytical solutions assume monotonic relationships between the adhesive parameters and the tests that are used to determine them. As efficient tools like the discrete cohesive zone method (DCZM) element become available and these parameters become widely used, it is important to determine if the underlying

[9]Though the DACE toolkit was designed for use with Matlab®, a one line change in the source code enabled it to be run within Octave©. The choice Octave© as a software package allowed for consistent and direct interaction with the scripted interfaces for data reduction.

assumptions are acceptable in context. The remaining variables (other than constitutive parameters) are chosen based on their likelihood of having significant effect on the output variable and their value as comparative inputs. The mixed mode failure criterion for all three tests is assumed to be:

$$\left(\frac{G_{\mathrm{I}}}{G_{\mathrm{Ic}}}\right)^{n} + \left(\frac{G_{\mathrm{II}}}{G_{\mathrm{IIc}}}\right)^{n} = 1. \tag{5.6}$$

Mode mixity is not addressed in this dissertation. The mode mixity exponent (n) is assumed to be one.

Since a primary focus of this dissertation is the effect of temperature on joint behavior, it is desirable to include temperature within the list of variables. The effect of temperature, however, often results in a change of the constitutive properties of the specimen or in thermal expansion. The current study has been done assuming identical adherends, thus nullifying the need to consider expansion effects. In context, the principal manifestation of temperature will be a change in the stiffness of the adherends and a change in the adhesive constitutive parameters. The latter are determined by the tests under investigation, therefore, only the former will be explicitly mentioned in the descriptive sections below. As a result, temperature is implicitly incorporated through the inclusion of stiffness and modulus uncertainty (D and E).

Having identified an appropriate set of design variables, a range of reasonable values was assigned to each. The Latin hypercube sampling (LHS) technique [68] (incorporated into DACE) was used to create an array of value sets (called sites) for the experimental variables. In this technique, the range of each variable is divided into n non-overlapping intervals. A point is sampled randomly from within each interval and the variables combinations are joined randomly from among the intervals. (A uniform distribution is assumed within the intervals and equally likely pairings are assumed for the random assignment.) The method ensures that the vector space is well represented and that each variable has as many unique values as there are sites. Using LHS, higher order effects and interactions can be identified with fewer sites than in a classical orthogonal array. The reduction in sites facilitates the inclusion of a larger number of variables, including variables which *may not* have significant effect on the model output.[10]

[10]These variables are often excluded from an orthogonal array since the number of required runs increases exponentially with the number of variables. The exclusion, based on the best judgment of the analyst, may or may not be appropriate. Conversely, LHS explicitly determines the importance of the variables while minimizing the impact of additional variables on the number of runs that are required.

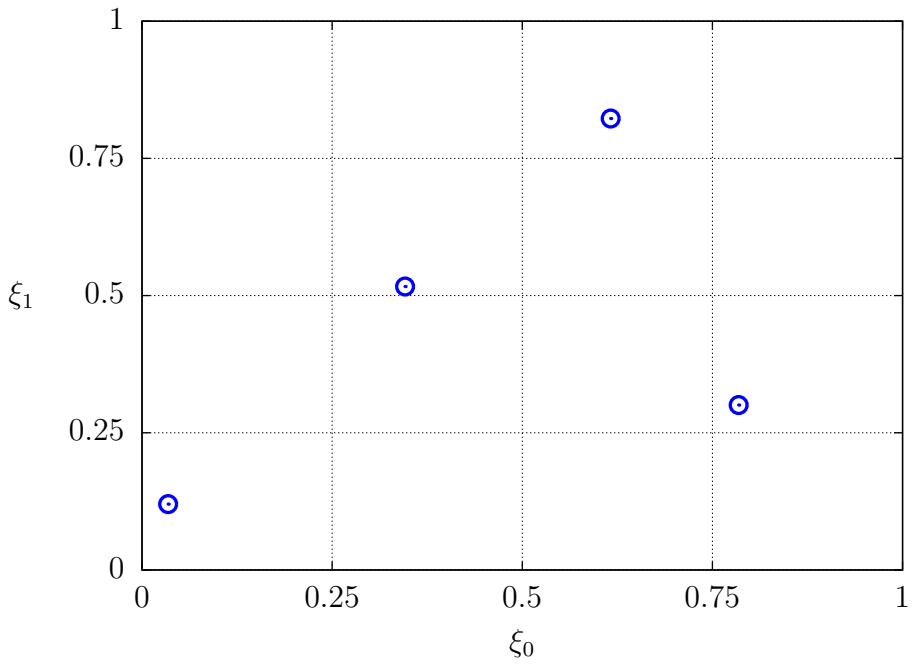

Figure 5.3 Example of LHS with two variables and four sites. Each variable takes on four unique values.

To quickly incorporate the sites into FE models, the FE mesh was parameterized based on the chosen variables. The assignment of variable values to the FE models was managed by an automated shell script (using the *bash* shell on a Linux platform). The script generated individual job files based on the variable values. Job submission, data reduction, and data set compilation were also managed by a set of *bash* shell scripts.

Data reduction and analysis of the compiled data sets were completed in Octave© using the DACE package. DACE provides a complete methodology for creation of a surrogate model. A complete description is provided in Lophaven [67]; a brief summary is provided here. The first step in creating the surrogate is normalization of the input and output variables so that each has a mean of zero and a standard deviation of one. The normalization is followed by a regression; a second order polynomial regression function is chosen from the available options.[11] The regression function and its coefficients are the surrogate model. A predictor script can be used to apply the surrogate model to any desired variable site (within the design space). The conclusions in this chapter are based on the output of the surrogate predictor and the properties of the surrogate model itself.

[11] DACE provides options for several built-in regression functions.

The principal outcome of this study is a quantification of the sensitivity of the output metrics to the input variables. These sensitivities are identified by the regression coefficients ($\beta_{k,l}$) of the surrogate model. Since the regression function is a second order function, each variable has a linear coefficient as well as a coefficient for the product of that variable with each other variable. The magnitude of the coefficients represent the output sensitivity to the input variables. If an output is highly sensitive to an input, the magnitude of the linear coefficients are approximately one:

$$|\beta_{k,l}| \approx 1.0. \tag{5.7}$$

If an output in insensitive to an input, then the linear coefficients are near zero:

$$|\beta_{k,l}| \approx 0.0. \tag{5.8}$$

Similarly, the magnitudes of the product coefficients are indicative of the relative importance of variable interactions.

The values of the regression coefficients are not independent of the range specified for each variable in the DACE array. Care must be taken to choose a range for each variable that is reasonable for a given test. An inappropriate range may overwhelm the other variables and distort the conclusion. An appropriate range can best be determined by systematic examination of the $\beta_{k,l}$ values and the DACE predictions. The predictions must be found reasonable in the context of experimental evidence.

Since the range of the variables affect the value of the $\beta_{k,l}$ coefficients, the coefficients should *not* be considered an absolute value. Rather, the relative magnitudes of the coefficients are important. If the magnitude of one $\beta_{k,l}$ is several times another, the variable has a larger effect on the output. If the magnitude of one $\beta_{k,l}$ is slightly larger than another value, they have relatively equal importance.

In the following sections, the sensitivities to some input variables are widely known and could have been predicted by examining the analytical solutions. These variables are included primarily to determine their relative importance in comparison to the adhesive parameters. For these known sensitivities, existing methods (such as CC) are available for mapping the output back to appropriate constitutive input. Conversely, the author found no studies that illustrate the sensitivities within the adhesive constitutive models. These sensitivities must be closely examined.

Each of the sensitivity studies reported below use the trapezoidal traction law (TTL) as the traction law for the FE model. This is deliberate despite the penalty paid in solution efficiency. In doing so, the relative importance of the shape of the traction law

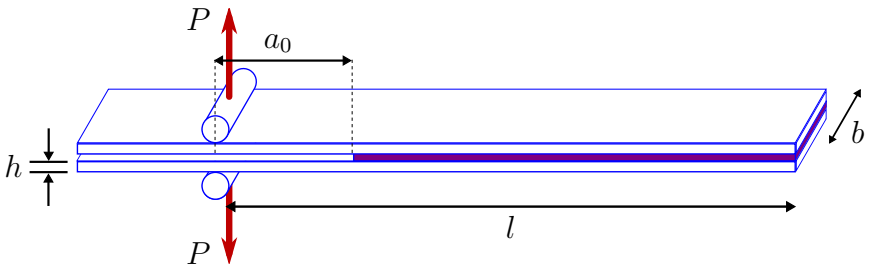

Figure 5.4 DCB specimen geometry

is included in the sensitivity study (and found to be insensitive). In fact, each traction law in chapter 4 was used in a separate DACE study for this work. The outcome of these studies were nearly identical, though they are not explicitly reported. The beta distribution traction law (BDTL) DACE analysis was used for data reduction of the Mode II test results in chapter 6. [12]

5.2 Sensitivity analysis for the double cantilever beam test

In this section, the DCB test is explored. A schematic of a DCB specimen is shown in figure 5.4, indicating the geometric variables in the DACE array. In addition to the geometric variables, the four primary adhesive parameters are included as well as the shape factor associated with the TTL. The variables and their ranges are listed in table 5.1. A representative FE result is shown in figure 4.3 and properties of the FE models are provided in table 5.2(a).

Recall that the maximum line load ($\bar{P}_{\max}$) is assumed to be proportional to the value of G_{Ic} and is the output of the DCB test. Since the magnitudes of $\beta_{k,l}$ indicate the sensitivity of $\bar{P}_{\max}$ to a given variable, $\beta_{k,l}$ is reported.

The linear $\beta_{k,l}$ values for each of the DCB variables are shown in figure 5.5. The most important predictor of $\bar{P}_{\max}$ is G_{Ic}, followed by a_0 and D. The model output, therefore, is most sensitive to G_{Ic}. The quadratic $\beta_{k,l}$ values shown in figure 5.6 further confirm these key variables, since the largest interactions are among these same variables. This result is not a surprise; the sensitivities to D and a_0 are widely known and the value of G_{Ic} is *supposed* to be proportional to the value of G_{Ic}. Presumably, the values of D and a_0 are known to a high degree of precision. If they are not, the

[12] The BDTL was the smooth law that was available during experimental data reduction. Design studies will likely use the BDTL or a similar law. Therefore the constitutive models developed in chapter 6 reflect this likelihood.

Table 5.1 Variables in the DCB DACE array

Variable	Min	Max
G_{Ic}	100 J/m^2	1000 J/m^2
G_{IIc}	100 J/m^2	2000 J/m^2
σ_{Ic}	1.5 MPa	25 MPa
τ_{IIc}	2.1 MPa	25 MPa
α_{pl}	0%	50%
D	6.6 Nm^2	21.0 Nm^2
l	110 mm	150 mm
a_0	20 mm	50 mm

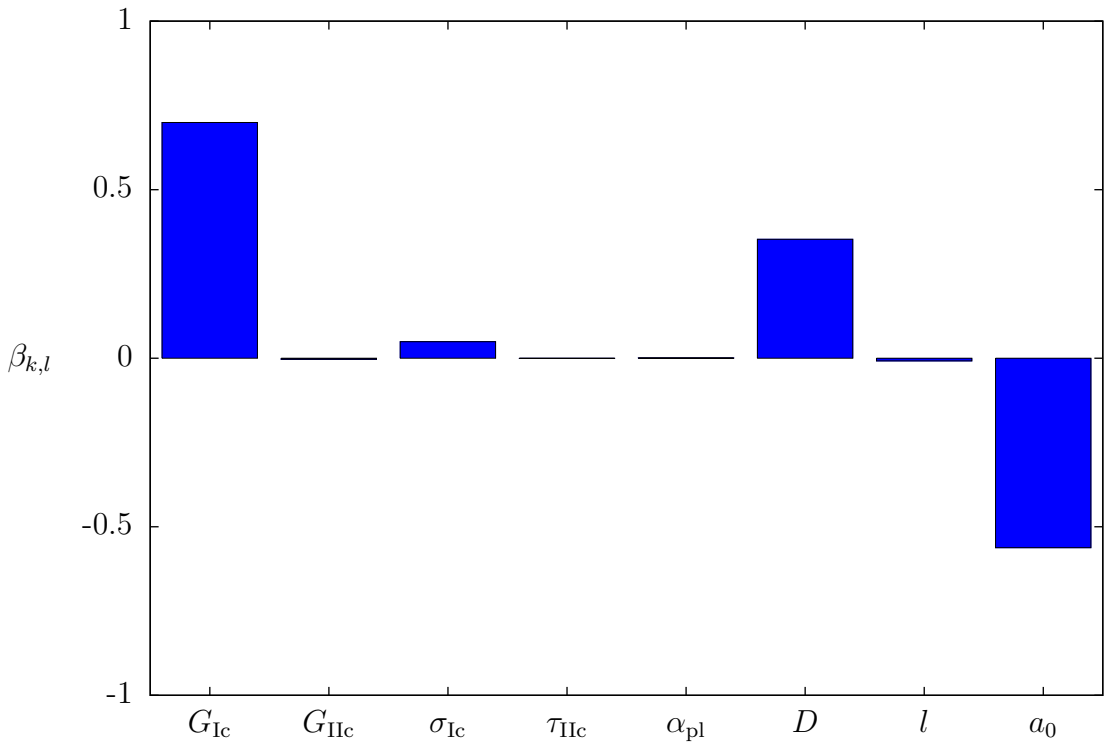

Figure 5.5 Linear $\beta_{k,l}$ values for variables in the DCB DACE array

Table 5.2 Approximate size of the DACE FE models

(a) The DCB FE model

Number of elements	5000
Number of user nodes	5300
Number of variables	29000

(b) The ENF FE model

Number of elements	16000
Number of user nodes	14000
Number of variables	97000

(c) The SLJ FE model

Number of elements	7400
Number of user nodes	7900
Number of variables	51000

sensitivity of $\bar{P}_{\max}$ to these variables can be accounted by CC methods, though this can be difficult in practice.[13]

An important observation from the $\beta_{k,l}$ values is that G_{Ic} is the only adhesive parameter which has a significant effect on $\bar{P}_{\max}$. Though this has been assumed in the analytical solutions, it has not been previously confirmed in the context of cohesive zone FE modeling techniques. This result confirms that the DCB test is ideally suited to determining the value of G_{Ic}. There are no interactions between the adhesive constitutive parameters that would cause difficulty in mapping the experimental value of $\bar{P}_{\max}$ to a specific value of G_{Ic}.

To illustrate the relative importance of the variables, figure 5.7 shows the interactions between the two most critical adhesive parameters (G_{Ic}, σ_{Ic}) in the DCB test. In these figures, both of which show the same effect in different forms, the values of G_{Ic} and σ_{Ic} are varied over their specified range while the remaining variables are fixed at their mean values. The value of $\bar{P}_{\max}$ from the DACE predictor is shown on the z-axis in figure 5.7(a), whereas figure 5.7(b) shows contours of $\bar{P}_{\max}$ over the same range. It is apparent that G_{Ic} (the adhesive parameter with the highest value of $\beta_{k,l}$) is far more critical than the second most important adhesive variable. Furthermore, there is little interaction between these two variables (or any other pair of adhesive variables), as evidenced by the near verticality of the contour lines in figure 5.7(b).

[13]The fixed hinge location makes CC of a single specimen unpractical. Multiple specimen CC would require uniformity from specimen to specimen that is unavailable in this study. This is particularly true with respect to the temperature effects on stiffness, since each temperature would require a new calibration.

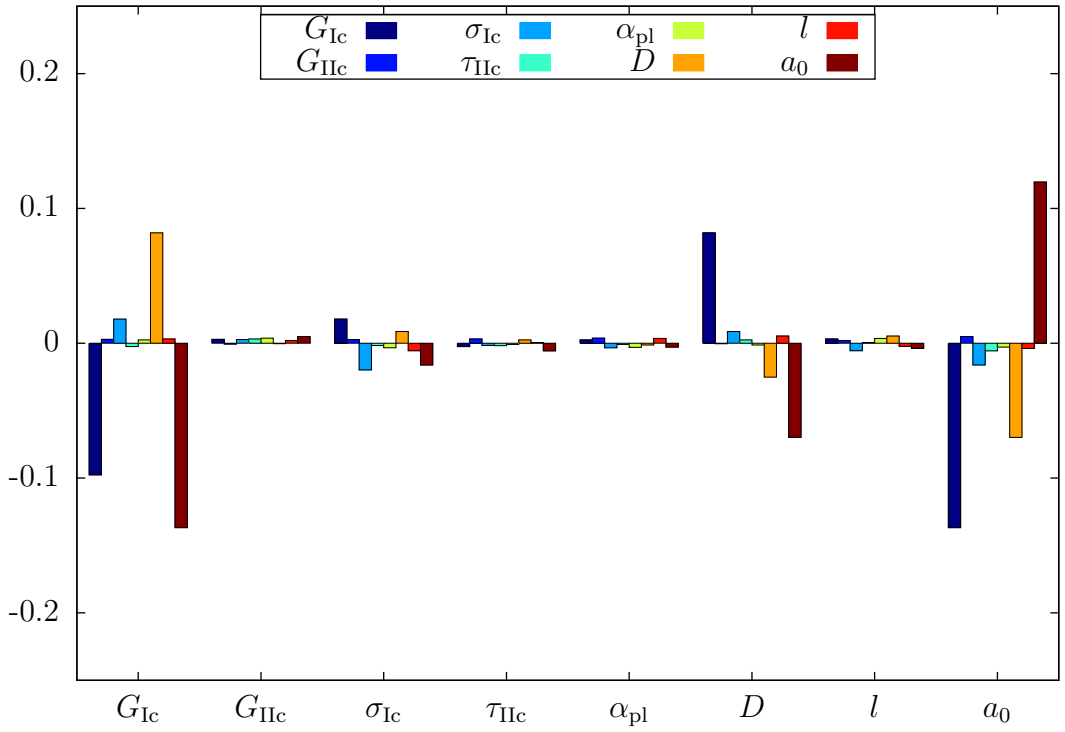

Figure 5.6 Quadratic $\beta_{k,l}$ values for variables in the DCB DACE array

The remaining plots in this subsection (figures 5.8-5.10) illustrate the interactions between the variables G_{Ic}, D, and a_0. For variables with significant interactions, any of an large number of combinations of these parameters will yield the same $\bar{P}_{max}$. For example, since a large initial crack length (a_0) would decrease the values of $\bar{P}_{max}$ relative to a small a_0 (with all other variables fixed) in the same way a lower G_{Ic} would decrease the value of $\bar{P}_{max}$ relative to a larger G_{Ic} (with all other variables fixed). The value $\bar{P}_{max}$ is not uniquely defined by one of the two variables. If adhesive parameters had significant interactions, it would be difficult to map the test data to a unique value G_{Ic}. This difficulty will be observed in the upcoming sections covering the ENF and SLJ tests.

The DCB output ($\bar{P}_{max}$) is relatively insensitive to the form of the traction law (varied by the shape factor α_{pl}). Since the relative magnitude of the linear and quadratic coefficients of $\beta_{k,l}$ are all near zero (see figure 5.5 and figure 5.6), the exact form of the traction law is not important to the outcome of the prediction. This confirms the expectation of an experiment that is dominated by the critical energy release rate. Finally, temperature is important during the DCB test due to its likely effects on stiffness (D). Stiffness uncertainty (in any form) needs to be addressed

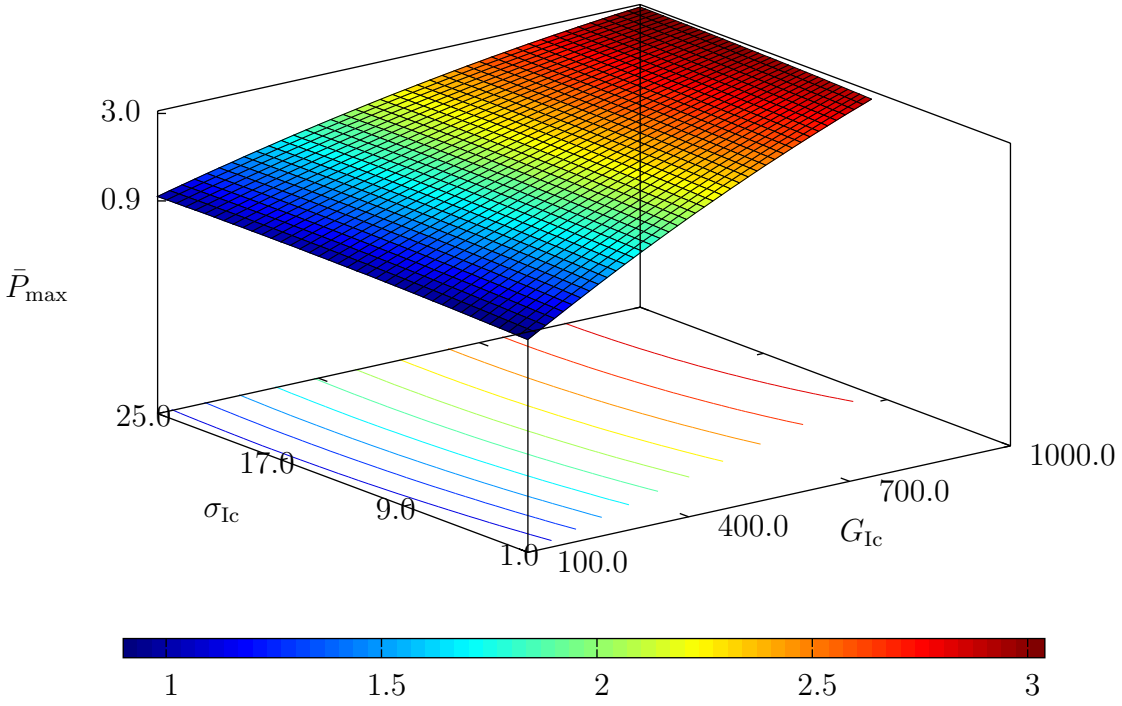

(a) Surface plot

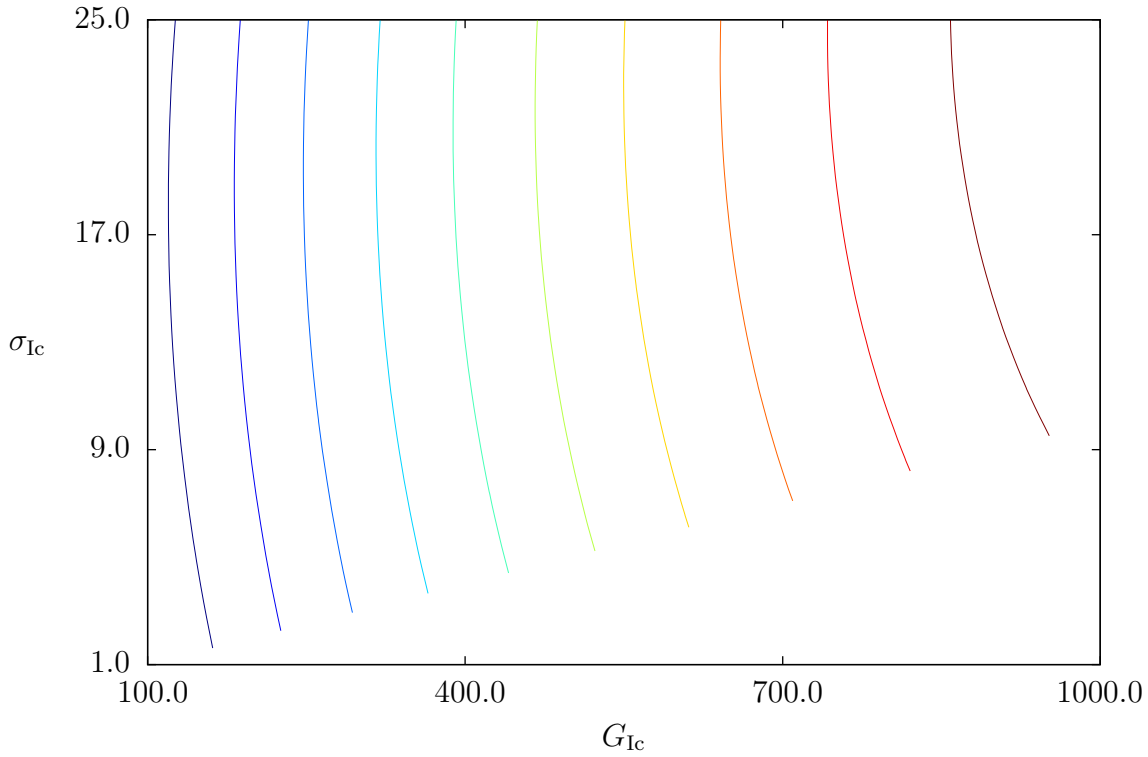

(b) Contour plot

Figure 5.7 Effect of variations of G_{Ic} and σ_{Ic} on DCB $\bar{P}_{\max}$

Table 5.3 Variables in the ENF DACE array

Variable	Min	Max
G_{Ic}	100 J/m^2	1000 J/m^2
G_{IIc}	100 J/m^2	2000 J/m^2
σ_{Ic}	1.5 MPa	25 MPa
τ_{IIc}	2.1 MPa	25 MPa
α_{pl}	0%	50%
D	6.56 Nm^2	21.2 Nm^2
$\frac{a_0}{l}$	40%	90%
μ	0	.50
$2\,l$	96.5 mm	107 mm

during data reduction.

5.3 Sensitivity analysis for the end notch flexure test

In this section, the end notch flexure test is explored. The geometry of the ENF specimen is shown in figure 5.11 as well as the geometric variables in the DACE array. As in the prior section, the four primary adhesive parameters are included in addition to the geometric variables and the shape factor for the TTL. These variables and their ranges are listed in table 5.3. Properties of the FE model are given in table 5.2(b) and a typical FE mesh is shown in figure 5.1.

The principal objective of the ENF test is to determine the value of G_{IIc} for a given adhesive. The accepted method for determining G_{IIc} from an experiment is the CC method and the value of G_{IIc} is assumed proportional to $\bar{P}_{\max}$. Under the assumptions of the CC method, the value of τ_{IIc} has no effect on the value of $\bar{P}_{\max}$ and therefore is not a factor in the calculation. In this section, that assumption is found to be insufficient in the context of FE cohesive zone modeling.

The linear $\beta_{k,l}$ values for the DACE variables are shown in figure 5.12 and the quadratic $\beta_{k,l}$ coefficients are shown in figure 5.13. In the ENF test, G_{IIc} is the most significant of the adhesive parameters; D and $\frac{a_0}{l}$ also have significance. These are *expected* sensitivities based on classical analysis of the ENF specimen. The τ_{IIc} parameter also has a significant effect on $\bar{P}_{\max}$. This important conclusion can be visualized in two ways. First, the linear $\beta_{k,l}$ coefficient magnitude (figure 5.12) is approximately one

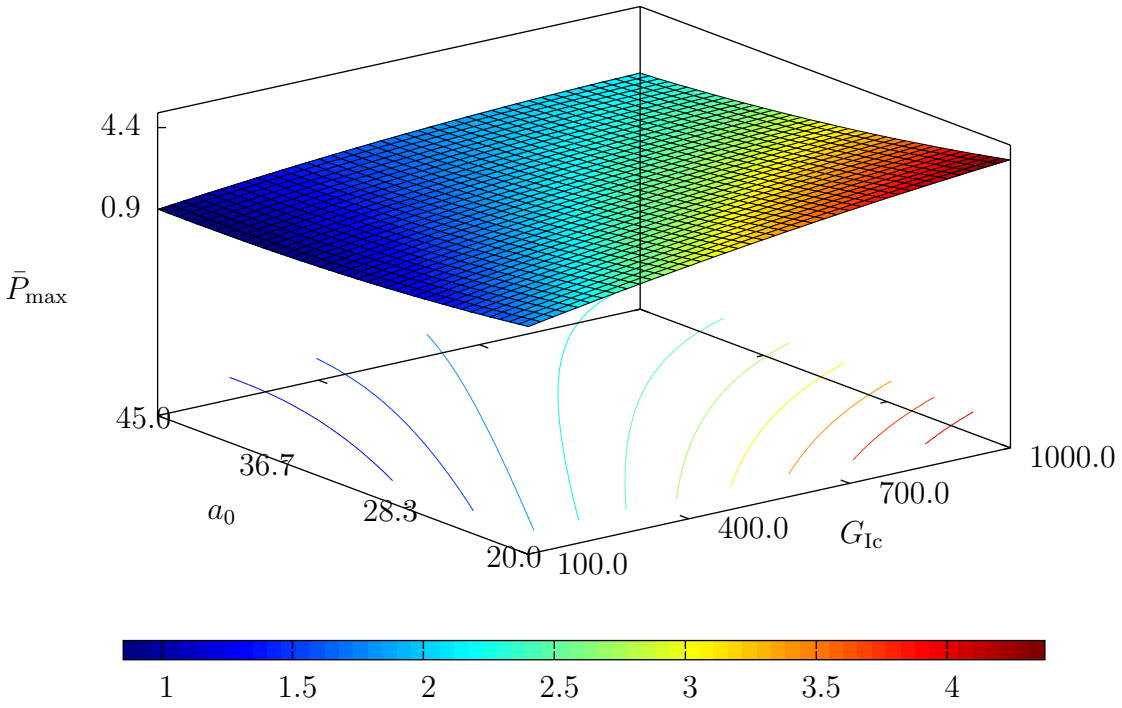

(a) Surface plot

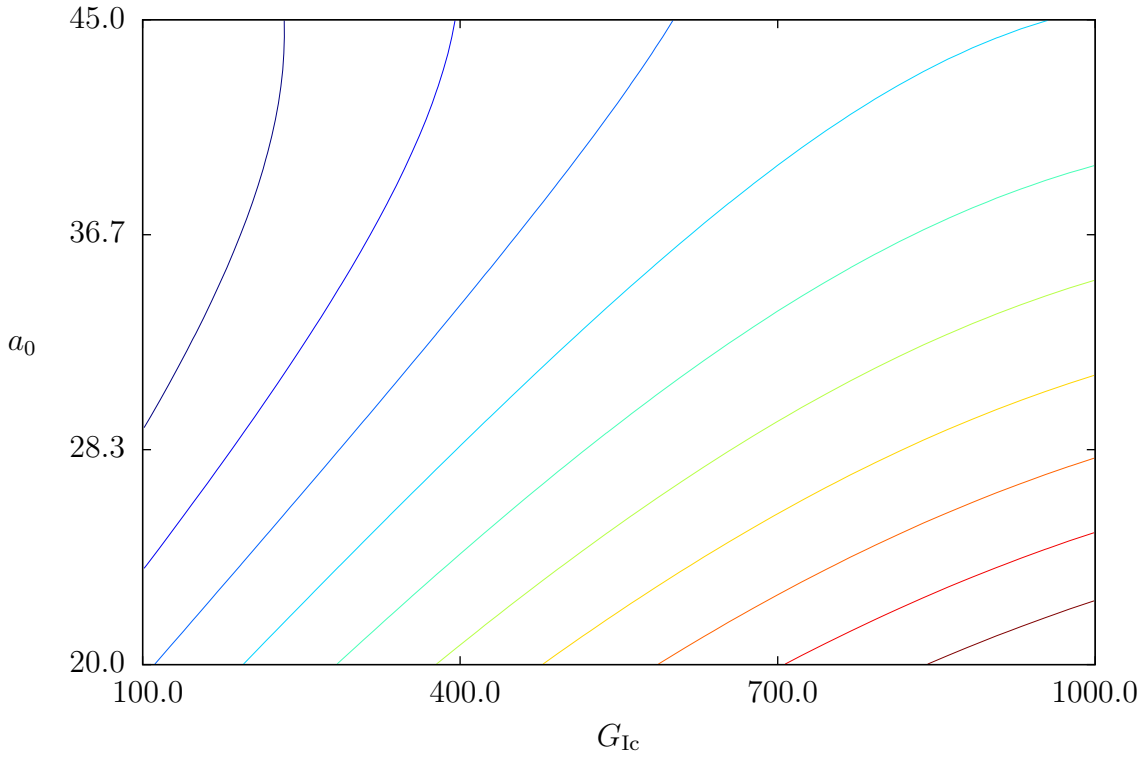

(b) Contour plot

Figure 5.8 Effect of variations of G_{Ic} and a_0 on DCB $\bar{P}_{\max}$

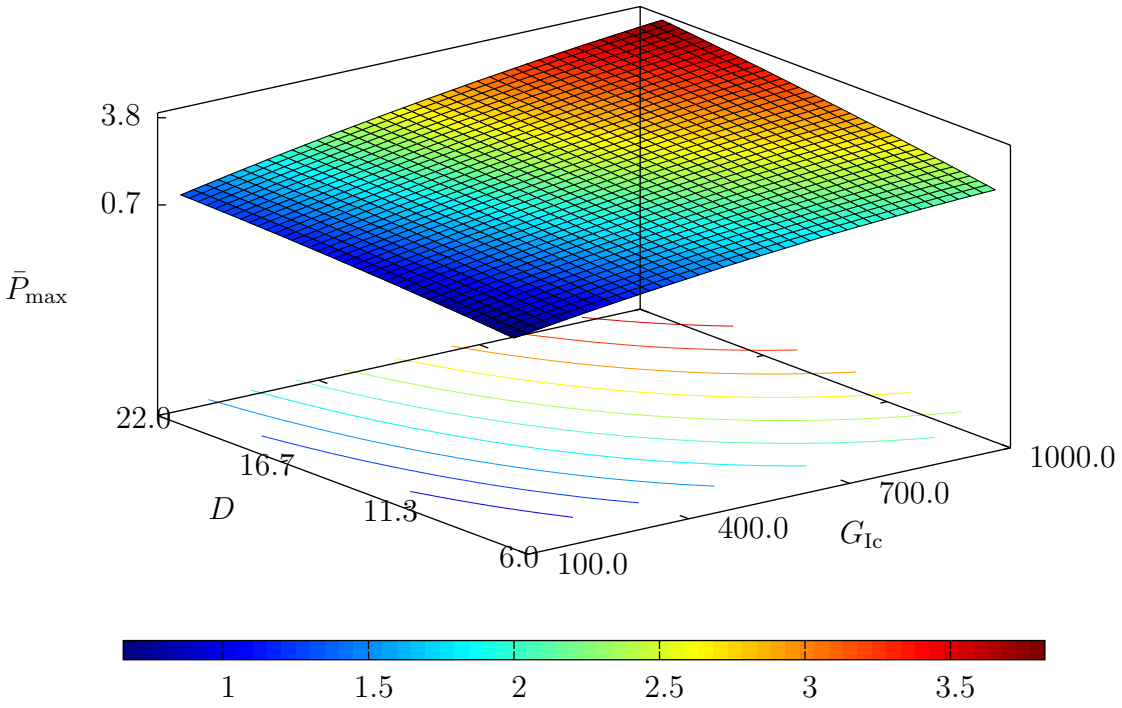

(a) Surface plot

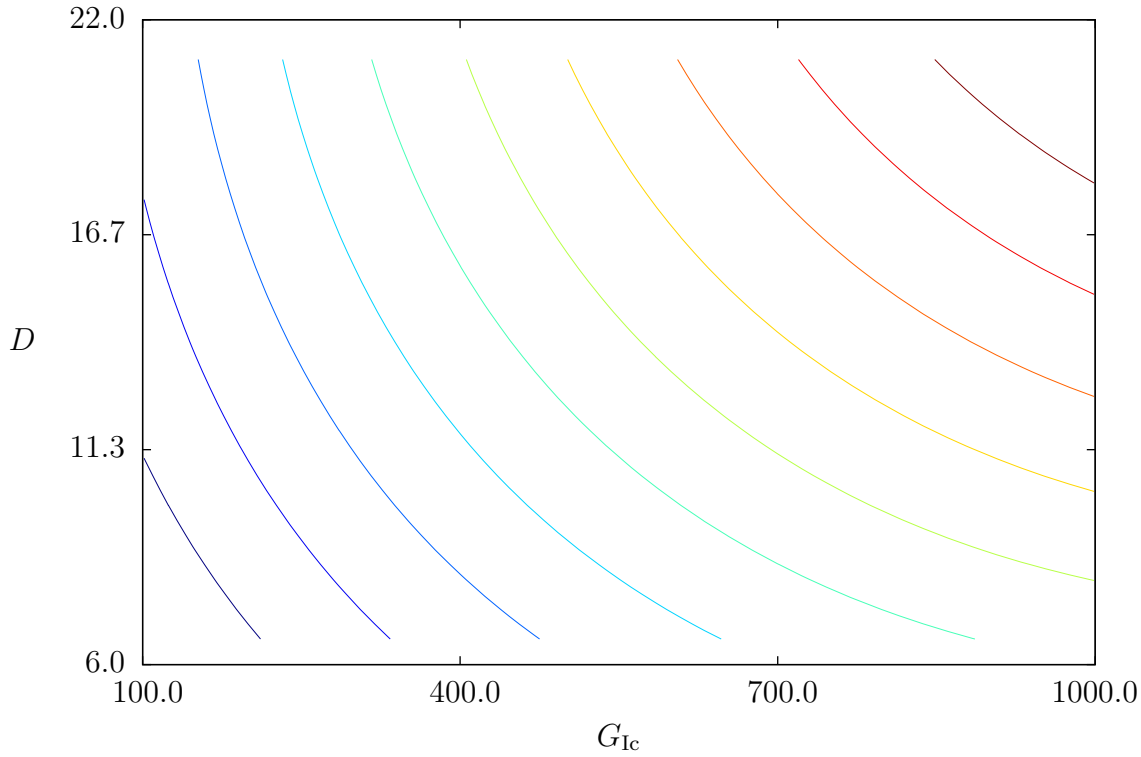

(b) Contour plot

Figure 5.9 Effect of variations of G_{Ic} and D on DCB $\bar{P}_{\max}$

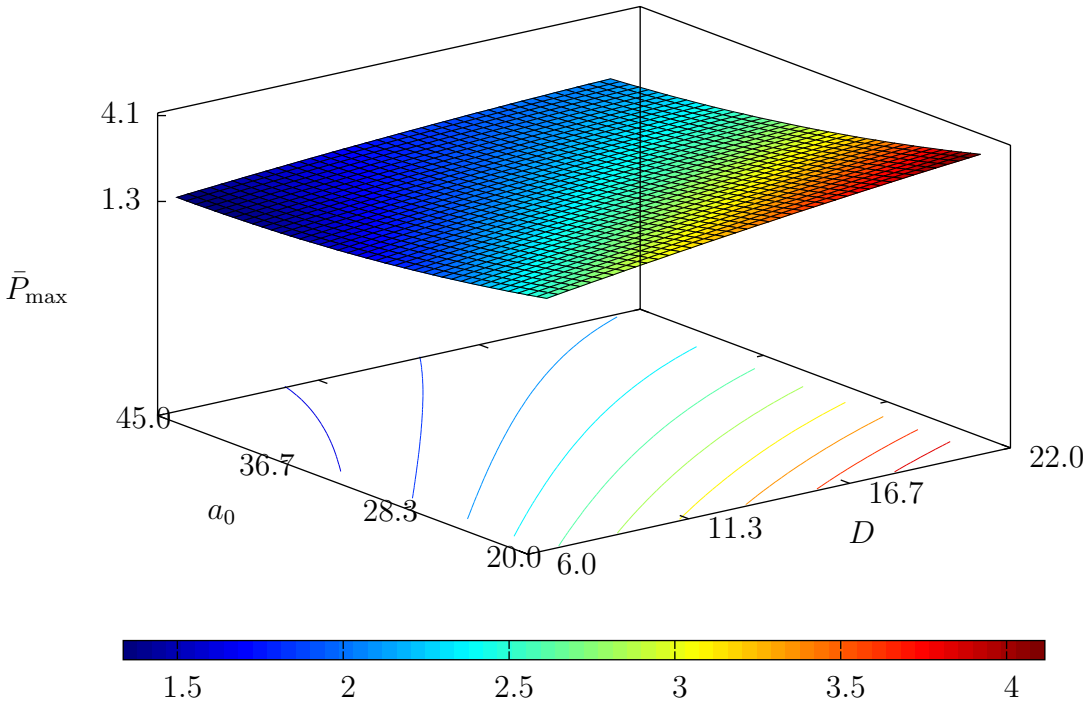

(a) Surface plot

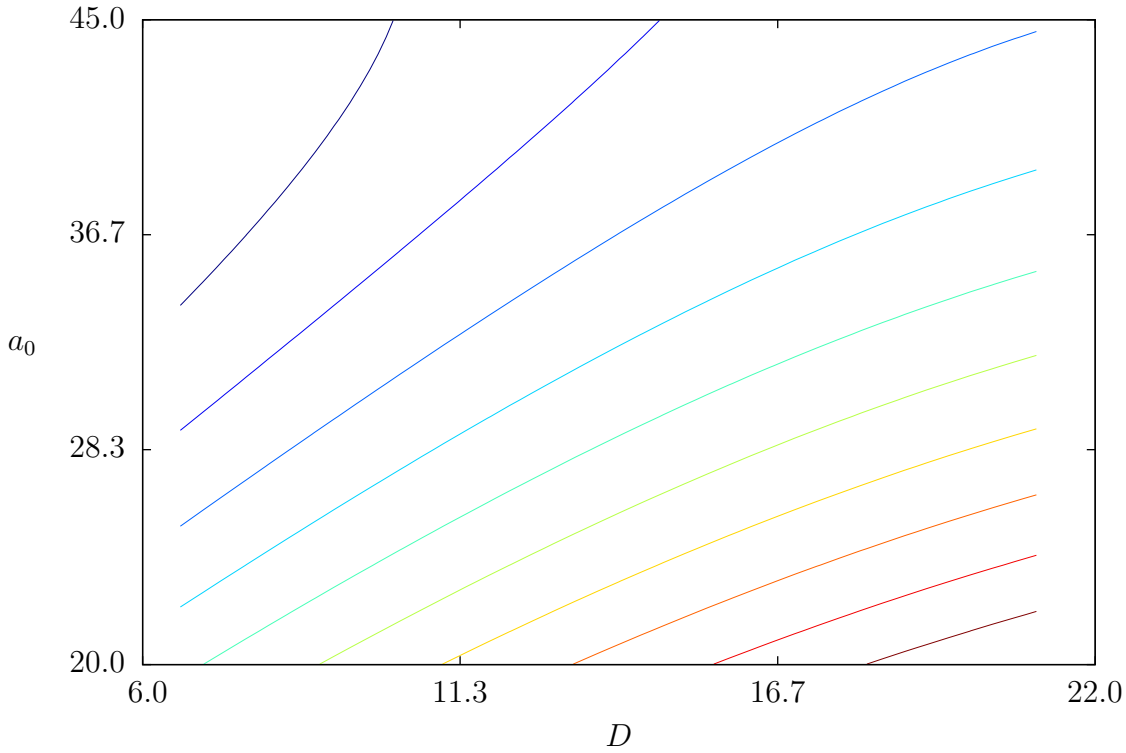

(b) Contour plot

Figure 5.10 Effect of variations of D and a_0 on DCB $\bar{P}_{\max}$

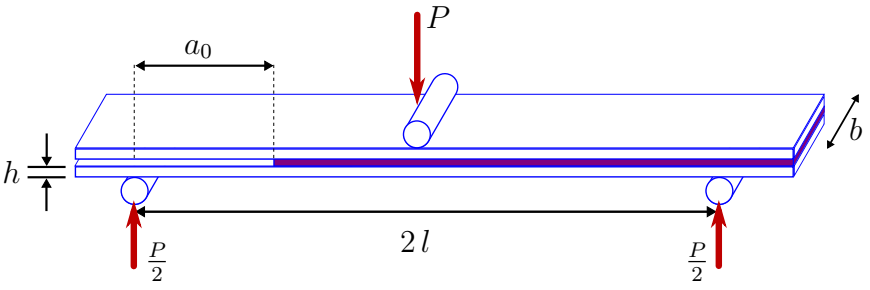

Figure 5.11 ENF specimen geometry

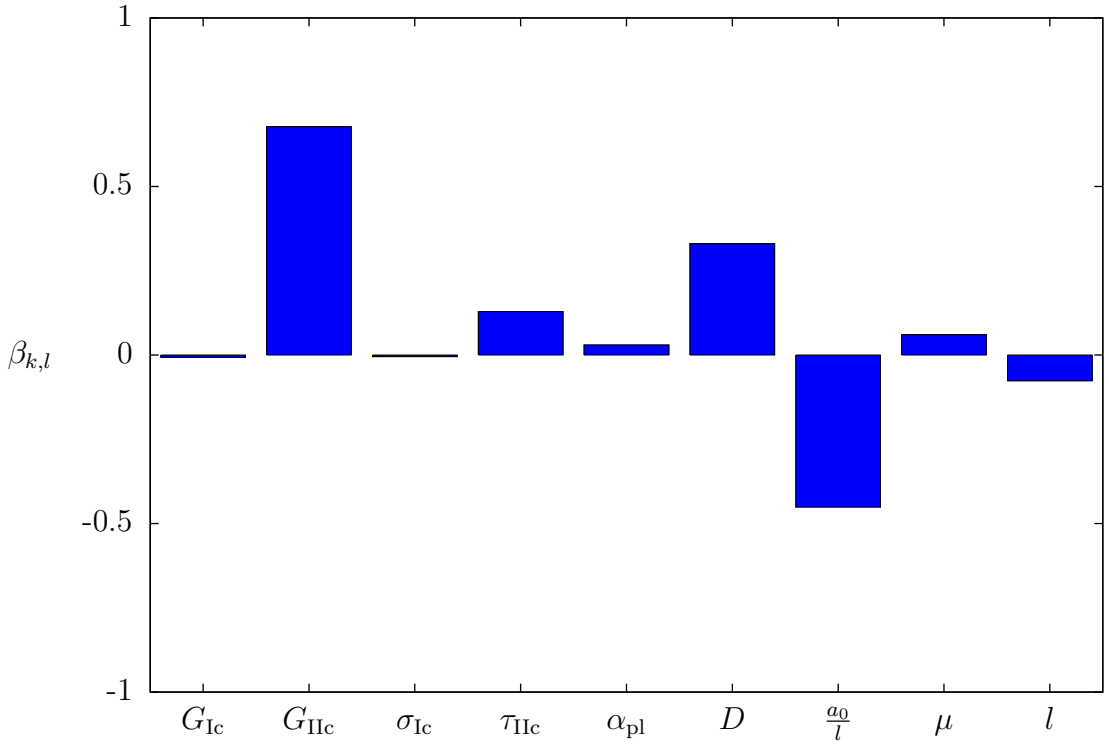

Figure 5.12 Linear $\beta_{k,l}$ values for variables in the ENF DACE array

fifth that of the $\beta_{k,l}$ coefficient of G_{IIc} (and approximately one third of the coefficients for D and $\frac{a_0}{l}$). Furthermore, the strength of the interaction between τ_{IIc} and $\frac{a_0}{l}$ is as strong as that between G_{IIc} and D (as revealed in figure 5.13). Based on these observations, the effect of τ_{IIc} on the ENF test *should not be neglected* when mapping the test results into a set of inputs for future models. At a minimum, a suitable test for τ_{IIc} (such as the SLJ test) must also be considered when preparing the adhesive constitutive model from the results of the ENF test.

This conclusion is more concretely illustrated in figure 5.14. In figure 5.14(a), the value of $\bar{P}_{\max}$ is plotted on the z axis while the range of values of G_{IIc} and τ_{IIc} are plotted on the x and y axes. In contrast to figure 5.7(b), the contour lines in

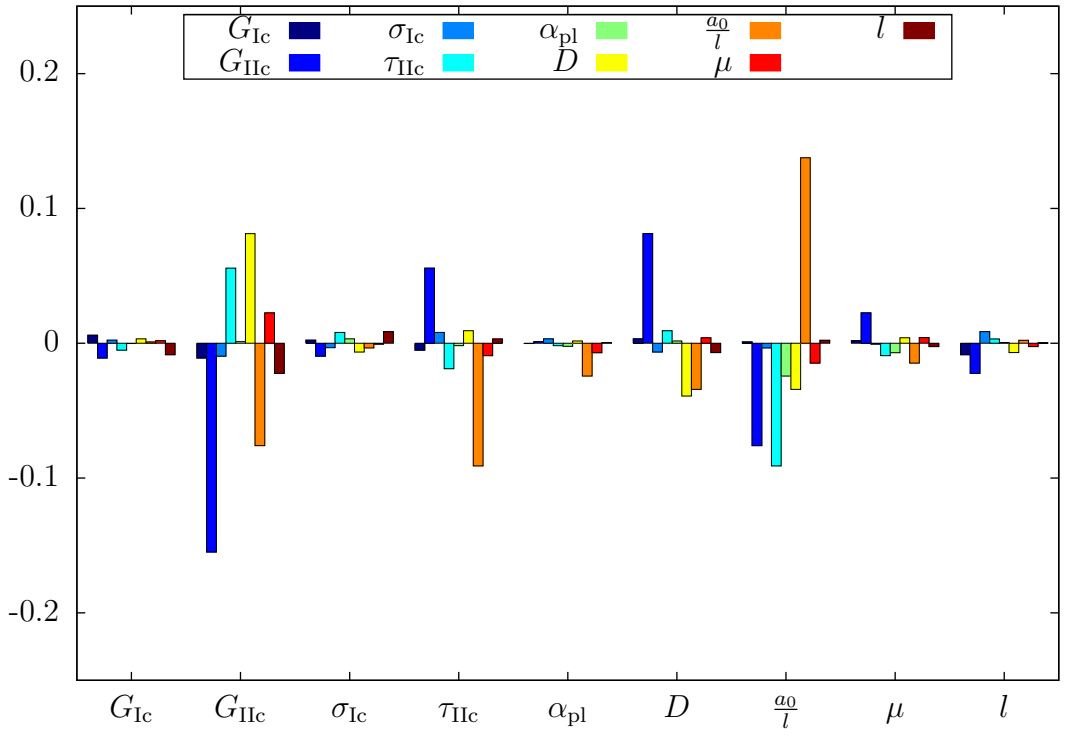

Figure 5.13 Quadratic $\beta_{k,l}$ values for variables in the ENF DACE array

figure 5.14(b) are *not* predominately vertical. A given value of $\bar{P}_{\max}$ can be achieved with any suitably chosen pair of (G_{IIc}, τ_{IIc}). The ENF test is *not* ideal for determining G_{IIc} and presents a challenge in mapping the experimental outcome back to a set of constitutive parameters. This mapping should be done in conjunction with the SLJ test (or another suitable test) in order to choose an appropriate pairing of constitutive parameters.

The effect of temperature is relevant to the stiffness parameter (D) in the ENF test. Although the value of $\bar{P}_{\max}$ is sensitive to the stiffness, this can be accounted for via CC techniques with relative ease. Also, the traction law is relatively unimportant to $\bar{P}_{\max}$ (as in the DCB test). In figure 5.12, the $\beta_{k,l}$ value for the shape parameter (α_{pl}) is relatively small. Further, no critical interactions are seen in figure 5.13.[14]

Although not explicitly described in the text, figures 5.15 and 5.16 are included in order to illustrate the interactions between the significant model inputs and the value of $\bar{P}_{\max}$ for the ENF test.

[14]The traction law is somewhat more important in the ENF test than the DCB test. This is expected in a test that shows some dependency on the stress parameters. The shape factor (α_{pl}), however, is still insignificant relative to the other variables.

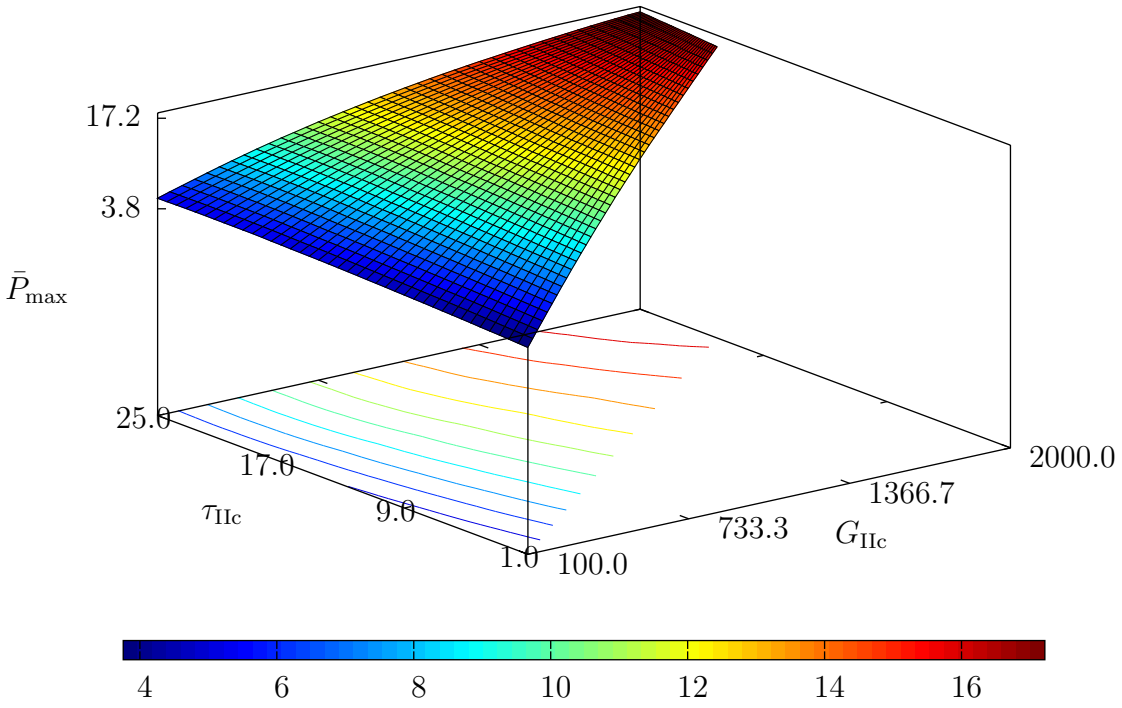

(a) Surface plot

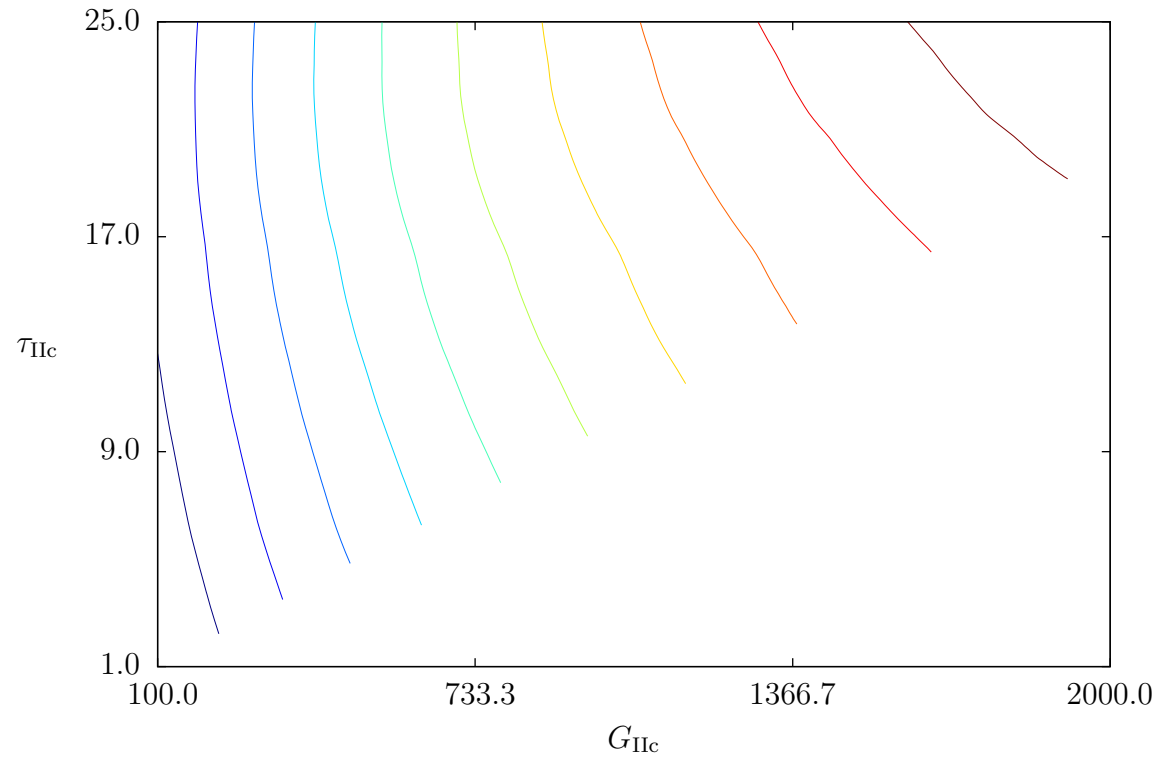

(b) Contour plot

Figure 5.14 Effect of variations of G_{IIc} and τ_{IIc} on ENF $\bar{P}_{\max}$

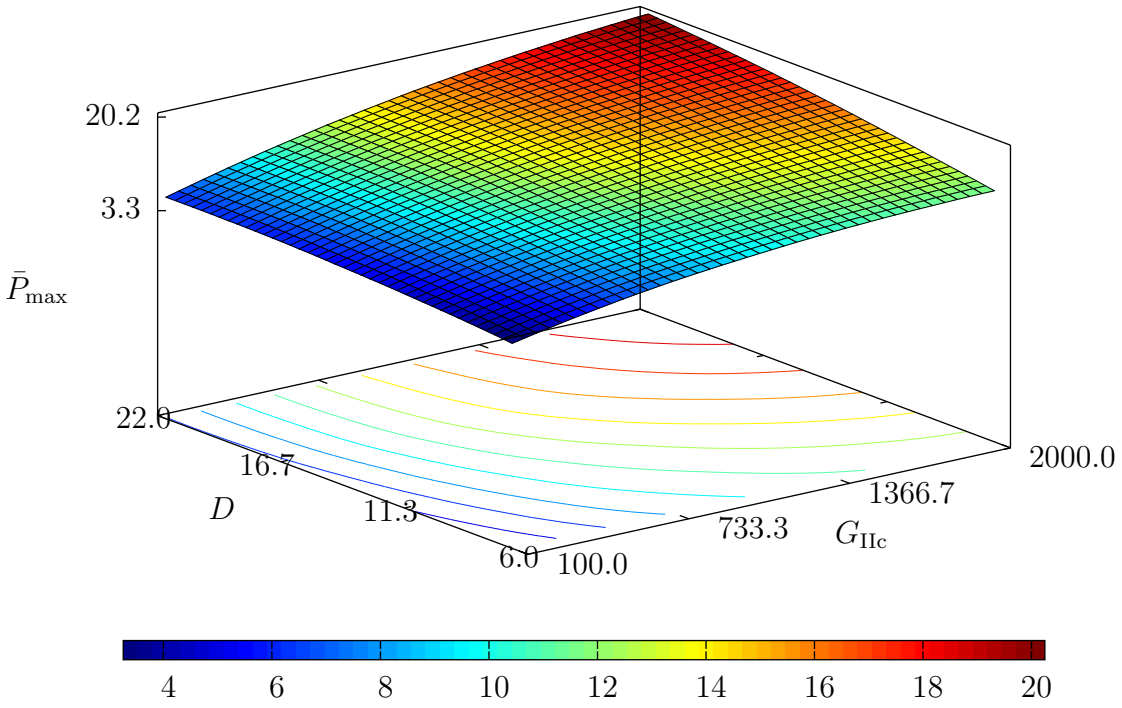

(a) Surface plot

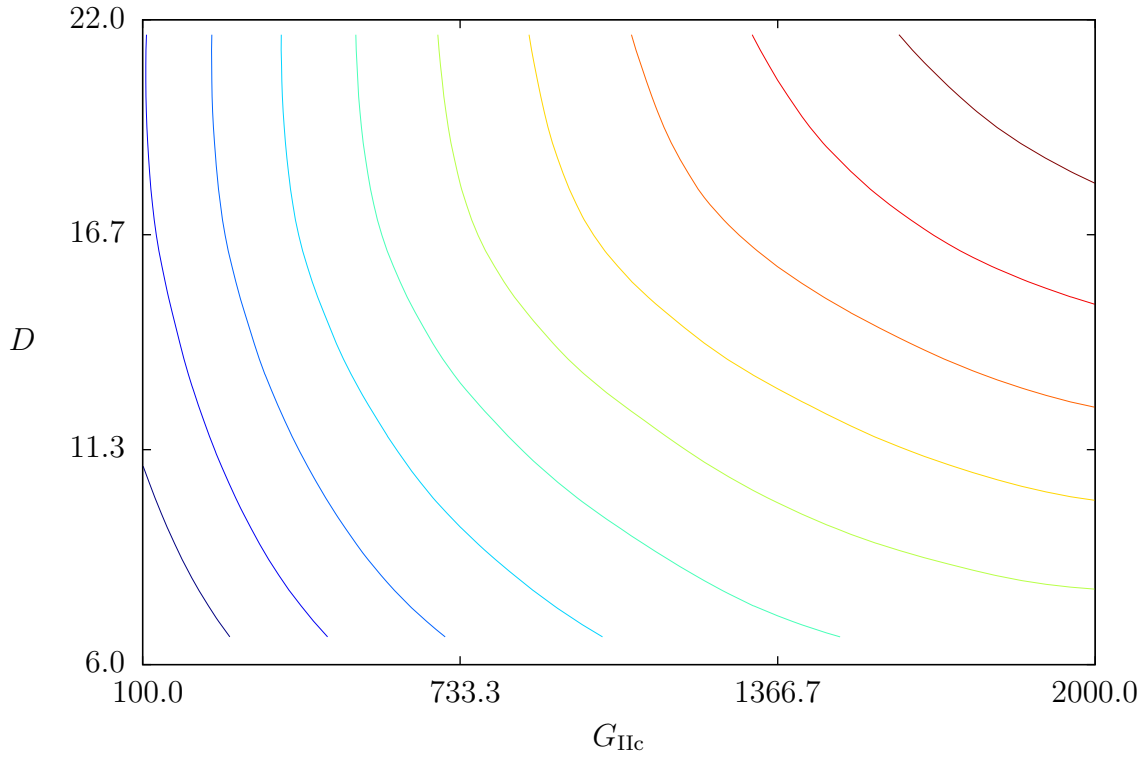

(b) Contour plot

Figure 5.15 Effect of variations of G_{IIc} and D on ENF $\bar{P}_{\max}$

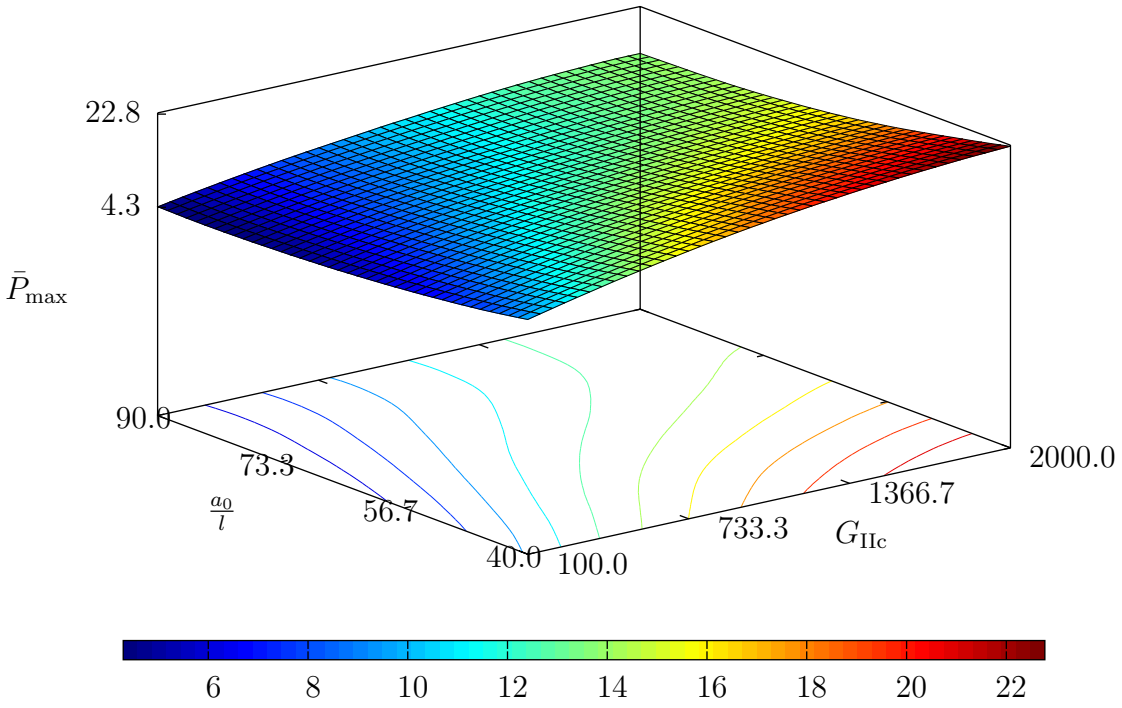

(a) Surface plot

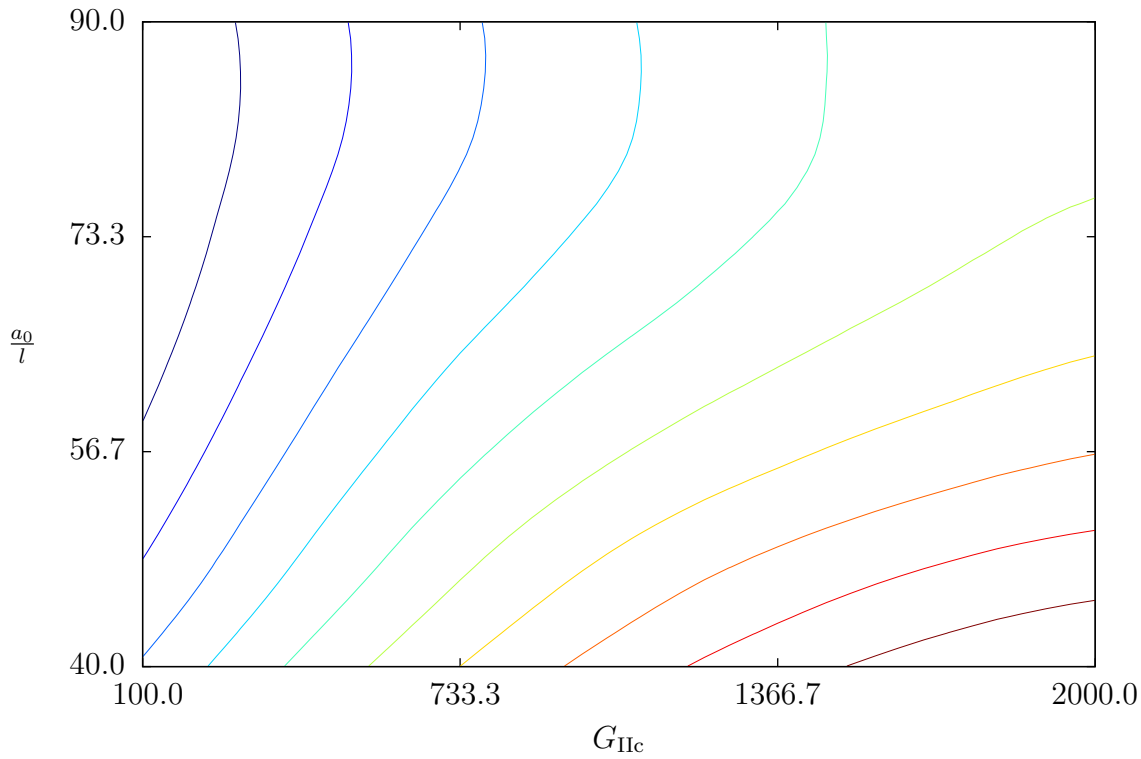

(b) Contour plot

Figure 5.16 Effect of variations of G_{IIc} and $\frac{a_0}{l}$ on ENF $\bar{P}_{\max}$

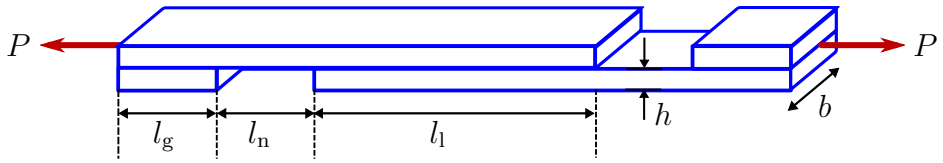

Figure 5.17 SLJ specimen geometry

Table 5.4 Variables in the SLJ DACE array

Variable	Min	Max
G_{Ic}	100 J/m^2	1000 J/m^2
G_{IIc}	100 J/m^2	2000 J/m^2
σ_{Ic}	1.5 MPa	25 MPa
τ_{IIc}	2.1 MPa	25 MPa
α_{pl}	0%	50%
E	59.5 GPa	80.5 GPa
l_l	10 mm	40 mm
l_g	2 mm	50 mm
l_n	2 mm	50 mm
h	1.06 mm	1.44 mm

5.4 Sensitivity analysis for the single lap joint test

Though it is viewed as a test for determining the *comparative apparent* value of τ_{IIc}, it is clear from section 5.3 that the SLJ test could play a more substantial role in determining the Mode II parameters in an adhesive characterization. To understand that role more fully, a sensitivity analysis is applied to the SLJ test. The geometric variables are shown in figure 5.17 and are used in addition to the adhesive constitutive parameters. The range of those variables is established in table 5.4. A representative model result is shown in figure 5.2(a) and properties of the model are given in table 5.2(c).

The linear correlation coefficients $\beta_{k,l}$ for the SLJ test are shown in figure 5.18. There are several parameters that have a significant effect on the value of $\bar{P}_{max}$. As expected, the two largest $\beta_{k,l}$ coefficients are the lap length (l_l) and the critical shear stress (τ_{IIc}). The critical strain energy release rate (G_{IIc}), however, is almost as important as τ_{IIc}. Finally, the Mode I critical strain energy release rate (G_{Ic}) is also important due to the eccentric loading of the specimen and mixed-mode field at the crack tip. In contrast to the statements in [13], it is G_{Ic} (not σ_{Ic}) that has significant effect on the failure of the SLJ specimen.

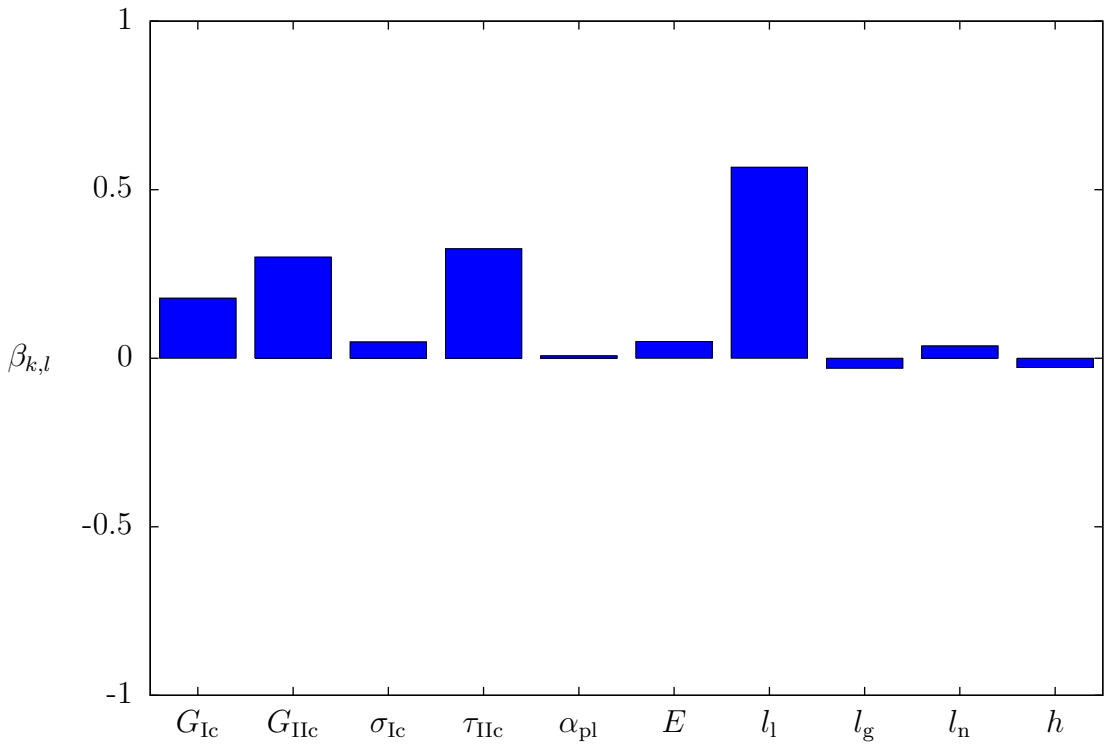

Figure 5.18 Linear $\beta_{k,l}$ values for variables in the SLJ DACE array

The most important interaction (for establishing a constitutive law) is between G_{IIc} and τ_{IIc}; it is illustrated in figure 5.20. For low values of G_{IIc}, the maximum load is dependent primarily on τ_{IIc}. In figure 5.20(b), this is seen as contours that are primarily vertical. As the value of G_{IIc} increases, however, the contour lines become more horizontal and the critical energy release rate becomes the dominant parameter for determining $\bar{P}_{\max}$. In this regime, the SLJ test in isolation would be ineffective in determining the value of τ_{IIc}.

A second interaction, between G_{Ic} and G_{IIc}, is illustrated in figure 5.21. For low values of G_{Ic}, the failure mode is either Mode I or mixed-mode such that the value of $\bar{P}_{\max}$ is limited by the value of G_{Ic}. For values of G_{Ic} over a critical value, however, this failure mode no longer dominates and the value of $\bar{P}_{\max}$ becomes more dependent on the value of τ_{IIc} and other parameters. A similar effect is seen in figures 5.22(a) and 5.22(b) relating G_{Ic} to τ_{IIc}.

Figure 5.25(b) illustrates the interaction between τ_{IIc} and l_{l}; the contour lines are almost diagonal. This is expected since the value of $\bar{P}_{\max}$ should increase with τ_{IIc} or l_{l} (for low values of l_{l}). A similar interaction is seen between G_{IIc} and l_{l} as illustrated in figure 5.24(b). The implicit variable temperature is most likely to affect the stiffness

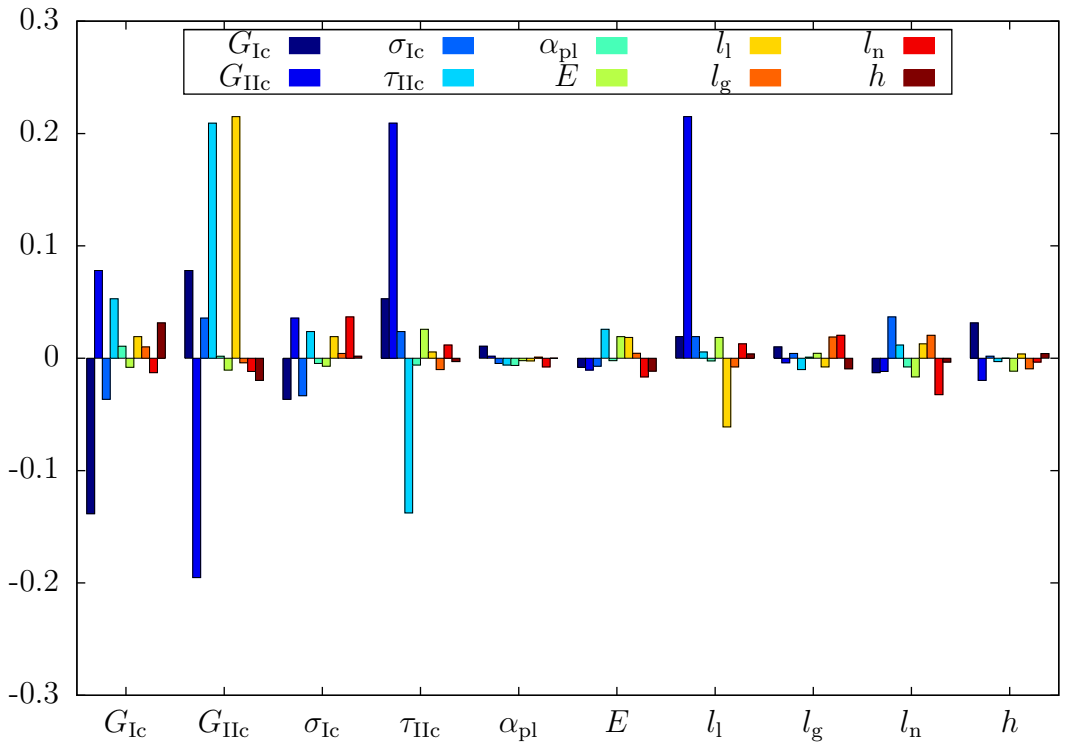

Figure 5.19 Quadratic $\beta_{k,l}$ values for variables in the SLJ DACE array

of the lap joint through the modulus parameter E. The sensitivity of $\bar{P}_{\max}$ to E, however, is relatively small. Therefore, the SLJ test is not likely to have uncertainties related to temperature.

In short, three out of the four primary adhesive constitutive parameters have critical importance in the SLJ test, despite its traditional use as a method of determining one parameter (τ_{IIc}). Therefore, it is necessary to examine G_{IIc} (based on the ENF test) and G_{Ic} (based on the DCB test) to properly interpret the results of a SLJ test. Only appropriate parameter sets can be used to to predict the values of $\bar{P}_{\max}$ in all three tests.

5.5 Interpretation of experimental results

It is evident that the interactions of the constitutive parameters should be accounted when mapping the experimental results into a set of constitutive inputs for FE analysis. This is a significant departure from traditional practice where parameters are considered properties that can be uniquely defined by a single test.

A mapping method for data reduction is described next. First, the Mode I param-

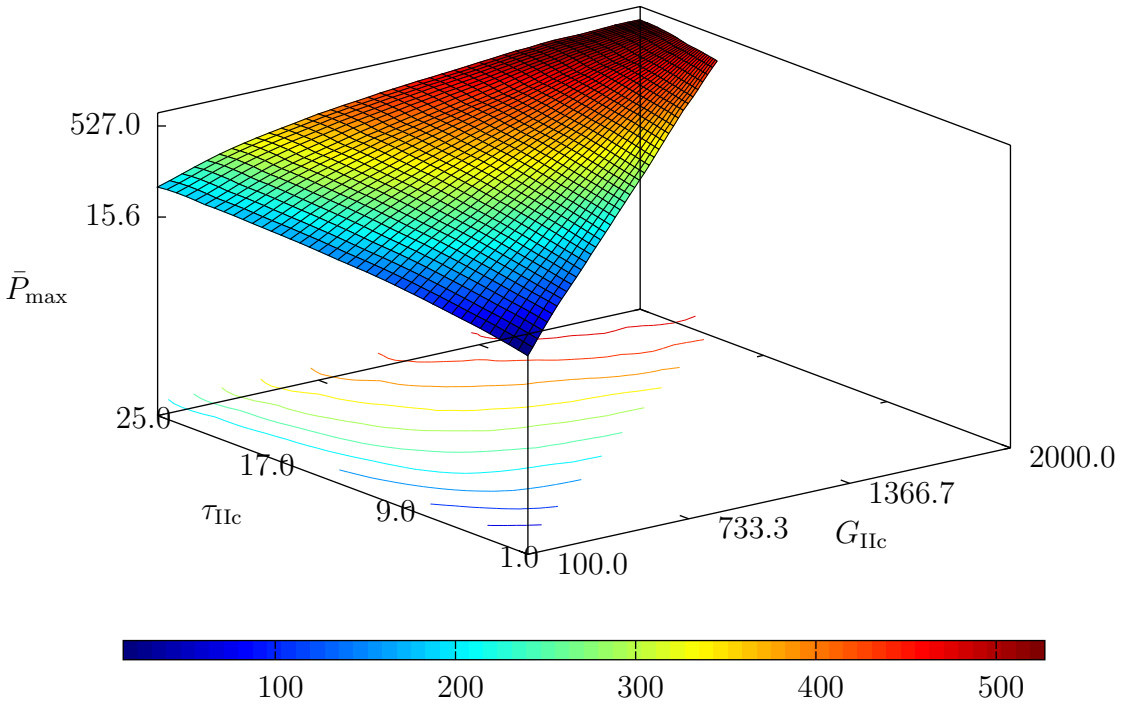

(a) Surface plot

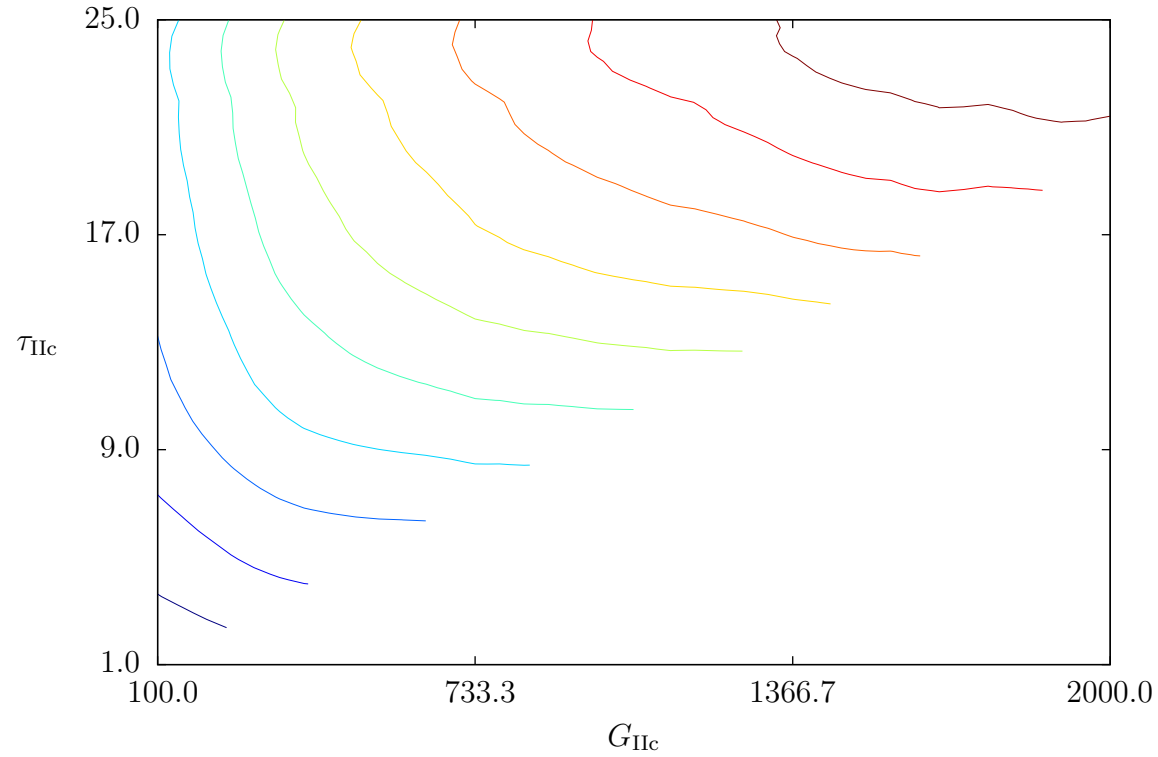

(b) Contour plot

Figure 5.20 Effect of variations of G_{IIc} and τ_{IIc} on SLJ $\bar{P}_{\max}$

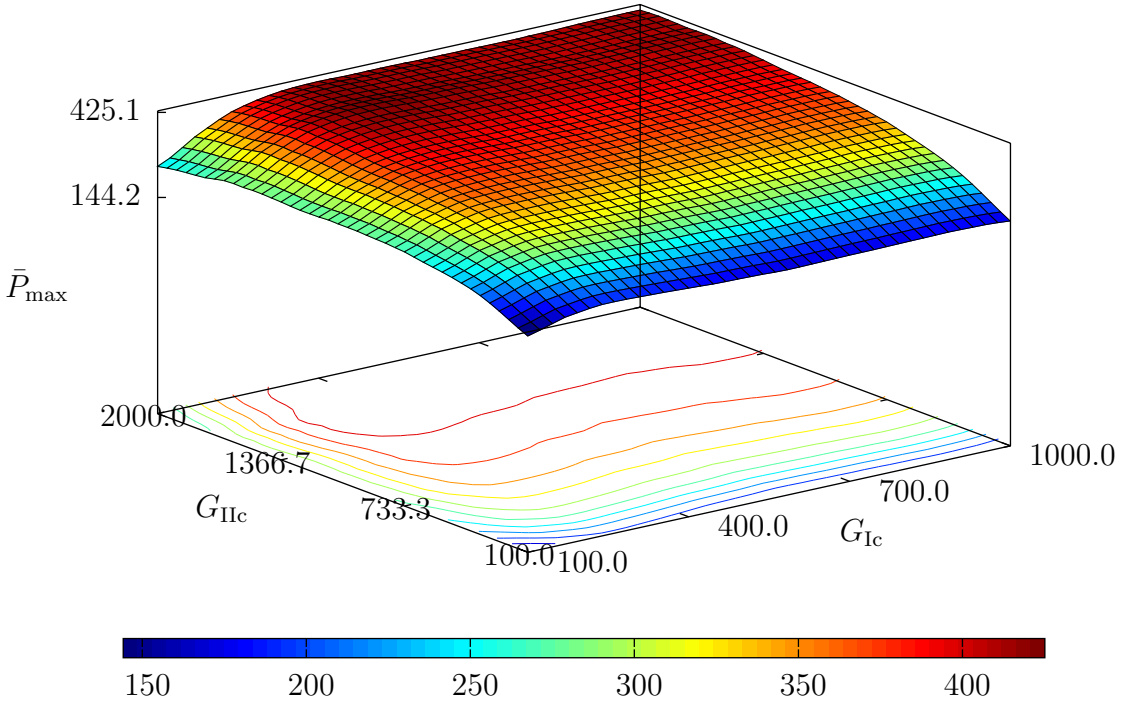

(a) Surface plot

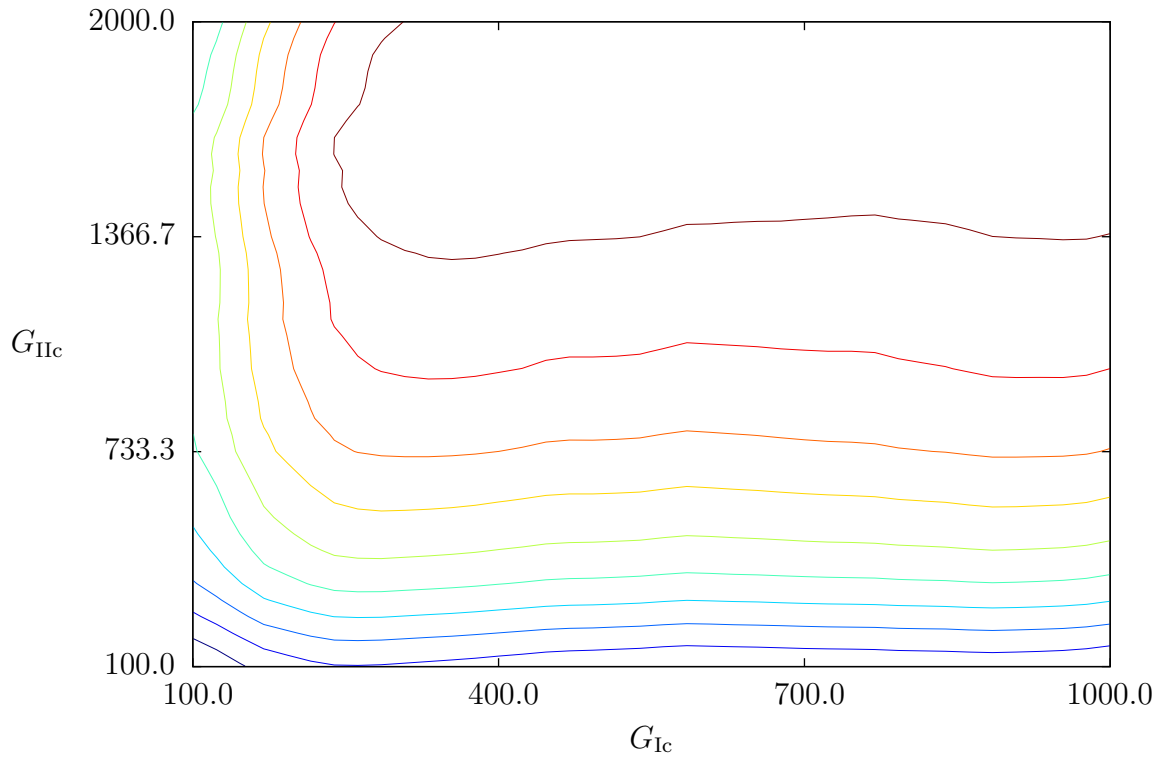

(b) Contour plot

Figure 5.21 Effect of variations of G_{Ic} and G_{IIc} on SLJ $\bar{P}_{\max}$

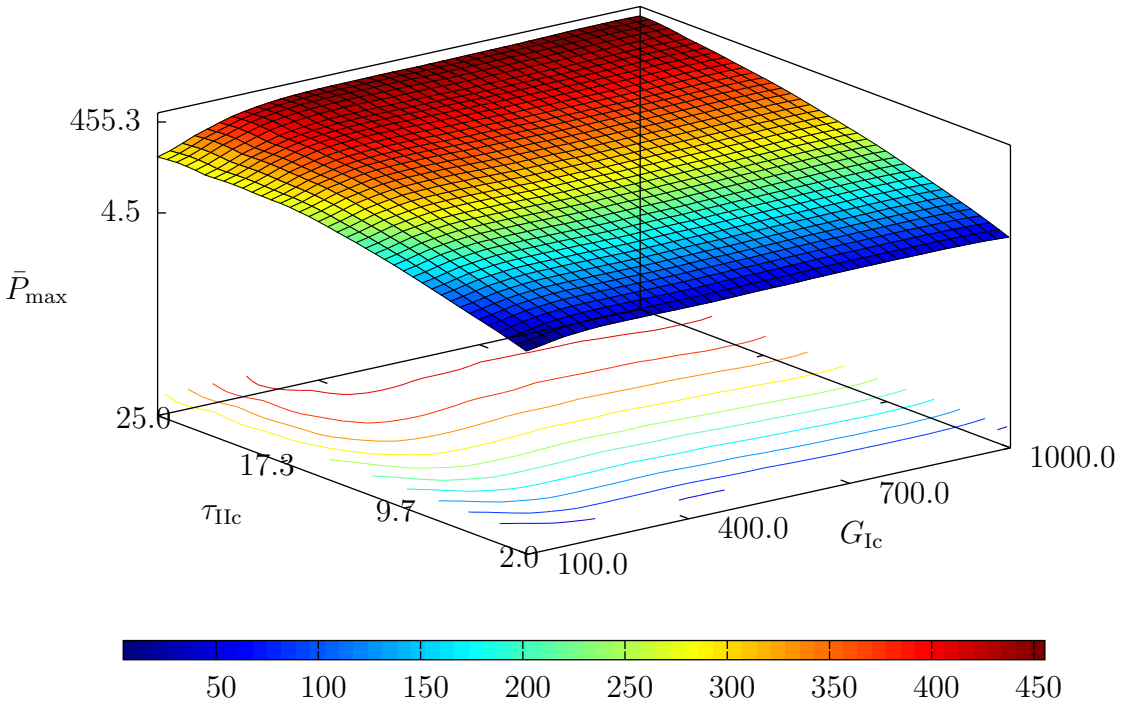

(a) Surface plot

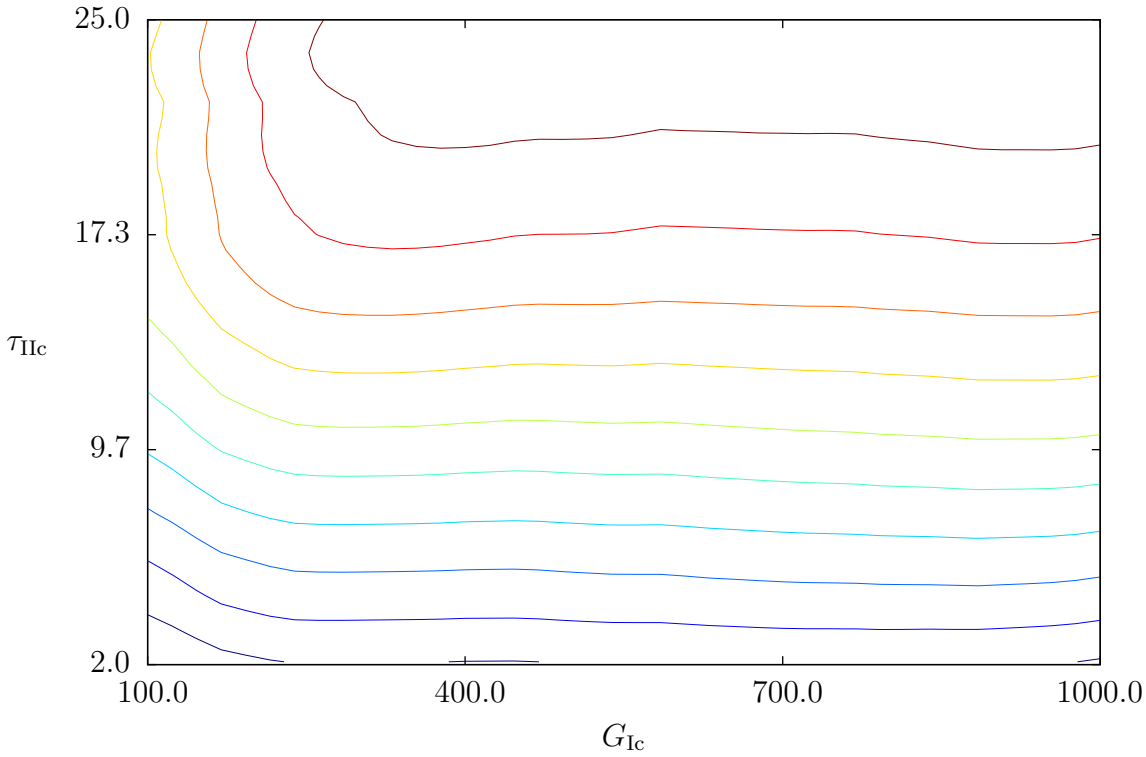

(b) Contour plot

Figure 5.22 Effect of variations of G_{Ic} and τ_{IIc} on SLJ $\bar{P}_{\max}$

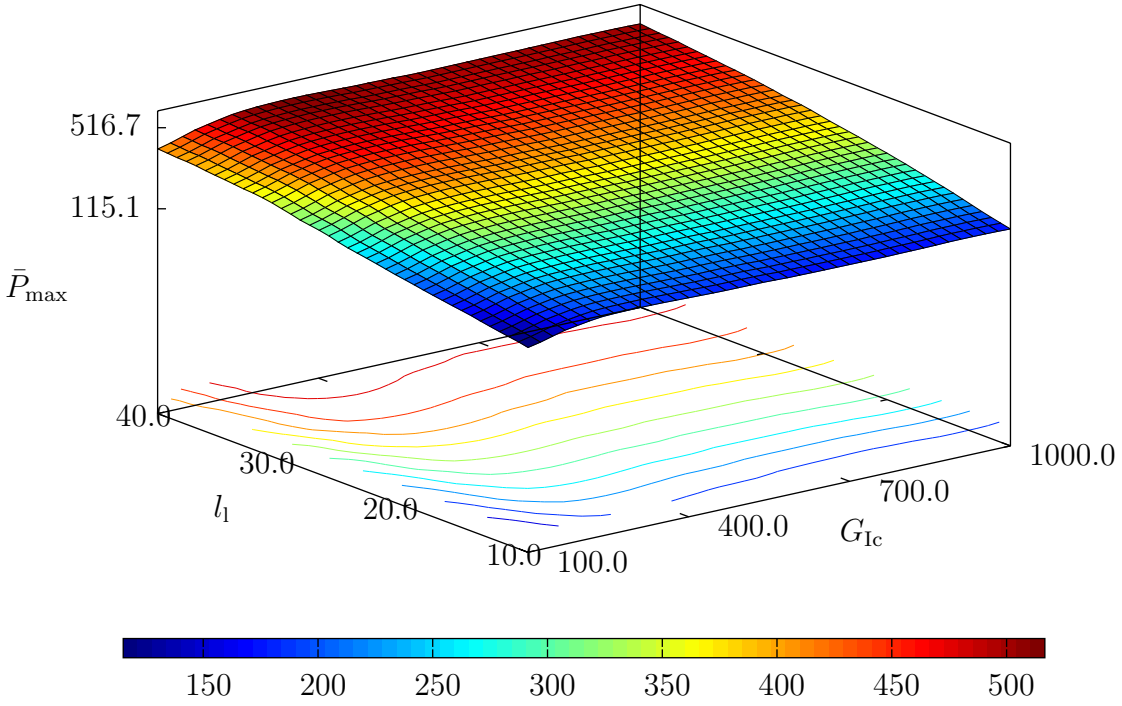

(a) Surface plot

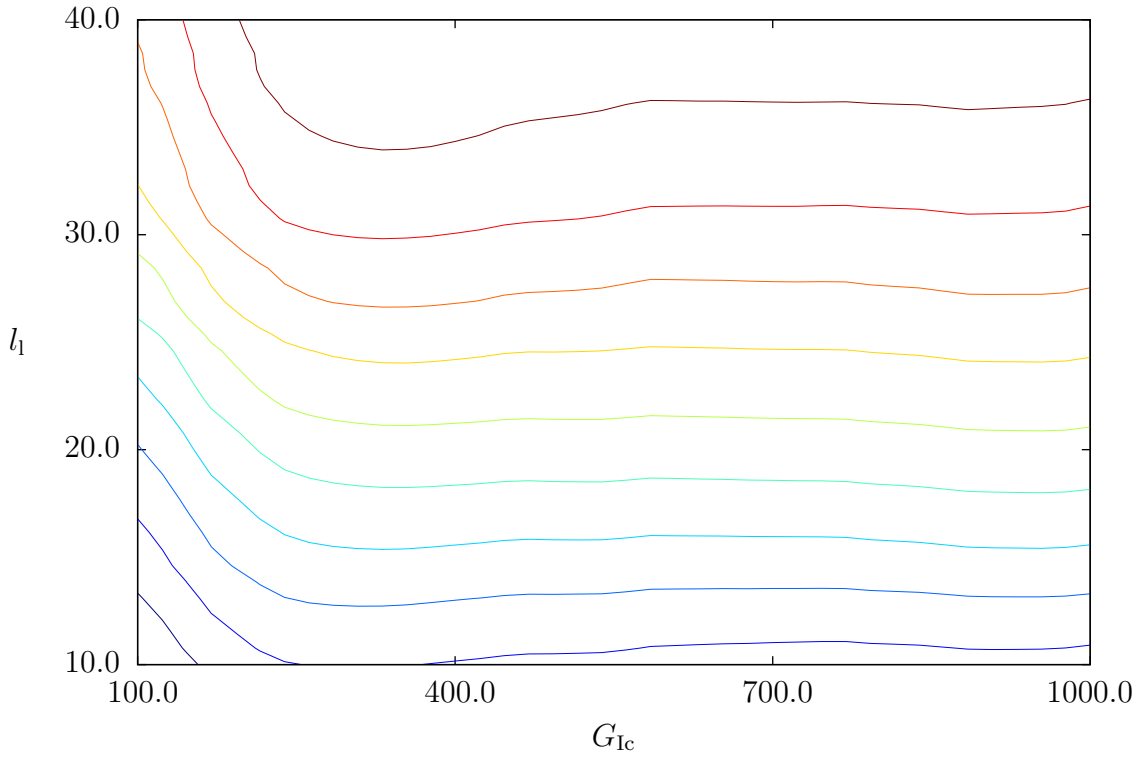

(b) Contour plot

Figure 5.23 Effect of variations of G_{Ic} and l_{l} on SLJ $\bar{P}_{\max}$

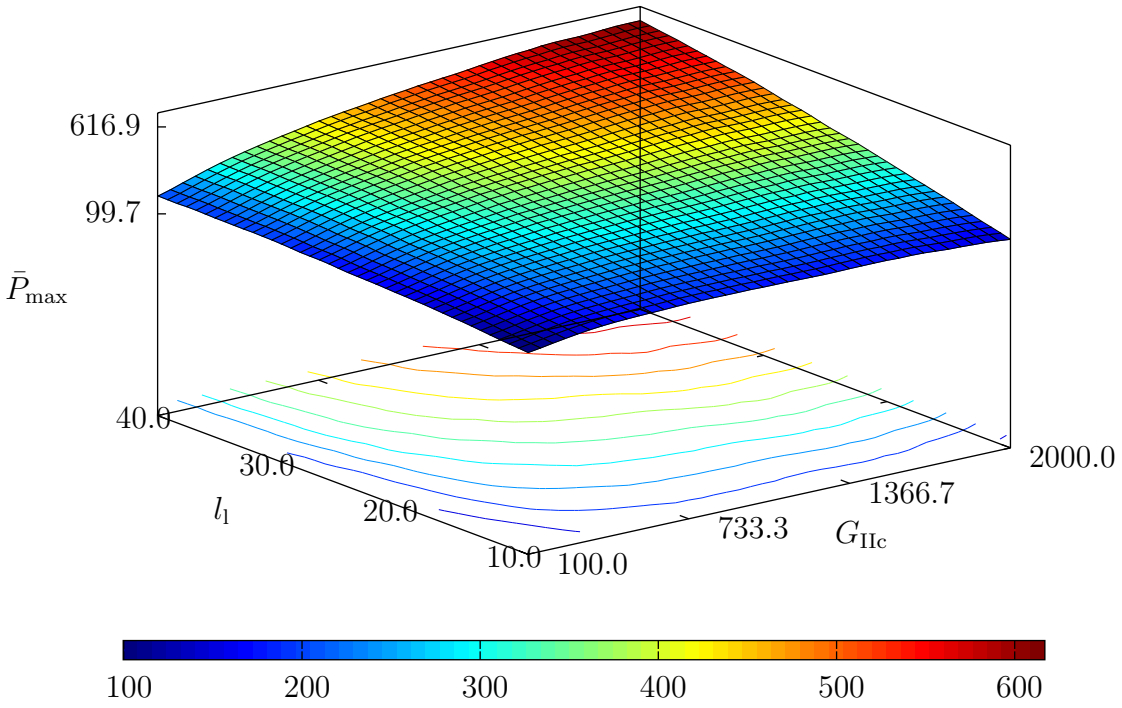

(a) Surface plot

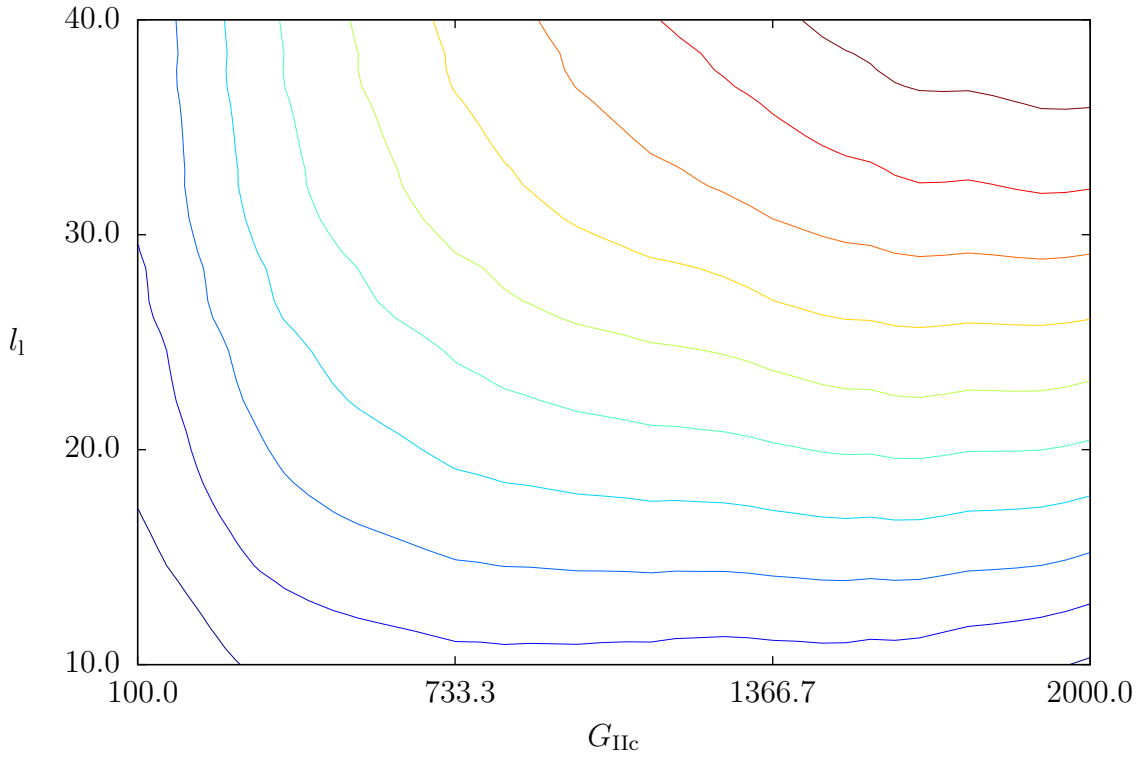

(b) Contour plot

Figure 5.24 Effect of variations of G_{IIc} and l_1 on SLJ $\bar{P}_{\max}$

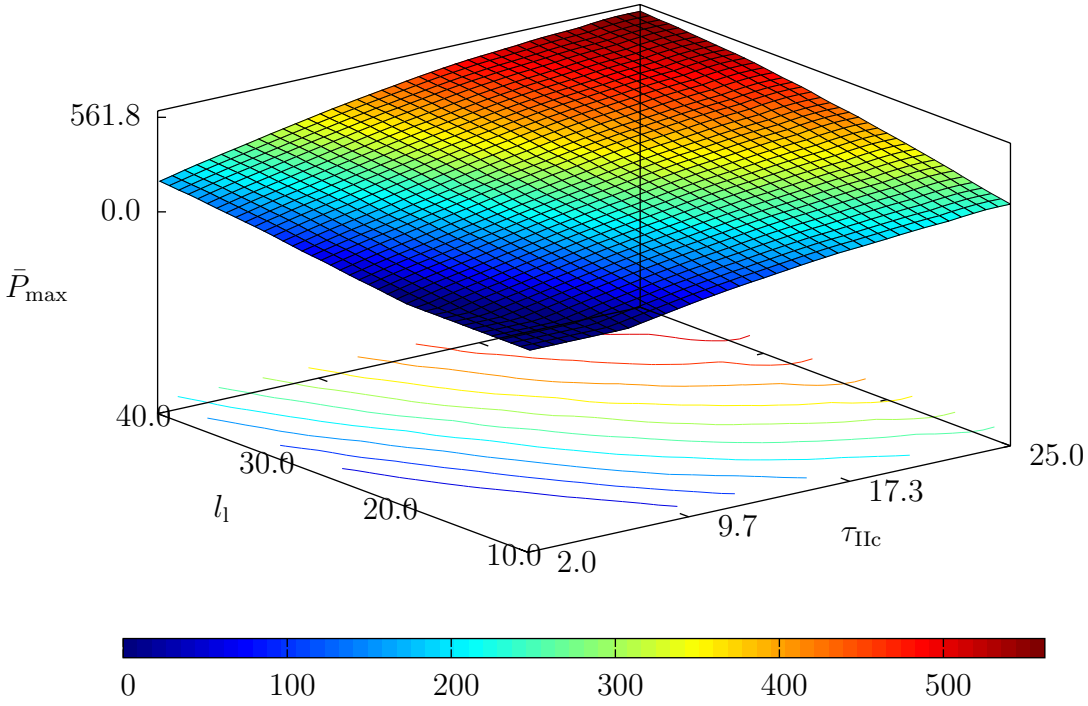

(a) Surface plot

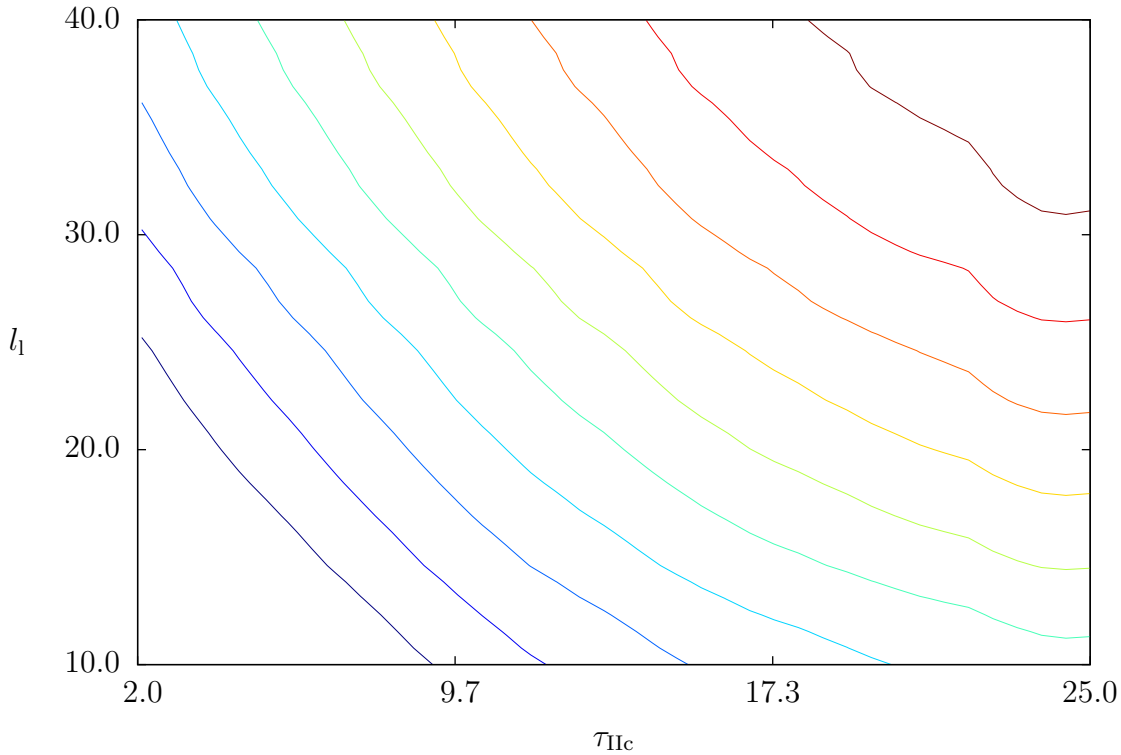

(b) Contour plot

Figure 5.25 Effect of variations of τ_{IIc} and l_1 on SLJ $\bar{P}_{\max}$

eters are should be determined using the DCB test (for G_{Ic}) and an appropriate BPS test (for σ_{Ic}). Then the ENF tests results should be interpreted using traditional CC methods (to determine a distribution of appropriate G_{IIc} values). Lastly, the single lap joint test results should be evaluated. The constitutive parameter values established in the other experiments must be used to determine the appropriate range of values for τ_{IIc} from the SLJ. A demonstration of this procedure is presented in chapter 6.

5.6 Conclusion

Finite element sensitivity studies have been presented for three experiments (double cantilever beam, end notch flexure, single lap joint) that are commonly used to determine adhesive constitutive parameters (G_{Ic}, G_{IIc}, τ_{IIc}). The variables in the studies included four adhesive parameters and a shape factor. Each was allowed to vary over a relatively wide range. Using the kriging analysis technique, it was determined that significant interactions exist between the Mode II parameters in the characterization tests.

Of the three experiments considered, only the double cantilever beam test exhibited limited interaction between the adhesive constitutive variables; therefore, it is useful as an independent test to determine the G_{Ic} parameter. Unlike the double cantilever beam test, parameter interactions were prevalent in the single lap joint and end notch flexure tests. Therefore, the results of these tests must be interpreted together. In the single lap joint test, the Mode I parameter G_{Ic} also plays a non-negligible role. Interpretation of this experimental result is the most difficult, since G_{IIc} should be considered and G_{Ic} could be considered when mapping the test output to τ_{IIc}.

Of the three tests that were included in the sensitivity study, none were significantly effected by the value of σ_{Ic}. Therefore, σ_{Ic} can be determined independently, given that the experiment for this test is considered unlikely to exhibit interaction effects. Though this conclusion is supported by Mi et al. [70], independent verification of this assumption should be included if a standard test for σ_{Ic} is developed.

Beyond the interactions of the adhesive constitutive parameters, the relevant geometric and adherend constitutive variables were also examined. Though the effects of these parameters are well understood, the relative magnitudes (with respect to the adhesive parameters) of the effects were presented. Of the effects, the stiffness (D and E) dependence on temperature is most relevant to the interpretation of the double cantilever beam and end notch flexure tests. These effects may be accounted through

the use of compliance calibration or inverse modeling techniques.

Finally, a method has been developed for mapping a set of experimental results to an appropriate set of constitutive parameters for an adhesive system. The method represents a departure from the traditional methods of interpreting test results individually, however, it is required in view of the significant interactions between the adhesive constitutive parameters.

Chapter 6

T650/AFR-PE-4/FM680-1 at high temperatures: experiments and numerical models

An experimental program to establish a constitutive model for the T650/AFR-PE-4/FM680-1 adhesive system is described next. The model is based on the four parameter beta distribution traction law described in chapter 4. A range of values for the four parameters (G_{Ic}, G_{IIc}, σ_{Ic}, τ_{IIc}) are computed from a set of experimental results and the parameter interactions found in chapter 5. Values of all four parameters are determined over the temperature range of 20 to 350 °C. Due to experimental limitations, two methods for determining G_{Ic} are reported; the area method critical energy release rate ($G^{\mathrm{a}}_{\mathrm{Ic}}$) and the inverse method critical energy release rate ($G^{\mathrm{i}}_{\mathrm{Ic}}$). The values of all the other parameters are based on the constitutive parameter mapping procedure described in chapter 5.

6.1 Background

Temperature resistant composite materials are currently being qualified for use as structural components of aeroshell systems and other high temperature structures. One candidate material system, T650/AFR-PE-4, has recently been the subject of an experimental program for material characterization, [107]. The AFR-PE4 resin, developed at the Air Force Research Laboratory, is a polyimide matrix with a glass transition temperature of 360 °C. It is likely to expand the operating temperatures over which long fiber reinforced composite structures are used. Composite components

based on AFR-PE4 (and similar resins) are expected to allow a reduction in the mass of the structural supports for ablative and resistive thermal protection systems.

It is critical that the T650/AFR-PE-4 material system be tested in a representative operating environment, therefore, qualification and other tests must be completed over the operating temperature range of the material. This is true for all components of a material system, including the adhesive systems which will allow for efficient joining. In this chapter, a material system composed of T650/AFR-PE-4 combined with FM680-1 adhesive is assembled into coupon level specimens and tested to determine the adhesive constitutive parameters. Loading was applied at temperatures between 20-350 °C.

A reference set of adhesive constitutive parameters for the T650/AFR-PE-4/FM680-1 material system is determined. Specifically, the values for G_{Ic}, σ_{Ic}, G_{IIc}, and τ_{IIc} are computed from experimental results. When combined with the beta distribution traction law (BDTL) and the discrete cohesive zone method (DCZM) finite element presented in chapter 4, these parameters provide the ability to model bond line failure in structures made from T650/AFR-PE-4/FM680-1. Other traction laws could be used with minimal changes to the reported values.

In section 6.3, double cantilever beam (DCB) experiments and analysis of the Mode I critical energy release rate (G_{Ic}) are presented (in two forms). First, the area method[1] critical energy release rate ($G^{\mathrm{a}}_{\mathrm{Ic}}$) is determined using image analysis of crack propagation. Second, the inverse method critical energy release rate ($G^{\mathrm{i}}_{\mathrm{Ic}}$) is determined through the use of inverse finite element (FE) analysis based on the DCZM methodology. In section 6.4, the Mode I strength (σ_{Ic}) is determined by a specialized button peel stress (BPS) experiment. Subsequently, the Mode II critical energy release rate (G_{IIc}) is determined (in section 6.5) by the compliance calibration (CC) analysis technique for the end notch flexure (ENF) test. Finally, the Mode II strength (τ_{IIc}) is determined (in section 6.6) based on single lap joint (SLJ) experimental results. The inverse design and analysis of computer experiments (DACE) mapping procedure (describe in chapter 5) is used to determine an appropriate value of τ_{IIc}. This allows the interactions between τ_{IIc}, G_{IIc}, and G_{Ic} to be properly accounted so that the resulting constitutive parameters are appropriate for all the coupon level tests as well as structures composed of the T650/AFR-PE-4/FM680-1 material system.

Due to ITAR restrictions on the subject materials, some detail is excluded from this dissertation. The measured material parameters are presented as normalized quantities. Some other properties and manufacturing details are omitted. All numeri-

[1]The area method is also known as the direct energy balance method.

cal values and plots are normalized by the mean of the Mode I inverse method critical energy release rate at room temperature ($G_{\mathrm{Ic}}^{\mathrm{i\ ave}}\ (T = 20)$).

$$\begin{aligned}
\bar{G}_{\mathrm{Ic}}^{\mathrm{a}} &= \frac{G_{\mathrm{Ic}}^{\mathrm{a}}}{G_{\mathrm{Ic}}^{\mathrm{i\ ave}}\ (T = 20)}, \\
\bar{G}_{\mathrm{Ic}}^{\mathrm{i}} &= \frac{G_{\mathrm{Ic}}^{\mathrm{i}}}{G_{\mathrm{Ic}}^{\mathrm{i\ ave}}\ (T = 20)}, \\
\bar{\sigma}_{\mathrm{Ic}} &= \frac{\sigma_{\mathrm{Ic}}}{G_{\mathrm{Ic}}^{\mathrm{i\ ave}}\ (T = 20)}, \\
\bar{G}_{\mathrm{IIc}} &= \frac{G_{\mathrm{IIc}}}{G_{\mathrm{Ic}}^{\mathrm{i\ ave}}\ (T = 20)}, \\
\bar{\tau}_{\mathrm{IIc}} &= \frac{\tau_{\mathrm{IIc}}}{G_{\mathrm{Ic}}^{\mathrm{i\ ave}}\ (T = 20)}, \\
\bar{P} &= \frac{P}{G_{\mathrm{Ic}}^{\mathrm{i\ ave}}\ (T = 20)}.
\end{aligned} \tag{6.1}$$

The experiments used to determine these parameters are approximately two-dimensional, therefore, P in equation 6.1 is reported as the line load (the load per unit depth).

6.2 Geometry selection and specimen preparation

The four adhesive characterization experiments in this chapter are the DCB test, the BPS test, the ENF test, and the SLJ test. The pre-preg material, T650/AFR-PE-4, was donated by Cytec, Inc. The adhesive, FM680-1, was donated by Goodrich, Inc. Due to the cost associated with each material, a limited quantity was available. As a result, a principle consideration in sizing each specimen was material consumption. To conserve material, all laminates were constructed of four plies. Four was considered the minimum number of layers for structural integrity.

6.2.1 The double cantilever beam geometry

A schematic of the DCB specimen is shown in figure 5.4. Manufacturing constraints were significant in sizing the overall geometry of the specimen. The specimen length is one half the manufacturable plate size. The specimen width, 20 mm, was set to maximize the specimen yield while ensuring measurable loads.

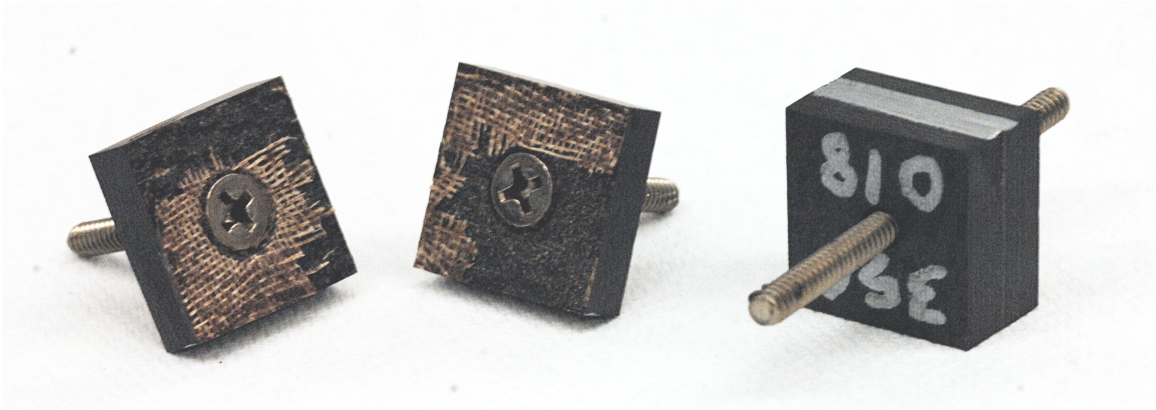

Figure 6.1 Typical BPS specimens before and after the experiment

6.2.2 The button peel stress geometry

Unlike the other coupon level specimens, the BPS specimen adherends were not laminated on site. Instead, they were cut from a plate (of the same material) that was donated by the Pratt & Whitney Corporation.[2] As with the other specimen types, manufacturing constraints dictated the geometry. Only one plate was available as a source for BPS specimens. The required number of BPS experiments dictated a minimum of sixteen specimens be manufactured from the plate (with additional specimens for pretesting).

There were several requirements in establishing the specimen geometry shown in figure 6.1. First, an accurate estimate of the adhesive surface area is required for computation of the peel stress. The uncertainty associated with adhesive spew precluded a geometry where the adhesive only covered a small portion of the adherend surface. Second, the cured adhesive layer is thin and prevents the insertion of a gripping fixture in a gap formed by the adhesive thickness. Third, the extreme temperatures during the experiment (and the high strength of FM680-1 at those temperatures) cause reliability concerns for any fixture attached by bonding. In view of the constraints, a machine screw with a tapered head was inserted through a counter-sunk hole in the center of each square adherend. The screws (shown in figure 6.1) were found to be an effective fixture. The square specimen was found to meet manufacturing constraints.

Initial testing showed that fast fracture was the failure mode of the BPS specimen. Fast fracture is a minimal criterion to establish that σ_{Ic} is the dominant parameter in failure, therefore, the specimen geometry was accepted.[3]

[2] Courtesy of Dr. R. A. Naik.

[3] No standard BPS specimen is currently available for composite materials. The current specimen is believed to yield an appropriate value for σ_{Ic}. Results with a variant of the BPS have been reported

6.2.3 The end notch flexure geometry

Sizing the ENF specimen was straightforward given the material and manufacturing constraints. The DCB geometry was found to be appropriate for the ENF specimen; therefore, it was selected. The DCB/ENF geometry conforms to the guidelines proposed by Davidson and Zhao [36] for the upcoming ASTM International (ASTM) standard.

6.2.4 The single lap joint geometry

The objective of the SLJ test is to determine the Mode II strength (τ_{IIc}) for use in the DCZM element traction law. Although the ASTM recommends a specific geometry for the SLJ test, initial tests showed that the failure load would exceed the load frame capacity (for the available Instron model 4201 electromechanical load frame with an Instron model 3119 temperature chamber).

To select an appropriate alternative geometry, an analytical design of experiments (DOE) was completed to assess specimen geometric variables. The base FE model was generated using parameters derived from initial experimental data. Notch length (l_{n}) was found to have a negligible effect on the output.[4] Since the specimen geometry was required to depart from the ASTM recommendation, the value of l_{n} was reduced to limit material consumption. The DOE and preliminary experiments indicated that a specimen width of 12.5 mm would be appropriate over the entire range of temperatures, therefore, it was selected as the nominal specimen width.

6.2.5 Specimen preparation

All specimens (with the exception of the BPS specimens) were prepared in batches using bidirectional woven T650 lamina pre-impregnated with AFR-PE-4. The layers were arranged by hand layup into $[0, 90]_s$ laminates and cured in a Wabash model 30-1515 press. The multi-step curing cycle followed the manufacturer's recommendation [107] as closely as possible with modifications required for hot press operations.[5] The cured laminate plate had two distinct surface textures referred to as smooth (released from the stainless steel mold plate) and rough (released from the peel ply/fiberglass batting). The cured plate geometry was approximately 315×315×1.25 mm.

by Sun [99] who examined a steel/adhesive/steel material system. The development of a standardized procedure and specimen would add confidence to the results.

[4] This was confirmed by the sensitivity analysis presented in chapter 5.

[5] The details of the curing cycle are ITAR restricted, contact the manufacturer for additional detail.

Following the cure cycle, each laminate was cut into four smaller plates of approximately 155×155×1.25 mm. This plate size set the total length of the DCB and ENF specimens. All specimens were prepared with adherends obtained from the same laminate. Prior to any bonding, the plates were lightly roughened with 200 grit sandpaper and cleaned with acetone.

For the DCB and ENF specimens, the small plates were bonded in pairs so that the adhesive covered a portion of the surface (sufficient to yield the bonded lengths shown in figures 5.4 and 5.11). For the SLJ specimens, two plates were bonded to overlap by 25.4 mm. Stainless steel mold plates supported the free ends of the SLJ adherends. In each assembly, the bonding was completed using Cytec FM680-1 adhesive film (an adhesive carried on a fiberglass scrim). The adhesive was cured during a separate step in the hot press.[6] The assemblies were arranged so that the adhesive layer was in contact with one rough and one smooth side of the adherends. A 50μm film sheet of Kapton (coated with Loctite 770-NC mold release) was inserted between the DCB and ENF adherends to initiate a crack.

In contrast to the other specimen types, the BPS specimens were cut from the laminate provide by Pratt & Whitney Corporation. The laminate allowed for additional adherend thickness and provided a robust hole/countersink structure that was able to withstand the experimental loads. The sixteen layer laminate was cut into square specimens with 20 mm (nominal) sides. The nominal laminate thickness was 5.7 mm. A 4 mm diameter hole was drilled into each square to accommodate the machine screw that was used as a fixture. The hole was countersunk until the screw head was below flush. The squares, in pairs, were then lightly roughened with the 200 grit sandpaper on the bonding face and cleaned with acetone. Prior to assembly, the #6-32 machine screws were coated with six coats of Freekote 770NC mold release to ensure minimal adhesion in the event of adhesive spew.[7] FM680-1 adhesive squares were placed over the bonding surfaces and a hole was cut in the adhesive scrim. The machine screw was passed through the adhesive so that the screw head remained free of adhesive. The faces of the adherends and the screw heads were aligned prior to the adhesive curing cycle.

Subsequent to curing, the assembly was post-cured according to the manufacturer's recommended cycle. For the SLJ specimens, the free adherend ends were cut roughly in half and used as the doubling section between the wedge grips.[8] The nominal size

[6]The adhesive cure cycle was also modified slightly from the manufacturer's recommendation due to hot press operations.

[7] Post-test inspection revealed that there was no significant adhesive spew over the screw head.

[8]The doubling was initially held in place by J-B Weld epoxy, however, at high temperatures this

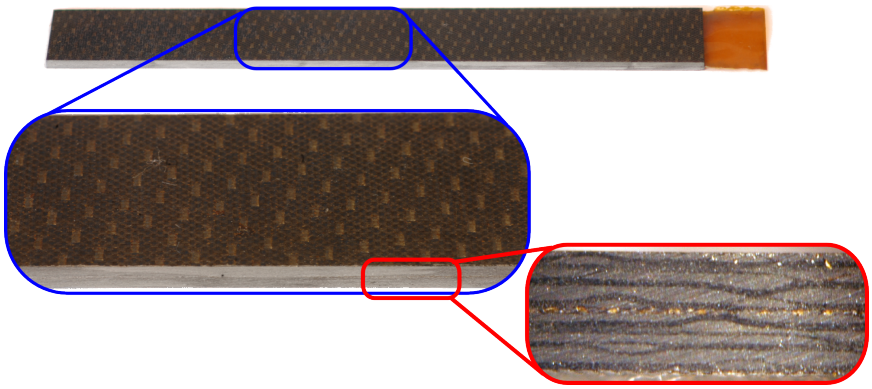

(a) A DCB/ENF specimen shown at different scales

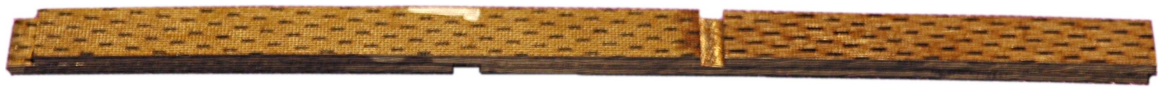

(b) A SLJ specimen

Figure 6.2 Typical DCB/ENF and SLJ specimens

of the notch (l_n) was 2 mm. In the last step of the DCB, ENF, and SLJ manufacturing process, the edges of the bonded plates were trimmed and individual specimens were cut from the remaining material.

The geometry of the DCB, ENF, and SLJ specimens are shown schematically in figures 5.4, 5.11, and 5.17. Figure 6.2(a) shows a typical DCB/ENF specimen at several visual scales. A typical SLJ specimen is shown in figure 6.2(b). BPS specimens (pre and post experiment) are shown in figure 6.1. After all trimming, the nominal length (l) of the DCB/ENF specimen was 130 ±3 mm and the nominal width (b) was 20 ± 0.3 mm. The nominal width of the SLJ specimen was 12.5 ± 0.3 mm. The nominal thickness (h) of the DCB/ENF/SLJ specimen adherends were 1.25 ± 0.05 mm and the nominal thickness of the BPS specimen was 5.7 mm± 0.03 mm.

The position of the Kapton (i.e. the position of the initial crack tip) for the DCB specimen was 20 ± 2 mm relative to the hinge. Due to the high temperatures to which the joints were subjected, the hinges were attached with #4-40 machine screws. Holes were drilled in the specimens to accommodate these screws. The hole size was set so that the conical heads of the machine screws were approximately flush with the inside surfaces of the DCB specimen (the screw shank protruded outward from the specimen centerline). The resulting hinged specimen (as tested) had less than 0.5 mm of initial displacement caused by the screw heads.

epoxy broke down. Although this required care in gripping, there were no significant adverse effects since the two adherends (in the doubling section) did not slip relative to each other.

6.3 Experimental determination of G_{Ic}

In this section, the Mode I critical energy release rate is reported for the T650/AFR-PE-4/FM680-1 material system over a broad range of temperatures.

6.3.1 The double cantilever beam experimental protocol

The DCB experiments were completed on an Instron model 5585 electro-mechanical loading frame.[9] The specimens, including grips, were enclosed in an Instron model 3119 environmental chamber and brought to the specified temperatures ($T = \{20, 150, 250, 350\}$ °C). Four specimens were tested at each temperature level. The air inside the environmental chamber was stirred constantly to ensure uniformity. The temperature was maintained to ±2 °C. A minimum of 20 minutes was allowed to obtain thermodynamic equilibrium after reaching the specified temperature. Prior to the measured load-displacement cycle, a natural crack was initiated by enforcing a crosshead displacement of 5 mm while at temperature. Therefore, the initial crack length (a_0) was determined by this initial enforced displacement. The DCB specimens were subsequently loaded via displacement control at 5 mm/min. An escalating sawtooth displacement pattern was prescribed. The bounding displacements were: $w_{\mathrm{tip}} = [0, 8, 0, 11, 0, 14, 0, 17, 0, 20]$ mm. Load and displacement measurements were acquired at a minimum of 10 Hz. Photographic images were taken at 5 second intervals (or faster) to determine the apparent crack position.

6.3.2 The area method: $G_{\mathrm{Ic}}^{\mathrm{a}}$

Representative test results

A set of typical load-displacement curves are shown in figure 6.4. The curves were numerically integrated to determine the total work done during each displacement cycle. The total work is composed of several components:

$$W_{\mathrm{tot}} = W_{\mathrm{frac}} + W_{\mathrm{pl}} + W_{\mathrm{dis}}, \tag{6.2}$$

where W_{tot} is the total work done, W_{frac} is the work done to create new fracture surfaces, W_{pl} is the work that causes permanent deformation (hereafter referred to

[9]The DCB tests were conducted on a Instron 5585 frame and thermal chamber in an alternate laboratory. This work was completed prior to the installation of a dedicated facility with the Instron 4201 frame used in the remainder of the experiments.

as plasticity) in the adherends, and W_{dis} is all other dissipative mechanisms. For a linear-elastic DCB specimen, the plastic and dissipative terms are absent in equation 6.2 and all the external work goes to the creation of fracture surfaces. The critical energy release rate (G_{Ic}) is equal to this fracture work divided by the new crack surface area:

$$G_{\text{Ic}} = \frac{W_{\text{frac}}}{\Delta a \cdot b}. \tag{6.3}$$

Equation 6.3 is a good approximation for the T650/AFR-PE-4/FM680-1 specimens at most temperatures. After the test, there was no visual indication of plastic deformation in the specimen. As shown in figure 6.4, the sawtooth loading pattern exhibits linear initial loading and linear unload-reload cycles with minimal hysteresis (for all but the 350 °C specimens). The specimen load goes to the zero load point as displacement goes to zero, indicating little or no permanent deformation. Equation 6.3 does not hold at 350 °C due to moderate permanent deformation. This can also be seen in figure 6.4, where the sawtooth displacement cycle exhibits some differences between the unload and reload load-displacement curves. This hysteresis is indicative of non-negligible dissipative mechanisms during the test. The unload path does not return to zero load at zero displacement, which re-enforces the observation of plastic deformation. Further, in two of the four specimens tested at 350 °C, the specimen failed due to adherend fracture. Large amounts of dissipated energy were associated with these fractures.[10]

Due to the uncertain non-linear constitutive and dissipative effects, the area method critical energy release rate is defined as:

$$G_{\text{Ic}}^{\text{a}} = \frac{W_{\text{tot}}}{\Delta a \cdot b}. \tag{6.4}$$

The area method critical energy release rate (G_{Ic}^{a}) must not confused with the "true" critical energy release rate at high temperature. There is insufficient information to completely determine the temperature dependence and contributions of plastic work (W_{pl}) and other dissipative mechanisms (W_{dis}) to the total work (W_{tot}) in the DCB test, therefore G_{Ic}^{a} cannot be considered a "true" G_{Ic}. An alternative method for determining G_{Ic} will be presented in section 6.3.3 to address this concern.

[10] In Whitley and Collins [107], the T650/AFR-PE-4 material system was found to suffer a significant reduction in the interlaminar shear strength at this temperature, therefore the two specimen failures at this temperature are not surprising.

The apparent crack advance

Image analysis was used to determine the time history of the apparent crack position. A label-paper grid with 0.5 mm spacing was adhered to the edge of each specimen and was used to aid in determining the crack position during data reduction. For each specimen, a pixel length calibration was done. A typical photograph had ≈ 50 pixels/mm. The initial crack position was measured from a line connecting the center of the hinges to the initial crack tip. In subsequent images, common points were identified and used to determine the prior and current crack position. Crack propagation was measured linearly from the prior crack position to the current crack position in each frame. In this way, the apparent crack position (a) and apparent crack increment (Δa) could be determined even when the global deflection made direct linear measurement from the hinge difficult. At a minimum, image analysis was completed at the beginning and end of the test cycle as well as the beginning of each unload phase of the cycle. Therefore, all sub-cycle crack positions were determined as well as the initial and final crack positions. Additional images were analyzed, as required, to track crack position throughout each test.

Distribution of $G_{\mathrm{Ic}}^{\mathrm{a}}$

The area method critical energy release rate $G_{\mathrm{Ic}}^{\mathrm{a}}$ was calculated with equation 6.4 and the time history of a for each specimen. The average and standard deviation (σ)[11] of the four specimens were calculated for each temperature and are shown in figure 6.5 as well as table 6.2. A loose positive correlation was found between the temperature and $G_{\mathrm{Ic}}^{\mathrm{a}}$.[12] This increase in $G_{\mathrm{Ic}}^{\mathrm{a}}$ is consistent with an increase in material ductility at higher temperatures in this mode, however, there is insufficient information to eliminate the possible influence of a gradual increase in adherend plasticity with temperature. Permanent deformation is apparent in the specimens tested at 350 °C.

Additional observations

The area method has been determined to be less reliable than the various compliance calibration methods, [95]. Unfortunately, individual compliance calibration per

[11] The standard deviations in this work are *sample standard deviations*, the square-root of the unbiased estimator for the variance.

[12] The mean and standard deviation at 350 °C in figure 6.5 are based on the two specimens which did not exhibit adherend fracture.

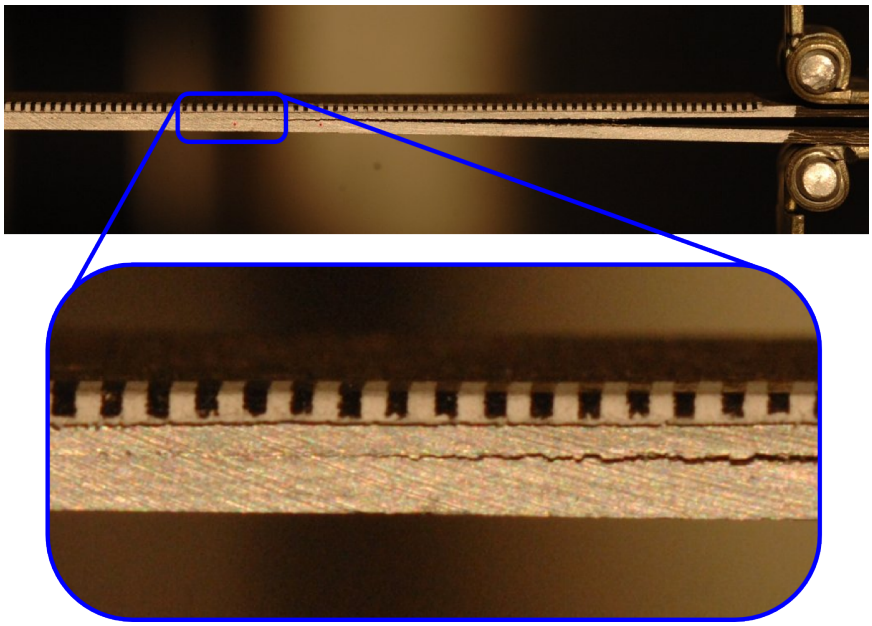

Figure 6.3 Typical image used for analysis of apparent crack propagation.

specimen is difficult for the DCB test due to the manufacturing constraint of a fixed hinge. A "general" compliance calibration for all specimens would be desired, however, it would require a consistent stiffness from specimen to specimen. In this set of experiments with thin adherends consisting of only a few layers, adherend stiffness may not be consistent from specimen to specimen. Small variations in thickness and small differences in fiber position within the cross section inevitably lead to differences in stiffness, since there is little opportunity for strain averaging in thin laminates. This stiffness uncertainty is further emphasized by the manufacturing variations inherent in the hand layup process. For the DCB adherends, the standard deviation of the measured stiffness was 7.4% of the mean stiffness (as determined by 3-point bend tests at room temperature). Additionally, since compliance is dependent on temperature, CC is difficult due to the number of specimens required. Therefore, the area and inverse methods (described in section 6.3.3) are used to determine G_{Ic} in T650/AFR-PE-4/FM680-1.

In the DCB test, the adhesive always failed at the interface with the rough side of the adherend. In each specimen, the fiberglass scrim carrier remained bonded to the smooth adherend. In a few specimens, small patches of scrim ($\sim$30 mm^2) were found on the rough adherend, however, this was uncommon. It is likely, therefore, that surface roughness played a role in the adhesive failure.

Finally, the critical energy release rates ($G_{\mathrm{Ic}}^{\mathrm{a}}$ and $G_{\mathrm{Ic}}^{\mathrm{i}}$) and the peak loads increased

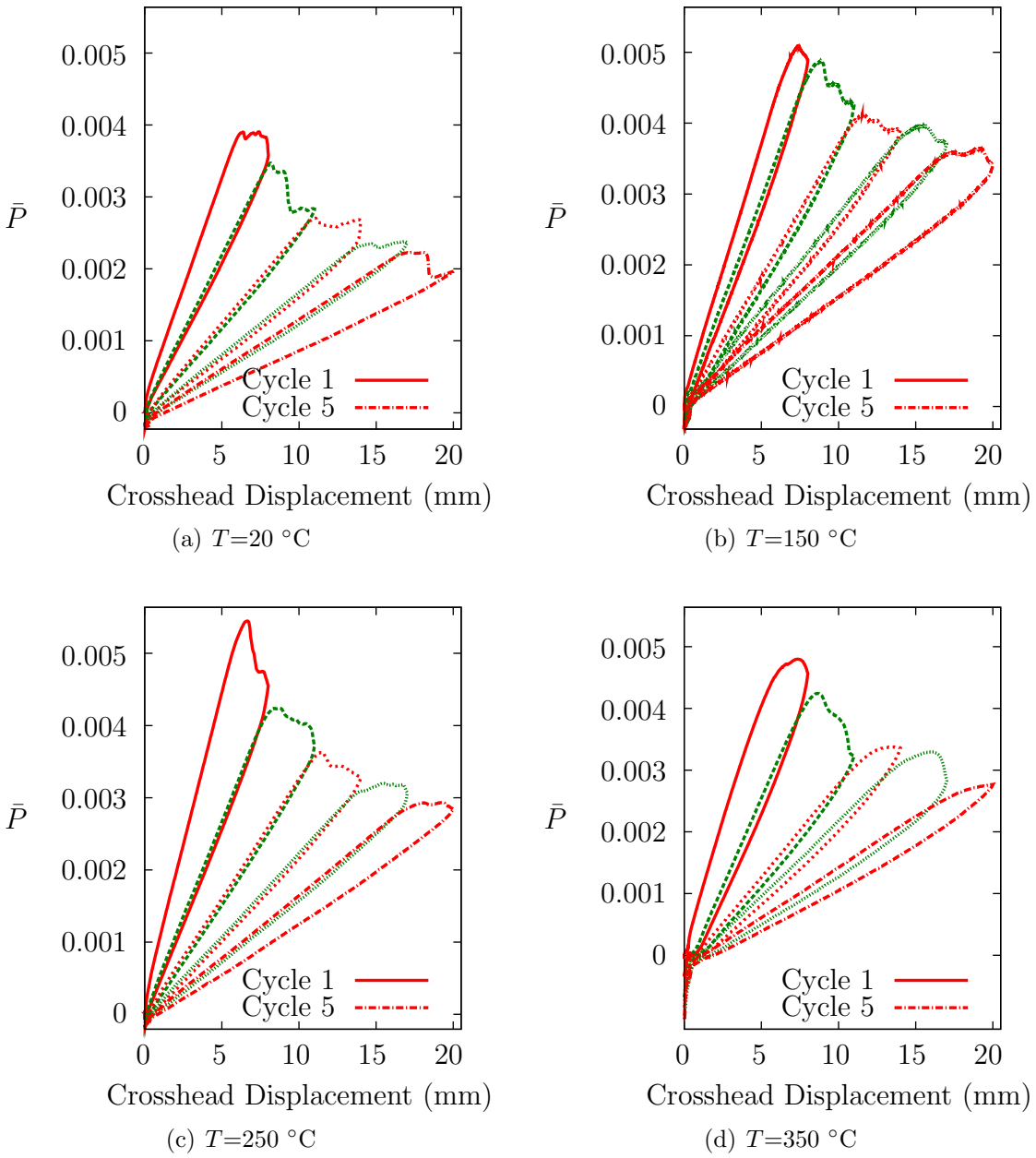

(a) T=20 °C (b) T=150 °C

(c) T=250 °C (d) T=350 °C

Figure 6.4 Typical load-displacement for T650/AFR-PE-4/FM680-1 DCB specimens.

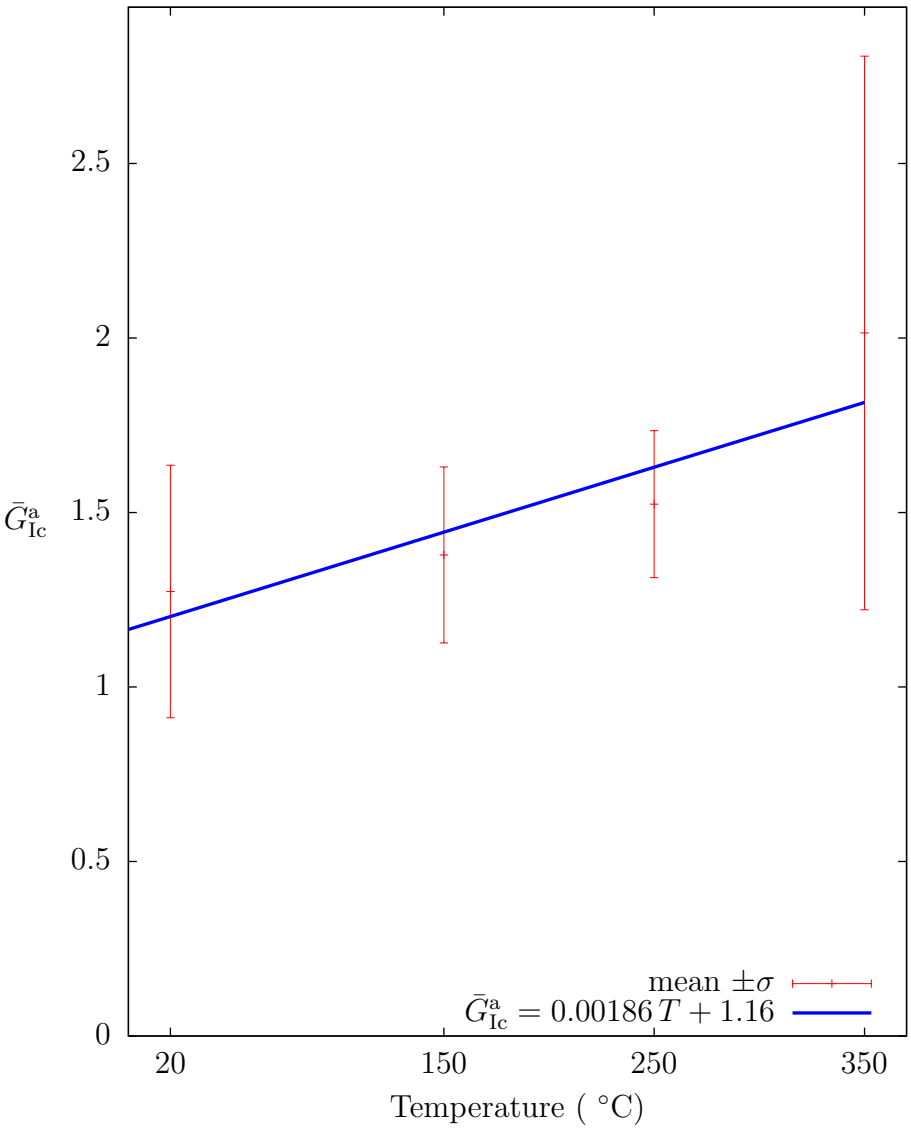

Figure 6.5 Distribution of $\bar{G}^{\mathrm{a}}_{\mathrm{Ic}}$ as a function of temperature

Table 6.1 Approximate size of the coarse and fine DCB FE models.

	Coarse Mesh	Fine Mesh
Elements	1050	4700
Nodes	1200	5000
Solution time (s)	25	145

with increasing temperature. This trend has been observed where material ductility increases with increasing temperature, [11, 95]. Asp [11] concluded, however, that the literature is ambiguous as to the effects of temperature on G_{Ic}. The decreasing values of G_{IIc} reported in section 6.5 support Asp's assertion.[13]

6.3.3 The inverse method: $G^{\mathrm{i}}_{\mathrm{Ic}}$

Description of the FE model

Due to the uncertainties in plastic work and other dissipative mechanisms, the DCB experimental results were used to generate a quantitative inverse model of the DCB test. A 2D model was created and Abaqus® [1] was used as the FE solver. The adherends were modeled with linear elastic, orthotropic, CPE4I elements. The adhesive was replaced by a layer of novel DCZM elements (described in chapter 4). To establish mesh convergence, two meshes were generated (shown in figure 6.6 with additional detail provided in table 6.1). They were found to provide nearly identical results in predicted load-displacement response as shown in figure 6.6(b). This result reinforces the claim made in Xie and Waas [113] that the DCZM element is essentially mesh independent. It was observed, however, that the model's ability to obtain a completed solution (i.e. solution convergence) is mesh dependent. Due to the small CPU time requirements of the model, the fine mesh was chosen for additional study. It exhibited slightly less "chatter"[14] during steady state crack propagation and was deemed more likely to obtain solution convergence for all model inputs.

[13] Asp's conclusion was with respect to interlaminar G_{Ic}, however, the result may be general to all modes.

[14] The "chatter" is tied to the mesh density and the εsoftening in the traction law. Larger elements have larger integration point areas; therefore, they are constrained to have larger increments of crack advance. The resulting global load-displacement response can lose smoothness.

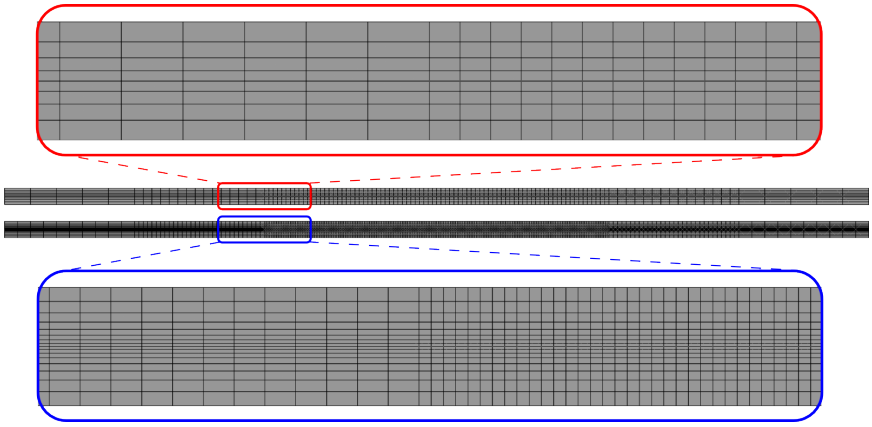

(a) The coarse (top) and fine (bottom) meshes used to evaluate convergence.

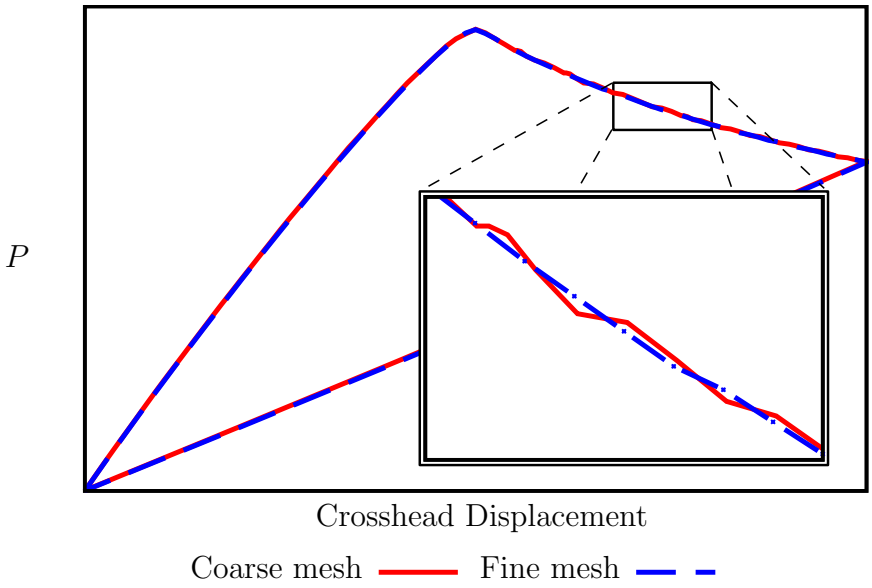

(b) Predicted load-displacement results for the coarse and fine meshes. The coarse mesh exhibits "chatter" that is not present in the fine mesh.

Figure 6.6 DCB FE models in two mesh densities

The inverse modeling procedure

With the experimental results and the DCZM element, a second value of the critical energy release rate ($G_{\mathrm{Ic}}^{\mathrm{i}}$) was established by inverse modeling the measured load-displacement in a FE environment. An iterative algorithm was developed using custom scripts developed for Octave© [45]. Within Octave©, the scripts supplied initial material parameters to the FE model, called the FE solver, extracted the load-displacement output, evaluated it against convergence criteria, and modified the input deck for re-analysis (if needed).

Criteria for inverse model acceptance

Inverse modeling requires metrics to evaluate model output. The objective in inverse modeling is to match experimentally measured loads while accurately representing geometry and material properties. This must be accomplished despite uncertainties and experimental variability. For the DCB test, the principal uncertainties are the stiffness of the adherends, the initial crack length (due to non-planer cracks and measurement error), and the critical energy release rate (due to manufacturing or material variability and unknown temperature dependence). Since G_{Ic} is the material parameter of interest, assumptions were made regarding the remaining uncertainties.

For the DCB test, two criteria were established as output metrics. The first criterion was to match the initial slope of the load-displacement curve within a tolerance of $\pm 1\%$. The initial slope of the load-displacement curve is a function of a_0 and the stiffness of the adherends. Though either could be modified during inverse modeling, the specimen stiffness was held constant and the initial crack position was modified. In matching the initial slope by adjusting a_0, initial crack position is determined within the error bounds of the specimen stiffness.

A second requirement in matching the experimental loads is to predict the load during crack advance. Once the stiffness and initial crack length are established, the load during crack advance is dependent on crack position and adherend plastic deformation. In an ideal specimen with no plasticity, the crack advance load would be governed by G_{Ic}. Significant adherend plasticity, however, will change the load during crack advance.

In the inverse modeling algorithm, it is assumed that G_{Ic} is constant and the crack position is the dominant variable in defining the load. Therefore, the Mode I critical energy release rate (G_{Ic}) was used to match the load during crack advance. No plasticity is included in the FE analysis, however, the predicted and experimental

load-displacement can be compared as one indication of the validity of the plasticity assumption.

The measured loads during crack advance are significantly more variable than is the initial slope, therefore, there is no clear inversion criterion with respect to where and how the loads should be evaluated. Common evaluation points (for the purposes of calculating G_{Ic} via CC techniques) are the onset of non-linearity, the 5% offset point, and the peak load point, [95]. Unfortunately, when evaluated at an isolated point, the calculated value of G_{Ic} is not an average value and may not be the best quantitative evaluation of material adhesion. In the inversion algorithm, an attempt was made to determine the average value of critical energy release rate over the entire crack advance. The criterion was, therefore, based on a curve fit of the whole load-displacement curve during crack advance.

The following procedure was established for determining the critical energy release rate via inverse modeling. First, the crack advance portions of the curves were identified from the measured and modeled load-displacement curves. The crack advance portion ranged from the displacement at the peak load to the maximum displacement for the specimen (excluding overlapping displacements due to cyclic loading). A linear, least-squares fit was applied to each of the isolated curves. A load value was calculated based on each of the fit lines; the evaluation point was 1/2 the distance from the peak load to the max displacement of the *measured* load-displacement curve. These "representative loads" allowed comparison of the measured and modeled crack propagation curves via the best fit equations. Therefore, the second inverse modeling criterion required that the representative load from the model be within 1% of the representative load from the measured data.

In the G_{Ic} inverse modeling scheme, there was no procedure for evaluating the cohesive strength of the T650/AFR-PE-4/FM680-1 material system, although, it could be added without significant difficulty. It was determined that the cohesive strength (σ_{Ic}) and the shape factor of the traction law (α_{pl}) govern the transition between the initial slope and the subsequent crack propagation portions of the load-displacement curve.[15] This transition could be used to invert these parameters, however, the BPS test described in section 6.4 is expected to provide a more precise method of determining the cohesive strength. Since the BPS results were not yet available when the inverse modeling was completed, effective values of these parameters were fixed based on

[15]The trapezoidal traction law was used in the inverse modeling procedure since the smooth traction laws were not yet available when the work was completed. The DCB is insensitive to the traction law shape factor (α_{pl}), therefore, any difference in results would be negligible.

Table 6.2 Distributions of $\bar{G}_{\mathrm{Ic}}$

Temperature T °C	area method $\bar{G}^{\mathrm{a}}_{\mathrm{Ic}} \pm \sigma$	Inverse Method $\bar{G}^{\mathrm{i}}_{\mathrm{Ic}} \pm \sigma$
20	1.27 ± 0.36	1.00 ± 0.21
150	1.38 ± 0.25	1.23 ± 0.21
250	1.52 ± 0.21	1.37 ± 0.07
350	2.01 ± 0.79	1.36 ± 0.22

observed transitions between initial load-displacement stiffness and crack propagation.

Distribution of $G^{\mathrm{i}}_{\mathrm{Ic}}$

Typical FE predictions of DCB load-displacement $G^{\mathrm{i}}_{\mathrm{Ic}}$ are shown in figure 6.7 as well as the associated experimental result for the same specimen. The measured load-displacement cycles are well captured by the inversion (at all temperatures). The values used to create these curves, summarized in table 6.2, are very likely to represent the G_{Ic} values present in the material system.

Figure 6.8 shows the distribution of $\bar{G}^{\mathrm{i}}_{\mathrm{Ic}}$ determined by inverse modeling. The values of $\bar{G}^{\mathrm{i}}_{\mathrm{Ic}}$ are found to be smaller and less variable than the values of $\bar{G}^{\mathrm{a}}_{\mathrm{Ic}}$. This is expected, since $\bar{G}^{\mathrm{a}}_{\mathrm{Ic}}$ contains energy that is associated with adherend plasticity and dissipation in the experiment, whereas the models used for $\bar{G}^{\mathrm{i}}_{\mathrm{Ic}}$ are linear elastic and contain minimal dissipation (to ensure a converged solution). The $\bar{G}^{\mathrm{i}}_{\mathrm{Ic}}$ values are more representative of "true" $\bar{G}_{\mathrm{Ic}}$ since they do not contain significant energy dissipation contributions other than the creation of new crack surfaces. The computed values of $\bar{G}^{\mathrm{i}}_{\mathrm{Ic}}$ are not "true" $\bar{G}_{\mathrm{Ic}}$, since the FE models did not include adherend plasticity that may be present (especially at high temperature).

Comparing the measured and modeled load-displacement in figure 6.7, it is apparent that the DCB test can be well modeled without the inclusion of adherend plasticity. Considering the excellent correlation between modeled and measured loads in the crack advance portion of the curves, it is likely that plasticity (W_{pl}) is a small portion of the total work (even at 350 °C). It is therefore likely that the other dissipative mechanisms (W_{dis}) are the bulk of the difference between $\bar{G}^{\mathrm{a}}_{\mathrm{Ic}}$ and $\bar{G}^{\mathrm{i}}_{\mathrm{Ic}}$ in table 6.2.

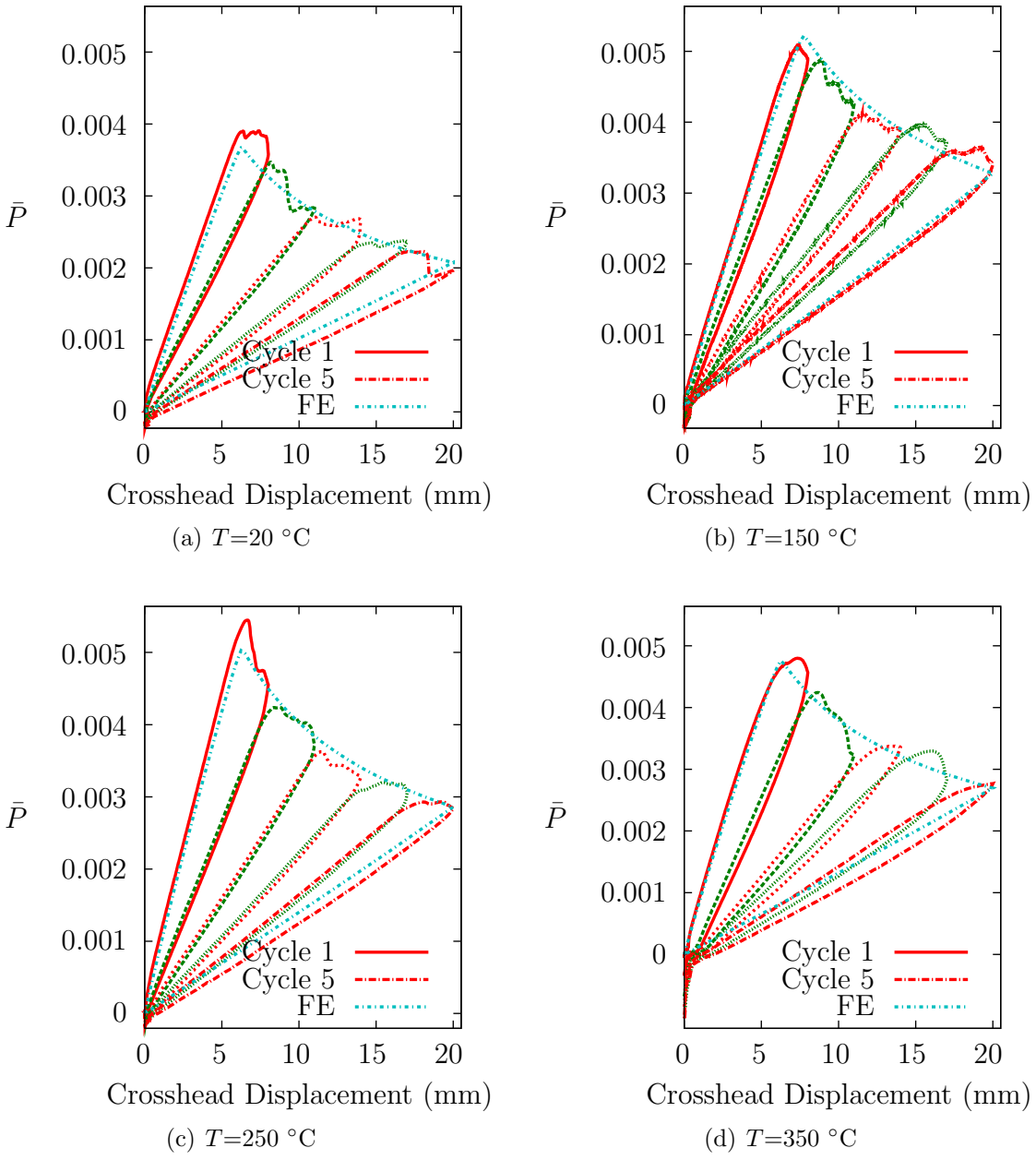

(a) T=20 °C (b) T=150 °C

(c) T=250 °C (d) T=350 °C

Figure 6.7 Typical normalized load-displacement and inverse model results for T650/AFR-PE-4/FM680-1 DCB specimens.

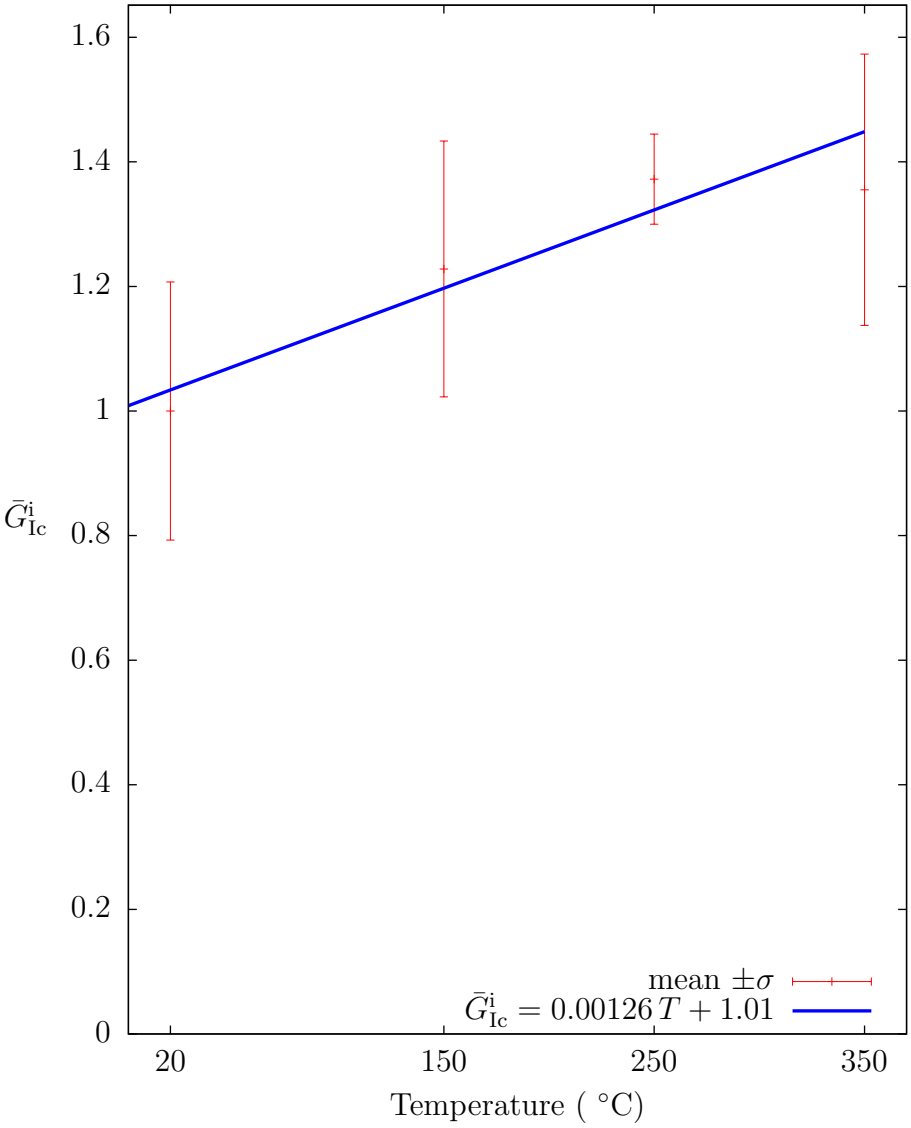

Figure 6.8 Distribution of $\bar{G}^{\mathrm{i}}_{\mathrm{Ic}}$ as a function of temperature. The error bars represent the average $\pm\sigma$ from the local mean.

6.4 Experimental determination of σ_{Ic}

The critical peel stress (σ_{Ic}) is the second parameter in the traction law and is determined by the button peel stress test. For this and the remaining experiments, an Instron model 4201 electromechanical load frame was used. An Instron model 3119 environmental chamber enclosed the specimen and controlled temperature to the tolerances described in section 6.3. Custom steel wedge grips (shown in figure 6.9) were used in this and the SLJ test (to be reported in section 6.6). Four BPS failure tests were completed at each of four temperatures.

6.4.1 The button peel stress experimental protocol

The BPS experimental protocol began with the specimens being placed into the wedge grips so that the machine screw threads and the knurled wedge grip faces interlocked. Very little clamping force was required to prevent slippage during the test, therefore, no compression beyond the natural compression of the wedge was required. The outer face of the specimen was flush with the tips of the wedge grips. The setup is shown in figure 6.9

The specimens were loaded in displacement control at 0.5 mm/min until fracture. High speed video was taken of the fracture event. The video showed that the initial fracture event completely severed interface in most specimens. In the remaining specimens (usually at high temperature), the crack propagated over the majority of the interface while leaving a few strands of fiberglass scrim bridging the crack. The bridging was at least partially due to increased friction in the wedge grips at high temperature. (The grips had to be knocked free with a malleable hammer at the conclusion of these tests.) Since the specimens were loaded in displacement control and friction prevented complete severance, the bridging scrim was deemed insignificant relative to the total surface area. For the purposes of data reduction, all specimens were considered to have failed instantly. Typical normalized load-displacement results for the BPS experiments are shown in figure 6.11. The critical stress values (σ_{Ic}) were calculated using:

$$\sigma_{\mathrm{Ic}} = \frac{P_{\mathrm{fail}}}{A_{\mathrm{BPS}}}. \tag{6.5}$$

In equation 6.5, P_{fail} is the failure load and A_{BPS} is the bonded surface area of the BPS specimen. In order to accurately account for the screw head and it's reduction of the bonded surface area, A_{BPS} was determined through photographic evaluation of the failed specimen. The evaluation consisted of a (manually guided) image threshold

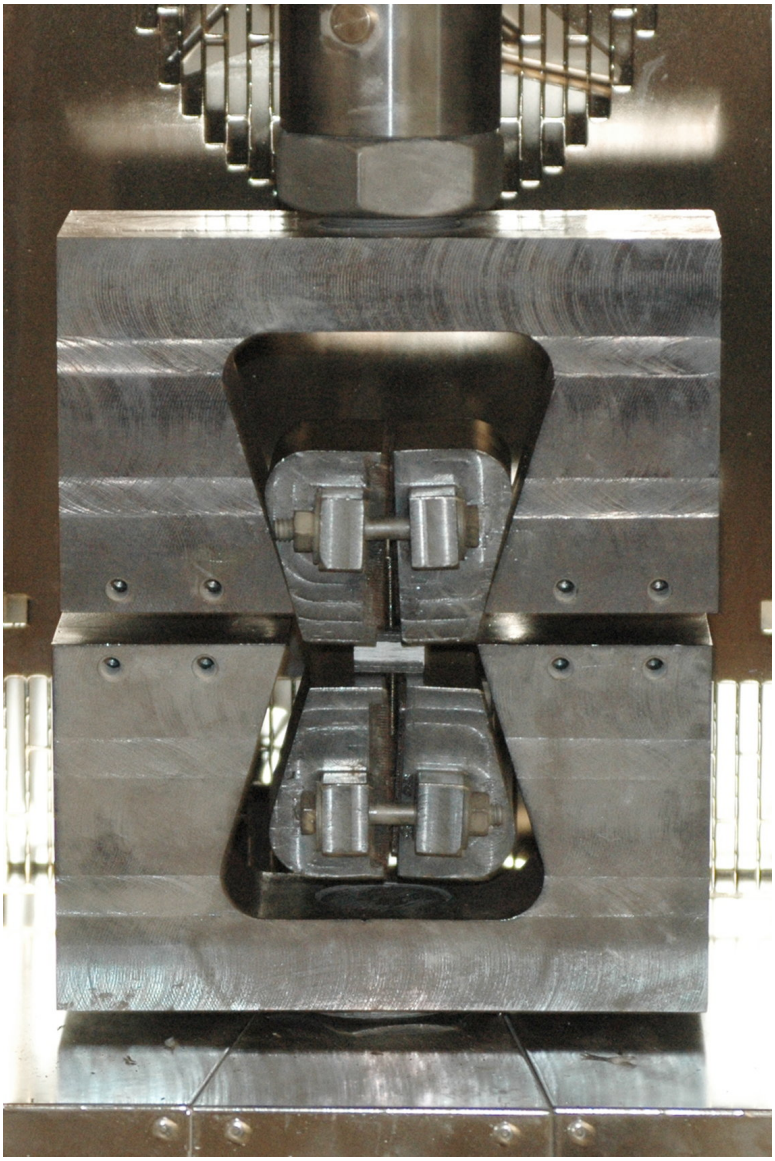

Figure 6.9 Setup of wedge grips for the BPS specimen. The outer surfaces of the specimen were flush with the grip tips at the start of each experiment. Friction between the grips and their housing prevented complete severance of the scrim in some specimens.

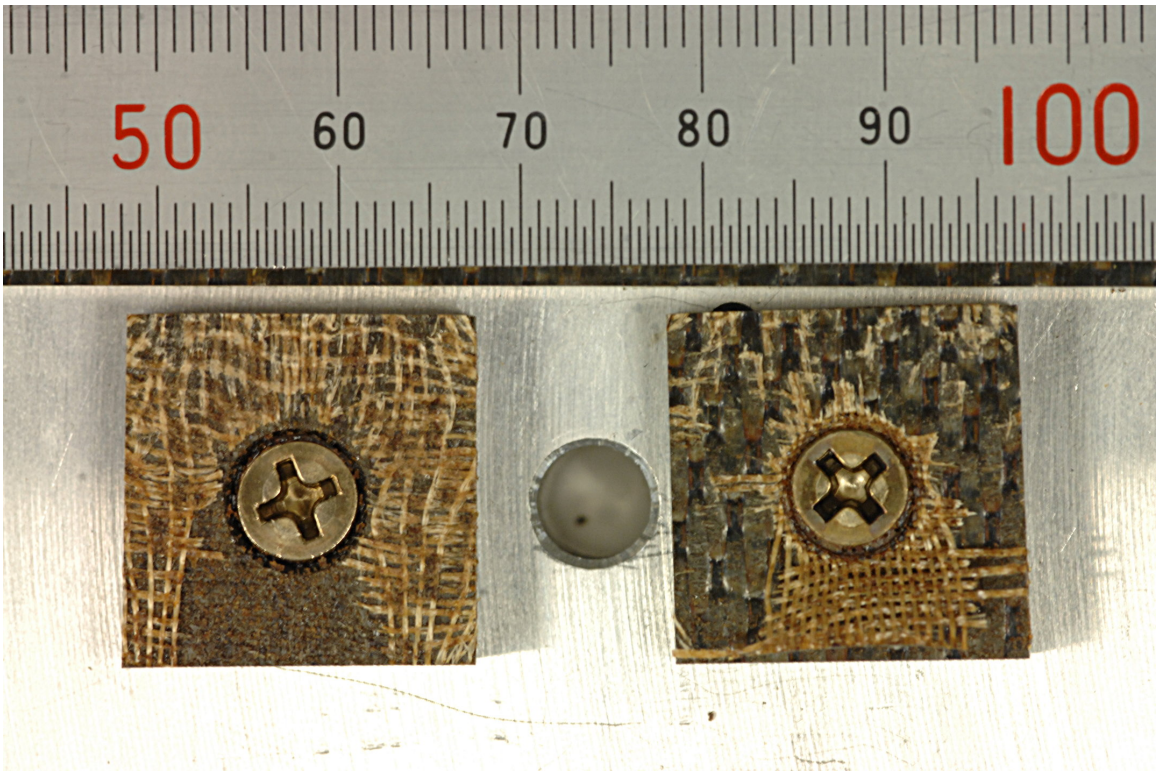

Figure 6.10 Typical photograph used to determine the BPS bonded area

of a surface image which allowed the pixels of the surface area to be counted. A linear ruler was included in the photograph in order to establish the pixel density, from which the area was calculated. A sample photograph from this process is shown in figure 6.10. The figure also illustrates a typical failure; the scrim was found to be distributed to both the smooth and rough sides of the specimen.

6.4.2 The button peel stress results for σ_{Ic}

The distributions of σ_{Ic} are shown as a function of temperature in figure 6.12. Unlike G_{Ic}, the value of σ_{Ic} decreases with temperature. Whereas increased plasticity was a likely cause of increased G_{Ic} at higher temperatures, it is also a likely cause of decreased σ_{Ic}. The variability of σ_{Ic} is similar in relative magnitude to variability of G_{Ic} (approximately 20% of the mean value). When combined with the G_{Ic} results in section 6.3, the Mode I parameters are now defined.

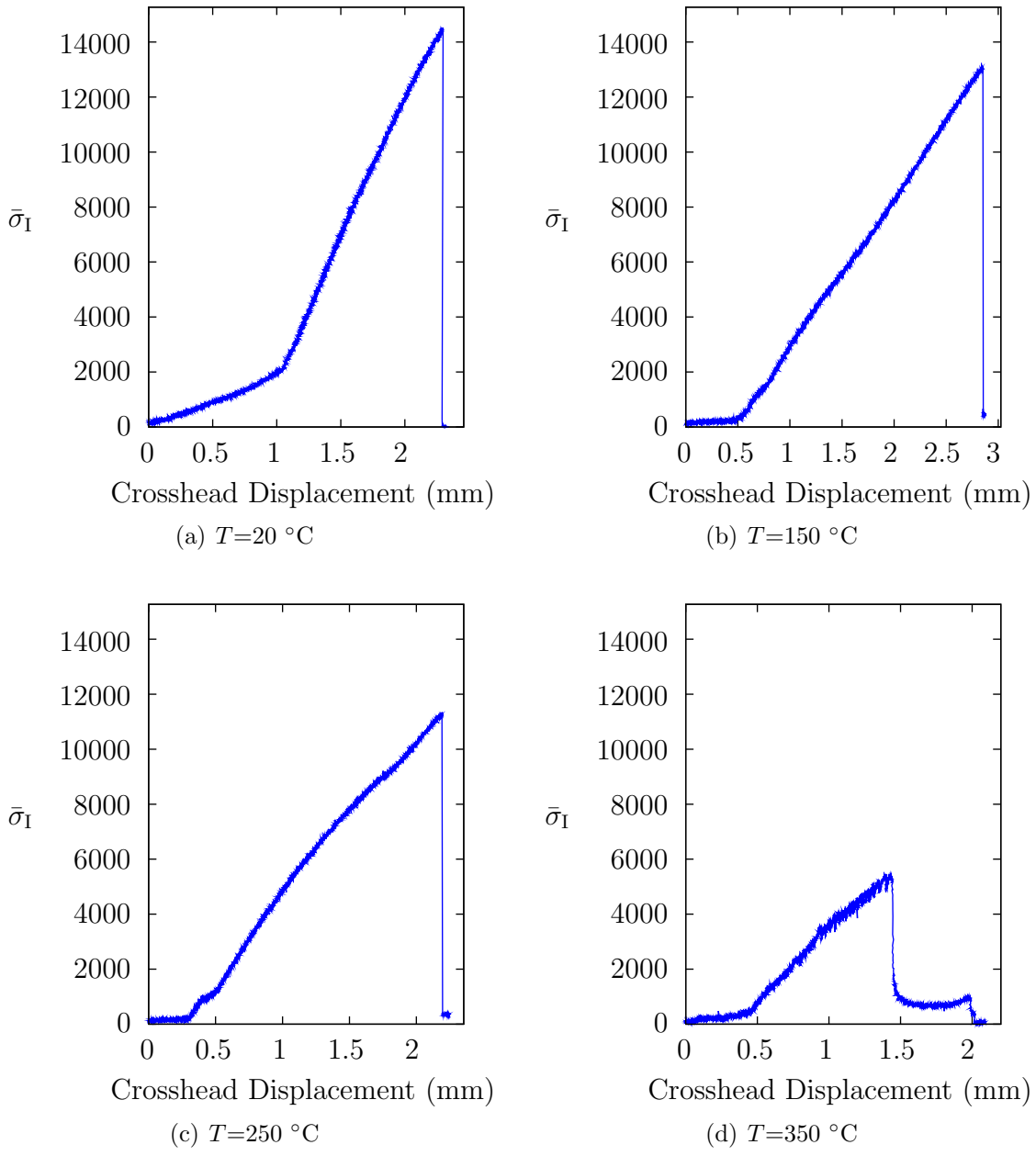

(a) T=20 °C (b) T=150 °C

(c) T=250 °C (d) T=350 °C

Figure 6.11 Typical normalized load-displacement for BPS specimens

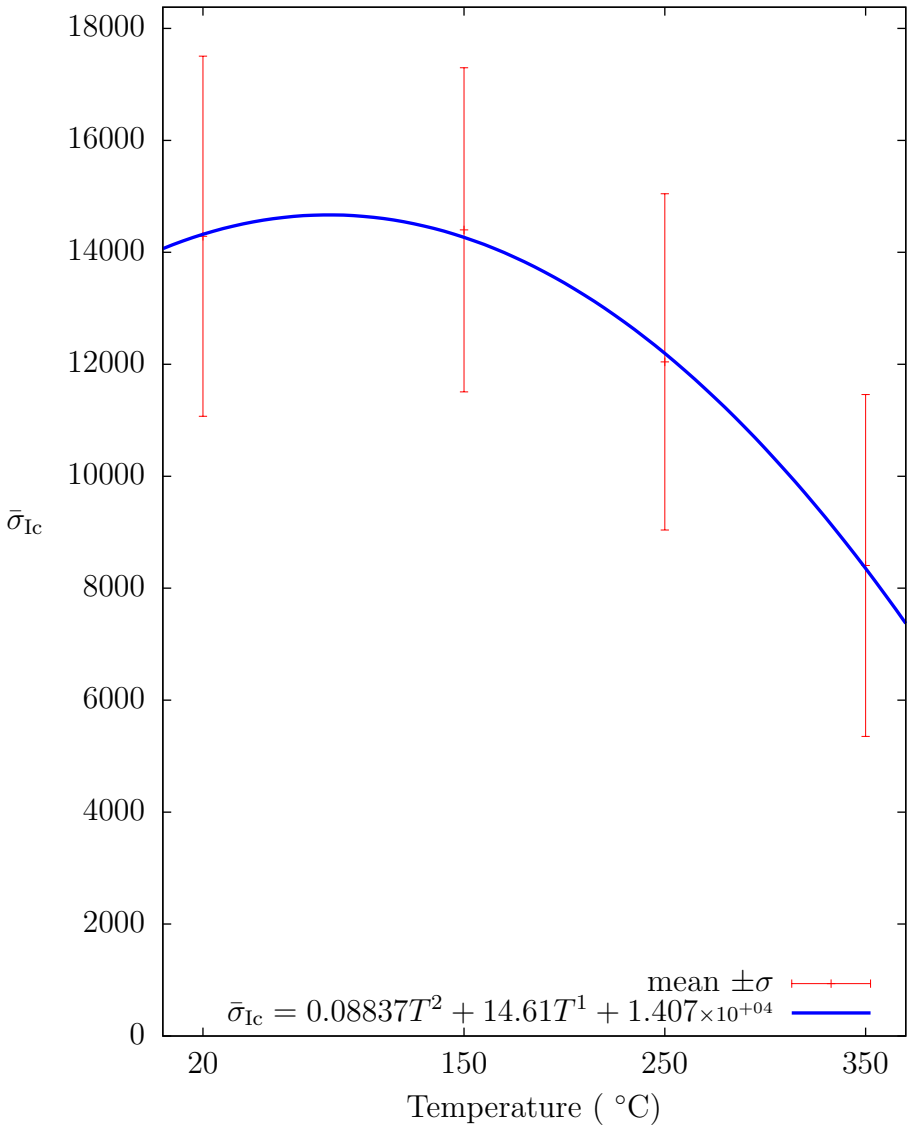

Figure 6.12 Distribution of $\bar{\sigma}_{\mathrm{Ic}}$ as a function of temperature

6.5 Experimental determination of G_{IIc}

The Mode II critical energy release rate (G_{IIc}) is the third parameter in the traction law for T650/AFR-PE-4/FM680-1 and is considered next. It is computed from the results of the end notch flexure test.

6.5.1 The end notch flexure experimental protocol

The ENF specimen geometry was described in section 6.2.3. The experiments were completed according to the geometric and data reduction recommendations presented by Davidson and Sun [37]. Four specimens were tested at each of the four temperatures. The specimen geometry was almost identical to the DCB specimens, except for the initial crack position. It was referenced to the roller support instead of the hinge. The total span ($2\,l$) was 104 mm and the support rollers had a diameter of 6.35 mm. The loading roller was 12.7 mm in diameter.

Whereas the hinge limited the ability to do compliance calibration in the DCB test, the ENF specimen had no such restriction. Therefore, a compliance calibration was completed for each specimen with the curve fitting equation given in equation 5.5. The nominal crack fractions for the calibration were {0.4, 0.5, 0.6, 0.7, 0.8} and the crosshead displacement was taken to 2.0 mm at all temperatures except 350 °C. At 350 °C, the crosshead displacement during calibration was limited to 1.5 mm to ensure no damage would occur. The nominal crack tip was determined by physical examination of both edges of the ENF specimen. There is significant uncertainty about the actual crack position due to the possibility of jagged crack fronts, [36].

The last calibration cycle was applied at a crack fraction of 0.5. Thereafter, the loading was continued from that point up to failure. After an initial crack propagation was observed during the experiment, the specimen was then partially unloaded to allow additional loading cycles. In this way, the same specimen was used to achieve at least three separate values of G_{IIc} for each specimen. These values were averaged prior to inclusion in the data set used to generate figure 6.14. The averaging technique is meant to provide a more representative value of G_{IIc} for the whole specimen.

6.5.2 The end notch flexure results for G_{IIc}

Typical load-displacement curves for the ENF test are shown in figure 6.13. The compliance calibration cycles are apparent in the figures; there are several curves at

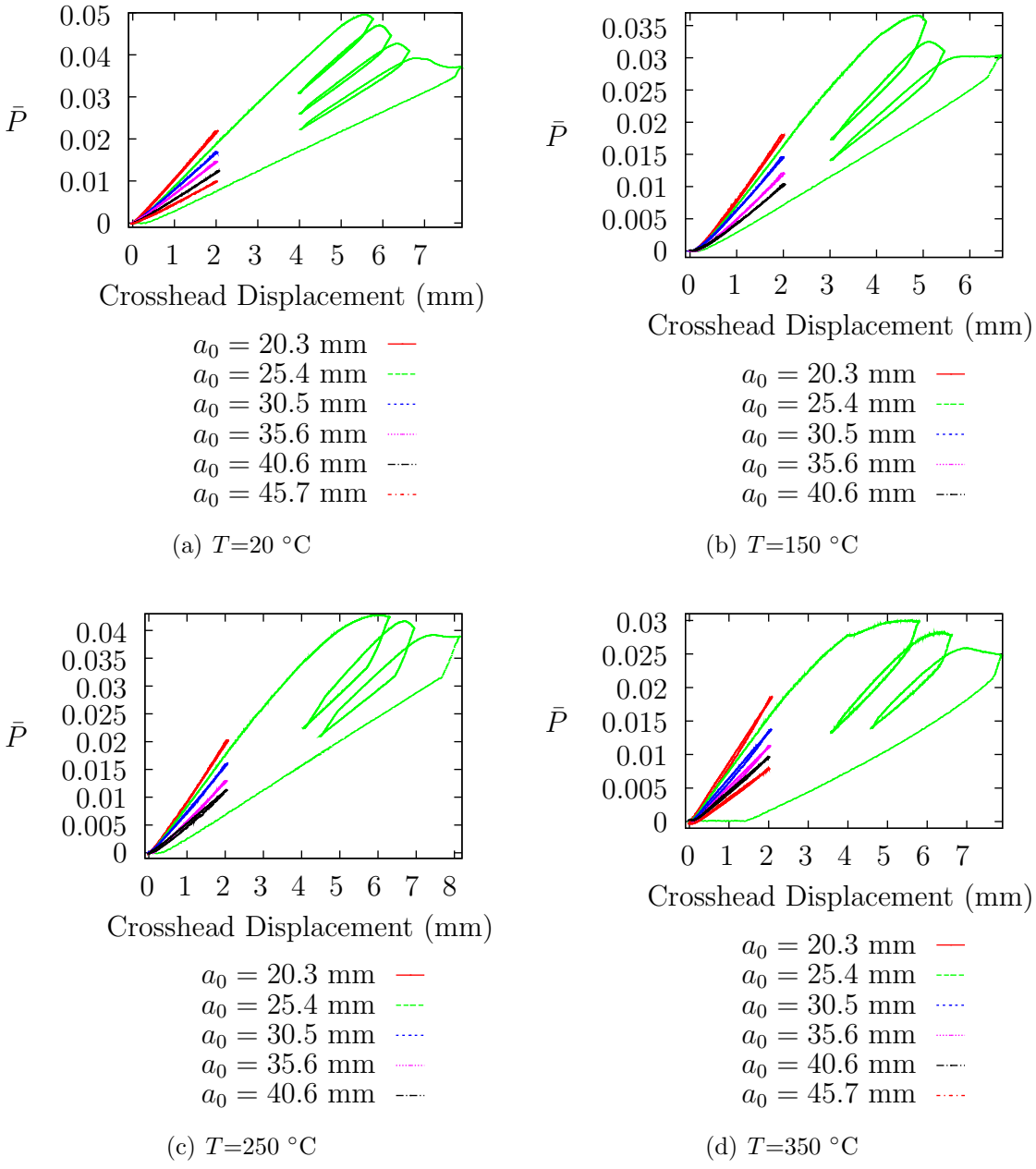

(a) T=20 °C

(b) T=150 °C

(c) T=250 °C

(d) T=350 °C

Figure 6.13 Typical load-displacement for ENF specimens

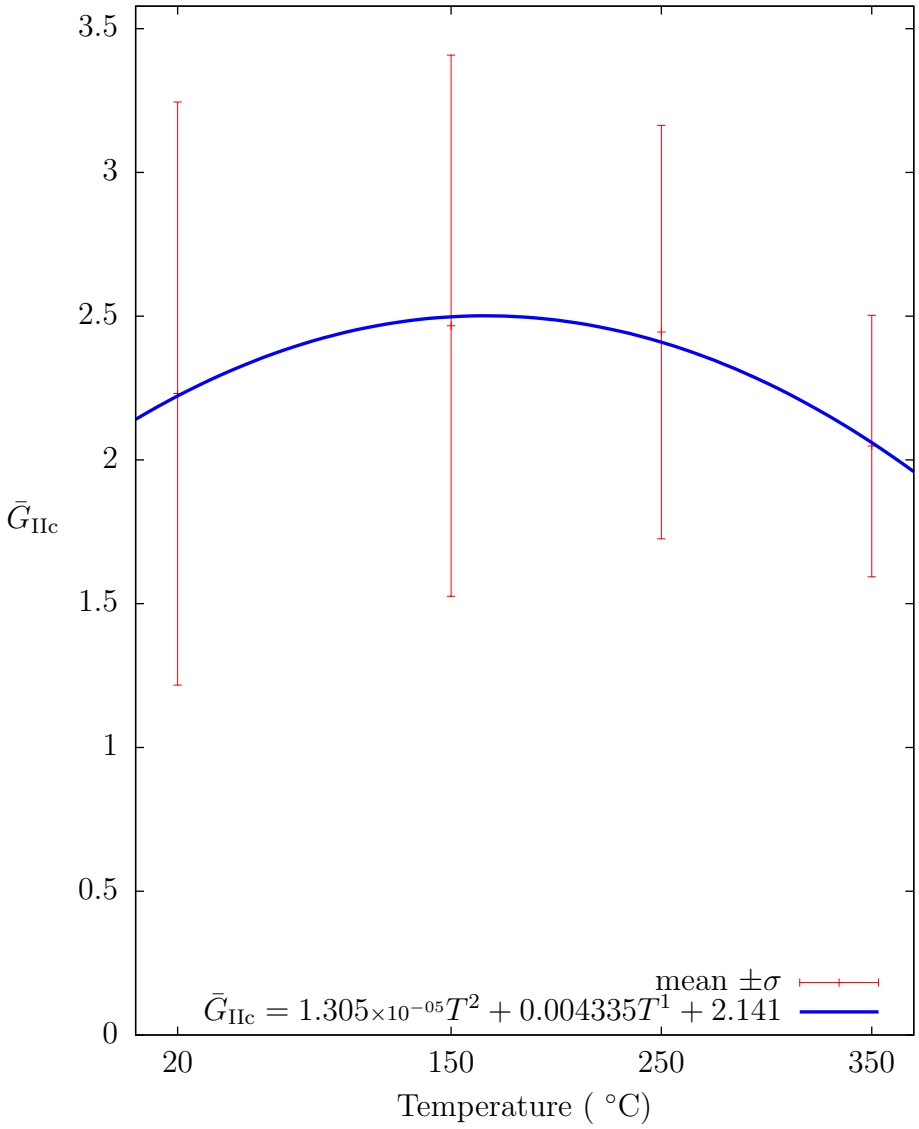

Figure 6.14 Distribution of $\bar{G}_{\mathrm{IIc}}$ as a function of temperature

different nominal crack lengths shown. Additionally, the loading and unloading cycles are also readily visible in the plots. The ENF experiments exhibited linear load-unload behavior in all specimens except at 350 °C.

The computed values of G_{IIc} are shown in figure 6.14. Comparing figure 6.14 with figures 6.8 and 6.12, it is apparent that the variability in G_{IIc} is far greater than for G_{Ic} and σ_{Ic}. This significant variability presents numerous challenges to be addressed in a later work. It is likely that the nature of the composite weave, with pockets of matrix material, contributes to the variability in the ENF results. It is possible that these pockets have greater effect on the ENF experiments than the other experiments.

Another possible source of variability is the rate of crack advance, [36, 99]. "Stick-slip" crack advance behavior was observed in some specimens, therefore, rate effects cannot be discounted. Despite the variability, the mean value of G_{IIc} is fairly consistent over the entire temperature range. The critical energy release rate in Mode II is approximately double the value in Mode I.

6.6 Experimental determination of τ_{IIc}

The final parameter in the adhesive constitutive law is the critical shear stress (τ_{IIc}). It is determined by proper interpretation of the single lap joint test.

6.6.1 The single lap joint experimental protocol

The single lap joint test was completed for four specimens at four temperatures. Specimens were prepared as reported in section 6.2.5. The wedge grip assembly was completed outside the oven and then placed into the load frame. (External assembly minimized heat losses during high temperature tests.) Unlike the BPS specimen, the relatively smooth surfaces of the adherends in the SLJ test caused difficulty with slippage in the wedge grips. In addition to the natural compression caused by the wedges, the knurled grip faces were compressed into the specimen with bolts. After the assembly reached the desired temperature, it was allowed to equilibrate for 20 minutes. Subsequently, displacement control was enforced at 0.5 mm/min until failure occurred.

6.6.2 The single lap joint results for τ_{IIc}

Representative normalized load-displacement curves for the SLJ test are shown in figure 6.16. After an initial displacement advance where wedge settling occurred, the load scaled linearly with displacement until failure. A few specimens, randomly over the temperatures, exhibited a small but noticeable crack advance with associated load drop prior to failure. An example of this is the 350 °C specimen in figure 6.16. One specimen (at 250 °C, highlighted in figure 6.16) was observed to slip in the grips, however, this only had the effect of unloading the specimen slightly. Loading was able to continue through the slippage up to a failure point. The slope of the load-displacement curve did not change appreciably after the slippage, therefore it

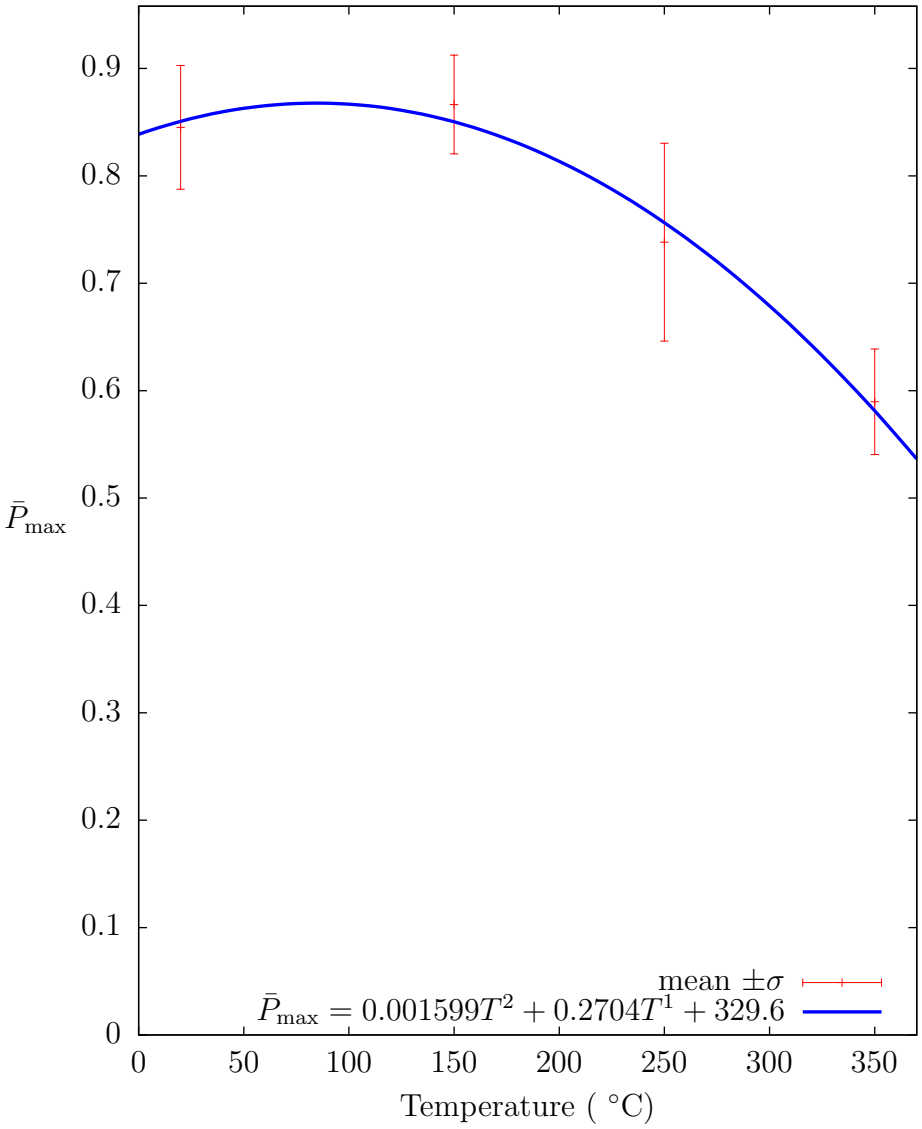

Figure 6.15 Distribution of SLJ $\bar{P}_{\max}$ as a function of temperature

was deemed to have negligible effect on the experiment. In two of the experiments (one at 20 °C and one at 350 °C), the failure was not entirely in the adhesive or at the adherend/adhesive interface. The specimens exhibited partial (20 °C) or total (350 °C) interlaminar failure. As a result, the values from these experiments are excluded from the results plotted in figure 6.15.

It was shown in chapter 5 that the SLJ test cannot be used in isolation to determine appropriate values for τ_{IIc}. To map the experimental results to a usable set of values for τ_{IIc}, the distribution of peak line loads was calculated at each temperature. This

distribution is shown in figure 6.15. Using the DACE surrogate model from chapter 5, contour lines were established in (G_{IIc}, τ_{IIc}) space from the values of the $\bar{P}_{\max}$ distributions. In the surrogate, G_{IIc} and τ_{IIc} were allowed to vary while the remaining variables were fixed at their experimental nominal values.[16]

The DACE equivalent contours of $\bar{P}_{\max}$ are shown as curving lines in figure 6.17. A conclusion of chapter 5 is apparent in this figure; there is a range of (G_{IIc}, τ_{IIc}) pairs that would predict the outcome of the SLJ experiments. To complete the parameter mapping, the ranges of G_{IIc} established by the ENF test are overlaid on the contour plot as vertical lines. The appropriate range of (G_{IIc}, τ_{IIc}) pairs for general use is the area within the two bands.

6.7 Application of the DCZM technique to a simple structural test

To explore the applicability of the parameters that have been determined in the prior sections, a simple structural test (SST) has been completed. The experimental setup, shown in figure 6.18, was designed to subject the material system to a complex state of stress in three dimensions.

Like the other tests in this chapter, the geometry of the SST was dictated by the limited supply of materials. To achieve the complex interfacial stress state without significant investment of materials, a stiffened plate specimen was designed via a series of FE models. A candidate geometry was proposed, manufactured, and tested. It was found to exhibit a repeatable failure with asymmetric adhesive fracture at the tip of one of the stiffeners. Therefore, the specimen was subjected to in-depth analysis.

The SST specimen was simply supported on the top and bottom ends and free on the sides. The plate was loaded in compression on the Instron 4201 frame.

6.7.1 The measured load-displacement curve and model results

A representative load-displacement curve for the SST is shown in figure 6.20. Initial loading was linear elastic which continued until global buckling of the specimen.

[16] In chapter 5, it was shown that the value of σ_{Ic} also affects the maximum load in the SLJ test (to a lesser degree than G_{IIc} and τ_{IIc}). In this application of the conclusions of that chapter, only G_{IIc} and τ_{IIc} are allowed to vary due to the significant variability in the experimentally determined G_{IIc}. The variability is likely to overwhelm the effects of σ_{Ic}.

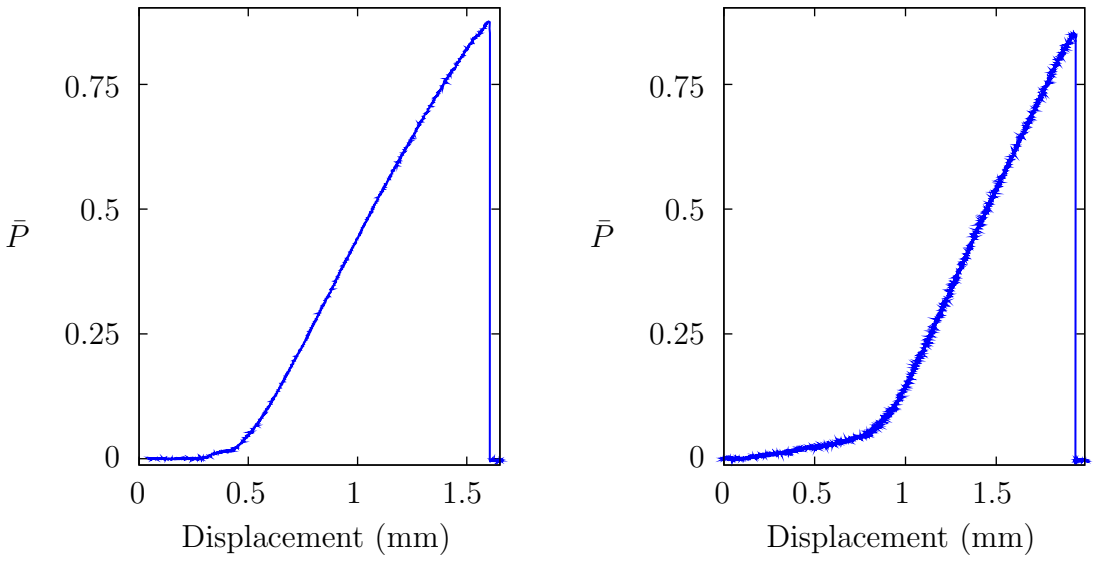

(a) T=20 °C

(b) T=150 °C

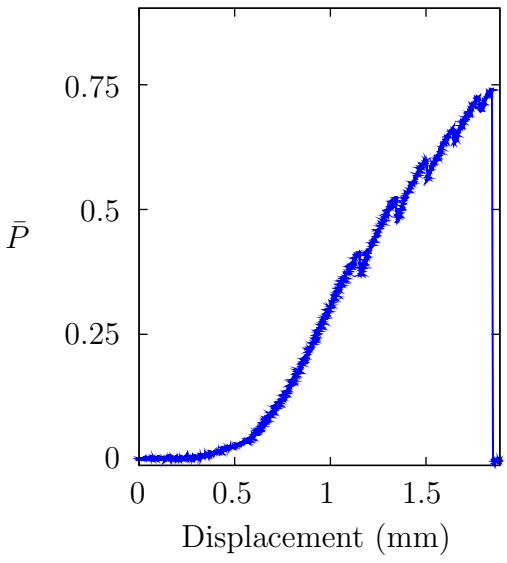

(c) T=250 °C

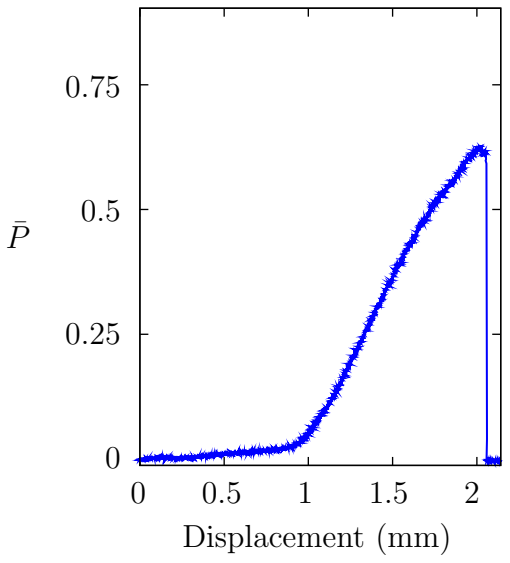

(d) T=350 °C

Figure 6.16 Typical load-displacement for SLJ specimens

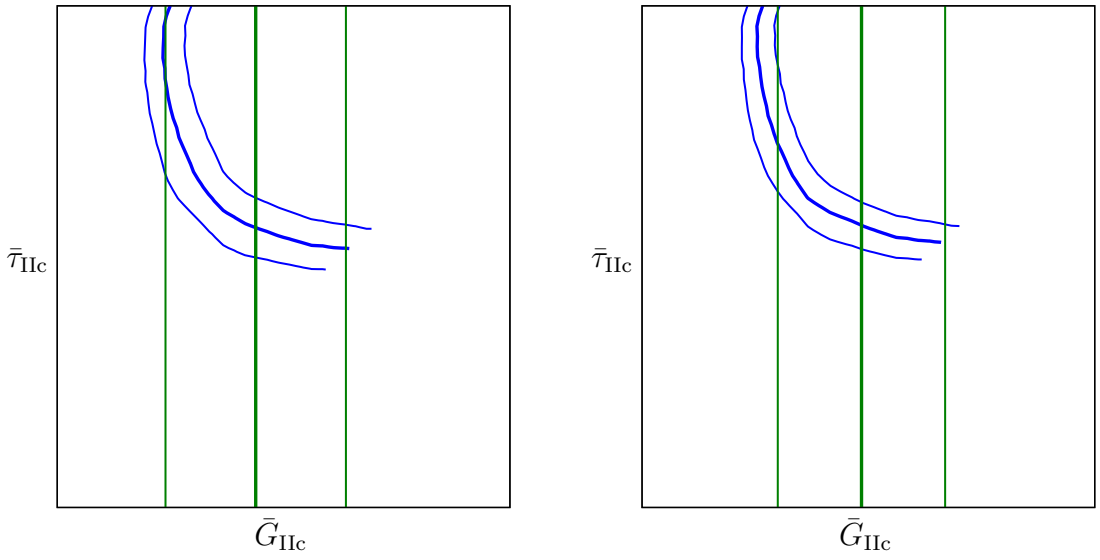

(a) T=20 °C (b) T=150 °C

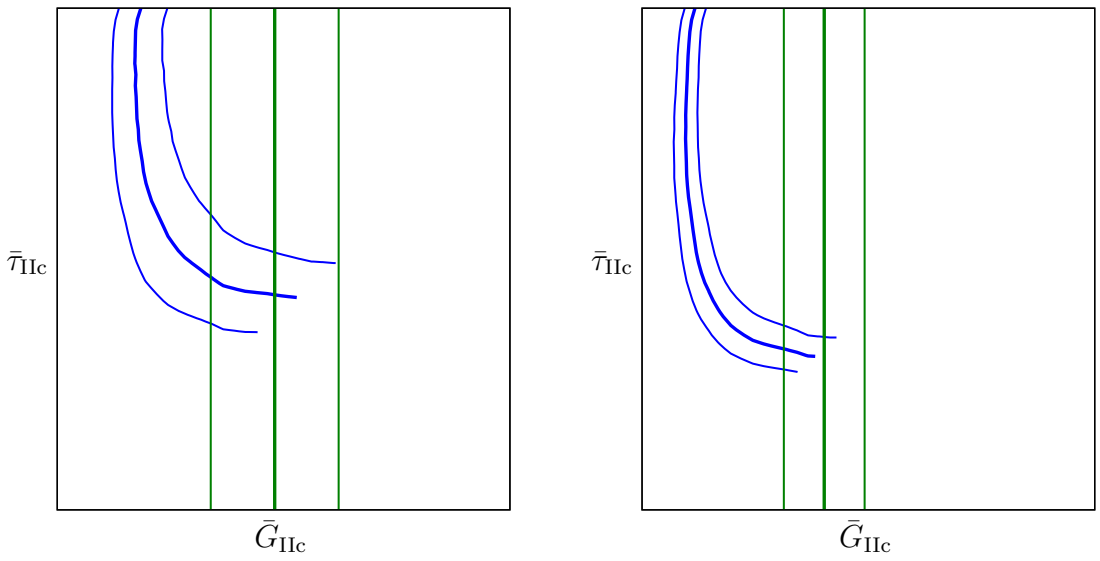

(c) T=250 °C (d) T=350 °C

Figure 6.17 Range of material parameters for Mode II

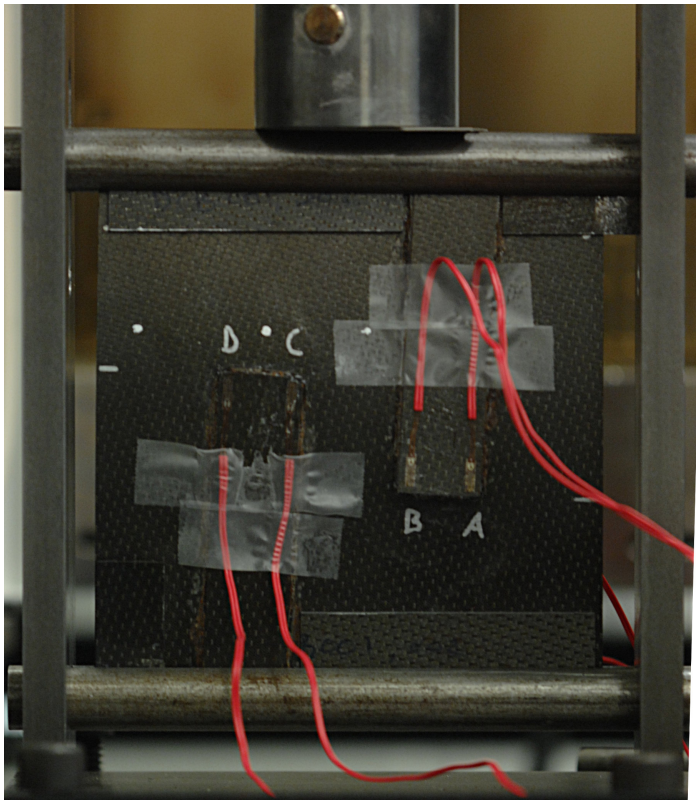

(a) Typical buckled SST specimen

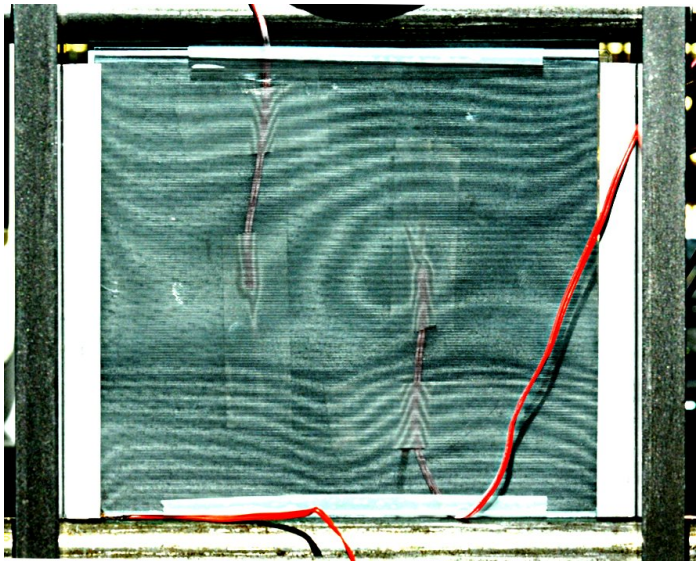

(b) Typical Moire fringe patterns of a buckled SST specimen

Figure 6.18 The experimental setup for the SST

Table 6.3 Approximate size of the SST FE model

Number of elements	79000
Number of user nodes	101000
Number of variables	1360000

Shortly after global buckling, all three SST specimens exhibited decohesion at one of the stiffener terminus locations.

FE models of the SST specimen were completed using the 3D version of the DCZM element and the adhesive constitutive law determined in the prior sections. A representative model result is shown in figure 6.19 and properties of the model are given in table 6.3. Three of these models are overlaid on top of the experimental results in figure 6.20.[17] The models are referred to as Nominal G_c, 20% of Nominal G_c, and Lower Bound. Looking first at the FE model which used nominal values of all the adhesive constitutive parameters ("Nominal G_c"), it is observed that the slope of the load displacement curve and the buckling load are both well predicted. The displacement at fracture, however, is *not* well captured; the fracture in the model occurs well past the displacement where fracture occurred in the experiment. Consequently, a subsequent model was completed using 20% of the nominal adhesive values of G_c. This model predicted failure at much lower values of crosshead displacement, however, fracture still occurred at a larger displacement than occurred in the experiment. Further reduction in the adhesive parameters resulted in convergence difficulty.

6.7.2 Possible reasons for over-prediction of fracture displacement

It is clear that some mechanism of failure is not captured by the FE model. To bound the model results, an analysis of the response for the plate with *decohered stiffeners* is shown in figure 6.20 as "Lower Bound". The FE model results correctly bound the structural response. Upon stiffener decohesion, the specimen jumps from one equilibrium path to another. The two equilibrium paths are well captured by the FE models.

Adequate prediction of the decohesion event remains an open question. There are

[17] The SST specimen was subject to initial settling of the loading frame prior to exhibiting purely linear elastic behavior. The intercept of the FE model predictions are shifted to reflect an appropriate intercept for the experimental results.

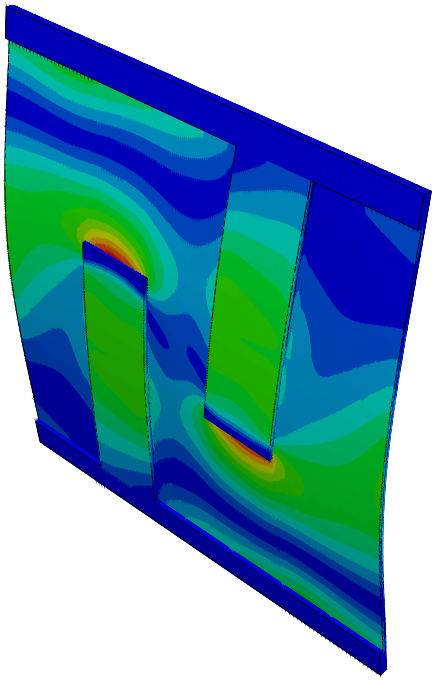

(a) Global view of buckled mode

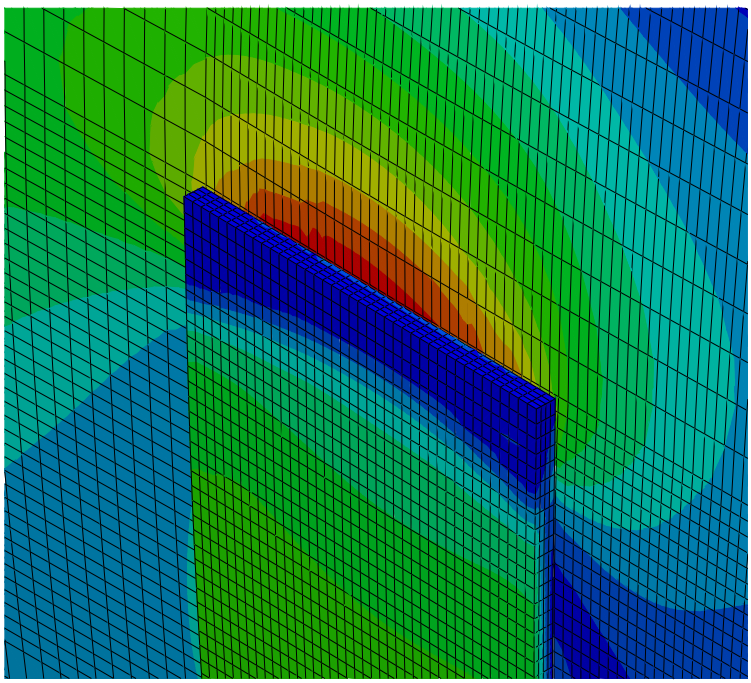

(b) Local view of stiffener terminus showing crack initiation

Figure 6.19 Representative model of the SST

several likely reasons why this event has not been captured. First, the SST specimen is subject to unstable crack propagation, however, it is also dependent on the toughness of the material system. The SST is likely to have substantial sensitivity to the large variability in Mode II critical energy release rate (G_{IIc}). A larger adhesive surface area is under active load transfer than in the ENF test, therefore, it is likely that an area of lower G_{IIc} exists under critical traction. If any surface area fails, the remaining areas are likely to follow due to unstable crack propagation. The failure event is dictated by the material that has the lowest critical energy release rate within the distribution in the specimen, hence an assumption of nominal G_{IIc} should be expected to over-predict the failure event.[18]

A second possible explanation for the over-prediction of failure load is rate dependency in the critical energy release rates. "Dynamic" crack advancement has been observed to have lower values of critical energy release rate than "quasi-static" crack advances, [36, 99]. The experimental values of G_{c} were all determined using a (relatively) slow rate of crack advance. If the T650/AFR-PE-4/FM680-1 material system is rate dependent, the dynamic crack propagation event in the SST specimen would be expected to occur at a lower failure load than the steady state values of G_{c} predict. Furthermore, rate dependence in G_{IIc} would help to explain the large variability in the quasi-static G_{IIc} values determined in section 6.5. Both the ENF and DCB specimens were observed to exhibit some level of "stick-slip" (piecewise crack advance) and the rates of those advances vary from specimen to specimen. Although no attempt was made to determine the rates of crack advance, it is possible that the wide variability in the G_{IIc} values is due (at least in part) to rate effects.

Finally, it is possible that the mixed-mode assumption[19] is not appropriate for T650/AFR-PE-4/FM680-1.[20]

Only additional testing in mixed mode loading and at different rates of crack advance can determine if these possible reasons are correct explanations for the difference between the predicted and measured response in the SST test. Unfortunately, the available material for experimentation has been exhausted. Acquisition of additional materials would have to be justified by ongoing interest and support from the sponsors of this work.

[18] Since the ENF specimen is subject to stable crack propagation, it is not dependent on the minimum toughness in the same way that the SST is dependent on the minimum toughness.

[19] See equation 5.6.

[20] A short list of references for mixed-mode fracture includes: [7, 9, 11, 17, 22, 23, 32, 35, 113]. The list is not exhaustive. Due to ITAR, no published mixed-mode data on T650/AFR-PE-4/FM680-1 is currently available.

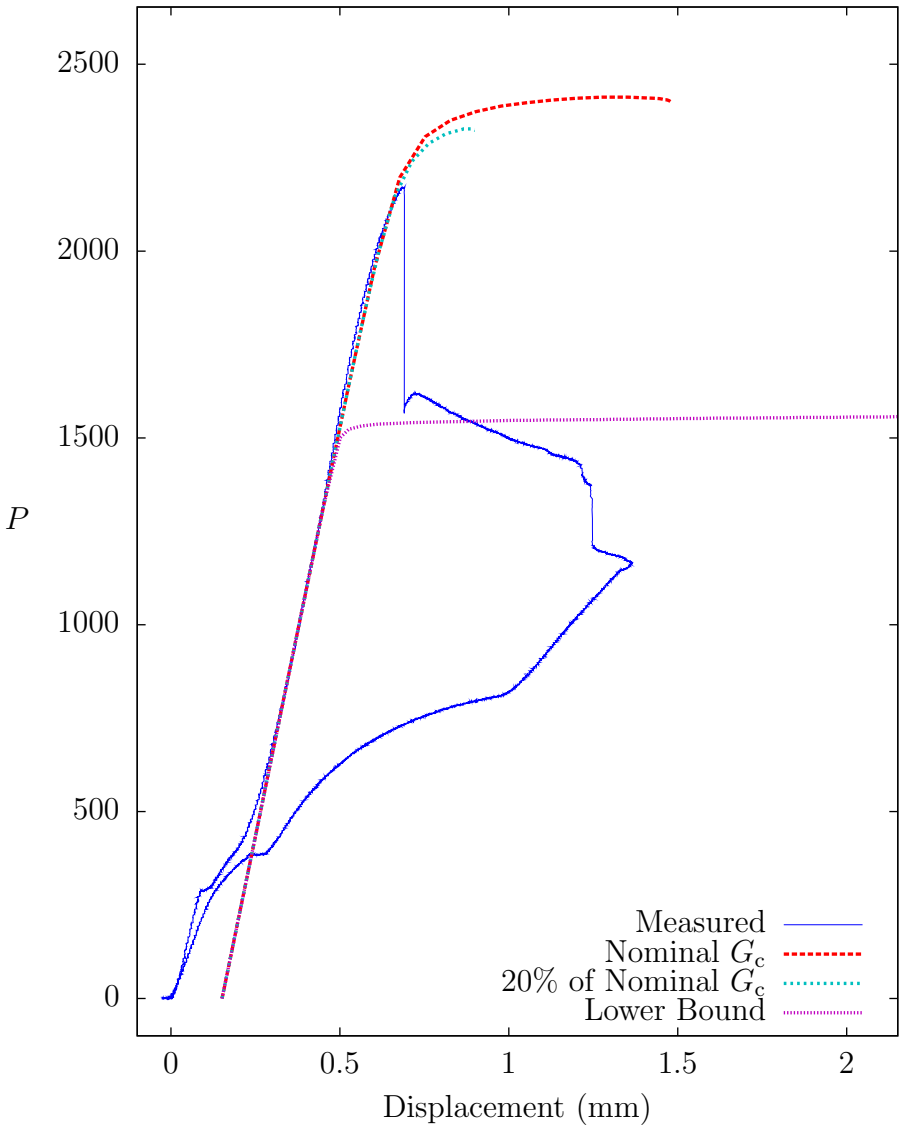

Figure 6.20 Typical load-displacement in the SST experiment and FE model. Nominal values of the adhesive parameters over-predict the maximum load. Diminished G_c values improve the correlation. The experimental results are well bounded by the FE model predictions.

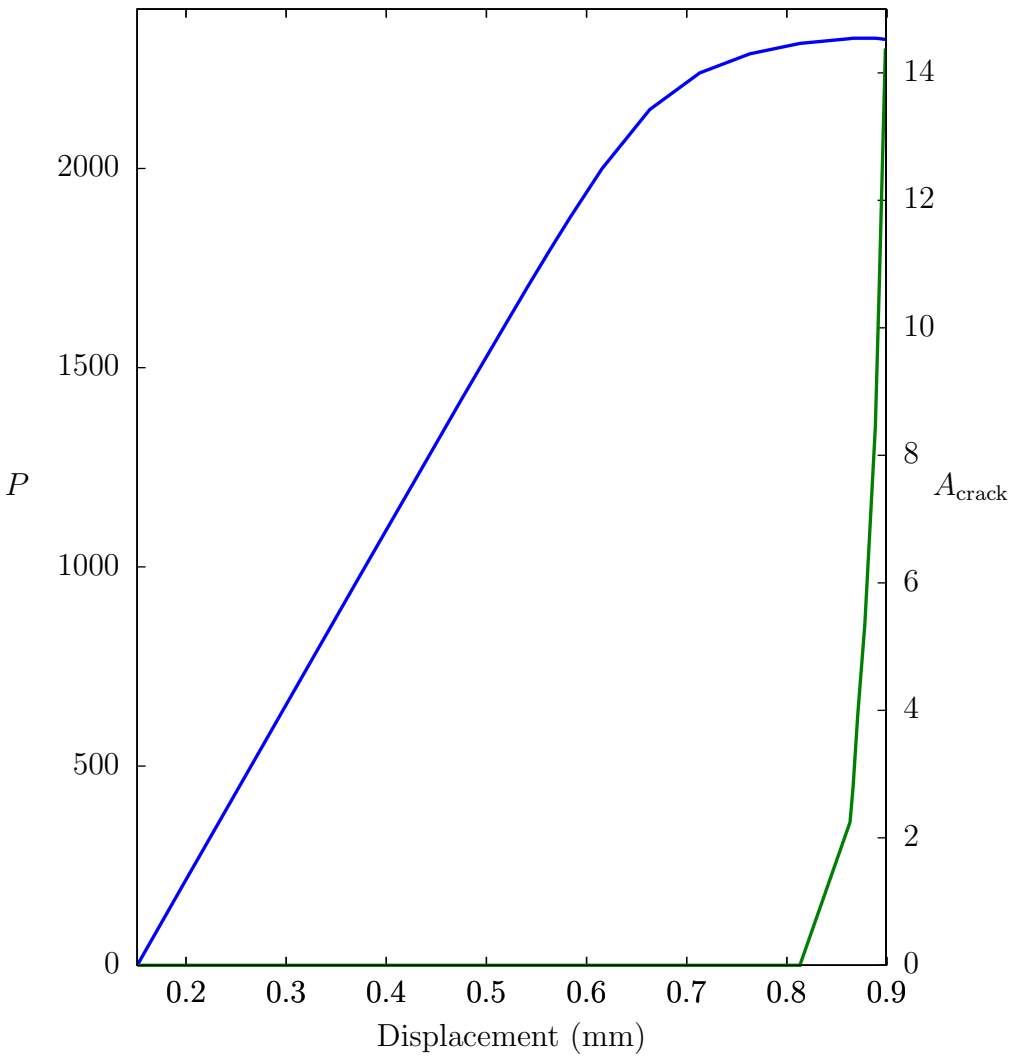

Figure 6.21 Typical crack advancement in the SST FE model

6.8 Conclusion

An experimental study of the adhesive parameters of a T650/AFR-PE-4/FM680-1 material system has been presented. A four parameter constitutive law (G_{Ic}, σ_{Ic}, G_{IIc}, and τ_{IIc}) has been developed for the DCZM element over the range of 20-350 °C. Four types of experiments were completed and a novel mapping approach was used to determine a complete set of parameter values that can properly account for the traction law interactions that occur in the characterization experiments.

The first parameter is the Mode I critical energy release rate (G_{Ic}) as determine by the double cantilever beam test. Two separate forms of the critical energy release rate were computed based on the area method ($G^{\mathrm{a}}_{\mathrm{Ic}}$) and the inverse method ($G^{\mathrm{i}}_{\mathrm{Ic}}$). The values of G_{Ic} were found to increase with increasing temperature. At 350 °C, the calculation of $G^{\mathrm{a}}_{\mathrm{Ic}}$ may have been effected by adherend plasticity as well as other dissipative mechanisms. The values of $G^{\mathrm{i}}_{\mathrm{Ic}}$, however, are not nearly as sensitive to dissipative effects and yield models with excellent experimental correlation. Finite elements and the discrete cohesive zone method were used to inverse model the experimental results. Two criteria were established to compare the experimental results with the inverse model output. At the conclusion of the inversion, the model results were found to be in excellent agreement with the experimental measurements.

The second parameter in the traction law was the critical peel stress (σ_{Ic}). This parameter was determined from a set of custom button peel stress experiments. The values were found to decrease with temperature. The remaining parameters in the traction law (G_{IIc} and τ_{IIc}) were determined by the mapping procedure recommended in chapter 5. First, the distributions of G_{IIc} were determined using compliance calibration and the ENF test. The adhesive retained its toughness through 250 °C; it decreased thereafter. The variability in G_{IIc} was higher than the other parameters. Subsequently, the SLJ test was completed and the results were mapped to τ_{IIc} (in the context of the established G_{IIc} values). The ranges of τ_{IIc} were found to decrease with temperature after 150 °C. This novel mapping of experimental results to appropriate material parameters was necessary due to parameter interactions in the standard experiments.

The four parameter constitutive law provides a distribution of model inputs for design and analysis of joints made from the T650/AFR-PE-4/FM680-1 material system. Generalization of the constitutive law to structural predictions will require additional investigation due to possible rate effects in the adhesive parameters.

Chapter 7

Conclusions and future work

In this dissertation, several methods are developed for the design and analysis of adhesively bonded joints. Those methods are briefly summarized in this chapter and suggestions are made for future work.

7.1 Summary of contributions

In chapter 2, two closed-form analytical solutions are developed which allow stress field prediction in orthotropic adhesively bonded symmetric double lap joints. The objective of the solutions is to reveal underlying joint performance characteristics via a set of dimensionless parameters. A critical dimensionless load ratio is found which predicts the character of the stress distribution based on the ratio of applied thermal and mechanical loads. The solutions are compared to finite element (FE) models and are found to provide directionally correct comparative results. Predictions using the analytical solutions are suitable for joint sizing and joint to joint comparison. The orthotropic material description in the solutions is important for composite materials, particularly with recent advancements in z-pin and 3D woven composites.

Closed-form analytical solutions provide valuable insight, however, their use is limited by the complexity of the equations. Numerical solutions have more flexibility, though, they too have limitations. In chapter 3, a compromise is found in the bonded joint finite element. The bonded joint finite element (BJFE) uses an accurate displacement interpolation for analyzing a specific type of joint. In doing so, it allows a complicated analytical solution to be used in the context of the numerical (FE) work flow. In the current implementation, the displacement interpolation within the BJFE is based on a closed-form analytical solution which would difficult to use in general

practice. In automated BJFE form, however, the element and its underlying solution accurately predict the field properties in a double lap joint. It does so in a manner that is accessible for an analyst. The BJFE enables the inclusion of multiple joints in a system or vehicle level FE analysis where doing so would be prohibitively expensive with classical techniques. The BJFE is mesh-independent, therefore, it removes the burdon of carefully constructed FE meshes and significantly reduces the total cost joint analysis. The BJFE is a mid-level analysis technique, bridging the gap between the inexpensive approach (no analysis) and the expensive approach (high level single joint analysis).

The objective of the BJFE analysis is to rapidly identify problem areas where the higher level techniques should be used. It is not intended to replace the detailed analysis techniques that are capable of precisely predicting joint failure. One higher level technique, referred to as the discrete cohesive zone method (DCZM), is presented in chapter 4. The DCZM element is intended to predict joint failure along a defined crack path. The prediction is accomplished via a set of non-linear spring elements which provide fracture initiation and propagation criteria. Localized plastic deformation and fracture energies are enveloped into a set of adhesive constitutive parameters. The resulting element provides a framework for 2D and 3D models of delamination, crack initiation, and crack propagation.

An important obstacle to widespread use of DCZM and similar techniques is the convergence of cohesive models. The unstable nature of many cohesive problems, when combined with the strain softening in the constitutive laws, yields poorly conditioned matrices and convergence difficulties. In additional to a general description of the current DCZM element, chapter 4 addresses convergence through the use of two smooth traction laws that are designed for convergence efficiency. The smooth laws, modeled after the beta probability distribution and sine functions, are found to exhibit significantly lower cost and greater robustness (relative to the triangular and trapezoidal laws that are in common use) in two canonical problems.

The justification for choosing a "smooth" traction law is presented in chapter 5. The sensitivities of standard experiments to experimental parameters are examined using techniques for design and analysis of computer experiments. In addition to showing that the form of the traction law is negligible (and thereby establishing justification for the use of a computationally efficient traction law), the sensitivities of the assumed adhesive parameters are quantified and compared to the well understood geometric and constitutive parameters. The double cantilever beam test is found to be an excellent test for determining the critical energy release rate in Mode I (G_{Ic}). The

end notch flexure test is a good test, however, a minor interaction is identified between the critical energy release rate (G_{IIc}) and the critical stress (τ_{IIc}) of the adhesive constitutive model. The interaction justifies careful consideration of the outcomes of other tests in mapping of the test results to a set of constitutive parameters. Finally, the single lap joint test is found to be highly sensitive to three adhesive constitutive parameters (G_{Ic}, G_{IIc}, τ_{IIc}). As a result, significant consideration must be given to other test results when mapping the single lap joint results to a set of constitutive parameters. At the conclusion of chapter 5, a mapping procedure is developed that accounts for the experimental interactions.

Finally, chapter 6 applies the DCZM analysis technique and the outcome of the sensitivity analysis to interpret a set of experimental results for a material system of current interest. The results of four sets of experiments are described and used to establish a range of appropriate material parameters for use in modeling structures of composed of T650/AFR-PE-4/FM680-1. The experiments were performed over the temperature range of 20-350 °C. The mapping procedure described in chapter 5 is demonstrated based on the experimental results. Finally, the outcome of a structural test is reported which highlights open issues in modeling adhesive joints in complex structures.

7.2 Future work

The techniques described in this dissertation have potential for improving the prediction of joint behavior over a range of temperatures. The field is developing, however, and significant research is still needed.

7.2.1 Additional bonded joint finite elements

There is a great need for analytical sizing tools for composite joints. Building on the BJFE technique developed in chapter 3, a "toolbox" of joint specific elements could be assembled for use in joint sizing, trade studies, and system level analysis. Several joint specific element types should be created. For example, candidate joints types include: single lap, scarf, bevel, step, and butt strap joints. Beyond the development of other joint element types, failure metrics could be embedded in the BJFE technique. This would extend their usefulness beyond sizing and comparative analysis to initial and/or progressive failure predictions. Furthermore, hybrid BJFE joint elements could

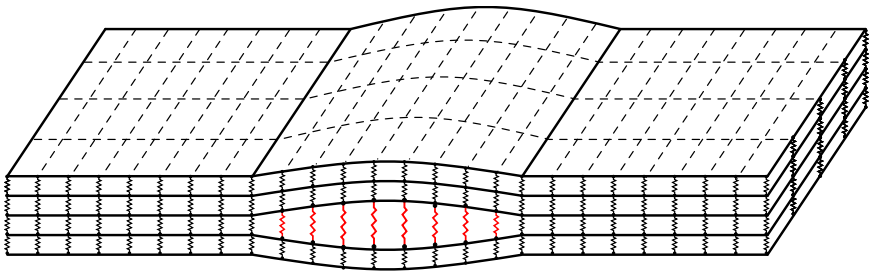

Figure 7.1 Schematic representation of a mesh of composite shell elements with ply-by-ply delamination capabilities.

be formulated that are predictive of bolted-bonded or other hybrid joints.

7.2.2 Prediction of delamination growth

A primary failure mechanism of composite materials is delamination. Among the causes of delamination in aircraft is impact (such as a bird strike, hail, ground debris, or other ballistic impacts).

To improve the engineering response to decohesion in joints and delamination, advanced composite manufacturing techniques are being developed which align fibers in the "out-of-plane" direction. These 3D woven composites and z-pin methods intimately stitch the interlaminar interfaces. As a result, these composite joints and laminates are likely to have higher delamination and decohesion strength and toughness values. In these materials, the fundamental physical mechanisms of delamination may differ from the traditional mechanisms; therefore, further research into fracture and failure are needed. Due to the complexity of these 3D woven composite systems, it is likely that advanced computational techniques will be required to marry the local behavior of the fibers and matrix to the global behavior of the structures.

Prediction of delamination can be accomplished through the integration of shell element and DCZM element formulations and is a natural extension of the research described in this chapter 4. This "delamination shell element", shown schematically in figure 7.1, could provide a physically based delamination scheme on a ply-by-ply basis within a composite model. The technique would provide cutting edge predictive capabilities that are essential to design and assessment of structural robustness. Delamination shell elements are directly applicable to the development of: aircraft, spacecraft, automobiles, nautical structures, defense applications, and energy generating structures.

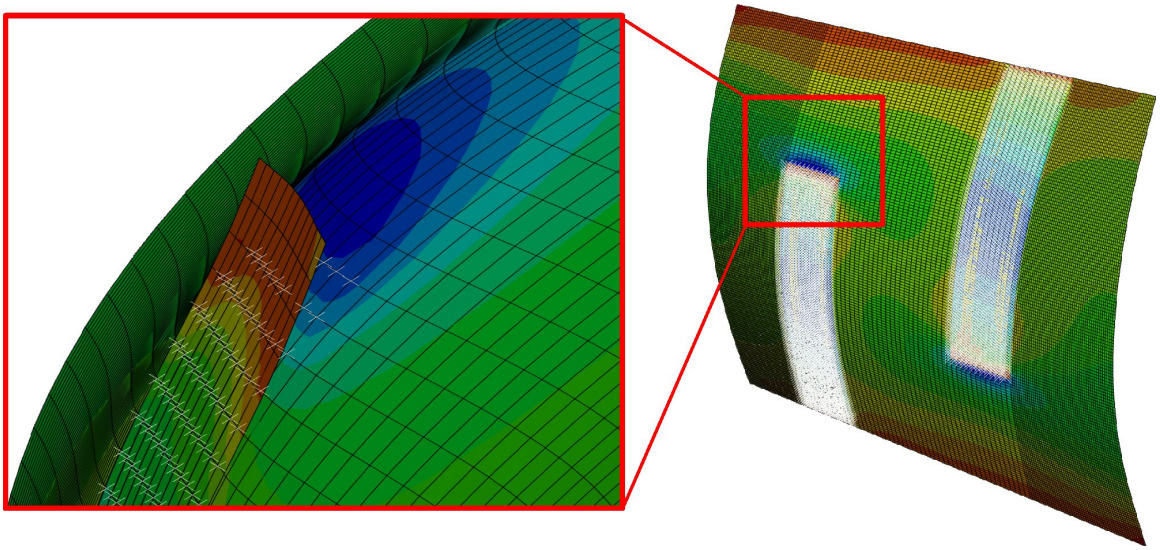

Figure 7.2 A stiffened composite specimen subjected to compression and modeled with delamination shell elements. Adhesive failure is predicted at the termination of the stiffener. Broad adoption of 3D delamination models is likely to require improvements in convergence efficiency and robustness of cohesive elements

7.2.3 Efficient analytical solutions for structural joints, composite delamination, and progressive failure

Although progress has been made, the DCZM and similar analysis techniques can be improved. An obstacle to widespread use is the lack of robust convergence and the associated computational cost. The concept of choosing a traction law with computational efficiency in mind is an improvement (reported in chapter 4), however, it does not completely eliminate convergence difficulties. For example, it is still difficult to obtain a solution when large numbers of integration points are simultaneously in a strain softening regime. Also, unstable crack advance remains a challenge. Further research is required to improve analysis robustness in the face of these challenges. Advancements will be necessary for larger 3D structural analysis and prediction of delamination via the delamination shell element.

7.2.4 Hybrid joints

Bolted joints have been viewed as sub-optimal when applied to fiber reinforced composite materials. They are, however, in common use in composite joint applications. Hybrids joints (bolted and bonded) are of current interest due to their redundant load

paths and relative improvement in load transfer efficiency.

As an example of the potential of hybrid joints, large scale wind turbines are likely to be an important contributor to world energy supplies in the middle and long term. Turbine blades are limited in size by transportation requirements. Transportation also adds considerably to the cost of installation of wind turbine facilities. As a result, turbine manufactures are investigating optimal methods by which turbine blades can be manufactured in sections and assembled on site. These methods include bolted and hybrid bolted/bonded joints along the blade span. Similarly, NASA's Project Constellation is considering the use of hybrid joints for the Orion Crew Module and other applications. The redundancy of load path is seen as necessary to ensure safety.

If turbine blades are to be optimally assembled and human space flight is to be conducted safely, it will be critical that these bolted and hybrid joint failure mechanisms are well understood and predicted. Experiments must be designed to illustrate critical aspects of bolted and hybrid joint failure. It is certain that the design (material selection, stacking sequence, etc) and fabrication of the composite layup will effect bolted joint failure mechanisms. Properly designed and executed experiments are necessary for determining these effects. Predictive computational capabilities must validated against the experiments. These computational capabilities may be based on (or similar to) the BJFE or may take a different form as dictated by the fundamental physics of the problem.

Other areas of direct applicability for bolted and hybrid joints are rocket bodies, reentry parachute attachments, aircraft fuselage, and many others. Bolted and hybrid joints compose parallel fields which deserves similar treatment as has been given to bonded joints at the center of this work.

7.2.5 Joint fatigue

Ongoing developments in non-destructive evaluation and integrated structural health monitoring will provide unprecedented capability to identify structural damage in composite structural applications such as joints. During initial design or after identification of damage, prediction of damage progression and life are essential steps in decision making with regard to safety and structural integrity.

Whereas the fatigue life of metallic structures has been studied for decades and is still an active area of research, the added complexity of composite materials will require a significant level of additional research. Damage progression models are necessary at the local and structural levels as well as in coupled local/global models.

Since composite materials do not exhibit an "endurance stress", a composite fatigue or joint fatigue approach is likely to require analytical tools that included load spectrum analysis and representative load selection. Matrix, adhesive, and fiber failure must be considered independently and in a coupled sense. Chemical composition/degradation and hygrothermal effects must also be evaluated in joints of polymeric composites.

Composite joint fatigue and life prediction is crucial to the aircraft industry. Cyclic pressurization of fuselages and repetitive loading of primary structural components are critical areas that require accurate prediction of damage progression and fatigue life.

7.2.6 Rate effects in T650/AFR-PE-4/FM680-1 and experimental correlation

Although a constitutive model has been established for prediction of cohesive failure of T650/AFR-PE-4/FM680-1 (chapter 6), this set of parameters has only been used in a limited set of circumstances. Open questions remain such as the possibility of rate dependence in the critical energy release rates and the appropriate mixed-mode failure criterion. Also, T650/AFR-PE-4/FM680-1 is an isolated material system among many systems. As new material systems become available, it is likely that unforeseen behavior will be observed.

Due to the complexity of joint responses and failure mechanisms, experimental correlation need be emphasized before consensus can be established on appropriate design parameters and modeling techniques.

7.3 Concluding remarks

The potential benefits of adhesively bonded joints are attractive to structural designers. Current analytical capabilities require larger design margins than are desired for validated analytical techniques. Additional improvements are needed if analytical, computation, and experimental methods are to enhance and extend the use of adhesively bonded joints in engineering practice.

Appendices

Appendix A

Extended description of the virtual work calculations

The principal of virtual work solutions are briefly summarized below. Equilibrium relations derived in sections 2.3 and 3.3 are given in tables A.1 and A.2 as well as their associated virtual stress quantities.

In tables A.1 and A.2, all virtual stress quantities can be written in terms of the central adherend virtual stress $\hat{\sigma}_{a11}$. The principal of virtual work is applied using:

$$\delta W = \sum_i \int (\hat{\sigma}_i \epsilon_i)\, dV_i = 0, \tag{A.1}$$

where i represents the quantities listed in tables A.1 and A.2 for each solution. Equation A.1 applies for an arbitrary virtual stress $\hat{\sigma}_{a11}(x)$. Plane strain constitutive relations (described in equation 2.1) govern each material (represented by the index κ). The field equations and boundary terms of the SO, SP, and BJFE solutions become apparent when integration of equation A.1 is performed by parts.

Table A.1 Stresses and virtual stresses included in the SO and SP solutions

(a) Quantities included in the both the SO and SP models

Equilibrium Stress	Virtual Stress
$\sigma_{a11}(x)$	$\hat{\sigma}_{a11}(x)$
$\tau_{b12}(x) = -\frac{t_a\left(\frac{d}{dx}\sigma_{a11}(x)\right)}{2}$	$\hat{\tau}_{b12}(x,y) = -\frac{t_a\left(\frac{d}{dx}\hat{\sigma}_{a11}(x)\right)}{2}$
$\sigma_{c11}(x) = \frac{P}{t_c} - \frac{t_a\,\sigma_{a11}(x)}{2\,t_c}$	$\hat{\sigma}_{c11}(x,y) = -\frac{t_a\,\hat{\sigma}_{a11}(x)}{2\,t_c}$

(b) Quantities included only in the SP model

Equilibrium Stress	Virtual Stress
$\sigma_{b22}(x,y) = \frac{t_a\left(\frac{d^2}{dx^2}\sigma_{a11}(x)\right)(y-t_b)}{2}$	$\hat{\sigma}_{b22}(x,y) = \frac{t_a\left(\frac{d^2}{dx^2}\hat{\sigma}_{a11}(x)\right)(y-t_b)}{2}$
$\sigma_{p22}(\bar{x}=0,y) = \frac{t_a\left(\frac{d}{dx}\sigma_{a11}(x)\right)(y-t_b)}{2\,t_p}$	$\hat{\sigma}_{p22}(\bar{x}=0,y) = \frac{t_a\left(\frac{d}{dx}\hat{\sigma}_{a11}(x)\right)(y-t_b)}{2\,t_p}$
$\sigma_{p22}(\bar{x}=1,y) = -\frac{t_a\left(\frac{d}{dx}\sigma_{a11}(x)\right)(y-t_b)}{2\,t_p}$	$\hat{\sigma}_{p22}(\bar{x}=1,y) = -\frac{t_a\left(\frac{d}{dx}\hat{\sigma}_{a11}(x)\right)(y-t_b)}{2\,t_p}$

Table A.2 Stresses and virtual stresses in the BJFE solution [a]

Equilibrium Normal Stress	Virtual Normal Stress
$\sigma_{a11}(x)$	$\hat{\sigma}_{a11}(x)$
$\sigma_{c11}(x) = \frac{P}{t_c} - \frac{t_a\,\sigma_{a11}(x)}{2\,t_c}$	$\hat{\sigma}_{c11}(x,y) = -\frac{t_a\,\hat{\sigma}_{a11}(x)}{2\,t_c}$
$\sigma_{a22}(x,y) = \frac{d^2}{dx^2}\sigma_{a11}(x)\left(\frac{y^2+t_a y}{2} - \frac{t_a(t_c+2t_b)}{4}\right)$	$\hat{\sigma}_{a22}(x,y) = \frac{d^2}{dx^2}\hat{\sigma}_{a11}(x)\left(\frac{y^2+t_a y}{2} - \frac{t_a(t_c+2t_b)}{4}\right)$
$\sigma_{b22}(x,y) = \frac{t_a\left(\frac{d^2}{dx^2}\sigma_{a11}(x)\right)(2y-t_c-2t_b)}{4}$	$\hat{\sigma}_{b22}(x,y) = \frac{t_a\left(\frac{d^2}{dx^2}\hat{\sigma}_{a11}(x)\right)(2y-t_c-2t_b)}{4}$
$\sigma_{c22}(x,y) = -\frac{t_a\left(\frac{d^2}{dx^2}\sigma_{a11}(x)\right)(y-t_c-t_b)^2}{4t_c}$	$\hat{\sigma}_{c22}(x,y) = -\frac{t_a\left(\frac{d^2}{dx^2}\hat{\sigma}_{a11}(x)\right)(y-t_c-t_b)^2}{4t_c}$
Equilibrium Shear Stress	**Virtual Shear Stress**
$\tau_{a12}(x,y) = -\frac{\frac{d}{dx}\sigma_{a11}(x)(2y+t_a)}{2}$	$\hat{\tau}_{a12}(x,y) = -\frac{\frac{d}{dx}\hat{\sigma}_{a11}(x)(2y+t_a)}{2}$
$\tau_{b12}(x) = -\frac{t_a\left(\frac{d}{dx}\sigma_{a11}(x)\right)}{2}$	$\hat{\tau}_{b12}(x,y) = -\frac{t_a\left(\frac{d}{dx}\hat{\sigma}_{a11}(x)\right)}{2}$
$\tau_{c12}(x,y) = \frac{t_a\left(\frac{d}{dx}\sigma_{a11}(x)\right)(y-t_c-t_b)}{2t_c}$	$\hat{\tau}_{c12}(x,y) = \frac{t_a\left(\frac{d}{dx}\hat{\sigma}_{a11}(x)\right)(y-t_c-t_b)}{2t_c}$
Equilibrium End Post Stress	**Virtual End Post Stress**
$\sigma_{p22}(\bar{x}=0,y) = \frac{t_a\left(\frac{d}{d\,x}\,\sigma_{a11}(x)\right)(y-t_b)}{2\,t_p}$	$\hat{\sigma}_{p22}(\bar{x}=0,y) = \frac{t_a\left(\frac{d}{d\,x}\,\hat{\sigma}_{a11}(x)\right)(y-t_b)}{2\,t_p}$
$\sigma_{p22}(\bar{x}=1,y) = -\frac{t_a\left(\frac{d}{d\,x}\,\sigma_{a11}(x)\right)(y-t_b)}{2\,t_p}$	$\hat{\sigma}_{p22}(\bar{x}=1,y) = -\frac{t_a\left(\frac{d}{d\,x}\,\hat{\sigma}_{a11}(x)\right)(y-t_b)}{2\,t_p}$

[a] The stresses and virtual stresses in this table differ from those in table A.1. In addition to keeping additional terms, the derivative $\frac{\partial}{\partial y}$ is non-zero.

Appendix B

Boundary conditions for the SP and BJFE solutions

The pre-simplified version of the longitudinal normal stress boundary conditions for the left and right edges of the joint are:

$$\begin{aligned} \bar{D} + \bar{C} + \bar{B} + \bar{A} - \frac{\bar{\phi}_{\Delta T}}{\bar{\gamma}} - \frac{\bar{\phi}_P}{\bar{\gamma}} &= 0, \\ e^{-\bar{\lambda}_3}\bar{D} + e^{\bar{\lambda}_3}\bar{C} + e^{-\bar{\lambda}_1}\bar{B} + e^{\bar{\lambda}_1}\bar{A} - \frac{\bar{\phi}_{\Delta T}}{\bar{\gamma}} - \frac{\bar{\phi}_P}{\bar{\gamma}} - \frac{2P}{E_{a11}t_a} &= 0. \end{aligned} \tag{B.1}$$

When normalized by the total load $\bar{\phi}_{\text{tot}}$, the normal stress boundary conditions become:

$$\begin{aligned} \bar{D} + \bar{C} + \bar{B} + \bar{A} - \frac{1}{\bar{\gamma}} &= 0, \\ e^{-\bar{\lambda}_3}\bar{D} + e^{\bar{\lambda}_3}\bar{C} + e^{-\bar{\lambda}_1}\bar{B} + e^{\bar{\lambda}_1}\bar{A} - \frac{1}{\bar{\gamma}} - \frac{2P}{E_{a11}t_a\bar{\phi}_{\text{tot}}} &= 0. \end{aligned} \tag{B.2}$$

The pre-simplified version of the shear stress boundary conditions at the edges of

the joint are:

$$
\begin{aligned}
&\frac{3\,\alpha_{b33}\,E_{b22}\,l^4\,\nu_{b32}\,\Delta T}{E_{a11}\,t_a\,t_b\,\nu_{b23}\,\nu_{b32}-E_{a11}\,t_a\,t_b}+\frac{3\,\alpha_{b22}\,E_{b22}\,l^4\,\Delta T}{E_{a11}\,t_a\,t_b\,\nu_{b23}\,\nu_{b32}-E_{a11}\,t_a\,t_b}\\
&+\frac{\left(E_{p^0}\,l^2\,\bar{\lambda}_3^2\,t_p\,\nu_{b23}\,\nu_{b32}-E_{p^0}\,l^2\,\bar{\lambda}_3^2\,t_p+E_{b22}\,l^3\,\bar{\lambda}_3\right)\,\bar{D}}{E_{p^0}\,t_p\,\nu_{b23}\,\nu_{b32}-E_{p^0}\,t_p}\\
&+\frac{\left(E_{p^0}\,l^2\,\bar{\lambda}_3^2\,t_p\,\nu_{b23}\,\nu_{b32}-E_{p^0}\,l^2\,\bar{\lambda}_3^2\,t_p-E_{b22}\,l^3\,\bar{\lambda}_3\right)\,\bar{C}}{E_{p^0}\,t_p\,\nu_{b23}\,\nu_{b32}-E_{p^0}\,t_p}\\
&+\frac{\left(E_{p^0}\,l^2\,\bar{\lambda}_1^2\,t_p\,\nu_{b23}\,\nu_{b32}-E_{p^0}\,l^2\,\bar{\lambda}_1^2\,t_p+E_{b22}\,l^3\,\bar{\lambda}_1\right)\,\bar{B}}{E_{p^0}\,t_p\,\nu_{b23}\,\nu_{b32}-E_{p^0}\,t_p}\\
&+\frac{\left(E_{p^0}\,l^2\,\bar{\lambda}_1^2\,t_p\,\nu_{b23}\,\nu_{b32}-E_{p^0}\,l^2\,\bar{\lambda}_1^2\,t_p-E_{b22}\,l^3\,\bar{\lambda}_1\right)\,\bar{A}}{E_{p^0}\,t_p\,\nu_{b23}\,\nu_{b32}-E_{p^0}\,t_p}=0,\\
&\frac{3\,\alpha_{b33}\,E_{b22}\,l^4\,\nu_{b32}\,\Delta T}{E_{a11}\,t_a\,t_b\,\nu_{b23}\,\nu_{b32}-E_{a11}\,t_a\,t_b}+\frac{3\,\alpha_{b22}\,E_{b22}\,l^4\,\Delta T}{E_{a11}\,t_a\,t_b\,\nu_{b23}\,\nu_{b32}-E_{a11}\,t_a\,t_b}\\
&+\frac{\left(E_{p^l}\,l^2\,\bar{\lambda}_3^2\,e^{-\bar{\lambda}_3}\,t_p\,\nu_{b23}\,\nu_{b32}-E_{p^l}\,l^2\,\bar{\lambda}_3^2\,e^{-\bar{\lambda}_3}\,t_p+E_{b22}\,l^3\,\bar{\lambda}_3\,e^{-\bar{\lambda}_3}\right)\,\bar{D}}{E_{p^l}\,t_p\,\nu_{b23}\,\nu_{b32}-E_{p^l}\,t_p}\\
&+\frac{\left(E_{p^l}\,l^2\,\bar{\lambda}_3^2\,e^{\bar{\lambda}_3}\,t_p\,\nu_{b23}\,\nu_{b32}-E_{p^l}\,l^2\,\bar{\lambda}_3^2\,e^{\bar{\lambda}_3}\,t_p-E_{b22}\,l^3\,\bar{\lambda}_3\,e^{\bar{\lambda}_3}\right)\,\bar{C}}{E_{p^l}\,t_p\,\nu_{b23}\,\nu_{b32}-E_{p^l}\,t_p}\\
&+\frac{\left(E_{p^l}\,l^2\,\bar{\lambda}_1^2\,e^{-\bar{\lambda}_1}\,t_p\,\nu_{b23}\,\nu_{b32}-E_{p^l}\,l^2\,\bar{\lambda}_1^2\,e^{-\bar{\lambda}_1}\,t_p+E_{b22}\,l^3\,\bar{\lambda}_1\,e^{-\bar{\lambda}_1}\right)\,\bar{B}}{E_{p^l}\,t_p\,\nu_{b23}\,\nu_{b32}-E_{p^l}\,t_p}\\
&+\frac{\left(E_{p^l}\,l^2\,\bar{\lambda}_1^2\,e^{\bar{\lambda}_1}\,t_p\,\nu_{b23}\,\nu_{b32}-E_{p^l}\,l^2\,\bar{\lambda}_1^2\,e^{\bar{\lambda}_1}\,t_p-E_{b22}\,l^3\,\bar{\lambda}_1\,e^{\bar{\lambda}_1}\right)\,\bar{A}}{E_{p^l}\,t_p\,\nu_{b23}\,\nu_{b32}-E_{p^l}\,t_p}=0.
\end{aligned}
\tag{B.3}
$$

Appendix C

Definition of the SP and BJFE solution parameters

C.1 System parameters $\bar{\lambda}_{[13]}$ in terms of the orthotropic material properties

$$\bar{\lambda}_{[13]}^2 = \frac{\pm\sqrt{\frac{9E_{b22}^2 l^4}{4G_{b12}^2 t_b^4(\nu_{b23}\nu_{b32}-1)^2} - \frac{12E_{b22}l^4(E_{a11}t_a\nu_{c13}\nu_{c31}+2E_{c11}t_c\nu_{a13}\nu_{a31}-2E_{c11}t_c-E_{a11}t_a)}{E_{a11}E_{c11}t_a t_b^3 t_c(\nu_{b23}\nu_{b32}-1)}}}{2} - \frac{3E_{b22}l^2}{4G_{b12}t_b^2\left(\nu_{b23}\nu_{b32}-1\right)} \tag{C.1}$$

C.2 μ parameters for the SP and BJFE solution basis functions

$$
\begin{aligned}
\mu_{A_T} &= \frac{\bar{\lambda}_3\left(e^{\bar{\lambda}_3}-1\right)}{\bar{\gamma}} \\
\mu_{B_T} &= \frac{e^{\bar{\lambda}_1}\bar{\lambda}_3\left(e^{\bar{\lambda}_3}-1\right)}{\bar{\gamma}} \\
\mu_{C_T} &= -\frac{\bar{\lambda}_1\left(e^{\bar{\lambda}_1}-1\right)}{\bar{\gamma}} \\
\mu_{D_T} &= -\frac{\bar{\lambda}_1\left(e^{\bar{\lambda}_1}-1\right)e^{\bar{\lambda}_3}}{\bar{\gamma}} \\
\mu_{A_P} &= -\left(\bar{\lambda}_3 e^{2\bar{\lambda}_3+\bar{\lambda}_1}-\bar{\lambda}_1 e^{2\bar{\lambda}_3+\bar{\lambda}_1}+2\bar{\lambda}_1 e^{\bar{\lambda}_3}-e^{\bar{\lambda}_1}\bar{\lambda}_3-\bar{\lambda}_1 e^{\bar{\lambda}_1}\right) \\
\mu_{B_P} &= e^{\bar{\lambda}_1}\left(-2\bar{\lambda}_1 e^{\bar{\lambda}_3+\bar{\lambda}_1}+\bar{\lambda}_3 e^{2\bar{\lambda}_3}+\bar{\lambda}_1 e^{2\bar{\lambda}_3}-\bar{\lambda}_3+\bar{\lambda}_1\right) \\
\mu_{C_P} &= \frac{\bar{\lambda}_1\left(\bar{\lambda}_3 e^{\bar{\lambda}_3+2\bar{\lambda}_1}-\bar{\lambda}_1 e^{\bar{\lambda}_3+2\bar{\lambda}_1}+\bar{\lambda}_3 e^{\bar{\lambda}_3}+\bar{\lambda}_1 e^{\bar{\lambda}_3}-2e^{\bar{\lambda}_1}\bar{\lambda}_3\right)}{\bar{\lambda}_3} \\
\mu_{D_P} &= -\frac{\bar{\lambda}_1 e^{\bar{\lambda}_3}\left(2\bar{\lambda}_3 e^{\bar{\lambda}_3+\bar{\lambda}_1}-e^{2\bar{\lambda}_1}\bar{\lambda}_3-\bar{\lambda}_3-\bar{\lambda}_1 e^{2\bar{\lambda}_1}+\bar{\lambda}_1\right)}{\bar{\lambda}_3} \\
\mu_1 &= \bar{\lambda}_3 e^{\bar{\lambda}_3+\bar{\lambda}_1}-\bar{\lambda}_1 e^{\bar{\lambda}_3+\bar{\lambda}_1}+\bar{\lambda}_3 e^{\bar{\lambda}_3}+\bar{\lambda}_1 e^{\bar{\lambda}_3}-e^{\bar{\lambda}_1}\bar{\lambda}_3-\bar{\lambda}_3-\bar{\lambda}_1 e^{\bar{\lambda}_1}+\bar{\lambda}_1 \\
\mu_2 &= \bar{\lambda}_3 e^{\bar{\lambda}_3+\bar{\lambda}_1}-\bar{\lambda}_1 e^{\bar{\lambda}_3+\bar{\lambda}_1}-\bar{\lambda}_3 e^{\bar{\lambda}_3}-\bar{\lambda}_1 e^{\bar{\lambda}_3}+e^{\bar{\lambda}_1}\bar{\lambda}_3-\bar{\lambda}_3+\bar{\lambda}_1 e^{\bar{\lambda}_1}+\bar{\lambda}_1 \\
\mu_3 &= \frac{E_{c11}\bar{\lambda}_3 t_b^3 t_c\left(\nu_{b23}\nu_{b32}-1\right)}{3E_{b22}l^4\left(\nu_{c13}\nu_{c31}-1\right)}
\end{aligned}
\tag{C.2}
$$

Appendix D

BJFE shape functions and derivatives within the lap region

$$
\begin{aligned}
\frac{N_a\left(\bar{x},\bar{\bar{\phi}}_P\right)}{l_e\bar{\bar{\Phi}}_{\mathrm{a}}} =& -\left(1-\nu_{a13}\nu_{a31}\right) \\
& \cdot\left(\frac{e^{-\bar{\lambda}_3\bar{x}}\bar{\bar{D}}\left(\bar{\bar{\phi}}_P\right)}{\bar{\lambda}_3}+\frac{-e^{\bar{\lambda}_3\bar{x}}\bar{\bar{C}}\left(\bar{\bar{\phi}}_P\right)}{\bar{\lambda}_3}+\frac{e^{-\bar{\lambda}_1\bar{x}}\bar{\bar{B}}\left(\bar{\bar{\phi}}_P\right)}{\bar{\lambda}_1}+\frac{-e^{\bar{\lambda}_1\bar{x}}\bar{\bar{A}}\left(\bar{\bar{\phi}}_P\right)}{\bar{\lambda}_1}+\frac{\bar{x}}{\bar{\gamma}}\right) \\
& +\bar{x}\chi_{\Delta T}\left(1-\bar{\bar{\phi}}_P\right)\left(\alpha_{a33}\nu_{a31}+\alpha_{a11}\right), \\
\frac{N_c\left(\bar{x},\bar{\bar{\phi}}_P\right)}{l\bar{\bar{\Phi}}_{\mathrm{c}}} =& \frac{E_{a11}t_a\left(1-\nu_{c13}\nu_{c31}\right)}{2E_{c11}t_c} \\
& \cdot\left(\frac{e^{-\bar{\lambda}_3\bar{x}}\bar{\bar{D}}\left(\bar{\bar{\phi}}_P\right)}{\bar{\lambda}_3}-\frac{e^{\bar{\lambda}_3\bar{x}}\bar{\bar{C}}\left(\bar{\bar{\phi}}_P\right)}{\bar{\lambda}_3}+\frac{e^{-\bar{\lambda}_1\bar{x}}\bar{\bar{B}}\left(\bar{\bar{\phi}}_P\right)}{\bar{\lambda}_1}-\frac{e^{\bar{\lambda}_1\bar{x}}\bar{\bar{A}}\left(\bar{\bar{\phi}}_P\right)}{\bar{\lambda}_1}\right) \\
& +\frac{\bar{x}\left(1-\nu_{c13}\nu_{c31}\right)}{E_{c11}t_c}\left(\bar{\bar{\phi}}_P\chi_P+\frac{E_{a11}t_a}{2\bar{\gamma}}\right) \\
& +\bar{x}\chi_{\Delta T}\left(1-\bar{\bar{\phi}}_P\right)\left(\alpha_{c33}\nu_{c31}+\alpha_{c11}\right),
\end{aligned}
\tag{D.1}
$$

$$
\begin{aligned}
\frac{B_a\left(\bar{x},\bar{\bar{\phi}}_P\right)}{l_e\bar{\bar{\Phi}}_{\mathrm{a}}} =& \left(1-\nu_{a13}\nu_{a31}\right) \\
&\cdot\left(e^{-\bar{\lambda}_3\bar{x}}\bar{\bar{D}}\left(\bar{\bar{\phi}}_P\right)+e^{\bar{\lambda}_3\bar{x}}\bar{\bar{C}}\left(\bar{\bar{\phi}}_P\right)+e^{-\bar{\lambda}_1\bar{x}}\bar{\bar{B}}\left(\bar{\bar{\phi}}_P\right)+e^{\bar{\lambda}_1\bar{x}}\bar{\bar{A}}\left(\bar{\bar{\phi}}_P\right)-\frac{1}{\bar{\gamma}}\right) \\
&+\chi_{\Delta T}(1-\bar{\bar{\phi}}_P)\left(\alpha_{a33}\nu_{a31}+\alpha_{a11}\right), \\
\frac{B_c\left(\bar{x},\bar{\bar{\phi}}_P\right)}{l_e\bar{\bar{\Phi}}_{\mathrm{c}}} =& -\left(1-\nu_{c13}\nu_{c31}\right)\frac{E_{a11}t_a}{2E_{c11}t_c} \\
&\cdot\left(e^{-\bar{\lambda}_3\bar{x}}\bar{\bar{D}}\left(\bar{\bar{\phi}}_P\right)+e^{\bar{\lambda}_3\bar{x}}\bar{\bar{C}}\left(\bar{\bar{\phi}}_P\right)+e^{-\bar{\lambda}_1\bar{x}}\bar{\bar{B}}\left(\bar{\bar{\phi}}_P\right)+e^{\bar{\lambda}_1\bar{x}}\bar{\bar{A}}\left(\bar{\bar{\phi}}_P\right)-\frac{1}{\bar{\gamma}}\right) \\
&+\frac{\bar{\bar{\phi}}_P\chi_P\left(1-\nu_{c13}\nu_{c31}\right)}{E_{c11}t_c}+\chi_{\Delta T}(1-\bar{\bar{\phi}}_P)\left(\alpha_{c33}\nu_{c31}+\alpha_{c11}\right).
\end{aligned}
\tag{D.2}
$$

Appendix E

BJFE solution parameters in terms of material properties and loads

The following parameters are used in the text in order to facilitate compact equations:

E.1 Dimensionless system parameters

Table E.1 Dimensionless system parameters

Load Parameters	Material Parameters
$\bar{\phi}_P = \frac{\theta_P P}{\Theta}$	$\bar{\beta} = \frac{\theta_\beta}{\Theta}$
$\bar{\phi}_{\Delta T} = \frac{\theta_{\Delta T} \Delta T}{\Theta}$	$\bar{\gamma} = \frac{\theta_\gamma}{\Theta}$

E.2 Dimensional material parameters

$$
\begin{aligned}
\theta_\beta =& + \frac{t_a^3}{24l^2}\left[\frac{(\nu_{a12}+\nu_{a13}\nu_{a32})}{E_{a11}}+\frac{(\nu_{a21}+\nu_{a23}\nu_{a31})}{E_{a22}}\right] \\
& - \frac{t_a^2 t_c}{24l^2}\left[\frac{(\nu_{c12}+\nu_{c13}\nu_{c32})}{E_{c11}}+\frac{(\nu_{c21}+\nu_{c23}\nu_{c31})}{E_{c22}}\right] \\
& + \frac{t_a^2}{4l^2 E_{a11}}\left(t_b\left(\nu_{a12}+\nu_{a13}\nu_{a32}\right)+\frac{t_c}{2}\left(\nu_{a12}+\nu_{a13}\nu_{a32}\right)\right) \\
& + \frac{t_a^2}{4l^2 E_{a22}}\left(t_b\left(\nu_{a21}+\nu_{a23}\nu_{a31}\right)+\frac{t_c}{2}\left(\nu_{a21}+\nu_{a23}\nu_{a31}\right)\right) \\
& - \frac{t_a^2}{8l^2}\left[\frac{t_c}{3G_{c11}}+\frac{t_b}{G_{b11}}\right] \\
\theta_\gamma =& \frac{t_a^2}{4E_{c11}t_c}\left(1-\nu_{c13}\nu_{c31}\right)+\frac{t_a}{2E_{a11}}\left(1-\nu_{a13}\nu_{a31}\right)
\end{aligned}
\tag{E.1}
$$

E.3 Dimensional load parameters

$$
\begin{aligned}
\theta_{\Delta T} =& \frac{t_a}{2E_{a11}}\left(\alpha_{a11}-\alpha_{c11}+\alpha_{a33}\nu_{a31}-\alpha_{c33}\nu_{c31}\right) \\
\theta_P =& -\frac{t_a}{2t_c E_{a11}E_{c11}}\left(1-\nu_{c13}\nu_{c31}\right)
\end{aligned}
\tag{E.2}
$$

E.4 Dimensional system parameter

$$
\begin{aligned}
\Theta =& + \left(1-\nu_{a23}\nu_{a32}\right)\frac{t_a^3}{8l^4E_{a22}}\left[\frac{t_a^2}{30}+\frac{t_a t_c}{6}+\frac{t_c^2}{4}+\frac{t_a t_b}{3}+t_b t_c+t_b^2\right] \\
& + \left(1-\nu_{b23}\nu_{b32}\right)\frac{t_a^2 t_b}{4l^4E_{b22}}\left[\frac{t_c^2}{4}+\frac{t_b^2}{3}+\frac{t_b t_c}{2}\right] \\
& + \left(1-\nu_{c23}\nu_{c32}\right)\frac{t_a^2 t_c^3}{80l^4E_{c22}}
\end{aligned}
\tag{E.3}
$$

E.5 Denominators of the elimination coefficients

The denominators from equation 3.36 are:

$$
\begin{aligned}
\bar{\bar{\Xi}}_{\mathrm{a}} = &+ l_e\bar{\lambda}_1\left(1-\nu_{a13}\nu_{a31}\right)\left(e^{\bar{\lambda}_3+\bar{\lambda}_1}-e^{\bar{\lambda}_1}\right)\bar{\bar{D}}\left(\bar{\bar{\phi}}_P\right)\\
&+ l_e\bar{\lambda}_1\left(1-\nu_{a13}\nu_{a31}\right)\left(e^{2\bar{\lambda}_3+\bar{\lambda}_1}-e^{\bar{\lambda}_3+\bar{\lambda}_1}\right)\bar{\bar{C}}\left(\bar{\bar{\phi}}_P\right)\\
&+ l_e\bar{\lambda}_3\left(1-\nu_{a13}\nu_{a31}\right)\left(e^{\bar{\lambda}_3+\bar{\lambda}_1}-e^{\bar{\lambda}_3}\right)\bar{\bar{B}}\left(\bar{\bar{\phi}}_P\right)\\
&+ l_e\bar{\lambda}_3\left(1-\nu_{a13}\nu_{a31}\right)\left(e^{\bar{\lambda}_3+2\bar{\lambda}_1}-e^{\bar{\lambda}_3+\bar{\lambda}_1}\right)\bar{\bar{A}}\left(\bar{\bar{\phi}}_P\right)\\
&- l_e\bar{\lambda}_1\bar{\lambda}_3 e^{\bar{\lambda}_3+\bar{\lambda}_1}\left(\frac{\left(1-\nu_{a13}\nu_{a31}\right)}{\bar{\gamma}}-\chi_{\Delta T}\left(1-\bar{\bar{\phi}}_P\right)\left(\alpha_{a11}+\alpha_{a33}\nu_{a31}\right)\right),\\
\bar{\bar{\Xi}}_{\mathrm{c}} = &-\frac{E_{a11}t_a}{2E_{c11}t_c}l_e\bar{\lambda}_1\left(1-\nu_{c13}\nu_{c31}\right)\left(e^{\bar{\lambda}_1}+e^{\bar{\lambda}_3+\bar{\lambda}_1}\right)\bar{\bar{D}}\left(\bar{\bar{\phi}}_P\right)\\
&-\frac{E_{a11}t_a}{2E_{c11}t_c}l_e\bar{\lambda}_1\left(1-\nu_{c13}\nu_{c31}\right)\left(e^{2\bar{\lambda}_3+\bar{\lambda}_1}-e^{\bar{\lambda}_3+\bar{\lambda}_1}\right)\bar{\bar{C}}\left(\bar{\bar{\phi}}_P\right)\\
&-\frac{E_{a11}t_a}{2E_{c11}t_c}l_e\bar{\lambda}_3\left(1-\nu_{c13}\nu_{c31}\right)\left(e^{\bar{\lambda}_3}+e^{\bar{\lambda}_3+\bar{\lambda}_1}\right)\bar{\bar{B}}\left(\bar{\bar{\phi}}_P\right)\\
&-\frac{E_{a11}t_a}{2E_{c11}t_c}l_e\bar{\lambda}_3\left(1-\nu_{c13}\nu_{c31}\right)\left(e^{\bar{\lambda}_3+2\bar{\lambda}_1}-e^{\bar{\lambda}_3+\bar{\lambda}_1}\right)\bar{\bar{A}}\left(\bar{\bar{\phi}}_P\right)\\
&+\frac{l_e\bar{\lambda}_1\bar{\lambda}_3 e^{\bar{\lambda}_3+\bar{\lambda}_1}}{2E_{c11}t_c}\left(\frac{\left(1-\nu_{c13}\nu_{c31}\right)}{\bar{\gamma}}\left(E_{a11}t_a+2\bar{\gamma}\bar{\bar{\phi}}_P\chi_P\right)\right)\\
&+\frac{l_e\bar{\lambda}_1\bar{\lambda}_3 e^{\bar{\lambda}_3+\bar{\lambda}_1}}{2E_{c11}t_c}\left(\chi_{\Delta T}\left(1-\bar{\bar{\phi}}_P\right)\left(\alpha_{c11}+\alpha_{c33}\nu_{c31}\right)\right).
\end{aligned}
\tag{E.4}
$$

E.6 Simplification coefficients

$$
\begin{aligned}
\bar{\bar{\Phi}}_{\mathrm{a}} &= \frac{\bar{\lambda}_1\bar{\lambda}_3 e^{\bar{\lambda}_3+\bar{\lambda}_1}}{\bar{\bar{\Xi}}_{\mathrm{a}}}\\
\bar{\bar{\Phi}}_{\mathrm{c}} &= \frac{\bar{\lambda}_1\bar{\lambda}_3 e^{\bar{\lambda}_3+\bar{\lambda}_1}}{\bar{\bar{\Xi}}_{\mathrm{c}}}.
\end{aligned}
\tag{E.5}
$$

$$
\begin{aligned}
\bar{\bar{\Xi}}_{\mathrm{a}} = &+ l_e\bar{\lambda}_1\left(1-\nu_{a13}\nu_{a31}\right)\left(e^{\bar{\lambda}_3+\bar{\lambda}_1}-e^{\bar{\lambda}_1}\right)\bar{\bar{D}}\left(\bar{\bar{\phi}}_P\right)\\
&+ l_e\bar{\lambda}_1\left(1-\nu_{a13}\nu_{a31}\right)\left(e^{2\bar{\lambda}_3+\bar{\lambda}_1}-e^{\bar{\lambda}_3+\bar{\lambda}_1}\right)\bar{\bar{C}}\left(\bar{\bar{\phi}}_P\right)\\
&+ l_e\bar{\lambda}_3\left(1-\nu_{a13}\nu_{a31}\right)\left(e^{\bar{\lambda}_3+\bar{\lambda}_1}-e^{\bar{\lambda}_3}\right)\bar{\bar{B}}\left(\bar{\bar{\phi}}_P\right)\\
&+ l_e\bar{\lambda}_3\left(1-\nu_{a13}\nu_{a31}\right)\left(e^{\bar{\lambda}_3+2\bar{\lambda}_1}-e^{\bar{\lambda}_3+\bar{\lambda}_1}\right)\bar{\bar{A}}\left(\bar{\bar{\phi}}_P\right)\\
&- l_e\bar{\lambda}_1\bar{\lambda}_3 e^{\bar{\lambda}_3+\bar{\lambda}_1}\left(\frac{\left(1-\nu_{a13}\nu_{a31}\right)}{\bar{\gamma}}-\frac{\Theta}{\theta_{\Delta T}}\left(1-\bar{\bar{\phi}}_P\right)\left(\alpha_{a11}+\alpha_{a33}\nu_{a31}\right)\right)\\
\bar{\bar{\Xi}}_{\mathrm{c}} = &-\frac{E_{a11}t_a}{2E_{c11}t_c}l_e\bar{\lambda}_1\left(1-\nu_{c13}\nu_{c31}\right)\left(e^{\bar{\lambda}_1}+e^{\bar{\lambda}_3+\bar{\lambda}_1}\right)\bar{\bar{D}}\left(\bar{\bar{\phi}}_P\right)\\
&-\frac{E_{a11}t_a}{2E_{c11}t_c}l_e\bar{\lambda}_1\left(1-\nu_{c13}\nu_{c31}\right)\left(e^{2\bar{\lambda}_3+\bar{\lambda}_1}-e^{\bar{\lambda}_3+\bar{\lambda}_1}\right)\bar{\bar{C}}\left(\bar{\bar{\phi}}_P\right)\\
&-\frac{E_{a11}t_a}{2E_{c11}t_c}l_e\bar{\lambda}_3\left(1-\nu_{c13}\nu_{c31}\right)\left(e^{\bar{\lambda}_3}+e^{\bar{\lambda}_3+\bar{\lambda}_1}\right)\bar{\bar{B}}\left(\bar{\bar{\phi}}_P\right)\\
&-\frac{E_{a11}t_a}{2E_{c11}t_c}l_e\bar{\lambda}_3\left(1-\nu_{c13}\nu_{c31}\right)\left(e^{\bar{\lambda}_3+2\bar{\lambda}_1}-e^{\bar{\lambda}_3+\bar{\lambda}_1}\right)\bar{\bar{A}}\left(\bar{\bar{\phi}}_P\right)\\
&+\frac{l_e\bar{\lambda}_1\bar{\lambda}_3 e^{\bar{\lambda}_3+\bar{\lambda}_1}}{2E_{c11}t_c}\left(\frac{\left(1-\nu_{c13}\nu_{c31}\right)}{\bar{\gamma}}\left(E_{a11}t_a+2\bar{\gamma}\bar{\bar{\phi}}_P\frac{\Theta}{\theta_P}\right)\right)\\
&+\frac{l_e\bar{\lambda}_1\bar{\lambda}_3 e^{\bar{\lambda}_3+\bar{\lambda}_1}}{2E_{c11}t_c}\left(\frac{\Theta}{\theta_{\Delta T}}\left(1-\bar{\bar{\phi}}_P\right)\left(\alpha_{c11}+\alpha_{c33}\nu_{c31}\right)\right)
\end{aligned}
\tag{E.6}
$$

Bibliography

[1] Abaqus, Inc. 2006. *Abaqus User Manual v6.6*, Electronic Version.

[2] Adams, R. D., J. Coppendale, V. Mallick, and H. Al-Hamdan. 1992. The effect of temperature on the strength of adhesive joints, *International Journal Of Adhesion And Adhesives*, 12(3), 185–190.

[3] Adams, R. D. and N. A. Peppiatt. 1974. Stress analysis of adhesive-bonded lap joints, *Journal Of Strain Analysis*, 9(3), 185–196.

[4] Adams, R.D., J. Comyn, and W.C. Wake. 1997. *Structural Adhesive Joints in Engineering*, Chapman and Hall.

[5] AECMA PREN 6034. 1995. *Aerospace Series Carbon Fibre Reinforced Plastics Test Method Determination of Interlaminar Fracture Toughness Energy Mode II - G_{IIc}.*

[6] Albouyso, V, O Allix, P Ladeveze, and D Leveque. 1999. Interfacial approach of delamination: possibilities and difficulties, in *Proceedings of the 12th International Conference on Composite Materials, Paris, France..*

[7] Alfano, G. and M. A. Crisfield. 2001. Finite element interface models for the delamination analysis of laminated composites: mechanical and computational issues, *International Journal For Numerical Methods In Engineering*, 50(7), 1701–1736.

[8] Alfano, G. and MA Crisfield. 2003. Solution strategies for the delamination analysis based on a combination of local-control arc-length and line searches, *International Journal for Numerical Methods in Engineering*, 58, 999–1048.

[9] Allix, O. and A. Corigliano. 1996. Modeling and simulation of crack propagation in mixed-modes interlaminar fracture specimens, *International Journal Of Fracture*, 77(2), 111–140.

[10] Allman, D.J. 1977. A theory for elastic stresses in adhesive bonded lap joints, *The Quarterly journal of mechanics and applied mathematics*, 30, 415.

[11] Asp, L. E. 1998. The effects of moisture and temperature on the interlaminar delamination toughness of a carbon/epoxy composite, *Composites Science And Technology*, 58(6), 967–977.

[12] ASTM International. 1996. *ASTM D3528-96 Standard Test Method for Strength Properties of Double Lap Shear Adhesive Joints by Tension Loading.*

[13] ASTM International. 2001. *ASTM D4896-01 Standard Guide for Use of Adhesive-Bonded Single Lap-Joint Specimen Test Results.*

[14] ASTM International. 2001. *ASTM D5528-01 (2007) Standard Test Method for Mode I Interlaminar Fracture Toughness of Unidirectional Fiber-Reinforced Polymer Matrix Composites.*

[15] ASTM International. 2001. *ASTM D5868-01 Standard Test Method for Lap Shear Adhesion for Fiber Reinforced Plastic (FRP) Bonding*.

[16] ASTM International. 2005. *ASTM D1002-05 Standard Test Method for Apparent Shear Strength of Single-Lap-Joint Adhesively Bonded Metal Specimens by Tension Loading (Metal-to-Metal)*.

[17] ASTM International. 2006. *ASTM D6671M-06 Standard Test Method for Mixed Mode I-Mode II Interlaminar Fracture Toughness of Unidirectional Fiber Reinforced Polymer Matrix Composites*.

[18] Aydemir, Alpay and Durmus Gunay. 2003. The fuzzy finite element stress analysis of adhesive-bonded single lap joints, *Turkish Journal Of Engineering & Environment Sciences*, 121–127.

[19] Bednarcyk, B. A., J. Zhang, C. S. Collier, Y. Bansal, and M. J. Pindera. 2006. Analysis tools for adhesively bonded composite joints, part 1: Higher-order theory, *AIAA Journal*, 44(1), 171–180.

[20] Benson, N.K. 1969. Influence of stress distribution on the strength of bonded joints, in N.K Benson, (Ed.) *Adhesion-Fundamentals and Practice*, MacLaren, 191–205.

[21] Camacho, GT and M. Ortiz. 1996. Computational modelling of impact damage in brittle materials, *International Journal Of Solids And Structures*, 33(20), 2899–2938.

[22] Camanho, P. P., C. G. Davila, and M. F. de Moura. 2003. Numerical simulation of mixed-mode progressive delamination in composite materials, *Journal Of Composite Materials*, 37(16), 1415–1438.

[23] Camanho, P.P. and C.G. Dávila. 2002. Mixed-mode decohesion finite elements for the simulation of delamination in composite materials, Tech. Rep. TM-2002-211737, NASA.

[24] Chaboche, J. L., F. Feyel, and Y. Monerie. 2001. Interface debonding models: a viscous regularization with a limited rate dependency, *International Journal Of Solids And Structures*, 38(18), 3127–3160.

[25] Chang, P., A.P. Mouritz, and B.N. Cox. 2007. Flexural properties of z-pinned laminates, *Composites Part A: Applied Science and Manufacturing*, 38(2), 244–251.

[26] Chen, W.T. and C.W. Nelson. 1979. Thermal stress in bonded joints, *Ibm Journal Of Research And Development*, 23(2), 179–188.

[27] Cook, Robert D., David S. Malkus, and Michael E. Plesha. 1989. *Concepts and applications of finite element analysis*, John Wiley & Sons.

[28] Corigliano, Alberto, Stefano Mariani, and Anna Pandolfi. 2003. Numerical modeling of rate-dependent debonding processes in composites, *Composites*, 61(1-2), 39–50.

[29] Corporation, Alpha STAR. 2008. *GENOA*, 5199 East Pacific Coast Highway, Suite 410 Long Beach, California 90804 USA.

[30] Cox, BN. 1999. Constitutive model for a fiber tow bridging a delamination crack, *Mechanics of Advanced Materials and Structures*, 6(2), 117–138.

[31] Cox, Brian N., Mahyar S. Dadkhah, and W. L. Morris. 1996. On the tensile failure of 3D woven composites, *Composites Part A: Applied Science and Manufacturing*, 27(6), 447–458.

[32] Crews, Jr., John H. and James R. Reeder. 1988. A mixed-mode bending apparatus for delamination testing, Tech. rep., NASA.

[33] Cui, W. and MR Wisnom. 1993. A combined stress-based and fracture-mechanics-based model for predicting delamination in composites, *Composites*, 24(6), 467–474.

[34] Davidson, B. D., R. Kruger, and M. Konig. 1996. Effect of stacking sequence on energy release rate distributions in multidirectional dcb and enf specimens, *Engineering Fracture Mechanics*, 55(4), 557–569.

[35] Davidson, Barry D., Simon J. Gharibian, and LiJie Yu. 2000. Evaluation of energy release rate-based approaches for predicting delamination growth in laminated composites, *International Journal Of Fracture*, V105(4), 343–365.

[36] Davidson, Barry D and Wenming Zhao. 2006. An accurate mixed-mode delamination failure criterion for laminated fibrous composites requiring limited experimental input, *Journal Of Composite Materials*, 0021998306071031.

[37] Davidson, B.D. and X. Sun. 2006. Geometry and data reduction recommendations for a standardized end notched flexure test for unidirectional composites, *Journal Of ASTM International*, 3(9).

[38] Davies, G. A. O., P. Robinson, J. Robson, and D. Eady. 1997. Shear driven delamination propagation in two dimensions, *Composites Part A: Applied Science and Manufacturing*, 28(8), 757–765.

[39] Davies, GAO. 1982. *Virtual work in structural analysis*, John Wiley & Sons.

[40] Davies, G.A.O., D. Hitchings, and J. Ankersen. 2006. Predicting delamination and debonding in modern aerospace composite structures, *Composites Science And Technology*, 66(6), 846–854.

[41] Davies, P., H. H. Kausch, J. G. Williams, A. J. Kinloch, M. N. Charalambides, A. Pavan, D. R. Moore, R. Prediger, I. Robinson, N. Burgoyne, K. Friedrich, H. Wittich, C. A. Rebelo, A. Torres Marques, F. Ramsteiner, B. Melve, M. Fischer, N. Roux, D. Martin, P. Czarnocki, D. Neville, I. Verpoest, B. Goffaux, R. Lee, K. Walls, N. Trigwell, I. K. Partridge, J. Jaussaud, S. Andersen, Y. Giraud, G. Hale, and G. McGrath. 1992. Round-robin interlaminar fracture testing of carbon-fibre-reinforced epoxy and PEEK composites, *Composites Science And Technology*, 43(2), 129–136.

[42] de Borst, R. 2001. Some recent issues in computational failure mechanics, *International Journal for Numerical Methods in Engineering*, 52(5), 63–96.

[43] de Borst, Rene. 2003. Numerical aspects of cohesive-zone models, *Engineering Fracture Mechanics*, 70(14), 1743–1757.

[44] Delale, F., F. Erdogan, and M.N. Aydinoglu. 1981. Stresses in adhesively bonded joints: a closed-form solution, *Journal Of Composite Materials*, 15, 249–271.

[45] Eaton, J.W. 2002. *Gnu Octave Manual*, Network Theory Ltd.

[46] Erdogan, F. and M. Ratwani. 1971. Stress distribution in bonded joints, *Journal Of Composite Materials*, 5, 378–393.

[47] Espinosa, Horacio D, Pablo D Zavattieri, and Sunil K Dwivedi. 1998. A finite deformation continuum discrete model for the description of fragmentation and damage in brittle materials, *Journal Of The Mechanics And Physics Of Solids*, 46(10), 1909–1942.

[48] Gilibert, Y. and A. Rigolot. 1988. Determination of stress distribution in double-lap joints, matched asymptotic expansions and conformal mapping, in W.S. Johson, (Ed.) *Adhesively Bonded Joints: Testing, Analysis, and Design*, Philadelphia: American Society for Testing and Materials, vol. ASTM STP 981, 145–159.

[49] Gillespie, J. W., Jr, L. A. Carlsson, and R. B. Pipes. 1986. Finite element analysis of the end notched flexure specimen for measuring mode ii fracture toughness, *Composites Science And Technology*, 27(3), 177–197.

[50] Glaessgen, E.H., I.S. Raju, and Jr. C.C. Poe. 1998. Fracture mechanics analysis of stitched stiffener-skin debonding, in *39th AIAA/ASME/ASCE/AHS/ASC Structures, Structural Dynamics, and Materials Conference*, 98-2022.

[51] Goland, M. and E. Reissner. 1944. The stresses in cemented joints, *Journal Of Applied Mechanics*, 66, A17–A27.

[52] Goncalves, J. P. M., M. F. S. F. de Moura, and P. M. S. T. de Castro. 2002. A three-dimensional finite element model for stress analysis of adhesive joints, *International Journal Of Adhesion And Adhesives*, 22(5), 357–365.

[53] Goyal, Vinay K., Eric R. Johnson, and Chris Cassino. 2003. Computational model for progressive failure of adhesivley bonded joints, in *44th AIAA/ASME/ASCE/AHS/ASC Structures, Structrual Dynamics and Materials Conference*.

[54] Hart-Smith, L.J. 1973. Adhesive-bonded double-lap joints, *NASA Contractor Report 112235*.

[55] Hart-Smith, L.J. 1973. Adhesive-bonded single-lap joints, *NASA Contractor Report 112236*.

[56] Her, Shiuh-Chuan. 1999. Stress analysis of adhesively-bonded lap joints, *Composites*, 47(1-4), 673–678.

[57] Herakovich, Carl T. 1998. *Mechanics of fibrous composites*, John Wiley and Sons, Inc.

[58] Hillerborg, A., M. Modeer, and P.E. Petersson. 1976. Analysis of crack formation and crack growth in concrete by means of fracture mechanics and finite elements, *Cement And Concrete Research*, 6, 773–782.

[59] Kafkalidis, M. S. and M. D. Thouless. 2002. The effects of geometry and material properties on the fracture of single lap-shear joints, *International Journal Of Solids And Structures*, 39(17), 4367–4383.

[60] Kamiya, Ryuta, Bryan A. Cheeseman, Peter Popper, and Tsu-Wei Chou. 2000. Some recent advances in the fabrication and design of three-dimensional textile preforms: a review, *Composites Part B: Engineering*, 60(1), 33–47.

[61] Kilic, B., E. Madenci, and D.R. Ambur. 2004. Global-local finite element analysis of bonded single-lap joints, in *45th AIAA/ASME/ASCE/AHS/ASC Structures, Structrual Dynamics and Materials Conference, April 19-22, Palm Springs, CA*, 1–13.

[62] Koutsourelakis, P.S., K. Kuntiyawichai, and G.I. Schueller. 2006. Effect of material uncertainties on fatigue life calculations of aircraft fuselages: A cohesive element model, *Engineering Fracture Mechanics*, 73(9), 1202–1219.

[63] Krueger, Ronald. 2004. Virtual crack closure technique: History, approach, and applications, *Applied Mechanics Reviews*, 57(2), 109–143.

[64] Li, S., M.D. Thouless, A.M. Waas, J.A. Schroeder, and P.D. Zavattieri. 2005. Use of a cohesive-zone model to analyze the fracture of a fiber-reinforced polymer-matrix composite, *Composites Science And Technology*, 65(3-4), 537–549.

[65] Li, S., M.D. Thouless, A.M. Waas, J.A. Schroeder, and P.D. Zavattieri. 2006. Competing failure mechanisms in mixed-mode fracture of an adhesively bonded polymer-matrix composite, *International Journal Of Adhesion And Adhesives*, 26(8), 609–616.

[66] Li, S., M.D. Thouless, A.M. Waas, J.A. Schroeder, and P.D. Zavattieri. 2006. Mixed-mode cohesive-zone models for fracture of an adhesively bonded polymer-matrix composite, *Engineering Fracture Mechanics*, 73(1), 64–78.

[67] Lophaven, Soren N. 2002. *DACE: A Matlab Kriging Toolbox*, Technical University of Denmark, DK-2800 Kgs. Lyngby, Denmark, version 2.0 edn.

[68] McKay, MD, RJ Beckman, and WJ Conover. 1979. A comparison of three methods for selecting values of input variables in the analysis of output from a computer code, *Technovation*, 21(2), 239–245.

[69] Mendels, D.-A., S. A. Page, Y. Leterrier, and J.-A. E. Manson. 2000. A modified double lap-shear test as a mean to measure intrinsic properties of adhesive joints, in *European conference on composite materials, June 4-7, Brighton, United Kingdom*.

[70] Mi, Y., M. A. Crisfield, G. A. O. Davies, and H. B. Hellweg. 1998. Progressive delamination using interface elements, *Journal Of Composite Materials*, 32(14), 1246–1272.

[71] Mortensen, F. and O. T. Thomsen. 2002. Analysis of adhesive bonded joints: a unified approach, *Composites Science And Technology*, 62(7-8), 1011–1031.

[72] Mortensen, F. and O. T. Thomsen. 2002. Coupling effects in adhesive bonded joints, *Composites*, 56(2), 165–174.

[73] Mouritz, A. P., M. K. Bannister, P. J. Falzon, and K. H. Leong. 1999. Review of applications for advanced three-dimensional fibre textile composites, *Composites Part A: Applied Science and Manufacturing*, 30(12), 1445–1461.

[74] Munoz, J.J., U. Galvanetto, and P. Robinson. 2006. On the numerical simulation of fatigue driven delamination with interface elements, *International Journal Of Fatigue*, 28(10), 1136–1146.

[75] Oterkus, E., A. Barut, E. Madenci, S.S. Smeltzer III, and D.R. Ambur. 2004. Nonlinear analysis of bonded composite single-lap joints, in *Proceedings of the AIAA/ASME/ASCE/AHS/ASC 45th Structures, Structural Dynamics, and Materials Conference, April 19-22, Palm Springs, CA*, American Institute of Aeronautics and Astronautics, 2004-1560.

[76] Oterkus, E., E. Madenci, S.S. Smeltzer III, and D.R. Ambur. 2005. Nonlinear analysis of bonded composite tubular lap joints, in *Proceedings of the AIAA/ASME/ASCE/AHS/ASC 46th Structures, Structural Dynamics, and Materials Conference, April 18-21, Austin, TX*, American Institute of Aeronautics and Astronautics, 2005-2380.

[77] Oterkus, E., E. Madenci, S.S. Smeltzer III, and D.R. Ambur. 2006. Thermomechanical analysis of bonded cylindrically curved composite shell structures, in

Proceedings of the AIAA/ASME/ASCE/AHS/ASC 47th Structures, Structural Dynamics, and Materials Conference, May 1-4, Newport, RI, American Institute of Aeronautics and Astronautics, 2006-1963.

[78] Pandolfi, A., P. Krysl, and M. Ortiz. 1999. Finite element simulation of ring expansion and fragmentation: The capturing of length and time scales through cohesive models of fracture, *International Journal Of Fracture*, 95(1), 279–297.

[79] Penado, F.E. 1993. A closed form solution for the energy release rate of the double cantilever beam specimen with an adhesive layer, *Journal Of Composite Materials*, 27(4), 383–407.

[80] Peppiatt, N.A. 1974. *Stress analysis of adhesive joints*, Ph.D. thesis, University of Bristol.

[81] Pietruszczak, S. and Z. Mroz. 1981. Finite element analysis of deformation of strain-softening materials, *International Journal For Numerical Methods In Engineering*, 17(3), 327–334.

[82] Pohlit, David J. 2007. *Dynamic Mixed-Mode Fracture of Bonded Composite Joints for Automotive Crashworthiness*, Master's thesis, Virginia Polytechnic Institute and State University.

[83] Polaha, J. J., B. D. Davidson, R. C. Hudson, and A. Pieracci. 1996. Effects of mode ratio, ply orientation and precracking on the delamination toughness of a laminated composite, *Journal Of Reinforced Plastics And Composites*, 15(2), 141–173.

[84] Reedy Jr, ED, FJ Mello, and TR Guess. 1997. Modeling the initiation and growth of delaminations in composite structures, *Journal Of Composite Materials*, 31(8), 812.

[85] Renton, W.J. and J.R. Vinson. 1975. The efficient design of adhesive bonded joints, *Journal Of Adhesion*, 7, 175–193.

[86] Roudolff, F. and Y. Ousset. 2002. Comparison between two approaches for the simulation of delamination growth in a d.c.b. specimen, *Aerospace Science And Technology*, 6(2), 123–130.

[87] Sandia National Laboratory. 2003. *Tahoe User Guide*, 3.4.1 edn.

[88] Schellekens, JCJ and R. de Borst. 1993. On the numerical integration of interface elements, *International Journal For Numerical Methods In Engineering*, 36(43-66), 30–31.

[89] Schon, Joakim, Tonny Nyman, Anders Blom, and Hans Ansell. 2000. Numerical and experimental investigation of a composite enf-specimen, *Engineering Fracture Mechanics*, 65(4), 405–433.

[90] Sen, Joyanto K. and Robert M. Jones. 1980. Stresses in double-lap joints bonded with a viscoelastic adhesive: Part I. Theory and experimental corroboration, *AIAA Journal*, 18(10), 1237–1244.

[91] Sen, Joyanto K. and Robert M. Jones. 1980. Stresses in double-lap joints bonded with a viscoelastic adhesive: Part II. Parametric study and joint design, *AIAA Journal*, 18(11), 1376–1382.

[92] Shahwan, K.W. and A.M. Waas. 1997. Non-self-similar decohesion along a finite interface of unilaterally constrained delaminations, *Proceedings: Mathematical, Physical and Engineering Sciences*, 453(1958), 515–550.

[93] Simulia, Inc. 2007. *Abaqus User Manual v6.7*, Electronic Version.

[94] Smeltzer III, Stanley S. and Eric Lundgren. 2006. Analytical and numerical results for an adhesively bonded joint subjected to pure bending, in *Proceedings of the AIAA/ASME/ASCE/AHS/ASC 47th Structures, Structural Dynamics, and Materials Conference, May 1-4 2006, Newport RI*, American Institute of Aeronautics and Astronautics, 2006-1960.

[95] Soffa, M. A., B. D. Davidson, and M. Kumar. 2006. Mode I toughness of a particulate interlayered composite as a function of moisture and temperature, in *Proceedings of the American Society of Composites 21st Annual Technical Conference*.

[96] Song, Seung J. and Anthony M. Waas. 1994. Mode I failure of laminated polymeric composites, *Engineering Fracture Mechanics*, 49(1), 17–27.

[97] Song, Seung J. and Anthony M. Waas. 1995. Energy-based mechanical model for mixed mode failure of laminated composites, *AIAA Journal*, 33(4), 739–745.

[98] Sridhar, N., R. Massab, B.N. Cox, and I.J. Beyerlein. 2002. Delamination dynamics in through-thickness reinforced laminates with application to DCB specimen, *International Journal Of Fracture*, 118(2), 119–144.

[99] Sun, Ce. 2007. *Fracture of plastically-deforming, adhesively-bonded structures: experimental and numerical studies*, Ph.D. thesis, University of Michigan.

[100] Tvergaard, V. and J.W. Hutchinson. 1992. The relation between crack growth resistance and fracture process parameters in elastic–plastic solids, *JournaL Of The Mechanics And Physics Of Solids*, 40(6), 1377–1397.

[101] Ungsuwarungsri, T. and WG Knauss. 1987. The role of damage-softened material behavior in the fracture of composites and adhesives, *International Journal Of Fracture*, 35(3), 221–241.

[102] Valoroso, Nunziante and Laurent Champaney. 2006. A damage-mechanics-based approach for modelling decohesion in adhesively bonded assemblies, *Engineering Fracture Mechanics*, 73(18), 2774–2801.

[103] Vinson, J R and J R Zumsteg. 1979. Analysis of bonded joints in composite material structures including hygrothermal effects, in *20th AIAA/ASME/ASCE/AHS Structures, Structural Dynamics, and Materials Conference*, St. Louis, Mo: AIAA/ASME/ASCE/AHS, 291–302.

[104] Volkersen, O. 1938. Die niektraftverteilung in zugbeanspruchten mit konstanten laschenquerschritten, *Luftfahrtforschung*, 15, 41–47.

[105] Wang, J. T., I. S. Raju, and D. W. Sleight. 1994. Fracture mechanics analyses of composite skin-stiffener debond configurations with shell elements, 94-1389 -CP.

[106] Weerts, U. and H. Kossira. 2000. Mixed mode fracture characterization of adhesive joints, in *ICAS Congress*, International Congress Aeronautical Sciences.

[107] Whitley, Karen S. and Timothy J. Collins. 2006. Mechanical properties of T650-35/AFR-PE-4 at elevated temperatures for lightweight aeroshell designs, in *Proceedings of the AIAA/ASME/ASCE/AHS/ASC 47th Structures, Structural Dynamics, and Materials Conference, May 1-4 2006, Newport RI*, American Institute of Aeronautics and Astronautics, 2006-2202.

[108] Whitney, James M. 1997. Stress analysis of a composite double-lap joint using higher order plate theory, in *Proceedings of the AIAA/ASME/ASCE/AHS/ASC 38th Structures, Structural Dynamics, and Materials Conference and Exhibit, Apr. 7-10, 1997, Kissimmee, FL*, 2004–2009.

[109] Wooley, Gary R. and Dale R. Carver. 1971. Stress concentration factors for bonded lap joints, *Journal Of Aircraft*, 8, 817–820.

[110] Xie, De and Sherrill B. Biggers, Jr. 2006. Progressive crack growth analysis using interface element based on the virtual crack closure technique, *Finite Elements In Analysis And Design*, 42(11), 977–984.

[111] Xie, De, Amit G. Salvi, Ce Sun, Anthony M Waas, and Ari Caliskan. 2006. Discrete cohesive zone model to simulate static fracture in 2d triaxially braided carbon fiber composites, *Journal Of Composite Materials*.

[112] Xie, De, Amit G. Salvi, Anthony M. Waas, and Ari Caliskan. 2005. Discrete cohesive zone model to simulate static fracture in carbon fiber textile composites, in *46th AIAA/ASME/ASCE/AHS/ASC Structures, Structrual Dynamics and Materials Conference*.

[113] Xie, De and Anthony M. Waas. 2006. Discrete cohesive zone model for mixed-mode fracture using finite element analysis, *Engineering Fracture Mechanics*, 73(13), 1783–1796.

[114] Xie, De, Anthony M. Waas, Khaled W. Shahwan, Jessica A. Schroeder, and Raymond G. Boeman. 2004. Computation of energy release rates for kinking cracks based on virtual crack closure technique, *Computer Modeling in Engineering & Sciences*, 6, 515–524.

[115] Xie, De, Anthony M. Waas, Khaled W. Shahwan, Jessica A. Schroeder, and Raymond G. Boeman. 2005. Fracture criterion for kinking cracks in a tri-material adhesively bonded joint under mixed mode loading, *Engineering Fracture Mechanics*, 72(16), 2487–2504.

[116] Xu, X.P. and A. Needleman. 1994. Numerical simulations of fast crack growth in brittle solids, *Journal Of The Mechanics And Physics Of Solids*, 42(9), 1397–1407.

[117] Yang, C, H Huang, J S Tomblin, and W Sun. 2004. Elastic-plastic model of adhesive-bonded single-lap composite joints, *Journal Of Composite Materials*, 38(4), 293–309.

[118] Yarrington, P., J. Zhang, C. Collier, and B. A. Bednarcyk. 2005. Failure analysis of adhesively bonded composite joints, in *Proceedings of the AIAA/ASME/ASCE/AHS/ASC 46th Structures, Structural Dynamics, and Materials Conference, April 18-21 2005, Austin TX*, American Institute of Aeronautics and Astronautics, 2006-1959.

[119] Zavattieri, P. D., P. V. Raghuram, and H. D. Espinosa. 2001. A computational model of ceramic microstructures subjected to multi-axial dynamic loading, *Journal Of The Mechanics And Physics Of Solids*, 49(1), 27–68.

[120] Zhang, J., B. A. Bednarcyk, C. Collier, P. Yarrington, Y. Bansal, and M. J. Pindera. 2005. 3D stress analysis of adhesively bonded composite joints, in *Proceedings of the AIAA/ASME/ASCE/AHS/ASC 46th Structures, Structural Dynamics, and Materials Conference, April 18-21 2005, Austin TX*, American Institute of Aeronautics and Astronautics, 2006-1959.

[121] Zhang, J., B. A. Bednarcyk, C. Collier, P. Yarrington, Y. Bansal, and M. J. Pindera. 2006. Analysis tools for adhesively bonded composite joints, part 2: Unified analytical theory, *AIAA Journal*, 44(8), 1709–1719.

[122] Zhang, James, Craig Collier, Yogesh Bansal, Brett A. Bednarcyk, and Marek-Jerzy Pindera. 2004. Analysis of adhesively bonded composite joints using a higher-order theory, in *45th AIAA/ASME/ASCE/AHS/ASC Structures, Structrual Dynamics and Materials Conference, April 19-22, Palm Springs CA*, 1–16.

[123] Zhou, F. and JF Molinari. 2004. Dynamic crack propagation with cohesive elements: a methodology to address mesh dependency, *International Journal for Numerical Methods in Engineering*, 59, 1–24.

Index

Li et al. [64], 36, 199
Li et al. [65], 36, 199
Li et al. [66], 76, 199
Lophaven [67], 104, 106, 200
McKay et al. [68], 105, 200
Mendels et al. [69], 9, 200
Mi et al. [70], 66, 78, 100, 131, 200
Mortensen and Thomsen [71], 9, 10, 200
Mortensen and Thomsen [72], 10, 200
Mouritz et al. [73], 10, 200
Munoz et al. [74], 36, 200
Oterkus et al. [75], 36, 65, 200
Oterkus et al. [76], 36, 65, 200
Oterkus et al. [77], 2, 200
Pandolfi et al. [78], 76, 201
Penado [79], 100, 201
Peppiatt [80], 9, 201
Pietruszczak and Mroz [81], 65, 201
Pohlit [82], 1, 201
Polaha et al. [83], 102, 201
Reedy Jr et al. [84], 76, 201
Renton and Vinson [85], 9, 201
Roudolff and Ousset [86], 78, 100, 201
Schellekens and de Borst [88], 65, 201
Schon et al. [89], 102, 201
Sen and Jones [90], 9, 10, 201
Sen and Jones [91], 9, 10, 202
Shahwan and Waas [92], 65, 202
Simulia [93], 54, 75, 202
Smeltzer III and Lundgren [94], 36, 38, 65, 202
Soffa et al. [95], 142, 146, 149, 202
Song and Waas [96], 65, 202
Song and Waas [97], 65, 202
Sridhar et al. [98], 10, 202
Sun [99], 137, 161, 169, 202
Tvergaard and Hutchinson [100], 65, 202
Ungsuwarungsri and Knauss [101], 65, 202
Valoroso and Champaney [102], 36, 66, 69, 76, 100, 202
Vinson and Zumsteg [103], 11, 202
Volkersen [104], 8–10, 103, 203
Wang et al. [105], 36, 203
Weerts and Kossira [106], 36, 203
Whitley and Collins [107], 4, 133, 137, 141, 203
Whitney [108], 10, 203
Wooley and Carver [109], 36, 65, 203
Xie and Waas [113], 36, 65, 66, 68, 76, 100, 146, 169, 203
Xie and Biggers, Jr [110], 36, 203
Xie et al. [111], 65, 203
Xie et al. [112], 36, 203
Xie et al. [114], 36, 203
Xie et al. [115], 36, 203
Xu and Needleman [116], 65, 204
Yang et al. [117], 9, 204
Yarrington et al. [118], 10, 204
Zavattieri et al. [119], 76, 204
Zhang et al. [120], 10, 204
Zhang et al. [121], 1, 10, 204
Zhang et al. [122], 10, 11, 37, 204
Zhou and Molinari [123], 65, 204
de Borst [42], 65, 198
de Borst [43], 65, 198
AECMA PREN 6034 [5], 102, 195
ASTM International [12], 24, 56, 195
ASTM International [13], 103, 122, 195
ASTM International [14], 101, 195
ASTM International [15], 103, 195
ASTM International [16], 103, 196
ASTM International [17], 169, 196